

Lehrstuhl für Computerunterstützte Klinische Medizin
der Medizinischen Fakultät Mannheim, Universität Heidelberg
unter Betreuung von Prof. Dr. rer. nat. Lothar R. Schad

- und -

Athinoula A. Martinos Center for Biomedical Imaging
des Massachusetts General Hospital, Charlestown, USA
unter Betreuung von Lawrence L. Wald, Ph.D.

Minimizing the Adverse Effects of Electric Fields in Magnetic Resonance Imaging using Optimized Gradient Encoding and Peripheral Nerve Models

Inauguraldissertation
zur Erlangung des Doctor scientiarum humanarum (Dr. sc. hum.)
der
Medizinischen Fakultät Mannheim
der Ruprecht-Karls-Universität
zu
Heidelberg

vorgelegt von
Mathias Davids

aus
Wismar

2017

Dean: Prof. Dr. med. Sergij Goerd
Instructor: Prof. Dr. rer. nat. Lothar R. Schad

Abstract

Magnetic Resonance Imaging (MRI) is an important imaging modality in both the clinic and in research. MRI technology has been trending toward increasing field strengths to improve the signal-to-noise ratio of the MR signal and fast excitation/encoding strategies to more flexibly target anatomical regions during excitation to reduce the total imaging time. While largely successful, both strategies rely on the application of increasingly strong and rapidly switched magnetic fields: the radio frequency (RF) field for excitation and the gradient field for encoding. The technology for generating these fields (and rapidly switching them) has advanced to the point that we are limited by biological responses to the switching fields. For the gradient field, the electric field generated in the tissue causes peripheral nerve stimulation (PNS) causing mild but bothersome sensations at low levels, up to pain or cardiac malfunction at higher levels. The electric fields created by the much faster time-varying RF cause heat deposition, ultimately denaturing proteins and causing tissue damage. In this thesis, methods are presented to characterize and minimize these two problems associated with the switched magnetic fields in MRI. The deposited RF energy (Specific Absorption Rate, SAR) incurred during shaped excitations can be significantly reduced by optimizing gradient and RF waveforms for inner-volume excitations that allow imaging of a sub-volume of the body without wrapping artifacts. The adverse effects of the switching gradient fields are addressed by designing time-optimal gradient encoding waveforms and by developing a method to predict and characterize PNS using field simulations and a full-body nerve model allowing these critical effects to be addressed at the gradient coil design stage. In the first part, time-optimal gradient trajectories are demonstrated that use the gradient hardware at the maximum available performance. The skeleton of the trajectory is defined by a set of k -space control points. The method optimizes gradient waveforms that traverse the k -space control points in the minimum possible amount of time. By using an analytic representation of the gradients (piece-wise linear), the design process is fast and numerically robust. The resulting trajectories sample k -space efficiently while using the gradient system at maximum performance. Compared to the leading Optimal Control method, the proposed method generates gradient waveforms that are 9.2% shorter. The computation process is $\sim 100\times$ faster and does not suffer from numerical instabilities such as oscillations. In the second part, a method is developed that jointly optimizes parallel transmission RF and gradient waveforms for fast and robust 3-D inner-volume excitation of the MRI signal in minimal time and with minimal energy deposition. The optimization of the k -space trajectories is based on a small number of shape parameters that are well-suited for joint optimization with the RF waveforms. Within each iteration of the trajectory optimization, a small tip-angle least-squares RF pulse design problem is solved. Using optimized 3-D cross (shells) trajectories, a cube shape (brain shape) region was excited with 3.4% (6.2%) NRMSE in less than 5 ms using a 7 T scanner with 8 Tx channels and a clinical gradient system ($G_{\max} = 40$ mT/m, $S_{\max} = 150$ T/m/s). Incorporation of off-resonance robustness in the pulse design significantly altered the k -space trajectory solutions and improved the practical performance of the pulses. In the final part, a framework is presented that simulates PNS thresholds for realistic gradient coil geometries and thus allows, for the first time, to directly address PNS in the coil design process. The PNS framework consists of an accurate body model for simulation of the induced electric fields, an atlas of peripheral nerves, and a neurodynamic model to predict the nerve responses to imposed electric fields. With this model, measured PNS thresholds of two leg/arm solenoid coils and three commercial actively-shielded MR gradient coils could be reproduced with good accuracy. The proposed method can be used to assess the PNS capability of gradient coils during the design phase, without building expensive prototype coils.

Kurzfassung

Die Magnetresonanztomographie (MRT) ist eine bedeutende Bildgebungsmodalität in Klinik und Forschung. Die MRT-Technologie strebt zu höheren Feldstärken zur Verbesserung des Signal-Rausch-Verhältnis sowie zu schnellen Anregungs-/Auslesetechniken mittels räumlich selektiver Radiofrequenzpulse (RF), um anatomische Regionen flexibler anzuregen und die Signalakquise zu beschleunigen. Beide Ansätze sind sehr erfolgreich, erfordern jedoch das immer schnellere Schalten immer stärkerer Magnetfelder, namentlich der RF-Felder (Anregung) und der Gradientenfelder (Ortskodierung). Die Technologie zur Erzeugung/Modulation dieser Felder ist soweit fortgeschritten, dass deren Nutzbarkeit durch Interaktionen mit dem menschlichen Körper stark eingeschränkt ist. Das schnelle Schalten der Gradientenfelder induziert elektrische Felder die periphere Nerven stimulieren können (PNS), was zu leichten Empfindungen bis hin zu Schmerzen und Herzrhythmusstörungen führen kann. Die RF-Felder erzeugen hochfrequente elektrische Felder die das Gewebe stark erwärmen und schädigen können. In dieser Arbeit werden Methoden entwickelt, um die Effekte ungewünschter elektrischer Felder in der MR zu modellieren, vorherzusagen und zu reduzieren. Die Gewebeerwärmung bei räumlich-selektiven Anregungen kann erheblich verringert werden durch die Optimierung der Ortskodierung sowie der RF-Pulse. Die unerwünschten Effekte der Gradientenfelder können vermindert werden durch zeit-optimierte Gradientenverläufe sowie durch ein neuartiges Verfahren das mittels elektromagnetischer Feldsimulationen und neurodynamischer Modelle PNS vorhersagen und charakterisieren kann. Im ersten Teil der Arbeit wird ein Verfahren entwickelt zur Generierung zeit-optimaler Gradientenverläufe, die die Leistungsfähigkeit des Gradientensystems optimal ausnutzen. Die Gradientenverläufe werden derart generiert, dass die resultierenden Trajektorien vordefinierte Stützpunkte im k -Raum in möglichst kurzer Zeit abtasten. Durch die Verwendung semi-analytischer Gradientenverläufe (stückweise linear) ist das Verfahren sehr schnell und numerisch stabil. Die Trajektorien tasten den k -Raum sehr effizient ab, ohne das Gradientensystem zu überlasten. Im Vergleich mit Standard-Verfahren sind die erzeugten Gradientenverläufe im Mittel 9.2% kürzer. Das Berechnungsverfahren ist bis zu 500-fach schneller und nicht anfällig für numerischen Instabilitäten wie Gradientenoszillationen. Im zweiten Teil der Arbeit wird eine Methode vorgestellt, die Gradientenverläufe und RF-Pulse simultan optimiert und dadurch sehr kurze, akkurate und robuste 3-D selektive Anregungspulse mit minimaler Gewebeerwärmung generiert. Die Optimierung der Gradientenverläufe basiert auf einer effizienten Beschreibung der Trajektorien durch Formparameter die sich numerisch sehr gut optimieren lassen. Während jeder Iteration der Formparameter-Optimierung wird ein Least-Squares RF-Puls berechnet. Mittels optimierter 3-D "Cross" ("Shells") Trajektorien wurden würfelförmige (bzw. hirnformige) Zielvolumen mit lediglich 3.4% (6.2%) NRMSE in < 5 ms mit einem 7 Tesla Scanner, acht Sendekanälen sowie einem klinischen Gradientensystem angeregt ($G_{\max} = 40$ mT/m, $S_{\max} = 150$ T/m/s). Das Einbeziehen statischer Feldvariationen in die Pulsoptimierung hatte einen großen Einfluss auf die Trajektorien. Im letzten Teil der Arbeit wird ein Verfahren entwickelt, das PNS Schwellwerte für realistische Spulengeometrien simuliert und damit erstmals eine direkte Einbeziehung von PNS in den Designprozess der Spule ermöglicht. Das Verfahren besteht aus einem detaillierten Körpermodell zur Simulation der induzierten elektrischen Felder, einem Atlas der peripheren Nerven sowie einem neurodynamischen Modell zur Vorhersage der Nervenreaktionen auf die elektrischen Felder. Mit diesem Modell konnten gemessene PNS Schwellwerte von zwei Bein/Arm Solenoidspulen sowie von drei kommerziellen aktiv-geschirmten Ganzkörper MR-Gradientenspulen mit guter Genauigkeit reproduziert werden. Dieses Simulationsverfahren erlaubt es, mögliche PNS durch MR-Gradientenspulen während der Entwurfsphase zu evaluieren, ohne teure Prototypspulen zu bauen.

Contents

1	Introduction	1
2	Theory	7
2.1	Basics of MR Signals	7
2.1.1	Electromagnetic Spin and MRI Basics	7
2.1.2	Bloch-Equation	9
2.1.3	Relaxation Effects	12
2.1.4	Slice-selective Excitation	13
2.1.5	Image Acquisition	16
2.1.6	The k -Space Formalism	17
2.2	State-of-the-Art RF Pulse Design	19
2.2.1	Multi-dimensional Excitation	19
2.2.2	Parallel Imaging and Sensitivity Encoding	22
2.2.3	Parallel Excitation: Transmit SENSE	24
2.2.4	RF Waveform Calculation	26
2.3	Simulation of Electromagnetic Fields	29
2.3.1	Maxwell's Equations	30
2.3.2	The Finite Difference Time Domain Method	31
2.3.3	The Finite Element Method	34
3	Methods	43
3.1	Optimal Gradient Waveform Design	43
3.1.1	Problem Formulation	43
3.1.2	Gradient Basis Functions	44
3.1.3	The Domain Mapping D and the Solution Mapping S	47
3.1.4	Global Trajectory Design	49
3.1.5	Further Constraints	52
3.1.6	Analytic Derivatives	53
3.1.7	Continuity and Differentiability	55
3.1.8	Convexity and Stationary Points	57
3.1.9	Formal Complexity	61

3.2	Joint Optimization of Gradient and RF Waveforms	62
3.2.1	Optimization Strategy	62
3.2.2	Parameterization of 3-D k -space Trajectories	64
3.2.3	Integer Shape Parameters	71
3.2.4	Gradient Trajectory Design	71
3.2.5	Evaluation of the Proposed Method	72
3.3	Off-resonance Robust Slice Excitation	75
3.3.1	Spokes Pulses	75
3.3.2	The Corkscrew Trajectory	77
3.3.3	Slice-Selective RF Pulse Design	79
3.3.4	Evaluation of the proposed Method	82
3.4	Prediction of Magnetostimulation Thresholds	83
3.4.1	Workflow	83
3.4.2	Surface Body Model	83
3.4.3	Nerve Atlas	86
3.4.4	Integrity of Body Model and Nerve Atlas	87
3.4.5	Nerve Membrane Model	88
3.4.6	Generation of PNS Threshold Curves	89
3.4.7	Preliminary Sensitivity Analysis	91
3.4.8	Validation against Experimentally Measured Thresholds	91
3.4.9	Sinusoidal vs. Trapezoidal Waveforms	92
3.5	PNS Simulations of Whole-Body Gradient Coils	93
3.5.1	Electromagnetic Field Simulation	93
3.5.2	Experimental Data and PNS Simulations	94
4	Results	97
4.1	Design of Optimal Gradient Waveforms	97
4.1.1	Design of a 2-D Spiral Trajectory	97
4.1.2	Comprehensive Evaluation using Random Trajectories	98
4.1.3	Numerical Stability I: Control Point Traversal	99
4.1.4	Numerical Stability II: Gradient Constraints	101
4.1.5	Three-dimensional Examples	103
4.2	Three-Dimensional Spatially Selective Excitations	105
4.2.1	Convexity Analysis	105
4.2.2	Trajectory Optimization	106

4.3	Off-resonance Robust Slice Excitation	113
4.3.1	Spokes RF Pulses	113
4.3.2	Corkscrew RF Pulse	114
4.4	Prediction of Magnetostimulation Thresholds	116
4.4.1	Neurodynamic Model Stimulation	116
4.4.2	Effect of Fiber Diameter	116
4.4.3	PNS Simulations in the Leg and Arm Solenoid Coils	118
4.4.4	Sinusoidal vs. Trapezoidal Waveforms	120
4.5	Simulated PNS Thresholds for Gradient Coils	121
4.5.1	Magnetic Fields	121
4.5.2	Electric Fields	122
4.5.3	E-Fields along Nerve Fibers	122
4.5.4	Simulated vs. Measured PNS Thresholds	124
5	Discussion	127
5.1	Optimal Gradient Waveform Design	127
5.2	Joint Gradient and RF Optimization	129
5.3	Prediction of Magnetostimulation Thresholds	131
6	Summary	137
	Bibliography	141
	Curriculum Vitae	151
	Acknowledgments	155

1

Introduction

Magnetic resonance imaging (MRI) has become one of the most important radiographic methods for diagnosing medical problems as well as planning and following their treatment. MRI starts with the excitation of the nuclear spins in water using an applied resonant radiofrequency (RF) pulse. The excitation phase is followed by the reception of the signal emitted by the spins during their decaying precession. The resonance frequency of the spins is determined by the strength of the total applied magnetic field as per the well-known Bloch relation [6]. Typically the applied field consists of a static magnetic field (usually 1.5 to 7 Tesla) together with the brief RF field pulse for excitation followed by a time-varying magnetic field gradient (in the kilohertz frequency range). Spatial encoding is performed by superimposing this time varying field gradient component to the magnetic field. The presence of this field alters the resonance frequency of the spins as a function of space, linking its spatial position to its precession frequency. These linear gradient field variations are created along the three spatial axes using three distinct gradient coils in order to spatially encode the 3-D space.

Applying the linear field gradients for a certain amount of time will generate a 3-D phase pattern in the nuclear spin magnetization. A single field gradient applied for a brief time period causes the phase pattern to correspond to a harmonic wave whose spatial frequency and normal direction are determined by the strength and direction of the imposed gradient field. The signal which survives this modulation is a sample of the objects intensity variation at that spatial frequency. Therefore, by varying the direction and strength of the MRI gradient coils, one can explore a signal space called "*k*-space" [118]. If sufficiently sampled, the signal matrix is a Fourier representation of the object's intensity pattern and the image is simply reconstructed by an inverse Fourier transform. The acquisition of *k*-space is performed along a path called *k*-space trajectory which is determined by the time integral history of the gradient waveforms.

A similar mechanism holds for the excitation (at least in the small flip-angle excitation regime) [86], where excitation *k*-space is sampled along a trajectory determined by the reversed time integral history of the excitation gradients (although the two concepts are similar, excitation and signal reception *k*-spaces are completely distinct and different). In both cases, it is preferable to sample *k*-space very quickly in order to avoid magnetization decay. Indeed, magnetization decay during excitation makes the excitation design and analysis much more complex as it introduces non-uniform T_1 and T_2 weighting across the image in a way that is difficult to predict. Although often the magnetization is sampled after a controlled delay designed to induce a source of image contrast, it is also generally not desirable to have contrast changes during the image readout. Decay during the readout does occur in encoding intensive sequences such as echo-planar imaging (EPI) and often it's desirable to speed up the readout as much as possible and to under-sample

k -space and reconstruct with parallel imaging methods to shorten the encoding period. The speed at which excitation and reception k -space can be fully sampled is dictated by the performance limits of the gradient coils (namely the achievable strength of the gradient fields, G_{\max} , and the maximum temporal rate of change for the gradient field called slew rate, S_{\max}). But increasingly the full capabilities of the gradient system cannot be used due to the physiological effects from rapidly switching gradients on the human body, i.e., peripheral nerve stimulation (PNS).

In light of the increasing problems caused by the time-varying fields used in MRI, this thesis focuses on the development of algorithms and methods to mitigate them through the design of RF/gradient waveforms and the detailed study and quantification of the PNS effect in gradient coils. Specifically, the following aspects of gradient encoding and coil engineering are presented:

- (i) A method for the design of time-optimal (i.e., fastest achievable) gradient waveforms given the gradient coil performance specifications [28, 26]
- (ii) A framework for the design of optimal gradient and RF waveforms for robust excitation of complex 3-D magnetization shapes within 5 ms using parallel transmission which limit the deposited energy associated with the RF fields [27, 29, 30, 32]
- (iii) Development and validation of a simulation pipeline for prediction of PNS thresholds and locations caused by rapidly switching magnetic fields in a realistic human body model [31, 34, 33]

The First Part of this thesis investigates gradient waveform design approaches that make optimal use of the gradient system constraints (G_{\max} and S_{\max}). For simple types of k -space sampling trajectories (like echo-planar trajectories or analytic spirals), analytic expressions of time-optimal gradient waveforms have been known for decades. For more complex k -space sampling strategies (such as 3-D trajectories), however, the gradient waveform design problem is more complex. The main reason for this complexity are the gradient system strength and slew rate constraints which render the optimal gradient design problem non-linear.

Several approaches have been proposed over the years in an attempt to solve the gradient trajectory design problem. Simonetti et al. [109] and Hargreaves et al. [55] used a discretization of the gradient waveforms using fine time steps and performed a constrained optimization of the gradient samples, subject to the gradient system constraints and k -space constraints (such as traversal of certain control points in k -space). Such a discretization approach, however, leads to a huge number of degrees-of-freedom to be optimized (especially for longer gradient waveforms), resulting in large computation times and numerical perturbations (the resulting problem is mathematically ill-conditioned). Dale et al. [22] used a Hamiltonian formulation of the gradient design problem to derive analytic solutions for simple one-dimensional waveforms. The Hamiltonian, however, becomes increasingly difficult to solve in multiple dimensions, which very often does not permit to design 2-D or 3-D gradient waveforms. A Gold-Standard method for the design of fast gradient waveforms is the Optimal Control method proposed by Lustig et al. [71, 120], that computes time-optimal gradient waveforms along a pre-defined k -space path constraint. The path constraint is usually obtained by interpolating a set of control points in k -space. For very smooth path constraints this method works well, however, in regions where the path constraints have sharp turns, this approach becomes extremely sensitive to numerical errors. This causes significant distortions of the waveforms (in terms of oscillations), resulting in violations of the gradient system constraints. Additionally, the method is computationally very expensive and the k -space constraint is overly restrictive, i.e., the method disregards strictly time-optimal solution.

In this work a method is developed that generates time-optimal gradient waveforms subject to gradient magnitude and slew rate constraints. The gradient waveform is designed such that the associated trajectory passes through an ordered set of control points in k -space. The gradient waveforms are assembled by piece-wise linear segments and are represented in a semi-analytic manner. This strategy achieves significantly reduced computation times and very high numerical stability and thus generates practically feasible gradient waveforms.

The Second Part analyzes the problem of the joint optimization of gradient and RF waveforms for the excitation of complex 3-D magnetization shapes. In MRI, spin excitation is usually performed using either spatially non-selective or slice- or slab-selective RF pulses. In some applications, it may be beneficial, however, to excite more complex 3-D magnetization shapes than slabs or slices. For example, excitation of cubic target regions may be used to reduce the volume that needs to be encoded using gradients in order to form an image. This may result in shorter acquisition times (TA) at constant resolution or, equivalently, improved resolution at constant TA, as well as reduction of the echo train length [76, 111]. Other applications could benefit from exciting volumes of magnetization that are not necessarily cubic. For example, vessel-specific arterial spin labeling (ASL) could be performed by inversion of the spins flowing in a specific artery to enhance existing ASL territory mapping techniques [57]. Another potential application of non-cubic spatially selective excitations is fat suppression in spectroscopic imaging by excitation of the brain only [64].

A simple approach for excitation of a cubic target region in spin-echo pulses is to excite the spins (90° pulse) in one slice, followed by refocusing of an orthogonal slice [11]. This strategy is limited to rectangular target profiles and spin-echo pulses (a significant exception is the STEAM pulse that uses a series of slice-selective excitation pulses in orthogonal directions for 3-D rectangular localization of the stimulated echoes [39, 50]). It has long been recognized that 2-D and 3-D spatial excitations of arbitrary shapes can be achieved by design of the RF and gradient waveforms used for excitation [53, 9, 65, 112]. However, the potential of these approaches has not yet been realized clinically because of the long duration of the resulting waveforms.

Schneider et al. [106] designed fast (3.2 ms) 3-D shells and stack-of-spirals trajectories for excitation of small target regions (rat brain and kidneys) using a powerful gradient system for small animal imaging ($G_{\max} = 660$ mT/m, $S_{\max} = 5600$ T/m/s). Malik et al. [72] attempted to extend this approach to a clinical imaging system with lower gradient performance ($S_{\max} = 180$ T/m/s), and used pTx to accelerate the excitation pulse (8 channels). Using unoptimized 3-D shells trajectories, they were able to excite cubic regions of reasonable quality in 12 ms. This pulse duration is still relatively long despite the pTx acceleration, which makes the resulting pulse sensitive to off-resonance effects (the authors minimized this problem by using the pulse in a turbo spin-echo sequence with non-selective refocusing pulses).

This previous work shows that pTx can help reduce the duration of these complex pulse excitations, but the problem of exciting arbitrary 3-D magnetization patterns is extremely demanding for conventional 8-channel pTx systems and additional degrees-of-freedom are needed. Increasing the number of transmit channels and using a gradient system with better performance can help, but this is costly. Another source of degrees-of-freedom is the k -space trajectory itself. Chen et al. [16] attempted to exploit the excitation degrees-of-freedom in the k -space trajectory by parameterizing 2-D k -space trajectories with approximately 150 control points, the positions of which were optimized using a greedy optimization approach. This process resulted in highly convoluted trajectories with many turns that are not efficient from a k -space sampling and gradient performance perspective. Deniz et al. [35] and Sun et al. [113] extended this approach

to 3-D selection. Like in the 2-D work of Chen et al., the highly convoluted nature of the resulting gradient waveforms limited the quality of the excitations (15% normalized root-mean-square-error, NRMSE) achievable in a short time (3.8 ms). Additionally, no information about the performance of such pulses in presence of off-resonance effects is given (the measurements shown in [16, 35, 113] were performed in homogeneous spherical or cylindrical phantoms that are easy to shim).

In this work, a framework is presented that allows designing ultra-short (less than 5 ms) 3-D spatially selective RF pulses with excellent spatial selection quality profiles, constrained peak powers and intrinsic robustness to off-resonance effects. This latter constraint is essential for clinical translation, as trajectories not robust to off-resonance effects are not useful in practice. The proposed framework uses an efficient parameterization of k -space trajectories which greatly reduces the dimensionality of the gradient optimization problem while preserving enough degrees-of-freedom for the optimizer to dramatically improve the excitation quality. The framework is demonstrated for two inner-volume excitation targets (cube and brain shaped targets) using Bloch simulations and experiments at 7 Tesla. An extension of the framework is presented and demonstrated that allows to design robust RF pulses for uniform slice-excitation in presence of severe off-resonance effects.

The Third Part of this thesis is, to the authors knowledge, the first ever published simulation pipeline for prediction of the physiological effects of rapidly switching gradient fields in a realistic body model. Since MRI gradient coils must be switched rapidly (at 100-2000 Hz) to image quickly, the time-varying magnetic field generates electric fields inside the body which can interact with the nerves, causing peripheral nerve stimulation (PNS). The PNS sensations range from tingling to, at extremely high switching speed that are not accessible to most clinical MRI scanners, severe pain. In modern MRI scanners with fast switching gradient amplifiers, PNS typically limits imaging speed [18, 43]. Most clinical MRI scanners have monitoring software and hardware to ensure that the switching gradients will not cause painful PNS. These monitors are calibrated by performing clinical stimulation studies in healthy subjects to measure the thresholds at which the gradient coil design induces PNS. In these studies, gradient waveforms with different lengths and shapes are used to obtain characteristics PNS thresholds curves. The time derivative of the waveforms planned for use in a patient study is then analyzed in a number of different frequency bands and compared to a similar analysis of the empirical curves to estimate the waveform's potential for stimulation [56].

Despite the importance of PNS as the practical limitation to use of high-performance MR gradient system in humans, the current "design-build-test" engineering cycle for gradient coils does not allow PNS considerations to guide the design of the gradient coils. Instead, PNS is controlled indirectly by controlling the size of the linear region of the gradient coil. It was found that the PNS threshold parameters (i.e., field threshold amplitude and chronaxie of the stimulation threshold curve) vary in an inverse linear manner with the size of the linear region [128]. The development of a robust method for estimating magnetostimulation would potentially allow PNS to be incorporated more directly into the coil design optimization phase. At present, MRI gradient coils are optimized numerically by simulating the current distribution on the coil former so as to achieve the target magnetic field (i.e., a linear gradient field pattern) [117]. Additional penalty terms are included to reduce energy consumption [100], improve heat dissipation [88], and simplify the manufacturing process [51]. In this framework, a PNS threshold predictor or "oracle" may be added as an additional penalty term in evaluating a design, potentially uncovering

geometries with significantly increased PNS thresholds. In Magnetic Particle Imaging (MPI), PNS is also a significant barrier that must be addressed to scale current scanner designs from the small animal dimension to human scale. The ability to calculate PNS thresholds for any gradient coil design might also be useful in evaluating specific situations where workers are exposed to time-varying magnetic and electric fields. Finally note that there are applications where coils are designed specifically to achieve stimulation of nerve fibers, for example transcranial magnetic stimulation (TMS) [46] and nerve conduction studies (NCS) [24] to evaluate the viability of motor and sensory nerves. These applications could also benefit from a realistic PNS threshold simulation framework.

The phenomenon of PNS arises from the interaction of the electric fields created by the coil with the nerve fibers in the human body [13, 19]. If an electric potential gradient is applied to a nerve, the nerve membrane will be charged electrically (depolarization or hyperpolarization). In case of a strong depolarization, an unwanted action potential (AP) will be initiated, that results in muscle contractions and sensory perceptions. If the applied potential is increased beyond this initial perception threshold, adverse effects can be generated such as pain, stimulation of the central nervous system (possibly triggering seizures), and stimulation of the autonomic nerves which might trigger adverse effects such as cardiac nerve stimulation (possibly causing arrhythmia). The mechanisms behind action potential generation by applied voltage potentials have been well understood for decades [75, 63, 42, 94, 17, 1]. For the magnetostimulation problem, the applied magnetic field is typically known. Based on this magnetic field, many approaches have used analytic or semi-analytic methods in order to describe the induced electric field and its effect on the nerve membrane [97, 25, 98, 15, 125], but analytic solutions are restricted to simple geometries (like a cylindrical geometry) and not applicable to complex structures of differing electrical properties such as those found in the body. Zhao et al., So et al., and Mao et al. studied the electric field pattern in a body model with heterogeneous electrical properties and used the electric field strength as a PNS threshold measure [129, 110, 77]. This is likely to mis-estimate PNS thresholds since it does not account for the fiber orientation relative to the electric field or the possible lack of nerve fibers in the peak E -field locations. A more accurate approach to assess the electric fields in the body is to use heterogeneous tissue models in conjunction with nerve membrane models to investigate the mechanism of magnetostimulation [67, 87, 91]. In these works, the simulations have been performed based on simplified nerve segments which does not allow for PNS threshold prediction unless it is a priori known that the analyzed segment has the lowest threshold in the body. Very recently, functionalized anatomical models have been introduced by Neufeld et al. [82, 81] where the nerve fibers were extended to study segments of the ulnar and sciatic nerves. While providing valuable insights about different neurodynamic model approaches and the effect of tissue heating on the excitability of nerve fibers, the limited nature of the nerve model precluded the calculation of general PNS thresholds. Comparison to experimental data was limited to these few nerve segments. In order to predict the stimulation thresholds that a person would experience from the magnetic and electric fields created by a specific coil winding pattern, a complete model of the peripheral nervous system is needed together with the map of the time-varying E -fields created by the coil within the conductive body model.

In this work, a framework is developed to predict magnetostimulation thresholds for realistic coil geometries. A realistic depiction of the peripheral nervous system is utilized, labeled with the relevant parameters of each segment's equivalent circuit model. The PNS model is embedded in a realistic body model of the body tissues, each labeled with its electrical properties. This

allows for the calculation of the internal time-varying electric fields experienced by the nerves. Knowing the relative geometry of the induced electric field to the nerve and the nerve's size and membrane parameters enable to estimate the location and threshold for the first action potentials generated by the applied fields. Increasing the strength of the electric field until an action potential is observed provides a measure of the maximum drive current and voltage that can be applied to the coil without causing PNS. Performing this simulation for different coil designs allows for comparison of the design's PNS thresholds during the design/optimization stage, prior to coil construction.

2

Theory

2.1 | Basics of MR Signals

2.1.1 Electromagnetic Spin and MRI Basics

The physical basis of nuclear magnetic resonance (NMR) and magnetic resonance imaging (MRI) is the electromagnetic spin – a quantum-mechanical entity of angular momentum inherent to elementary particles, composite particles, and atomic nuclei. This entity is equivalent to the force phenomenon that rotating bodies experience in presence of an external force field. A precessing body reacts to an external force field (e.g., the gravitational field of the earth), in a way that the rotation axis starts to rotate around an axis parallel to the gravitational field (i.e., the direction of the experienced force is given by the cross product of these two axes). This holds, if the rotation axis of the body and the gravitational axis enclose an angle unequal to zero. The enclosed angle induces a force pointing away from both the axis of the rotating body and the axis perpendicular to the gravitational force field. Due to the inertia of the rotating body, however, the body experiences a compensatory movement tangential to the circular movement of the axis. As the axis reacts on this force with a finite movement that changes the axis itself, the direction of the force rotates as the axis moves. The induced circular movement of the axis around the direction of the gravitation is called *precession*.

An analogue of the mechanical precession of the inert body due to the gravitational force is present for particles that possess the above mentioned quantum-mechanical spin. The spin is associated with a magnetic dipole moment that induces a precession around an external magnetic field. Two significant differences can be identified compared to the mechanical spin described above that allow the electromagnetic spin to be employed for imaging purpose, as it is done in MRI.

Contrarily to the mechanical spin, the *quantum mechanical* spin cannot take arbitrary values. In fact, in presence of an external magnetic field, the spectrum of energies (each arising from the magnetic dipole moment) is split into discrete components, each of which associated with a different potential energy level. This phenomenon of discrete energy splitting is called the *Zeeman* effect. The number N of valid energy levels depends on the particle's spin l and is given by

$$N = 2l + 1 . \tag{2.1}$$

Each energy state is associated with the *magnetic quantum number* m , given by

$$m = -l, -l + 1, \dots, l - 1, l . \quad (2.2)$$

For protons having a spin of $l = 1/2$, this results in $N = 2$ discrete energy levels with magnetic quantum numbers $m_1 = -1/2$ and $m_2 = +1/2$ that the spin can take. The energy level itself is linked to the quantum number via

$$E_m = -\gamma \hbar m B_0 \quad (2.3)$$

where \hbar denotes the Planck constant and B_0 denotes the external static magnetic field strength. The gyromagnetic ratio γ is defined as the ratio of a particle's magnetic dipole moment to its angular momentum and has, in the case of protons with a spin of $l = 1/2$, a value of $\gamma = 42.6$ MHz/T. For particles that populate the lower energy level E_1 the spin is aligned parallel to the magnetic field; spins in the higher energy level E_2 are aligned anti-parallel.

The equilibrium distribution of these energy states in a macroscopic probe is determined by Boltzmann statistics:

$$\frac{N_{\uparrow}}{N_{\downarrow}} = \exp\left(\frac{-\Delta E}{k_B T}\right) . \quad (2.4)$$

In the above equation, N_{\uparrow} and N_{\downarrow} denote the relative amount of spins populating the parallel and anti-parallel energy level, respectively, ΔE denotes the difference between the respective energy levels, k_B denotes the Boltzmann constant and T denotes the temperature in Kelvin. The relative difference is (in first approximation) proportional to the external field strength and inversely proportional to the temperature [49]. The ratio between spins populating the parallel and anti-parallel states, respectively, is very close to 1, but it is not 1. The difference between the two energy levels is approx. 6.6 ppm at room temperature (37 °C) in presence of an external magnetic field with $B_0 = 1$ T. The overhead of spins populating the parallel state over the anti-parallel state creates a measurable equilibrium magnetization which is aligned along the external magnetic field, referred to as *longitudinal* magnetization.

Although, on a microscopic level, the precessing spins do possess a magnetization component perpendicular to the static magnetic field, i.e., in the *transverse* plane, the macroscopic transverse magnetization of the entire spin compartment remains zero as long as the individual spins precess non-resonantly (i.e., the spins are out of phase). In this case the individual transverse magnetization components cancel each other statistically. If, on the other hand, an electromagnetic field with a suitable frequency is applied to the probe, given by the precession frequency of the proton, the Larmor frequency $\omega = \gamma B_0$, resonant absorption leads to an energy transfer to the spin system. This energy transfer has two major effects on the macroscopic magnetization:

- (i) The spin collective starts to precess resonantly, creating a non-zero macroscopic magnetization component in the transverse plane that precesses around the static field axis by the Larmor frequency.
- (ii) The distribution of the two energetic levels of the spin compartment (parallel and anti-parallel) is changed, which alters the longitudinal magnetization component (i.e., the spin collective is not in the equilibrium state as determined by the Boltzmann statistics).

The two distinct magnetization components (the rotating transverse vector component and the longitudinal vector component) add up, yielding a macroscopic 3-D magnetization vector.

Despite the 3-D nature of the probe's magnetization, it is the transverse component (i.e., the component in a 2-D plane) which is measurable by Faraday induction.

Over time, the excited probe returns to the equilibrium state via *relaxation*. In this equilibrium state only a longitudinal magnetization component is present. Each component (transverse and longitudinal component) experiences a temporally different relaxation phenomenon. Either of these relaxation effects is a decisive characteristic of the probe and varies spatially with different properties of the probe. Along with the locally varying magnitude of the 3-D magnetization vector right after excitation (this magnitude is associated with the number of excitable spins, i.e., the *proton density*), these characteristics are exploited in MRI to generate images with exceptional contrast.

The processes in NMR and MRI that have been described phenomenologically – the precession of the spin compartment, the effect of resonant electromagnetic radiation, the two distinct magnetization components, as well as the relaxation effects – are described by a fundamental differential equation that is introduced in the following section. This differential equation will be characterized in detail, and a strong focus will be placed on the effect of MR gradient fields.

2.1.2 Bloch-Equation

On the *microscopic* scale (i.e., considering a single nuclei), the mechanisms of spin precession are based on quantum mechanics and, therefore, need to be treated as such. On the *macroscopic* scale, however, the large number of spins under consideration allows for a description via classical physics. The basic formulation of this macroscopic description is the so called *Bloch-equation* [6, 49]

$$\frac{d}{dt}\mathbf{M} = \gamma(\mathbf{M} \times \mathbf{B}). \quad (2.5)$$

where $\mathbf{M} = (M_x, M_y, M_z)$ denotes the vector of the macroscopic magnetization and $\mathbf{B} = (B_x, B_y, B_z)$ denotes the magnetic field strength. Equation 2.5 describes a system of coupled linear differential equations that temporally links the magnetization vector \mathbf{M} and the applied magnetic field vector \mathbf{B} . As was mentioned before, a static magnetic field B_0 is used to create a precessing spin collective along the static field. The orientation of the static magnetic field along the spatial z -axis separates the three dimensional magnetization vector M into two components, the *longitudinal* magnetization parallel to the B_0 field and the *transverse* magnetization which is oriented perpendicular to the B_0 field. The longitudinal and transverse components experience different relaxation effects that can be quantified by time constants T_1 and T_2 , respectively. These time constants T_1 and T_2 can be incorporated into the Bloch equation, yielding

$$\frac{dM_x}{dt} = \gamma [\mathbf{M} \times \mathbf{B}]_x - \frac{M_x}{T_2} = \gamma [M_y B_z - M_z B_y] - \frac{M_x}{T_2}, \quad (2.6a)$$

$$\frac{dM_y}{dt} = \gamma [\mathbf{M} \times \mathbf{B}]_y - \frac{M_y}{T_2} = \gamma [M_z B_x - M_x B_z] - \frac{M_y}{T_2}, \quad (2.6b)$$

$$\frac{dM_z}{dt} = \gamma [\mathbf{M} \times \mathbf{B}]_z - \frac{M_z - M_0}{T_1} = \gamma [M_x B_y - M_y B_x] - \frac{M_z - M_0}{T_1}. \quad (2.6c)$$

The transverse entities (i.e., those in the x - y -plane) in this system of equations are commonly combined into a single complex formulation for the transverse magnetization M_{\perp} and the magnetic field component B_{\perp} as

$$M_{\perp} = M_x + iM_y \quad \text{and} \quad B_{\perp} = B_x + iB_y . \quad (2.7)$$

Using the complex notation, the Bloch equations reduce to

$$\frac{dM_{\perp}}{dt} = -i\gamma [M_{\perp}B_z - M_zB_{\perp}] - \frac{M_{\perp}}{T_2} , \quad (2.8a)$$

$$\frac{dM_z}{dt} = -i\gamma [M_{\perp}B_{\perp}^* - M_{\perp}^*B_{\perp}] - \frac{M_z - M_0}{T_1} , \quad (2.8b)$$

where i denotes the complex number and $(\cdot)^*$ denotes the complex conjugate. Assuming that no magnetic field other than the static magnetic field is present ($B_z = B_0$ and $B_{\perp} = 0$) and further neglecting any relaxation effects, i.e., $T_1, T_2 \rightarrow \infty$, Eqs. 2.8a and 2.8b become

$$\frac{dM_{\perp}}{dt} = -i\gamma M_{\perp} B_0 \quad \text{and} \quad (2.9a)$$

$$\frac{dM_z}{dt} = 0 , \quad (2.9b)$$

respectively. These are uncoupled linear differential equations that can be solved very easily, yielding

$$M_{\perp}(t) = (M_{\perp})_0 e^{-i\gamma B_0 t} , \quad (2.10a)$$

$$M_z(t) = (M_z)_0 = \text{const} . \quad (2.10b)$$

Equation 2.10a illustrates that the static magnetic field B_0 gives rise to a precession of the transverse magnetization component M_{\perp} around the z -axis. The rotation proceeds at an angular velocity

$$\omega = \gamma B_0 , \quad (2.11)$$

that is referred to as the *Larmor frequency*. This B_0 -induced precession is constant over time and complicates the mathematical treatment of the magnetization. Fortunately, the rotation can be dropped from the Bloch equation without impairing its validity. This can be achieved by introducing a *rotating frame of reference*, in which the transverse magnetization M_{\perp} is rotated at an angular velocity of Ω while the longitudinal magnetization M_z is kept unaltered. In this rotating coordinate system, the effect of the static field B_0 on the magnetization vector \mathbf{M} vanishes if $\Omega = \omega$. The transformed equations of the longitudinal and transverse magnetization read

$$M'_{\perp}(t) := e^{i\Omega t} M_{\perp}(t) , \quad (2.12a)$$

$$M'_z(t) := M_z(t) . \quad (2.12b)$$

The Bloch equation for the transverse magnetization component, complemented by the rotating frame transformation (by substituting Eq. 2.12a into Eq. 2.8a) reads as

$$\begin{aligned}
\frac{dM'_T(t)}{dt} &= e^{i\Omega t} \frac{dM_T(t)}{dt} + i\Omega e^{i\Omega t} M_T(t) \\
&= e^{i\Omega t} \left[-i\gamma \left(M_T(t) B_z(t) - M_z(t) B_T \right) - \frac{M_T(t)}{T_2} \right] + i\Omega M'_T(t) \\
&= \left[-i\gamma \left(\left[e^{i\Omega t} M_T(t) \right] B_z(t) - M_z(t) \left[e^{i\Omega t} B_T(t) \right] \right) - \frac{M_T(t)}{T_2} \right] + i\Omega M'_T(t) \\
&= -i\gamma \left(M'_T(t) B'_z(t) - M'_z(t) B'_T(t) \right) + i\Omega M'_T(t) - \frac{M_T(t)}{T_2}. \tag{2.13}
\end{aligned}$$

In a similar way, the longitudinal magnetization in the rotating frame of reference becomes

$$\frac{dM_z(t)}{dt} = i\frac{\gamma}{2} \left[M'_T(t) (B'_T)^*(t) - (M'_T)^*(t) B'_T(t) \right] - \frac{M_z(t) - (M_z)_0}{T_1}. \tag{2.14}$$

The Bloch equations formulated in Eqs. 2.13 and 2.14 illustrate the coupling between the magnetization vector and the applied magnetic fields. The static magnetic field has already been introduced as the first fundamental magnetic field component present in an MR scanner. However, two additional magnetic field components are required in order to 1) achieve excitation of the probe (i.e., to drive the magnetization away from the resting state) and 2) to achieve spatial encoding.

Magnetic Field Components

The magnetic field \mathbf{B} used in an MR scanner consists of a variety of different field components required for excitation and signal acquisition:

- 1) a static magnetic field B_0 needed for polarization of the probe and to induce the spin precession,
- 2) a spatially and temporally varying linear gradient field $B_G = \langle \mathbf{G}(t), \mathbf{r} \rangle$ with $\mathbf{G} = (G_x, G_y, G_z)$ where G_x , G_y , and G_z have the unit [T/m]; these fields locally change the precession frequency to achieve spatial encoding,
- 3) radio-frequency (RF) fields denoted by \mathbf{B}_1 used to resonantly transfer energy to the spin system.

These three components are limited to certain spatial dimensions, namely

$$\mathbf{B}_0 = \begin{bmatrix} 0 & , & 0 & , & B_0 \end{bmatrix}, \tag{2.15a}$$

$$\mathbf{B}_G = \begin{bmatrix} 0 & , & 0 & , & \langle \mathbf{G}(t), \mathbf{r} \rangle \end{bmatrix}, \tag{2.15b}$$

$$\mathbf{B}_1 = \begin{bmatrix} (B_1)_x & , & (B_1)_y & , & 0 \end{bmatrix}, \tag{2.15c}$$

i.e., the static field is limited to the z-axis and the \mathbf{B}_1 field is restricted to the x-y-plane as the $(B_1)_z$ component is not observed by the spin. This is due to the static field that exceeds its strength by several orders of magnitude. The gradient fields \mathbf{B}_{G_x} , \mathbf{B}_{G_y} , \mathbf{B}_{G_z} (created by three

distinct coils) produce a linear field variation of the z-component of the static field along the different spatial axes:

$$\frac{d(\mathbf{B}_{Gx})_z}{dx} =: G_x, \quad \frac{d(\mathbf{B}_{Gy})_z}{dy} =: G_y, \quad \frac{d(\mathbf{B}_{Gz})_z}{dz} =: G_z. \quad (2.16)$$

It is important to note that, although for the imaging process, only the z-components of the gradient fields \mathbf{B}_{Gx} , \mathbf{B}_{Gy} , \mathbf{B}_{Gz} are relevant, the gradient coils produce so-called *concomitant fields* (i.e., fields not needed for image encoding) that are of significant strength. These concomitant field terms can induce substantial levels of electric fields, that can cause stimulation of nerve fibers in the human body. This mechanism will be investigated in detail in Sec. 3.4. Assembling the effective magnetic field terms for each spatial dimension yields

$$B_x(t, r_x) = (B_1)_x(t) = \text{Re} \{ B_T(t) \}, \quad (2.17a)$$

$$B_y(t, r_y) = (B_1)_y(t) = \text{Im} \{ B_T(t) \}, \quad (2.17b)$$

$$B_z(t, r_z) = \langle \mathbf{G}(t), \mathbf{r} \rangle + B_0 + \delta B_0. \quad (2.17c)$$

where δB_0 denotes static magnetic field inhomogeneities. These inhomogeneities partially arise from system imperfections of the MR scanner and partially from susceptibility effects, e.g., those caused by the metabolism of the human in the brain (cf. BOLD-contrast [115]). Substituting these distinct field components into Eq. 2.13 and rearranging the terms yields

$$\begin{aligned} \frac{dM'_T(t)}{dt} &= -i\gamma \left(M'_T(t) B'_z(t) - M'_z(t) B'_T(t) \right) + i\Omega M'_T(t) - \frac{M_T(t)}{T_2} \quad (2.18) \\ &= \underbrace{i(\Omega - \omega_0) M'_T(t)}_{\text{Larmor precession}} - \underbrace{i\gamma \delta B_0 M'_T(t)}_{\text{Field inhomogeneity}} - \underbrace{i\gamma \langle \mathbf{G}(t), \mathbf{r} \rangle M'_T(t)}_{\text{Spatial encoding}} + \underbrace{i\gamma B'_T(t) M_z(t)}_{\text{RF excitation}} - \underbrace{\frac{M_T}{T_2}}_{\text{Relaxation effects}}. \end{aligned}$$

The second line of Eq. 2.18 combines all major effects of the applied magnetic field components into a single equation: the first term describes the Larmor precession in the transverse plane and illustrates that, due to the coordinate transformation into the rotating frame of reference, the precession vanishes if $\Omega = \omega_0$. Potentially present field inhomogeneities δB_0 of the static magnetic field B_0 influence the transverse magnetization, resulting in the so called T_2^* -relaxation (second term). An RF pulse that is applied at time point t will only have an effect on the transverse magnetization if the longitudinal magnetization $M_z(t)$ is unequal to zero.

2.1.3 Relaxation Effects

The differential equations given by Eqs. 2.13 and 2.14 indicate that, if both $M_z = M_0$ and $M_{x/y} = 0$ hold (equilibrium magnetization) and if no RF field is applied ($B_1 = 0$), the magnetization vector \mathbf{M} does not experience any temporal change, i.e. $\frac{d}{dt} \mathbf{M} = 0$ (the entire system is at resting state). If the magnetization is not in the equilibrium state there are two separate physical effects that will restore the equilibrium over time. The first effect recovers the initial longitudinal magnetization M_z with a time constant T_1 , a second effect decreases the transverse magnetization M_T with time constant T_2 (such that M_T will vanish eventually).

The T_2 -relaxation formulation is derived from Eq. 2.18. Assuming that no gradient fields ($\mathbf{G}(t) = 0$) and no RF fields ($B'_T(t) = 0$) are applied, the differential equation of the transverse magnetization simplifies to

$$\frac{dM'_T(t)}{dt} = -\frac{M'_T(t)}{T_2}. \quad (2.19)$$

Equation 2.19 is a linear ordinary differential equation, whose solution is obtained via common separation of variables and subsequent integration, written

$$\begin{aligned} \int \frac{1}{M'_T(t)} dM'_T &= \int \frac{1}{T_2} dt \\ \rightarrow M'_T(t) &= C e^{-t/T_2}, \end{aligned} \quad (2.20)$$

which, with respect to the initial conditions, yields

$$M'_T(t) = (M'_T)_0 e^{-t/T_2}. \quad (2.21)$$

Here, $(M'_T)_0$ denotes the initial transverse magnetization at $t = 0$. An analogous approach is used for the derivation of the T_1 -relaxation. Once again, under the assumption of no gradient and RF fields being present, $B'_T(t) = 0$, the differential equation given by Eq. 2.14 becomes

$$\frac{dM_z(t)}{dt} = -\frac{M_z(t) - M_0}{T_1}, \quad (2.22)$$

whose solution is given by

$$M_z(t) = M_0 + [(M_z)_0 - M_0] e^{-t/T_1}. \quad (2.23)$$

2.1.4 Slice-selective Excitation

The previous subsection was dedicated to derive a general formulation for the coupling between the magnetization vector and the applied magnetic fields. The magnetization components and magnetic field components were separated into transverse and longitudinal entities which simplifies the mathematical handling of the Bloch equations. Using this complex notation the differential equation can be solved to design a B_1 pulse shape that when accompanied by appropriate gradient fields achieve a certain excited state of the magnetization. The most commonly used type of excitation pulses are *slice-selective pulses*. For this kind of pulse an analytic solution for the required B_1 waveform can be derived. A commonly used simplification applied in the pulse design problem is to neglect relaxation effects. This is a reasonable assumption as long as the RF pulses to be designed are significantly shorter than the relaxation times (e.g., in the order of 5 ms which compares to $T_1 \approx 1000$ ms and $T_2 \approx 100$ ms [49]).

In this case, Eq. 2.18 expressed with an explicit dependency on the spatial location r_z , becomes

$$\frac{dM'_T(t, r_z)}{dt} = -i\gamma G_z(t) r_z M'_T(t) + i\gamma B'_T(t) M_z(t). \quad (2.24)$$

In this formulation gradient fields are only present in z ($G_x = G_y = 0$) and the spatial dependency is limited the z -axis (r_z), meaning that the selectivity of the slice-selective RF pulse is only

achieved along the z-direction. Nonetheless, the same formulation holds when playing multiple gradient axes simultaneously. In this case the first term on the right hand side remains as $-i\gamma \langle \mathbf{G}(t), \mathbf{r} \rangle M'_T(t)$. An RF pulse that is accompanied by more than a single gradient field axis is referred to as a *multi-dimensional RF pulse* (see Sec. 2.2.1).

The differential equation stated in Eq. 2.24 can only be solved under the assumption that the $M_z(t)$ magnetization component is not affected by the RF pulse. Although from the physical perspective this assumption only holds for very small flip angles, accurate RF pulses can be achieved for flip angles up to 90° . This assumption is referred to as *small tip angle regime* (STA) and is widely used for the design of RF excitation pulses [86]. Using the small flip angle assumption the right hand side simplifies to

$$\frac{dM'_T(t, r_z)}{dt} = -i\gamma G_z(t) r_z M'_T(t) + i\gamma B_1(t) M_0. \quad (2.25)$$

In the above equation, the term B'_T is replaced by the more common term B_1 (very often the notation B_1^+ is used where the "+" superscript indicates that the B_1 -field is transmitted; for the receive case the field is denoted by B_1^-). Eq. 2.25 is an ordinary linear first order differential equation. The generalized form of this kind of differential equations is written as

$$\frac{d}{dt}y(t) + f(t)y(t) = g(t) \quad , \quad (2.26)$$

which can be solved by multiplication with an integrating factor

$$\exp\left(\int_T f(t) dt\right) \quad , \quad (2.27)$$

leading to

$$\begin{aligned} g(t) \exp\left(\int_T f(t) dt\right) &= \frac{d}{dt}y(t) \exp\left(\int_T f(t) dt\right) + f(t)y(t) \exp\left(\int_T f(t) dt\right) \\ &= \frac{d}{dt}\left[y(t) \exp\left(\int_T f(t) dt\right)\right] \end{aligned} \quad (2.28)$$

where the right hand side was reformulated using the product rule of integration. Integrating and solving for $y(t)$ results in

$$y(t) = \exp(-a(t)) \left(\int_T g(t) \exp(a(t)) dt + c \right) \quad \text{where } a(t) = \int f(t) dt. \quad (2.29)$$

which is the general solution for Eq. 2.26. Using this generalized form, the solution of Eq. 2.24 can be written as

$$M'_T(t, r_z) = \exp\left(-i\gamma \int_{t_0}^t G_z(\tau) r_z d\tau\right) \cdot \int_{t_0}^t i\gamma B_1(\tau) M_0 \cdot \exp\left(\int_{t_0}^{\tau} i\gamma G_z(\eta) r_z d\eta\right) d\tau \quad (2.30)$$

with t_0 denoting the beginning of the RF pulse. In this case, the constant c is associated with the initial transverse magnetization $M'_T(t_0) = (M'_T)_0$ that is assumed to be zero and, therefore,

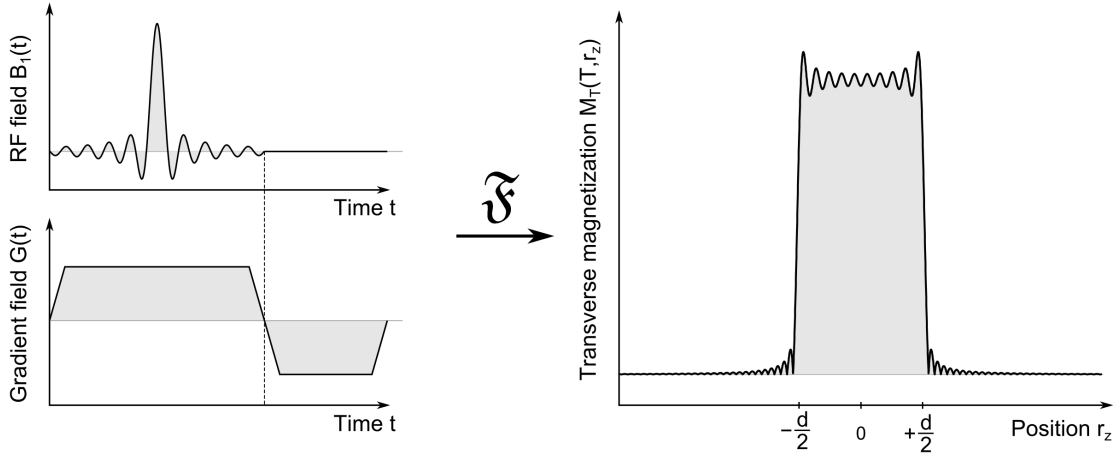


Figure 2.1: Slice-selective excitation, Left: RF waveform (top) and gradient waveform (bottom) applied within the excitation (note the refocusing gradient at the end with negative polarity and half the length); Right: the applied sinc waveform results in a rectangular excitation profile

was dropped. Assuming an RF pulse with duration denoted by T_p with $t_0 = -T_p/2$ and playing a constant gradient $G_z(t) = G_z$ during the pulse, Eq. 2.30 further simplifies to

$$\begin{aligned}
 M'_T(T_p/2, r_z) &= \exp(-i\gamma G_z r_z T_p) \cdot \int_{-T_p/2}^{+T_p/2} i\gamma B_1(\tau) M_0 \cdot \exp(i\gamma G_z r_z (\tau + T_p/2)) d\tau \\
 &= i\gamma M_0 \cdot \exp(-i\gamma G_z r_z T_p) \cdot \exp(i\gamma G_z r_z T_p/2) \cdot \int_{-T_p/2}^{+T_p/2} B_1(\tau) \exp(i\gamma G_z r_z \tau) d\tau \\
 &= i\gamma M_0 \underbrace{\exp(-i\gamma G_z r_z T_p/2)}_{\text{Phase dispersion after RF pulse}} \cdot \underbrace{\int_{-T_p/2}^{+T_p/2} B_1(\tau) d\tau}_{\text{Slice profile}} \cdot \underbrace{\exp(i\gamma G_z r_z \tau)}_{\text{Fourier harmonics}} d\tau. \quad (2.31)
 \end{aligned}$$

At this point a few important conclusions can be drawn from the above equation:

- 1) The magnetization M'_T at the end of the RF pulse and the applied B_1 field are linked by a Fourier transform.
- 2) The Fourier counterpart to the spatial location r_z is given by the gradient strength G_z times the duration of the pulse τ times the gyromagnetic ratio γ , or more generally, by the gradient field induced phase accumulation. If variable gradient waveforms are employed $G_z \tau$ is replaced by the time integral of the gradient waveform.
- 3) The gradient which is played during the pulse induces a phase dispersion of the magnetization after the pulse; the strength of this dispersion corresponds to *half* of the pulse duration $T_p/2$ and needs to be compensated for by playing a so-called refocusing gradient lobe after the slice-excitation.

The Fourier relation between magnetization in the spatial domain and the B_1 field in time-domain is very useful, because this often allows to design RF pulses "on-the-fly" using analytic Fourier

transforms of desired magnetization profiles (like rectangular or Gaussian profiles). If, for example, a slice with rectangular profile is to be excited along the z -axis, the RF waveform to be played corresponds to a sinc function, depicted in Fig. 2.1 (the sinc function is the Fourier transform of the box function). Mathematically, the sinc has an infinite extent which would require an infinitely long RF pulse. In practice, only a few side lobes of the sinc are incorporated which limits the accuracy of the excited profile. As a result of this limitation, so-called Gibbs artifacts are present (cf. Fig. 2.1, right). To some extent, these artifacts can be diminished by multiplying the RF waveform by a smooth window function (such as a Gaussian or a Hanning window). This window function creates a smooth decay of pulse at the cut-off time which in turn eliminates high-frequency components in the slice profile.

2.1.5 Image Acquisition

The slice-selective excitation pulse described above allows to generate a magnetization distribution $M_T(\mathbf{r})$ in the probe which is spatially limited to a plane of certain thickness (slice thickness). The exact shape and location of the excited slice are determined by the played RF waveform as well as the gradient strength. Excitation of a magnetization profile with 1-D spatial selectivity means that the remaining 2-D signal needs to be encoded and acquired via the readout phase in order to form an image.

The spatial encoding during reception is based on the exact same mechanism that is used for excitation which is the generation of phase patterns corresponding to 3-D Fourier harmonic waves and acquiring the signal that the probe emits in this phase state. Assuming that the slice-selective RF pulse created a refocused in-phase magnetization pattern in the x - y -plane: applying a gradient field in a probe for a certain amount of time will change the precession frequency of the spin system as a function of the respective axis coordinate, e.g., for the x -gradient as a function of x . The different spins accumulate a phase which depends on the spatial location along the x -axis. Due to the linearity of the gradient field, the *global* phase pattern in the image plane corresponds to a 3-D harmonic wave. The normal direction and frequency of the harmonic wave are determined by the time course of the gradient field that has been played until that time point. Playing a certain gradient field strength for a long time will lead to a large phase accumulation and thus to a high spatial-frequency harmonic wave, whereas playing the same gradient field strength for only a short time will generate a harmonic wave phase pattern with a lower spatial frequency. Note that the signals being emitted by the probe under a certain phase pattern are unique, i.e., different 3-D harmonic phase patterns generated in the probe will induce different signals to be emitted. The creation of 3-D harmonic waves as a result of the applied gradient fields once again illustrates the relationship between magnetization pattern in spatial domain and the emitted electromagnetic signals in time domain: these two entities are linked by the Fourier transform.

The "collective" of all harmonic waves is usually denoted as k -space. Creating the different harmonic waves by applying gradient fields and receiving the respective emitted RF signals means: acquiring k -space. In order to be able to reconstruct the 2-D image k -space needs to be sampled sufficiently dense. Since the measured information corresponds to the complex Fourier coefficients of certain harmonic waves, the amount of information for image reconstruction is determined by Fourier mathematics, particularly by the Nyquist sampling theorem [83]. This theorem states that in order for a band-limited signal to be accurately discretized, the signal must be sampled with a frequency greater than twice the maximum frequency component present in the sampled signal. Otherwise high-frequency components are incorrectly estimated by the signal

sampling, leading to aliasing artifacts in the reconstructed signal. Because the signal in MRI is effectively sampled in frequency domain, and the image (in spatial domain) is reconstructed by performing an inverse Fourier transform, these aliasing artifacts manifest themselves in image domain as fold-over or "ghosting" artifacts, meaning that the image is periodically overlaid onto the reconstructed image. In order to avoid this kind of artifact in MRI the sampling step size in k -space, $\Delta k_{x/y}$, and the size $W_{x/y}$ of the field-of-view (FOV) are linked by

$$\Delta k_x \leq \frac{1}{W_x} \quad \text{and} \quad \Delta k_y \leq \frac{1}{W_y} . \quad (2.32)$$

Equivalently, the minimum spatial feature (i.e., the pixel size $\Delta x/y$) that can be reconstructed via the inverse Fourier transform is determined by the largest k -space components $k_{x/y,\max}$, i.e., the maximum frequency harmonic wave that has been acquired in k -space along the respective axis, namely

$$\Delta x \geq \frac{1}{k_{x,\max}} \quad \text{and} \quad \Delta y \geq \frac{1}{k_{y,\max}} . \quad (2.33)$$

These two conditions determine the amount of k -space information required to correctly reconstruct an image. In the following the concept of k -space will be given a mathematical foundation.

2.1.6 The k -Space Formalism

The derivation of slice-selective RF pulses revealed that there is a relation between the applied RF pulse shape and the magnetization created by that pulse that corresponds to a Fourier transform (at least for sufficiently small flip angles). The exponential term in the Fourier transform depends on the time integral of the gradient waveform $G_z(t)$ (cf. Eq. 2.31). This integral defines the transform variable in frequency domain, whereas the coordinate r_z defines the respective variable in spatial domain.

Neglecting relaxation effects, the total complex transverse magnetization $M_T(t)$ is given by

$$M_T(t) = \int_R m(\mathbf{r}) \exp\left(-i \int_0^t \omega(t, \mathbf{r}) dt\right) d\mathbf{r} , \quad (2.34)$$

with $m(\mathbf{r}) = m(x, y, z)$ denoting the spatial magnetization distribution right after the excitation. The spatially and temporally varying exponential term describes a phase pattern accumulated by the magnetization. This phase pattern is determined by the time course of the local angular velocity ω that in turn is proportional to the gradient fields $\mathbf{G}(t)$ (that change the Larmor frequency as a function of space), namely

$$\omega(t, \mathbf{r}) = \gamma \langle \mathbf{G}(t), \mathbf{r} \rangle . \quad (2.35)$$

Therefore, the integral in the exponential can be rewritten as a time integral of gradient fields $\mathbf{G}(t)$ given by

$$\begin{aligned}\Omega(T, \mathbf{r}) &:= \int_0^T \omega(t, \mathbf{r}) dt \\ &= \int_0^T \gamma \langle \mathbf{G}(t), \mathbf{r} \rangle dt \\ &= x \cdot \gamma \int_0^T G_x(t) dt + y \cdot \gamma \int_0^T G_y(t) dt + z \cdot \gamma \int_0^T G_z(t) dt .\end{aligned}\quad (2.36)$$

Note that each gradient field produces an *independent* phase contribution to the entire phase dispersion $\Omega(T, \mathbf{r})$. This motivates the introduction of a coordinate space which is more convenient when dealing with the spatial magnetization distribution (i.e., in spatial domain) and the signals induced by the precessing magnetization (i.e., in time domain). This coordinate space is referred to as *k-space* and is a central concept in MRI. The *k-space* coordinates $\mathbf{k}(t)$ are defined via

$$\mathbf{k}(t) = \begin{pmatrix} k_x(t) := \gamma \int_0^T G_x(t) dt \\ k_y(t) := \gamma \int_0^T G_y(t) dt \\ k_z(t) := \gamma \int_0^T G_z(t) dt \end{pmatrix} .\quad (2.37)$$

The time series of *k-space* coordinates is referred to as *k-space trajectory*. Substituting the *k-space* coordinates back into Eq. 2.34 leads to

$$\begin{aligned}M_T(t, \mathbf{r}) &= \int_R m(\mathbf{r}) \exp(-i \langle \mathbf{k}(t), \mathbf{r} \rangle) d\mathbf{r} \\ &= \int_R m(\mathbf{r}) \exp(-i[k_x(t)x + k_y(t)y + k_z(t)z]) d\mathbf{r} .\end{aligned}\quad (2.38)$$

This expression illustrates that the total transverse magnetization $M_T(t)$ (that determines the signal induced in receive coils via Faraday induction) can be expressed as a multi-dimensional Fourier transform of the magnetization distribution $m(\mathbf{r})$ from spatial to frequency domain (similarly to the 1-D case for slice-selective excitation pulses). Note that there is a close resemblance between the reception phase (where the electromagnetic field is emitted by the spins and received by the coil) and the excitation phase (where an electromagnetic field is emitted by a coil in order to excite the spin system). Both the receive and transmit mechanisms can be simplified by making use of the *k-space* formalism.

2.2 | State-of-the-Art RF Pulse Design

2.2.1 Multi-dimensional Excitation

In Sec. 2.1.4, the Bloch equation was solved to allow for the design of RF waveforms accompanied by an encoding gradient such that a slice is excited in the probe, see Eq. 2.31. This solution of the Bloch equation is computed based on the small flip angle approximation that assumes that the longitudinal magnetization is not affected by the excitation (i.e., it stays at $M_z = 1$, independently of the flip angle). This allows for deriving analytic pulse shapes: in fact, the shape of the RF pulse and the resulting slice profile are linked together by the Fourier transform. Accordingly a sinc-pulse can be used to generate a rectangular slice profile, whereas a Gaussian-shaped RF pulse excites a Gaussian slice profile. The term "slice-excitation" refers to the fact that spatial selectivity is achieved along a single spatial axis (most commonly the z -axis) whereas no variation of the magnetization along the other two spatial axes (x and y) is generated. The slice-selection strategy only requires one MR gradient field to be applied along the slice selection axis (in this case the G_z gradient). Note that slices can be excited with arbitrary orientations, i.e., additionally to orientations that correspond to the "pure" gradient axes x , y , and z , multiple gradient axes can be combined in order to arbitrarily orient the slice in 3-D space.

In case of slice-selectivity along the spatial z -axis, the differential equation is given by

$$\frac{dM'_T(t, r_z)}{dt} = -i\gamma G_z(t) r_z M'_T(t) + i\gamma B'_T(t) M_z(t) \quad (2.39)$$

whose solution (in the small tip angle regime $M_z(t) = M_0 = \text{const.}$) is given by

$$M'_T(t, r_z) = \exp\left(-i\gamma \int_{t_0}^t G_z(\tau) r_z d\tau\right) \cdot \int_{t_0}^t i\gamma B_1(\tau) M_0 \exp\left(\int_{t_0}^{\tau} i\gamma G_z(\eta) r_z d\eta\right) d\tau. \quad (2.40)$$

A detailed derivation of this expression is given above. Again, RF pulse and the resulting magnetization pattern are linked via the Fourier transform, with the Fourier harmonics being determined by the gradient waveform (i.e., by the k -space coordinates).

This Fourier relation can be extended to 2-D and 3-D, i.e., multi-dimensional gradient waveforms can be employed in order to achieve multi-dimensional selectivity of the magnetization pattern to be excited by the RF pulse. In this case the Bloch equation in Eq. 2.39 modifies towards

$$\frac{dM'_T(t, \mathbf{r})}{dt} = -i\gamma \langle \mathbf{G}(t), \mathbf{r} \rangle M'_T(t) + i\gamma B'_T(t) M_z(t). \quad (2.41)$$

where $\mathbf{G}(t) = (G_x(t), G_y(t), G_z(t))$ is the 3-D gradient waveform. Equivalently to the 1-D case, the solution to the differential equation (using the small tip approximation) is given by

$$\begin{aligned} M'_T(t, \mathbf{r}) &= \exp\left(i\gamma \int_{t_0}^t \langle \mathbf{G}(\tau), \mathbf{r} \rangle d\tau\right) \cdot \int_{t_0}^t i\gamma B_1(\tau) M_0 \exp\left(i\gamma \int_{t_0}^{\tau} \langle \mathbf{G}(\eta), \mathbf{r} \rangle d\eta\right) d\tau \\ &= \underbrace{i\gamma M_0 \exp\left(i\gamma \int_{t_0}^t \langle \mathbf{G}(\tau), \mathbf{r} \rangle d\tau\right)}_{\varphi(t, \mathbf{r})} \cdot \int_{t_0}^t B_1(\tau) \exp\left(-i\gamma \int_{\tau}^t \langle \mathbf{G}(\eta), \mathbf{r} \rangle d\eta\right) d\tau. \end{aligned} \quad (2.42)$$

The integration bounds were adjusted, assuming that the pulse duration is given by T . For the sake of simplicity, the first exponential term on the right hand side is replaced by $\varphi(t, \mathbf{r})$ in the following. Again this term describes the phase dispersion at the end of the pulse arising from the applied gradient fields; the phase dispersion needs to vanish in order to establish a refocused magnetization after the excitation pulse. This requirement holds both for 1-D excitation pulses (slice-selection) and multi-dimensional excitation pulses. Note that this requirement is intrinsically satisfied if the associated k -space trajectory ends at the center of k -space, i.e., $\mathbf{k}(T) = 0$. Using the definition of k -space given in Sec. 2.1.6, Eq. 2.42 becomes

$$M'_T(t, \mathbf{r}) = i\gamma M_0 \cdot \varphi(t, \mathbf{r}) \int_{t_0}^t B_1(\tau) \cdot \exp(i \langle \mathbf{k}(t), \mathbf{r} \rangle) d\tau \quad (2.43)$$

with

$$\mathbf{k}(t) = -\gamma \int_{\tau}^T \mathbf{G}(\eta) d\eta. \quad (2.44)$$

The coordinates in $\langle \mathbf{k}(t), \mathbf{r} \rangle$ define the Fourier pair in the multi-dimensional excitation case, i.e., the k -space formalism is extended to multiple dimensions. The time dependency of the k -space term in the Fourier harmonic can be eluded using the three dimensional delta function ${}^3\delta(\mathbf{k})$, namely

$$\begin{aligned} M'_T(t, \mathbf{r}) &= i\gamma M_0 \cdot \varphi(t, \mathbf{r}) \int_{t_0}^t B_1(\tau) \cdot \exp(i \langle \mathbf{k}(\tau), \mathbf{r} \rangle) d\tau \\ &= i\gamma M_0 \cdot \varphi(t, \mathbf{r}) \int_{t_0}^t B_1(\tau) \int_K {}^3\delta(\mathbf{k}(\tau) - \mathbf{k}) d\mathbf{k} \cdot \exp(i \langle \mathbf{k}(\tau), \mathbf{r} \rangle) d\tau \\ &= i\gamma M_0 \cdot \varphi(t, \mathbf{r}) \underbrace{\int_K \int_{t_0}^t B_1(\tau) {}^3\delta(\mathbf{k}(\tau) - \mathbf{k}) d\tau}_{:= f(\mathbf{k})} \cdot \exp(i \langle \mathbf{k}, \mathbf{r} \rangle) d\mathbf{k}. \end{aligned} \quad (2.45)$$

The expression denoted by $f(\mathbf{k})$ defines the k -space information pattern, i.e., the k -space path weighted by the RF information as deposited by the B_1 -field. Substituting t by $\mathbf{k}(t)$ results in

$$\begin{aligned} f(\mathbf{k}) &= \int_{t_0}^t B_1(\tau) {}^3\delta(\mathbf{k}(\tau) - \mathbf{k}) d\tau \\ &= \int_{t_0}^t \frac{B_1(\mathbf{k}) \rho(\mathbf{k})}{\|\gamma \mathbf{G}(\mathbf{k})\|_2} {}^3\delta(\mathbf{k}(\tau) - \mathbf{k}) \left| \frac{d\mathbf{k}(\tau)}{d\tau} \right| d\tau \\ &= \underbrace{\frac{B_1(\mathbf{k}) \rho(\mathbf{k})}{\|\gamma \mathbf{G}(\mathbf{k})\|_2}}_{W(\mathbf{k})} \underbrace{\int_{t_0}^t {}^3\delta(\mathbf{k} - \mathbf{k}(\tau)) \left| \frac{d\mathbf{k}(\tau)}{d\tau} \right| d\tau}_{P(\mathbf{k})} \end{aligned} \quad (2.46)$$

where

$$f(\mathbf{k}(t)) {}^3\delta(\mathbf{k}(t) - \mathbf{k}) = f(\mathbf{k}) {}^3\delta(\mathbf{k} - \mathbf{k}(t)) \quad (2.47)$$

was used. The expression of the k -space information pattern was separated into two entities: the term denoted by $W(\mathbf{k})$ describes the RF energy that is deposited along the k -space sampling pattern denoted by $P(\mathbf{k})$. The local sampling density of the k -space trajectory is given by $\rho(\mathbf{k})$. The term $\|\gamma\mathbf{G}(\mathbf{k})\|_2$ corresponds to the k -space velocity of the trajectory which inversely scales the deposited energy. Mathematically, $W(\mathbf{k})$ (neglecting the RF waveform $B_1(\mathbf{k})$) represents the Jacobian determinant which performs the variable substitution, namely

$$d\mathbf{k} \rightarrow \frac{B_1(\mathbf{k}) \rho(\mathbf{k})}{\|\gamma\mathbf{G}(\mathbf{k})\|_2} dt \quad (2.48)$$

in Eq. 2.46. In the case of a 1-D RF pulse (e.g., slice-selective pulses), the sampling density $\rho(\mathbf{k})$ is equal to one and $W(\mathbf{k})$ reduces to

$$W(\mathbf{k}) = \frac{B_1(\mathbf{k})}{\|\gamma\mathbf{G}(\mathbf{k})\|_2} . \quad (2.49)$$

This means that the RF energy deposited at the current k -space location is inversely weighted by the velocity at which k -space is sampled. The same holds for multi-dimensional pulses, if the gradient trajectory is designed such that excitation k -space is sampled uniformly.

If, on the other hand, non-uniform gradient trajectories are used, the sampling density $\rho(\mathbf{k})$ established by the trajectory is needed in order to correctly weight the coefficients for the RF waveforms. For rather simple k -space sampling patterns (like spirals) analytic expressions of the weighting function can be derived from the gradient waveforms. For more complex trajectories (especially those for which no closed analytic expression exist), the Jacobian determinant and thus the sampling density cannot be quantified analytically. In this case the sampling density can be estimated, e.g. by performing a so-called *Voronoi tessellation* of the time series of k -space samples [92]. Another more straight forward approach for solving the k -space sampling density problem, is referred to as the *Spatial Domain RF Pulse Design* method proposed by Grissom et al. [45]. This method makes use of the linearity of the Fourier transform to assemble the full system matrix and directly solve for the RF waveforms, including the sampling density and k -space velocity terms (this method will be described in detail in a following section).

Using the weighted k -space information pattern $f(\mathbf{k})$ (i.e., the sampling pattern weighted by the deposited RF energy), the transverse magnetization at the end of the RF pulse (at time point T) can now be written as

$$M_T(T, \mathbf{r}) = i\gamma M_0 \int_K f(\mathbf{k}) \cdot \exp(i\langle \mathbf{k}, \mathbf{r} \rangle) d\mathbf{k} . \quad (2.50)$$

In the above equation it was assumed that the trajectory ends at the center of k -space, $\mathbf{k}(T) = \mathbf{0}$, and thus leaves a magnetization pattern which is refocused (i.e., $\varphi(t, \mathbf{r}) = 1$). Using the separation of $f(\mathbf{k})$ into the RF deposition term $W(\mathbf{k})$ and the k -space sampling term $P(\mathbf{k})$, Eq. 2.50 can reformulated by

$$\begin{aligned} M_T(T, \mathbf{r}) &= i\gamma M_0 \int_K W(\mathbf{k}) P(\mathbf{k}) \cdot \exp(i\langle \mathbf{k}, \mathbf{r} \rangle) d\mathbf{k} \\ &= i\gamma M_0 \cdot \mathfrak{F}\left\{W(\mathbf{k}) P(\mathbf{k})\right\} \\ &= i\gamma M_0 \cdot \mathfrak{F}\left\{W(\mathbf{k})\right\} * \mathfrak{F}\left\{P(\mathbf{k})\right\} . \end{aligned} \quad (2.51)$$

where $\mathfrak{F}(\cdot)$ is used to denote the Fourier transform. The last row of Eq. 2.51 arises from the property of Fourier transforms that a multiplication of two functions in frequency domain can be expressed as a convolution of the respective Fourier transformed functions in spatial domain (and vice versa).

Equation 2.51 illustrates an important property of MR imaging sequences: the Fourier transform of the k -space sampling pattern specifies the so-called *Point-Spread-Function* of the imaging system and, therefore, characterizes the resolution capabilities. Trajectories that achieve a rather uniform k -space sampling pattern (like echo planar and spiral trajectories) establish a point-spread-function that (in first approximation) corresponds to a periodic sequence of delta peaks. This means that the excitation pulse accurately creates the target magnetization within the field-of-excitation (FOX) with a periodic repetition of the target outside the FOX. Note that in the excitation case, the sampling pattern can be non-uniform (creating a non-uniform point-spread-function) as long as the target magnetization profile is not degraded by the point-spread-function. In other words: different k -space trajectories may be designed specifically for different target magnetization profiles to make efficient use of the spatial characteristics of the target. This is an important degree-of-freedom that will be exploited in the methods (Sec. 3.2) for the design of ultra-short 3-D spatially selective RF pulses.

2.2.2 Parallel Imaging and Sensitivity Encoding

In the previous section the idea of multi-dimensional RF excitation was described as the traversal of excitation k -space following a trajectory (defined by the gradient waveforms) along which information is deposited by an applied RF field. From Eq. 2.46 it is apparent that the location $\mathbf{k}(t)$ of RF deposition can be written

$${}^3\delta(\mathbf{k}(\tau) - \mathbf{k}) \quad (2.52)$$

i.e., by the three dimensional delta function. The mechanism of RF energy distribution in k -space is illustrated in Fig. 2.2 A, where the Fourier harmonic $k_{x/y} = 25 \text{ m}^{-1}$ (left) and its Fourier transform, i.e., the k -space kernel (right) are shown. The applied gradient fields created a harmonic wave (top row) whose normal direction and spatial frequency correspond to the location of the peak in k -space (bottom row). By transmission of RF power using a coil with uniform sensitivity, RF energy is deposited at a single location in k -space at each time point t . In practice, this only holds if the B_1^+ field has a uniform sensitivity throughout the entire field-of-excitation. If there is sensitivity variation present in the B_1^+ field, the information is deposited in a neighborhood of the k -space location: the size of the k -space neighborhood increases as the sensitivity of the B_1^+ field becomes more non-uniform (see Fig. 2.2, B and C). This property – that a non-uniform B_1 field is associated with an extended neighborhood in k -space – holds both for the reception case (B_1^-) and the transmission case (B_1^+). In the reception case, the coil receives a signal mixture arising from an extended region of k -space harmonics. In the transmission case, the coil deposits the RF energy not at a single k -space location, but the information is smeared across a k -space neighborhood.

What seems as an implication for MR imaging at first sight, has led to one of the most important inventions of MR imaging: *Parallel Imaging* [90]. The "imperfect" coil profiles can be used to undersample k -space during the excitation and reception beyond the Nyquist sampling condition (Eq. 2.32) to speed up the imaging protocol. The parallel imaging mechanism is applicable to both reception (speeding up the signal acquisition) and transmission (speeding up the signal

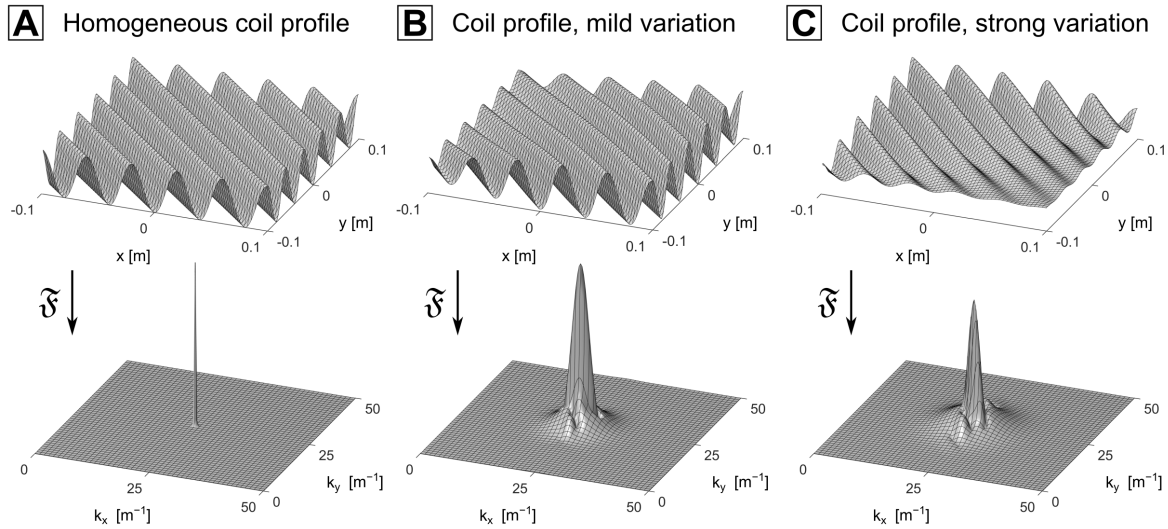


Figure 2.2: *Top:* Fourier harmonics ($k_{xy} = 25 \text{ m}^{-1}$) in spatial domain, modulated by a perfectly homogeneous coil profile (A) and coil profiles with mild (B) and strong (C) sensitivity variation. *Bottom:* for each Fourier harmonic, the respective k -space kernels (i.e., the Fourier transform of the coil profiles) are shown.

excitation). With respect to the transmission case, the general idea is to use independent transmit coils with different sensitivity profiles (i.e., different k -space kernels), where each coil is driven by an independent transmit signal. Therefore, each coil deposits a different complex information in k -space in a region determined by the k -space kernel. In order to ensure that RF information in the entire k -space neighborhood is generated correctly, the individual complex signals are designed such that, in summation, the anticipated information is restored in the neighborhood. The advantage is that the sampling density can be reduced substantially, and the missing k -space information can be recovered by the parallel imaging functionality. The drawback is that the complex weights of the different channels need to be computed in advance which requires knowledge about the coil sensitivity profiles, i.e., a B_1^+ mapping (or similar) needs to be performed to characterize the k -space kernels. The computation of the complex channel weights – often referred to as *unfolding* problem – is a linear problem which can be solved very efficiently. The unfolding process, however, causes a loss in the signal-to-noise ratio (SNR) that depends on the suitability of the coil sensitivity profiles with respect to parallel imaging.

For example, if the sensitivity profile of a single coil is too homogeneous, the k -space kernel approaches a delta peak that does not allow for energy deposition in the k -space neighborhood. If, on the other hand, the coil sensitivity drops very quickly, the k -space kernel covers a large k -space area, however, the peak amplitude of the kernel decreases. This decreases the efficiency of energy deposition (i.e., the coil efficiency) and, therefore, increase the Specific Absorption Rate (SAR). In short, a coil profile which is suited for parallel imaging establishes a feasible balance between undersampling capabilities and the SAR penalty. The three situations are shown in Fig. 2.3: for three coils with continuously decreased penetration depth (80 % for A, 60 % for B, 30 % for C), the k -space kernels are shown. It can be observed that a reduction of the sensitivity broadens the k -space kernel, but also decreases the peak of the kernel.

A third condition affects the pair-wise similarity of the sensitivity profiles produced by the different transmit coils: as a rule of thumb a set of coils whose sensitivity profiles vary substantially between the different coils is well suited for parallel imaging/parallel excitation, unlike a set of coils whose

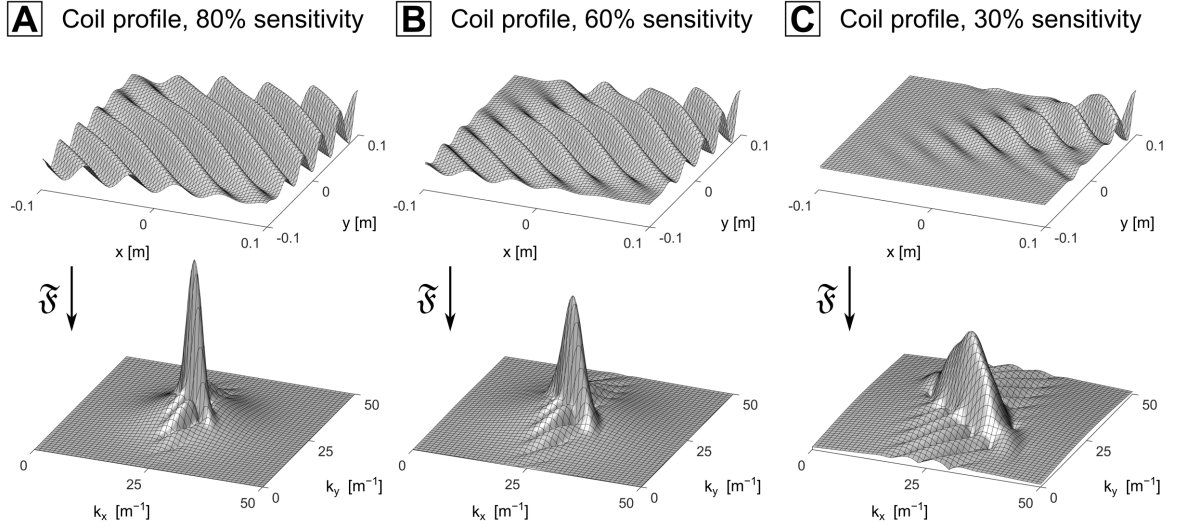


Figure 2.3: *Top:* Fourier harmonics ($k_{xy} = 25 \text{ m}^{-1}$) in spatial domain, modulated by coil sensitivity profiles with penetration depths of 80 % (A), 60 % (B), and 30 % (C). *Bottom:* for each Fourier harmonic, the respective k -space kernels (i.e., the Fourier transform of the coil profiles) are shown.

sensitivity profiles are very similar. This is due to the fact that the reconstruction of k -space neighborhood information (both for the receive and transmit case) can be formulated as a linear system, whose columns are determined by the respective k -space kernels. If the k -space kernels vary significantly between the different coils, the associated linear system is well-conditioned (the columns are linearly independent). If, on the other hand, the k -space kernels are very similar, the linear system becomes under-determined and the k -space neighborhood cannot be recovered sufficiently well. An excellent and very illustrative overview about these properties, a more detailed mathematical description of the effect of coil kernels onto the associated linear system, and implementation details of the different parallel imaging approaches has been published by Prüssmann et al. [89].

2.2.3 Parallel Excitation: Transmit SENSE

In the derivation of multi-dimensional excitation pulses it was shown that the k -space trajectory has to satisfy the Nyquist sampling theorem [83]. This generates a periodic point-spread-function for which the different peaks are separated by at least the size of the FOX to ensure that the anticipated target is accurately excited in the FOX without aliasing effects. Because the pulse duration is usually limited to a few milliseconds, sufficiently dense sampling of excitation k -space may not be feasible, especially for 3-D excitations of inner-volume targets where 3-D excitation k -space needs to be sampled. A powerful method to overcome the pulse duration constraint has been described in the previous section, referred to as parallel excitation (pTx), where multiple independently driven transmit coils are used to undersample excitation k -space beyond the Nyquist criterion.

A time varying RF waveform $B_1(t)$ played along the k -space sampling pattern $P(\mathbf{k})$ generates a transverse magnetization given by

$$M_T(\mathbf{r}) = i\gamma M_0 \int_{\mathcal{K}} \frac{B_1(\mathbf{k}) \rho(\mathbf{k})}{\|\gamma \mathbf{G}(\mathbf{k})\|_2} P(\mathbf{k}) \cdot \exp(i \langle \mathbf{k}, \mathbf{r} \rangle) d\mathbf{k}, \quad (2.53)$$

where $\rho(\mathbf{k})$ specifies the sampling density of the k -space trajectory at \mathbf{k} . If $\rho(\mathbf{k}(t))$ is known, the inverse Fourier transform can be used to design the RF waveform required to produce the target magnetization pattern M_T^{tar} :

$$B_1(t) = \frac{\|\gamma\mathbf{G}(\mathbf{k})\|_2}{i\gamma M_0 \rho(\mathbf{k}(t))} \int_R M_T^{\text{tar}}(\mathbf{r}) \cdot \exp(-i\langle \mathbf{k}, \mathbf{r} \rangle) d\mathbf{r}. \quad (2.54)$$

If the sampling density $\rho(\mathbf{k}(t))$ exists (which is not the case for so-called "pathological" self-crossing k -space trajectories), the B_1 waveform is uniquely defined by the inverse Fourier transform.

In the spirit of parallel imaging/excitation, multiple RF coils with superscript $c = 1, \dots, C$ can be employed for RF energy deposition. The sensitivity profile of each transmit coil is denoted by $S^{(c)}(\mathbf{r})$; for each coil an individual RF waveform $B_1^{(c)}(t)$ is defined. Due to the linearity of the Fourier transform, every transmit coil driven by the individual RF waveform creates its own complex magnetization profile that in sum define the full magnetization $M_T(\mathbf{r})$:

$$M_T(\mathbf{r}) = \sum_{c=1}^C S^{(c)}(\mathbf{r}) \cdot i\gamma M_0 \int_K \frac{B_1^{(c)}(\mathbf{k}) \rho(\mathbf{k})}{\|\gamma\mathbf{G}(\mathbf{k})\|_2} P(\mathbf{k}) \cdot \exp(i\langle \mathbf{k}, \mathbf{r} \rangle) d\mathbf{k}. \quad (2.55)$$

Equation 2.55 describes a system of linear equations. The channel specific RF waveforms $B_1^{(1)}, \dots, B_1^{(C)}$ can be designed such that – compared to the single-channel case – the exact same k -space information is deposited. As opposed to the single-channel case where the RF pulse is uniquely defined by the inverse Fourier transform of the target magnetization pattern, using multiple transmit channels substantially increases the number of degrees-of-freedom with respect to the RF waveform design. In other words: the system of equations (Eq. 2.55) is wildly over-determined. The level of over-determination is characterized by the sensitivity profiles $S^{(c)}(\mathbf{r})$ of the individual RF channels, especially by the pair-wise similarity of the sensitivity profiles (as was motivated in the previous section).

As a consequence of the over-determination one can decrease the sampling density of the k -space trajectory roughly by the level of over-determination of the system of equations. In this case every single transmit channel will produce an aliased magnetization profile. However, the degrees-of-freedom provided by the different RF waveforms can be chosen such that the aliasing artifacts of the different transmit channels cancel each other. The "goodness" at which the aliasing artifacts can be tailored to cancel each other depends on the pair-wise dissimilarity of the sensitivity profiles (which improves the condition of the associated linear problem in Eq. 2.55). The theoretical undersampling limit is defined by the number of transmit channels, i.e., excitation k -space can (theoretically) be C -fold undersampled compared to Nyquist-conform sampling. Since the RF coil design has physical and technical limitations that do not allow for designing optimal coil setups in practice, the maximum level of undersampling that still allows for accurate excitation of the target magnetization profile is usually smaller than the number of transmit channels.

Nonetheless, significant undersampling factors can be achieved which directly translates to accelerated RF excitation pulses. As a rule of thumb, in order for RF pulses to be practically useful, the duration must be limited to approximately 5 ms (the RF pulses developed in this work are developed to be shorter than this limit). Keeping in mind this pulse duration limit, the acceleration capabilities provided by the parallel excitation functionality are an indispensable technique (especially for 3-D target magnetization targets).

2.2.4 RF Waveform Calculation

For single channel transmission, the RF waveform that achieves a desired transverse magnetization profile is, according to Eq. 2.51, directly related to the sampling pattern of the k -space trajectory and the Fourier transform of the magnetization target. The k -space sampling pattern incorporates both the sampling density (i.e., the distance between the different turns of the k -space trajectory) as well as the velocity at which k -space is traversed. The applied RF field strength must be normalized to the k -space velocity in order to achieve a constant overall sampling density. This RF pulse design approach provides valuable insights into the excitation mechanisms in MRI, but the applicability to parallel transmission (pTx) RF pulses is limited (as the unfolding problem cannot be directly solved in this frame). For parallel transmission RF pulses, the "unfolding" problem must be solved as part of the RF waveform design based on

$$M_{\tau}(\mathbf{r}) = \sum_{c=1}^C S^{(c)}(\mathbf{r}) \cdot i\gamma M_0 \int_0^T \frac{B_1^{(c)}(\mathbf{k}) \rho(\mathbf{k})}{\|\gamma \mathbf{G}(\mathbf{k})\|_2} \cdot \exp(i \langle \mathbf{k}(t), \mathbf{r} \rangle) dt. \quad (2.56)$$

This formulation is similar to Eq. 2.55, however, an integral with time parameterization was used instead of an integral with k -space parametrization.

A more straight-forward approach for solving the pTx RF design problem is the *Spatial Domain RF Pulse Design* method proposed by Grissom et al. [45]. For a given transmit channel c and spatial location \mathbf{r} , the time continuous formulation can be discretized using a small time step τ , namely

$$\begin{aligned} i\gamma M_0 \int_0^T \frac{B_1^{(c)}(t) \rho(t)}{\|\gamma \mathbf{G}(t)\|_2} \cdot \exp(i \langle \mathbf{k}(t), \mathbf{r} \rangle) dt &\approx i\gamma M_0 \frac{1}{\tau} \sum_{n=1}^N \frac{B_1^{(c)}(n\tau) \rho(n\tau)}{\|\gamma \mathbf{G}(n\tau)\|_2} \cdot \exp(i \langle \mathbf{k}(n\tau), \mathbf{r} \rangle) \\ &= \mathbf{a} \mathbf{b}^{(c)} \end{aligned} \quad (2.57)$$

where

$$\mathbf{a} = (a_1, \dots, a_N) \quad \text{with} \quad a_n = \exp(i \langle \mathbf{k}(n\tau), \mathbf{r} \rangle) \quad (2.58)$$

$$\mathbf{b}^{(c)} = (b_1^{(c)}, \dots, b_N^{(c)})^T \quad \text{with} \quad b_n^{(c)} = i\gamma M_0 \frac{1}{\tau} \cdot \frac{B_1^{(c)}(n\tau) \rho(n\tau)}{\|\gamma \mathbf{G}(n\tau)\|_2}. \quad (2.59)$$

The vector $\mathbf{b}^{(c)}$ incorporates the "theoretical" RF waveform $B_1^{(c)}(t)$ as well as the density compensation terms $\|\gamma \mathbf{G}(t)\|_2$ and $\rho(t)$. Both of which are considered to be unknown in the RF pulse design at this point. The vector \mathbf{a} represents the value of the Fourier harmonic at spatial location \mathbf{r} for the time step series $0, \tau, 2\tau, \dots, n\tau$. This discretion scheme is applied to the entire spatial domain, i.e., for M Cartesian grid points

$$\mathbf{r}_1, \dots, \mathbf{r}_M \quad \text{with} \quad \mathbf{r}_m = (x_m, y_m, z_m). \quad (2.60)$$

The Fourier encoding vectors \mathbf{a}_m (one vector per spatial location \mathbf{r}_m) are assembled to generate a matrix A given by

$$A = \begin{bmatrix} \mathbf{a}_1 \\ \mathbf{a}_2 \\ \vdots \\ \mathbf{a}_M \end{bmatrix}^{M \times N}, \quad (2.61)$$

where \mathbf{a}_m denotes the Fourier encoding vector linked to the m -th spatial location \mathbf{r}_m . Using the matrix A , Eq. 2.57 can be written for all spatial locations for a single transmit channel c as

$$\mathbf{m} = A\mathbf{b}^{(c)}. \quad (2.62)$$

where $\mathbf{m} = (m(\mathbf{r}_1), m(\mathbf{r}_2), \dots, m(\mathbf{r}_M))$ denotes the magnetization at the different spatial locations. The matrix A is usually referred to as the *Fourier encoding matrix* and represents the relationship between the RF waveform in time domain and the resulting transverse magnetization in spatial domain. An equivalent formulation can be written for the parallel transmit case, i.e., when C separate transmit channels with sensitivity profile $S^{(c)}(\mathbf{r}_m)$ are employed, each of which driven by an individual RF waveform $\mathbf{b}^{(1)}, \dots, \mathbf{b}^{(C)}$. The system matrix is then extended to

$$A = \begin{bmatrix} S^{(1)}(\mathbf{r}_1) \cdot \mathbf{a}_1 & S^{(2)}(\mathbf{r}_1) \cdot \mathbf{a}_1 & \dots & S^{(C)}(\mathbf{r}_1) \cdot \mathbf{a}_1 \\ S^{(1)}(\mathbf{r}_2) \cdot \mathbf{a}_2 & S^{(2)}(\mathbf{r}_2) \cdot \mathbf{a}_2 & \dots & S^{(C)}(\mathbf{r}_2) \cdot \mathbf{a}_2 \\ \vdots & \vdots & \ddots & \vdots \\ S^{(1)}(\mathbf{r}_M) \cdot \mathbf{a}_M & S^{(2)}(\mathbf{r}_M) \cdot \mathbf{a}_M & \dots & S^{(C)}(\mathbf{r}_M) \cdot \mathbf{a}_M \end{bmatrix}^{M \times CN}. \quad (2.63)$$

The magnetization vector \mathbf{m} for given channel-specific RF waveforms $\mathbf{b}^{(1)}, \dots, \mathbf{b}^{(C)}$ is given by

$$\mathbf{m} = A\mathbf{b} \quad \text{where} \quad \mathbf{b} = \begin{bmatrix} \mathbf{b}^{(1)} \\ \vdots \\ \mathbf{b}^{(C)} \end{bmatrix}. \quad (2.64)$$

Assuming that the system matrix A is invertible, the solution of the system of equations in 2.64 for a given target magnetization \mathbf{m}^{tar} is given by

$$\mathbf{b} = A^{-1}\mathbf{m}^{\text{tar}}. \quad (2.65)$$

For under-determined systems this can be approximated in a least-squares sense by the minimization problem

$$\arg \min_{\mathbf{b}} \left\{ \left\| A\mathbf{b} - \mathbf{m}^{\text{tar}} \right\|_2^2 \right\} \quad (2.66)$$

with reasonable computational effort. The problem in Eq. 2.66 is linear and thus convex; for this problem type a number of efficient solvers such as *conjugate gradient* methods exist [58]. The RF waveform is usually constrained by a maximum voltage V_{max} that can be fed to the RF coil, namely

$$|\mathbf{b}_n^{(c)}| \leq V_{\text{max}} \quad (2.67)$$

is satisfied for all channels $c = 1, 2, \dots, C$ and time points $n = 1, 2, \dots, N$. This can be achieved by incorporating a *Tikhonov* regularization in Eq. 2.66 [127]. The minimization then reads

$$\arg \min_{\mathbf{b}} \left\{ \left\| A\mathbf{b} - \mathbf{m}^{\text{tar}} \right\|_2^2 + \lambda^2 \left\| \mathbf{b} \right\|_2^2 \right\}, \quad (2.68)$$

where λ is a non-negative regularization parameter. As λ is increased, more weight is placed upon reducing the energy deposition by the RF waveform rather than on achieving a high excitation fidelity. The regularization parameter is usually initialized by a rather small value and then iteratively increased (in a logarithmic manner) until the V_{max} constraint is satisfied. A more accurate but computationally more expensive method is to use a non-linear constrained optimization algorithm, written

$$\arg \min_{\mathbf{b}} \left\{ \left\| A\mathbf{b} - \mathbf{m}^{\text{tar}} \right\|_2^2 \right\} \quad \text{subject to} \quad \left\| \mathbf{b} \right\|_{\infty} \leq V_{\text{max}}. \quad (2.69)$$

This attempt directly incorporates the maximum voltage constraint and thus obtains better results, however, at the cost of increased computation times.

2.3 | Simulation of Electromagnetic Fields

In the previous sections it was shown that a number of different magnetic field components is required in an MR scanner for image generation. The static magnetic field B_0 produces a strong uniform magnetic field with only B_z field components without concomitant field terms $B_{x/y}$. Most often, the RF field B_1 is designed to produce a field with uniform magnitude and negligible spatial phase variation to achieve an in-phase magnetization pattern in the probe. Finally gradient coils are required to locally vary the precession frequency of the spin and thus achieve spatial encoding. This is achieved by creating \mathbf{B}_{Gx} , \mathbf{B}_{Gy} , \mathbf{B}_{Gz} fields (by the X, Y, and Z-gradient coil, respectively) whose z-component varies linearly along the three spatial axes:

$$\frac{d(\mathbf{B}_{Gx})_z}{dx} =: G_x, \quad \frac{d(\mathbf{B}_{Gy})_z}{dy} =: G_y, \quad \frac{d(\mathbf{B}_{Gz})_z}{dz} =: G_z. \quad (2.70)$$

Note that only the z-component of the magnetic vector field is relevant for the image generation whereas the concomitant field terms are negligible (at least for image generation). The quality characteristics of each magnetic field component (such as linearity for the gradient fields) determines the image quality that can be achieved by an MR system. It is, therefore, crucial to be able to assess the field characteristics of these coils at the design stage, prior to building expensive prototype coils. Another important aspect of the MRI coils are the imposed electric fields that can interact with the human body. The electric fields created by the RF cause heat deposition (SAR), that can denature proteins and damage tissue. Rapid switching of the gradient fields generates electric fields in the tissue that can cause peripheral nerve stimulation (PNS), leading to mild sensations at low levels, up to pain or cardiac malfunction at higher levels.

A powerful tool that has become more and more popular in the recent years due to affordable and powerful computing resources are *electromagnetic (EM) field simulations* that can be used to predict both the magnetic and electric fields imposed by arbitrary coil geometries. EM simulations attempt to find approximate solutions of Maxwell's equations, which is a set of coupled differential equations that describes the relationship between source entities (charges and currents) and electromagnetic fields and fluxes. There is a large variety of problem types in the field of EM simulations, including static problems (electrostatic and magnetostatic problems), low-frequency problems (especially eddy current calculations) as well as high-frequency problems (and many others). For each of these problem types, different approaches are used to represent and simplify Maxwell's equations. For example, different terms of the full set of Maxwell equations become negligible for different frequency ranges, spatial dimensions or electromagnetic properties of the simulated physical system. Additionally different problem types may require different strategies how to handle the problem numerically in an accurate and efficient manner (e.g., some problem types can be treated in different domains, such as time or frequency domain which can greatly affect numerical aspects such as stability or convergence characteristics).

In this work, EM field simulations are an important tool to model the electromagnetic fields induced by the MR gradient coils. Both the magnetic fields (to assess the accuracy of gradient encoding) and the electric fields (to assess interactions with the human body) imposed by the gradient coil will be investigated. The coils considered in this work (MRI gradient coils and MPI drive coils) are operated in the low kilohertz frequency range (in the order of 500 Hz to 10 kHz), i.e., these EM simulations are amenable to low-frequency approximations of Maxwell's equations.

2.3.1 Maxwell's Equations

Naturally, all methods for solving an EM field distribution are directly derived from Maxwell's equations (given here in differential formulation):

$$\text{Poisson's equations: } \nabla \cdot \mathbf{E} = \frac{\rho}{\epsilon_0} \quad (2.71)$$

$$\text{Gauss's law for magnetism: } \nabla \cdot \mathbf{B} = 0 \quad (2.72)$$

$$\text{Faraday's law of induction: } \nabla \times \mathbf{E} = -\frac{\partial \mathbf{B}}{\partial t} \quad (2.73)$$

$$\text{Ampere's circuital law: } \nabla \times \mathbf{B} = \mu_0 \left(\mathbf{J} + \epsilon_0 \frac{\partial \mathbf{E}}{\partial t} \right) \quad (2.74)$$

where \mathbf{E} denotes the electric field strength, \mathbf{B} denotes the magnetic flux density, \mathbf{J} denotes the electric current density, and ρ , ϵ_0 , and μ denote the electric charge density, the electric permittivity, and the magnetic permeability, respectively. The two homogeneous equations – the Poisson equation (Eq. 2.71) and Gauss's law for magnetism (Eq. 2.72) – prescribe how the electric and magnetic fields circulate around their respective field sources (with the magnetic field forming closed field lines). The two inhomogeneous differential equations – Faraday's law of induction (Eq. 2.73) and Ampere's law (Eq. 2.74) – describe how the fields vary spatially due to their sources. The Faraday's law indicates that the electric field circulates around a temporally changing magnetic field (this property becomes particularly important when the interactions of the magnetic fields in MRI with the human body are investigated). Similarly, Ampere's law states that the magnetic field circulates around electric current sources and around temporally varying electric fields.

Further more, we have

$$\mathbf{B} = \mu \mathbf{H} \quad (2.75)$$

that relates the magnetic flux density \mathbf{B} with the magnetic field strength \mathbf{H} via the magnetic permeability and

$$\mathbf{D} = \epsilon \mathbf{E} \quad (2.76)$$

that relates the electric displacement \mathbf{D} with the electric field \mathbf{E} via the electric permittivity. Finally

$$\mathbf{J} = \sigma \mathbf{E} \quad (2.77)$$

links the electric current density \mathbf{J} to the electric field \mathbf{E} in electrically conductive media with conductivity σ .

The general approach for most EM field simulation methods is to translate Maxwell's equations into a linear form, that is, to translate a *small* number of highly coupled differential equations (that are hard to capture numerically) to a rather *large* number of linear equations (which are efficiently processable using computer arithmetic). In order to do so, approximations need to be applied to Maxwell's equations, especially to the differential operators, e.g., approximating the curl or gradient operators on a finite neighborhood using *finite difference* methods.

In the following sections, the mathematical foundation of two common EM simulation approaches will be derived: the *Finite Difference Time Domain* (FDTD) method and the *Finite Element*

method (FEM). Although the FDTD method has only limited applicability to low-frequency problems, the derivation provides excellent insights into the mechanisms behind Maxwell's equations.

2.3.2 The Finite Difference Time Domain Method

A first popular approach for EM field simulations is the *Finite Difference Time Domain* method (FDTD) that evaluates how the electromagnetic fields evolve over time [21, 84]. The time evolution of the EM fields is approximated by applying finite difference methods both on a spatial grid and on a temporal grid. The physical system under consideration is excited by feeding an electromagnetic wave (*excitation signal*) to it and approximating the propagation of the wave through the modeled domain. In order to fully prescribe the propagation of the EM fields, Maxwell's equations can be reduced to a smaller set of differential equations which still correctly captures all physical dependencies.

For example, taking the divergence of Ampere's law (given in terms of magnetic field strength \mathbf{H} and electric displacement \mathbf{D})

$$\nabla \times \mathbf{H} = \mathbf{J} + \frac{\partial \mathbf{D}}{\partial t} \quad (2.78)$$

yields

$$\nabla \cdot \nabla \times \mathbf{H} = \nabla \cdot \mathbf{J} + \frac{\partial}{\partial t} \nabla \cdot \mathbf{D} \quad (2.79)$$

$$\text{i.e., } 0 = \nabla \cdot \mathbf{J} + \frac{\partial}{\partial t} \nabla \cdot \mathbf{D} \quad (2.80)$$

Replacing the divergence of the electric current density, $\nabla \cdot \mathbf{J}$, using the equation of electric charge continuity

$$\frac{\partial \rho}{\partial t} + \nabla \cdot \mathbf{J} = 0 \quad (2.81)$$

results in

$$\frac{\partial \rho}{\partial t} = -\frac{\partial}{\partial t} \nabla \cdot \mathbf{D} \quad (2.82)$$

which is nothing but the temporal derivative of Poisson's equation. Therefore, as long the initial EM fields satisfy Poisson's equation, Ampere's law in conjunction with the conservation of electric charge can be used to correctly advance the EM fields over time. Similarly, taking the divergence of Faraday's law, i.e.,

$$\nabla \cdot \nabla \times \mathbf{E} = -\frac{\partial}{\partial t} \nabla \cdot \mathbf{B} \quad (2.83)$$

$$\text{i.e., } 0 = -\frac{\partial}{\partial t} \nabla \cdot \mathbf{B} \quad (2.84)$$

shows that it is sufficient to ensure that the initial EM field satisfies $\nabla \cdot \mathbf{B} = 0$. Accordingly, a correct time evolution of the electromagnetic fields is completely specified by

$$\epsilon \frac{\partial \mathbf{E}}{\partial t} = \nabla \times \mathbf{H} - \mathbf{J} \quad (2.85)$$

$$\mu \frac{\partial \mathbf{H}}{\partial t} = -\nabla \times \mathbf{E} \quad (2.86)$$

as long as the initial conditions $\nabla \cdot \mathbf{D} = \rho$ and $\nabla \cdot \mathbf{B} = 0$ are fulfilled. Writing the two equations in an element-wise manner yields

$$\epsilon \frac{\partial E_x}{\partial t} = \frac{\partial H_z}{\partial y} - \frac{\partial H_y}{\partial z} \quad (2.87a)$$

$$\epsilon \frac{\partial E_y}{\partial t} = \frac{\partial H_x}{\partial z} - \frac{\partial H_z}{\partial x} \quad (2.87b)$$

$$\epsilon \frac{\partial E_z}{\partial t} = \frac{\partial H_y}{\partial x} - \frac{\partial H_x}{\partial y} \quad (2.87c)$$

for Ampere's law and

$$\mu \frac{\partial H_x}{\partial t} = \frac{\partial E_y}{\partial z} - \frac{\partial E_z}{\partial y} \quad (2.88a)$$

$$\mu \frac{\partial H_y}{\partial t} = \frac{\partial E_z}{\partial x} - \frac{\partial E_x}{\partial z} \quad (2.88b)$$

$$\mu \frac{\partial H_z}{\partial t} = \frac{\partial E_x}{\partial y} - \frac{\partial E_y}{\partial x} \quad (2.88c)$$

for Faraday's law. These six equations are used in the FDTD method to compute the evolution of \mathbf{E} and \mathbf{H} over time, as they can be implemented very efficiently.

Staggered Grids

For the FDTD method to achieve accurate results for the EM fields, it is crucial to implement an efficient and numerically stable method to evaluate the finite differences. An approach that is particularly suited for the system of equations (Eqs. 2.87 and 2.88) is the use of so-called *staggered grids*. This means that the electric and magnetic fields are evaluated on different grids, shifted towards one another by half a cell size. The shift is applied both spatially (i.e., the spatial grid points are shift by half a cell size in x , y , and z) and temporally (the finite differences are evaluated at integer and half-integer time steps Δt). In other words, if a variable is located at an integer point, its first-order derivative is best evaluated at the surrounding half-integer points. To illustrate this approach, let's consider propagation of a plane wave along the z -axis given by the following differential equations

$$\epsilon \frac{\partial E_x}{\partial t} = -\frac{\partial H_y}{\partial z} \quad (2.89)$$

$$\mu \frac{\partial H_y}{\partial t} = \frac{\partial E_x}{\partial z} \quad (2.90)$$

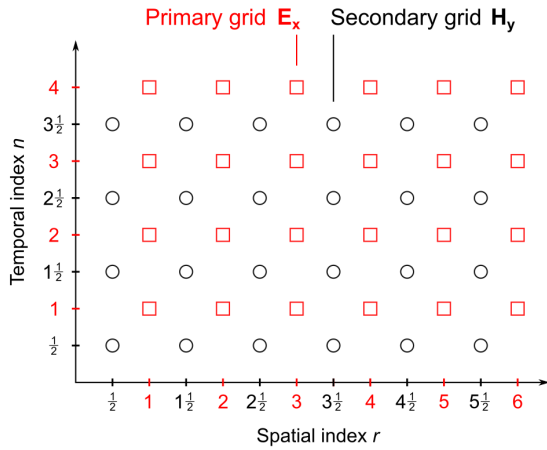


Figure 2.4: Staggered grid scheme both in space (x -axis) and in time (y -axis) to ensure accurate estimation of finite differences in the FDTD method.

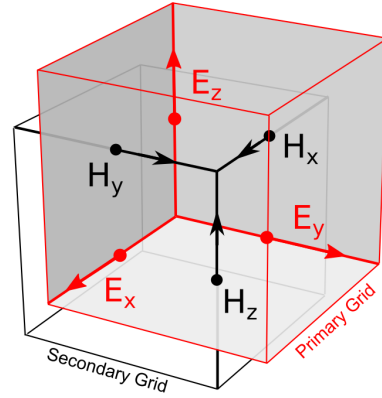


Figure 2.5: Three-dimensional spatial grid according to the Yee-Cell scheme with the respective \mathbf{E} and \mathbf{H} field components.

Applying the staggered grid approach of finite difference evaluation to these equations yields

$$\frac{E_x|_r^{n+1} - E_x|_r^n}{\Delta t} = -\frac{1}{\epsilon} \frac{H_y|_{r+1/2}^{n+1/2} - H_y|_{r-1/2}^{n+1/2}}{\Delta z}, \quad (2.91)$$

$$\frac{H_y|_{r+1/2}^{n+1/2} - H_y|_{r+1/2}^{n-1/2}}{\Delta t} = -\frac{1}{\mu} \frac{E_x|_{r+1}^n - E_x|_r^n}{\Delta z}. \quad (2.92)$$

The index $|_r$ refers to the r -th spatial location and the index $|^n$ to the n -th time point, so that $f|_r^n = f(r\Delta z, n\Delta t)$. The finite difference in time for the electric field E_x is evaluated using the magnetic field by shifting the spatial and temporal locations by half an integer step. Equivalently, the finite difference in time for the magnetic field (at a half integer grid point) is evaluated at integer spatial and time points based on the electric field. The "time"- "position" grid is illustrated in Fig. 2.4, where the x -axis carries the spatial locations and the y -axis carries the temporal locations for the both \mathbf{E} and \mathbf{H} fields.

In 3-D an arrangement of the spatial points according to the so-called *Yee-Cell* [126] has proven very favorable: again the spatial locations for the \mathbf{E} -field (red grid lines) and the \mathbf{H} -field (black grid lines) are shifted against each other by half a spatial step.

Excitation Signal and Time Stepping

The FDTD simulation is excited by feeding an electromagnetic wave of limited length (*excitation signal*) into the physical system (using so-called *ports*) and modeling the propagation of the stimulus throughout the physical domain. The simulation continues until the wave in the physical domain has decayed. The properties of the excitation signal are determined by the resonance frequencies of the physical system that are of interest (e.g., for EM simulations in the frame of MRI that often deal with RF receive or transmit coils, this is often the frequency of the spin precession). A very short excitation signal covers a large variety of frequency components, including very high-frequencies. Because the mesh size is determined by the highest frequency component (i.e., the mesh needs to be chosen such that it can resolve the propagating waves), an excessively short excitation signal will dramatically increase the number of cells in the simulation

mesh. Furthermore, a sharp excitation signal will excite resonances which are not of interest. In this case the energy is stored in the resonant structures, meaning that the decay of the wave progresses very slowly and the simulation will not converge within reasonable runtime. Additionally an excessively short pulse may lead to the fact the frequencies which are of interest, are not resolved accurately. On the other hand an excessively long excitation signal (which in turn has a rather sharp frequency spectrum) increases the number of time samples as the entire signal needs to fit into the simulation time. In particular a requirement for accurate EM field estimates is that the excitation signal has vanished by the end of the excitation phase to avoid generation of high-frequency components during the cut-off of the excitation.

In short, the simulation time of the FDTD method is determined by the complexity of the grid itself (i.e., the number of the mesh cells), the time step Δt and the number of time steps N , determining the full simulation time. In order for the finite difference scheme to accurately model the EM field propagation, the spatial steps Δx , Δy , and Δz and the temporal step Δt must be chosen according to the *Courant-Friedrich-Levy* condition

$$\Delta t \leq \frac{1}{c \sqrt{\left(\frac{1}{\Delta x}\right)^2 + \left(\frac{1}{\Delta y}\right)^2 + \left(\frac{1}{\Delta z}\right)^2}} . \quad (2.93)$$

This condition states that the wave must not travel more than a single cell per time step. If this condition is not satisfied there is substantial numerical dispersion which leads to degenerate solutions for the EM fields.

For the simulation of high-frequency problems (i.e., RF receive and transmit coils), the FDTD method is a very powerful tool, as it covers a large range of resonance frequencies and is, therefore, perfectly suited to investigate tuning and matching characteristics of RF coils in MRI. The applicability of the FDTD method to low-frequency EM problems, however, is limited. In order for the low-frequency to be resolved by the simulation, an extremely long excitation signal must be used. The maximum time step, however, is in this case dictated by the physical model, i.e., by the feature size that needs to be resolved. In short this means that the low-frequency simulation requires a very long excitation signal (to resolve the low-frequency component) and a very small time step (to resolve spatial properties of the model), resulting in an infeasible computational effort.

An EM field simulation method, which is much more suited for the low-frequency range is the finite element method that will be explained in the following.

2.3.3 The Finite Element Method

Another approach for simulating electromagnetic fields in highly heterogeneous models (like human body models) is the finite element method (FEM). In the FEM, the domain at which the electromagnetic fields are to be computed is divided into smaller elements, each of which having homogeneous electromagnetic properties. The same approach is taken in the FDTD method, where the domain is approximated by the Cartesian grid. The big advantage of the FEM domain division (compared to the FDTD method), is that the elements must not necessarily be hexahedral (i.e., cubical) regions, but other types of elements like tetrahedral elements (i.e., pyramids) can be chosen. This is an important and powerful feature, especially when dealing with highly complex curved geometries (like human body models involving many tissue objects or complex coil wire patterns), because the accurate representation of the model by using tetrahedral elements requires substantially fewer elements (compared to using hexahedral elements). From

the mathematical perspective, the FEM is more complex than the FDTD method. In the following a brief introduction to the basic principle of the FEM will be given. In this explanation the FEM concepts are formulated in the frame of *Variational Problems* which is an approach very close to a physical interpretation in terms of *energy conservation principles*.

2.3.3.1 Variational Methods

The basic idea of applying variational methods to the problem of solving differential equations is to find a solution that minimizes a certain integral (called *functional*). Very often, the integral characterizes the energy stored in the modeled system. Hence, the solution that minimizes the functional also minimizes the stored energy which closely resembles the real world phenomenon. The general problem can be formulated in *operator* notation which is applicable to a wide range of problem types. The so-called deterministic problem associated with an operator L can be written as

$$Lu = f \quad (2.94)$$

where $f = f(r)$ is a function of space, L is the operator that defines the problem type and u is the solution to be found. For example, for $L = -(\nabla^2 + k^2)$ and $f = 0$ being a known charge distribution, Eq. 2.94 represents one vector component of an inhomogeneous Helmholtz equation.

The set of valid functions that u may be chosen from (i.e., the *function space*) belongs to the field of definition of the operator L , i.e., $u \in D_L$. These functions are required to be sufficiently differentiable and must obey the boundary condition of the differential equation under consideration (although a central element in the handling of differential equations, the boundary conditions will not be treated in detail here). Very often, a Hilbert space is a convenient choice of a function space. A Hilbert function space is spanned by functions satisfying the following conditions:

$$\text{Symmetry: } \langle u, v \rangle = \langle v, u \rangle^* \quad (2.95a)$$

$$\text{Linearity: } \langle a_1 u_1 + a_2 u_2, v \rangle = a_1 \langle u_1, v \rangle + a_2 \langle u_2, v \rangle \quad (2.95b)$$

$$\text{Positive Definiteness: } \langle u, u \rangle \geq 0 \text{ with } \langle u, u \rangle = 0 \text{ if and only if } u = 0 \quad (2.95c)$$

where $(\cdot)^*$ denotes the conjugate transpose. As for the operator in Eq. 2.94, only so-called *self-adjoint* operators L are considered, meaning that $\langle Lu, v \rangle = \langle u, Lv \rangle$ where $\langle u, v \rangle$ denotes the inner product of the function u and v given by

$$\langle u, v \rangle := \int_{\Omega} uv^* d\Omega. \quad (2.96)$$

This formulation can be interpreted as the continuous extension of the dot-product, i.e., it calculates the component of a function u along a second function v (or vice versa) and thus is a measure of orthogonality.

Another important property in the frame of variational methods, especially when investigating methods to obtain the solution u of the problem in Eq. 2.94, is *positive definiteness*, meaning that

$$\langle Lu, u \rangle > 0 \quad (2.97)$$

holds for all u that are not identical to zero, and that the above term only vanishes for $u = 0$. These two properties ensure the uniqueness of any u that solves Eq. 2.94. This can be proofed easily by supposing two solutions denoted by u_1 and u_2 , such that

$$L u_1 = L u_2 = f . \quad (2.98)$$

Letting $w = u_1 - u_2$, then the linearity of the operator L leads to $\langle L w, w \rangle = 0$. Since L is required to be positive-definite, w must be equal to zero, meaning that $u_1 = u_2$.

The solution to the differential equation in Eq. 2.94 corresponds to a stationary point of a functional F in *quadratic form*, given by

$$F = \langle L u, u \rangle - 2 \langle u, f \rangle \quad (2.99)$$

where u and f are real-valued functions. In case of complex functions, the functional is slightly modified by substituting $2 \langle u, f \rangle$ by $\langle u, f \rangle + \langle f, u \rangle$. The minimum value F_{\min} that the functional takes for the solution u_0 is given by

$$F_{\min} = -\langle L u_0, u_0 \rangle \quad (2.100)$$

which is equal to the energy stored in the system. In other words, the field quantity u arranges itself so as to minimize the stored energy, which very closely resembles the physical interpretation of the problem.

The obvious question is how to obtain the solution of the differential equation, i.e., how to determine the function u_0 that minimizes the functional F . A popular approach to solve this problem is the *Rayleigh-Ritz* method (which is closely related to the *Galerkin* method). The basic idea is to assemble the solution by a weighted sum of basis functions ϕ_j for $j = 1, \dots, n$ with coefficients a_j , namely

$$u_n = \sum_{j=1}^n a_j \phi_j . \quad (2.101)$$

This means that instead of directly solving for a solution u_0 , the solution is approximated by a weighted sum u_n of basis functions, and the coefficients a_j , rather than the solution function itself is to be found. Incorporating Eq. 2.101 into the functional to be minimized, Eq. 2.99, yields

$$\begin{aligned} F &= \left\langle \sum_{j=1}^n a_j L \phi_j, \sum_{k=1}^n a_k \phi_k \right\rangle - 2 \left\langle \sum_{j=1}^n a_j \phi_j, f \right\rangle \\ &= \sum_{j,k=1}^n \langle L \phi_j, \phi_k \rangle a_j a_k - 2 \sum_{j=1}^n \langle \phi_j, f \rangle a_j . \end{aligned} \quad (2.102)$$

The weighting coefficients a_j are chosen such that the derivatives of the functional F vanish,

$$\frac{\partial F}{\partial a_j} = 0 \quad \text{for all } j = 1, \dots, n \quad (2.103)$$

i.e., that u_n is a stationary point. Eq. 2.102 is rearranged such that terms containing a_i are separated by power terms, i.e.,

$$F = \langle L\phi_i, \phi_i \rangle a_i^2 + \underbrace{\sum_{k \neq i} \langle L\phi_i, \phi_k \rangle a_i a_k + \sum_{j \neq i} \langle L\phi_j, \phi_i \rangle a_j a_i}_{= 2 \sum_{k \neq i} \langle a\phi_i, \phi_k \rangle a_i a_k} - 2 \langle f, \phi_i a_i \rangle + F_{\text{res}} \quad (2.104)$$

where F_{res} summarizes the functional terms that do not depend upon a_i . The second and third term have been combined by making use of self-adjointness of the operator L . Taking the partial derivative of the function F with respect to a_i leads to

$$\frac{\partial F}{\partial a_i} = 2 \langle L\phi_i, \phi_i \rangle a_i + 2 \sum_{k \neq i} \langle L\phi_i, \phi_k \rangle a_k - 2 \langle f, \phi_i \rangle \quad (2.105)$$

$$= 2 \sum_{k=1}^n \langle L\phi_i, \phi_k \rangle a_k - 2 \langle f, \phi_i \rangle . \quad (2.106)$$

Setting the above equation to 0 results in

$$\sum_{k=1}^n \langle L\phi_i, \phi_k \rangle a_k = \langle f, \phi_i \rangle \quad (2.107)$$

which can be conveniently written in matrix notation as

$$\begin{bmatrix} \langle L\phi_1, \phi_1 \rangle & \langle L\phi_1, \phi_2 \rangle & \dots & \langle L\phi_1, \phi_n \rangle \\ \langle L\phi_2, \phi_1 \rangle & \langle L\phi_2, \phi_2 \rangle & \dots & \langle L\phi_2, \phi_n \rangle \\ \vdots & \vdots & \ddots & \vdots \\ \langle L\phi_n, \phi_1 \rangle & \langle L\phi_n, \phi_2 \rangle & \dots & \langle L\phi_n, \phi_n \rangle \end{bmatrix} \begin{bmatrix} a_1 \\ a_2 \\ \vdots \\ a_n \end{bmatrix} = \begin{bmatrix} \langle f, \phi_1 \rangle \\ \langle f, \phi_2 \rangle \\ \vdots \\ \langle f, \phi_n \rangle \end{bmatrix} . \quad (2.108)$$

The above system of equations can be readily solved for the coefficients a_i that in turn determine the approximate solution of the differential equation.

2.3.3.2 Application to EM Field Problem

In order to apply the basic framework derived above to the problem of EM field simulations, the two equations from the first section will be used, that characterize the time evolution of the electric field \mathbf{E} depending on the magnetic field \mathbf{H} (Eq. 2.85) and the evolution of the magnetic field \mathbf{H} depending on the electric field \mathbf{E} (Eq. 2.86). These two first-order differential equations can be combined into a single second-order equation given by

$$\nabla \times \frac{1}{\mu} \nabla \times \mathbf{E} + \epsilon \frac{\partial^2 \mathbf{E}}{\partial t^2} = -\frac{\partial \mathbf{J}}{\partial t} . \quad (2.109)$$

The above equation is referred to as the *curl-curl equation* or vector wave equation. Initial conditions that need to be satisfied for this second-order differential equation are the electric field and its time derivative at time $t_0 = 0$. An approach that is generally used for applying FEM to electromagnetic field problems is to solve Eq. 2.109 in *frequency domain*. In this case

time derivatives $\partial/\partial t$ are replaced by a harmonic dependence given by $\exp(i\omega t)$ where ω denotes the angular frequency at which the physical system is solved. In frequency domain, Eq. 2.109 becomes

$$\nabla \times \frac{1}{\mu} \nabla \times \mathbf{E} - \epsilon\omega^2 \mathbf{E} = -i\omega \mathbf{J} . \quad (2.110)$$

In order find a solution for this problem, a *weak formulation* in the spirit of the variational approach needs to be formulated. As was done above, this means multiplication by a "test function" and integration over the physical domain Ω , leading to

$$\int_{\Omega} \frac{1}{\mu} (\nabla \times \mathbf{E}) \cdot (\nabla \times \mathbf{F}) - \omega^2 \int_{\Omega} \epsilon \mathbf{E} \cdot \mathbf{F} = -i\omega \int_{\Omega} \mathbf{J} \cdot \mathbf{F} \quad (2.111)$$

where Ω denotes the physical domain and \mathbf{F} is the "test function" which is to be approximated in order to find the best solution of the differential equation.

2.3.3.3 Low-Frequency Approximation

A common modification which is usually applied to Eq. 2.110 is to neglect displacement currents which is a reasonable assumption for low-frequencies where ohmic currents dominate the displacement currents. In particular this kind of approximation can be employed if the worst case diagonal of the physical domain d is much smaller than the wavelength λ of electromagnetic fields to be simulated, namely

$$\left(\frac{d}{\lambda}\right)^2 \ll 1 . \quad (2.112)$$

Specifically, neglecting displacement currents in Maxwell's equations is achieved by setting the permittivity ϵ to zero. Separating the right hand side of Eq. 2.110 into a conductive current density characterized by $\sigma \mathbf{E}$ and an externally applied current density \mathbf{J}_{ext} leads to

$$\nabla \times \frac{1}{\mu} \nabla \times \mathbf{E} + i\omega\sigma \mathbf{E} = -i\omega \mathbf{J}_{\text{ext}} . \quad (2.113)$$

Note that the external current density \mathbf{J}_{ext} is often used to prescribe a current path, e.g., following the wire pattern of MRI gradient coils. Physically speaking, the low-frequency approximation avoids electromagnetic waves in the Maxwell equations, which allows to take time steps which are significantly larger, e.g., compared to the steps required by the FDTD method. However, neglecting this aspect of Maxwell's equations renders mathematical treatment of the differential equation more complex because in non-conductive regions ($\sigma = 0$) the time derivative of the electric field is unspecified, meaning that the field evolution cannot be modeled in this region (for the investigations carried out in this work, this limitation is not significant as the method is used to evaluate electromagnetic fields only in the conductive human body).

The differential equation given in Eq. 2.113 is usually solved by introducing the so-called magnetic vector potential $\mathbf{A}(\mathbf{r})$ such that for the magnetic field

$$\mathbf{B} = \nabla \times \mathbf{A} \quad (2.114)$$

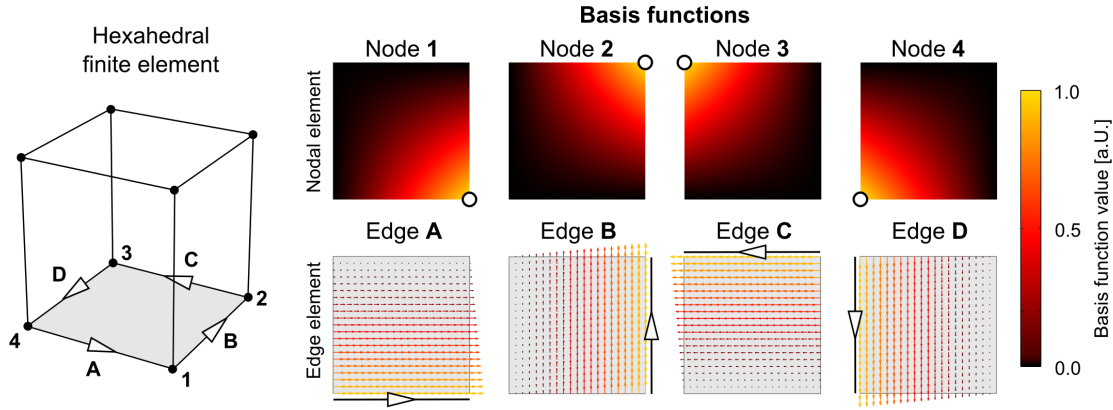


Figure 2.6: Hexahedral finite element (left) along with local basis functions to approximate scalar (top right) and vector-valued quantities (bottom right) within the element.

holds. The electric field is given by

$$\mathbf{E} = -i\omega\mathbf{A} - \nabla\phi \quad (2.115)$$

where ϕ denotes the electrostatic potential. Using these two definitions for the magnetic field \mathbf{B} and the electric field \mathbf{E} , Ampere's law (Eq. 2.113) can be rewritten as

$$\nabla \times \frac{1}{\mu} \nabla \times \mathbf{A} + \sigma (i\omega\mathbf{A} + \nabla\phi) = \mathbf{J}_{\text{ext}} . \quad (2.116)$$

Additionally two constraints need to be defined based on the fact that setting $\epsilon = 0$ in Ampere's law means that both the excitation coil current \mathbf{J}_{ext} and the conduction currents determined by $-\sigma (i\omega\mathbf{A} + \nabla\phi)$ have zero divergence. This means that both the coil currents and the conduction currents form closed loops of current flow. This is enforced by the equations

$$\nabla \cdot \mathbf{J}_{\text{ext}} = 0 \quad (2.117)$$

$$\nabla \cdot \sigma (i\omega\mathbf{A} + \nabla\phi) = 0 \quad (2.118)$$

which along with Eq. 2.116 represent a common formulation for handling low-frequency electromagnetic field problems.

2.3.3.4 Mesh Generation

One of the major advantages of the FEM over the FDTD approach is the flexibility with respect to the choice of mesh cell types. In Sec. 2.3.2 it was illustrated that in order for the finite difference scheme used in the FDTD method to be implemented and evaluated efficiently, the FDTD method is based on hexahedral grids. When dealing with complex curved geometries (like human body models or MR gradient coils) the number of hexahedral mesh cells needs to be increased dramatically in order to preserve small geometric features of the model. In particular, the FDTD method is generally not capable to locally adapt to the feature size of the body model, i.e., if small local features need to be preserved, the entire grid needs to be refined (even if the small features are only present in a few locations of the model).

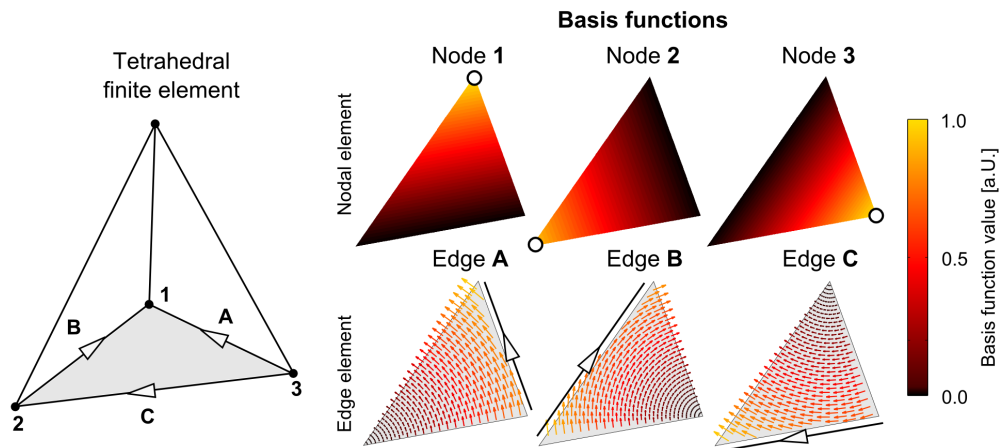


Figure 2.7: Tetrahedral finite element (left) along with local basis functions to approximate scalar (top right) and vector-valued quantities (bottom right) within the element.

On the contrary, the FEM approach can be applied using a wide range of mesh cell types or "element" types; the two most commonly used element types are *hexahedral* (i.e., cubical, see Fig. 2.6) and *tetrahedral* (i.e., pyramidal, see Fig. 2.7) finite elements. Independently of the finite element type, the elements are defined by nodes and edges (connecting two nodes). The hexahedral element is defined by 8 nodes and 12 edges, the tetrahedral element consists of 4 nodes and 6 edges. Especially tetrahedral elements are perfectly suited to approximate complex curved structures. Due to the irregular shape of the tetrahedral elements, the size of the elements can vary locally: in regions of fine geometric details, very small elements can be used, whereas other regions (e.g., the background region) can be discretized by only few very large elements without significant penalties in accuracy. Due to this local adaptation feature, switching from hexahedral to tetrahedral finite elements often allows to reduce the number of mesh cells by up to 50-fold. The mesh generation, however, i.e., the process of discretizing a geometric object by tetrahedral finite elements, is considerably more complex compared to hexahedral elements. After a geometric object has been approximated by a finite element mesh, the basis functions (see Eq. 2.101) are defined locally in the mesh cells. Most commonly the scope of each basis function is limited to a single mesh cell (referred to as *local* basis functions). The problem of defining an appropriate (mathematically complete) set of basis functions is rather complex, and its detailed handling is beyond the scope of this work. Instead a rather phenomenological description will be given here, but the reader is referred to the very comprehensive literature (see e.g. [123]).

There is a wide range of different approaches on how to select and define local basis functions. The choice of an appropriate basis function type greatly depends on the type of differential equation, the physical quantity to be approximated by the basis functions (e.g., scalar vs. vector field quantities), as well as implementation details of the FEM solver architecture. Two common types of basis functions for the two element types are illustrated on the right hand side of Fig. 2.6 (hexahedral element) and Fig. 2.7 (tetrahedral element). The basis functions are usually defined as *nodal basis functions* or *edge basis functions*, hence the number of basis functions defined in a single mesh cell is determined by the number of nodes or edges, respectively. Nodal basis functions are usually defined as scalar functions that are linear within the cell. Given a weight a_j for the j -th node, the scalar basis function is specified such that it is equal to the weight a_j at the node j , and vanishes for all other nodes. Hence the FEM simulation using nodal basis

functions implements the degrees-of-freedom via the mesh nodes. Because the weight a_j affects all neighboring cells (i.e., the respective basis functions) this formalism ensures that the entire modeled scalar function (i.e., the sum of all weighted local basis functions) is continuous.

As opposed to nodal basis functions, edge basis functions are associated with the edges of the mesh. These basis functions are commonly used to approximate vector field quantities. The degrees-of-freedom of the FEM simulation (i.e., the weights) are assigned to the edges of the mesh (rather than the nodes). A schematic depiction of edge basis functions is shown in Figs. 2.6 and 2.7. These basis functions are defined such that the tangential component of the locally described vector field is continuous along the edges of the element. The normal component, however, can be discontinuous at the element boundary. Edge elements are so-called *curl-conform*, meaning that the curl of the element does not induce delta functions at the boundaries of the element. This ensures that a vector field which is expanded by edge elements is square-integrable. Note that a large variety of other types of mesh elements and basis functions exist that have been developed specifically for different FEM problem types.

3

Methods

3.1 | Optimal Gradient Waveform Design

In this section, a mathematical framework will be derived to generate time-optimal 3-D gradient waveforms subject to constraints on the gradient magnitude (G_{\max}) and slew rate (S_{\max}) [28, 26]. In short this methods assembles the gradient waveforms in terms of piece-wise linear gradient segments. This allows to generate triangular and trapezoidal wave shapes which are time-optimal for the given set of constraints. The length and slope of each linear segment in each of the three dimensions is then optimized in order to accelerate the entire gradient waveform while ensuring that the anticipated shape of the k -space trajectory (spanned by an ordered set of k -space control points) is maintained.

3.1.1 Problem Formulation

For a set of control points $\mathbf{k}^{(1)}, \dots, \mathbf{k}^{(N)}$ in three-dimensional k -space with $\mathbf{k}^{(q)} = (k_x^{(q)}, k_y^{(q)}, k_z^{(q)})$ a gradient trajectory $\mathbf{k}(t)$ is to be generated that satisfies the following three constraints:

- (1) $\mathbf{k}(t^{(q)}) = \mathbf{k}^{(q)}$ and $0 = t^{(1)} \leq t^{(2)} \leq \dots \leq t^{(N)} = T$, i.e., the trajectory traverses the k -space control points one after another in the specified order,
- (2) $\left\| \frac{d}{dt} \mathbf{k}(t) \right\|_{\infty} \leq G_{\max}$ and $\left\| \frac{d^2}{dt^2} \mathbf{k}(t) \right\|_{\infty} \leq S_{\max}$ in $t \in [0, T]$, i.e., the gradient waveforms underlying the k -space trajectory satisfy the gradient system constraints,
- (3) the k -space trajectory minimizes the duration T .

Consequently, the exact shape of the trajectory in between two consecutive control points is kept flexible in order to be optimized to generate a gradient waveform of minimal duration T , subject to the gradient magnitude (G_{\max}) and slew rate constraints (S_{\max}).

The problem formulation is valid both in the reception [118] and transmission regime [9], with the trajectories being specified by

$$\mathbf{k}_R(t) = \gamma \int_0^t \mathbf{G}(\tau) d\tau \quad \text{and} \quad \mathbf{k}_T(t) = -\gamma \int_t^T \mathbf{G}(\tau) d\tau. \quad (3.1)$$

Note that these formulations ensure that, in the reception case $\mathbf{k}_R(t)$, the trajectory always starts at the center of k -space ($\mathbf{k}_R(0) = \mathbf{0}$) whereas in the transmission case, the trajectory

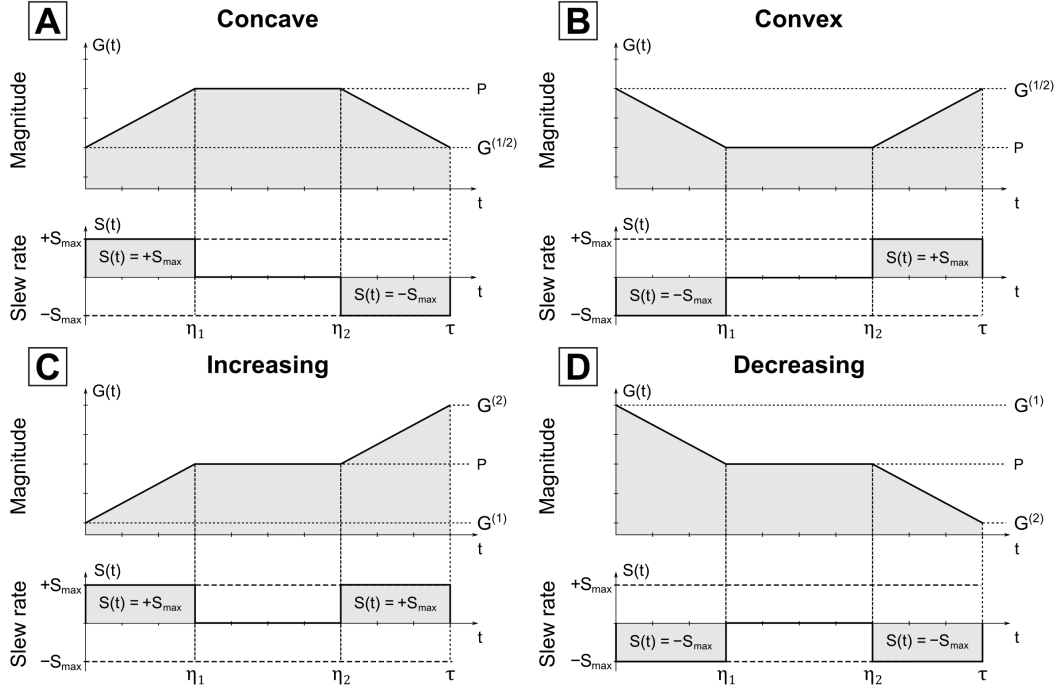


Figure 3.1: Gradient Basis Functions: Four basis functions can be used to establish the traversal between two consecutive control points in one-dimensional k -space: a concave (**A**) and convex basis (**B**) as well as an increasing (**C**) or decreasing one (**D**); for each basis the gradient magnitude (top) and slew rate (bottom) are shown. The integral of the gradient waveform is equal to $\Delta k = k^{(2)} - k^{(1)}$. The solution of a basis function based on the problem vector $(G^{(1)}, G^{(2)}, \Delta k, \tau)$ is specified by the basis function parameters (P, η_1, η_2) .

ends at the center of k -space ($\mathbf{k}_T(T) = \mathbf{0}$) to ensure a refocused magnetization at the end of the RF pulse. It is very straight forward to translate between these two cases by compensating for the constant k -space distance when the integration bounds are changed:

$$\mathbf{k}_R(t) = \underbrace{-\gamma \int_t^T \mathbf{G}(\tau) d\tau}_{= \mathbf{k}_T(t)} + \underbrace{\gamma \int_0^T \mathbf{G}(\tau) d\tau}_{= \mathbf{k}^{(N)} - \mathbf{k}^{(1)}}. \quad (3.2)$$

3.1.2 Gradient Basis Functions

Due to the complexity of designing time-optimal gradient waveforms in three-dimensional k -space based on a large number of control points, the problem is first approached on a *local* scale. In this frame, *local* refers to a gradient trajectory segment connecting two consecutive control points (denoted by $k^{(1)}$ and $k^{(2)}$) in a single dimension. In addition, it is assumed that the gradient strengths in each control point, denoted by $G^{(1)}$ and $G^{(2)}$, are known. The local one-dimensional problem can then be formulated as defining a gradient waveform $G(t)$ in the time interval $[0, \tau]$ that accumulates the k -space distance

$$\Delta k = k^{(2)} - k^{(1)} = \gamma \int_0^\tau G(t) dt \quad (3.3)$$

and satisfies $G(0) = G^{(1)}$ and $G(\tau) = G^{(2)}$ as well as the gradient magnitude and slew rate constraints

$$|G(t)| \leq G_{\max} \quad \text{and} \quad \left| \frac{d}{dt} G(t) \right| = |S(t)| \leq S_{\max} \quad (3.4)$$

for any $t \in [0, \tau]$. Although, on the *global* scale (including all control points in three dimensions) the aim is to eventually generate *time-optimal* trajectories, the local duration τ (in a single dimension) may also be chosen sub-optimally (because usually only one gradient axis is driven at the performance limit whereas the other two axes do not reach the limits). In other words, the local gradient design problem is solved for arbitrary but valid durations τ . Without exception, time-optimal gradient waveforms are of triangular or trapezoidal shape. This fact motivates the introduction of generalized so-called *Gradient Basis Functions*. Each gradient basis function specifies a certain sequence of switching the slew rate (note that the introduced basis functions are not basis functions in the common mathematical sense where they are used, e.g., in the theory of approximating solutions of differential equations). Since a triangular gradient wave shape can be represented by a trapezoidal wave shape having a plateau phase of zero length, two basis functions are needed, a convex and a concave basis (cf. Fig. 3.1, A and B). For these basis functions the gradient magnitude is always driven at $\pm S_{\max}$ at the ramps and possibly at $\pm G_{\max}$ during the plateau phase, if the gradient strength reaches the G_{\max} constraint. Additionally to these time-optimal basis functions, two sub-optimal bases are defined that generate wave shapes that are monotonically increasing or decreasing. Again, the ramps of these gradient wave shapes are driven at $+S_{\max}$ or $-S_{\max}$ and have a plateau phase of constant gradient strength in between the two ramps. These two sub-optimal basis functions are depicted in Fig. 3.1 (C and D). It can be shown that this set of four basis functions is sufficient to assemble a time-optimal gradient waveform that obeys the three conditions formulated above. In other words, if an arbitrarily shaped gradient waveform can be found that is time-optimal, it is also possible to formulate a gradient waveform using these gradient basis functions that has exactly the same duration.

In addition to the capability of handling strictly time-optimal gradient wave shapes of trapezoidal and triangular shape, the definition of basis functions has two advantages: Firstly, since the basis functions are defined such that for every ramp the gradient magnitude is driven at the slew rate constraint $\pm S_{\max}$, this constraint must not be considered any further. Secondly, the restriction to these waveform shapes also limits the accessible shapes of the resulting k -space trajectories. This is important as generally no unique solution exists for the problem of finding time-optimal k -space trajectories from a set of control points. On the contrary, for other mathematical approaches that may also be used to solve the gradient design problem (such as optimal control methods based on systems of ordinary differential equations or differential algebraic equations), the non-uniqueness of the optima increases the complexity and, therefore, the computation time and makes these methods more vulnerable to numerical instabilities. It will be shown later that the restriction to these limited set of wave shapes allows for solving the design problem in a time-efficient and numerically very robust manner.

Each of the four basis functions can be assembled by concatenation of three piece-wise linear gradient segments g_1 , g_2 , and g_3 , namely

$$g_1(t) := \pm S_{\max} \cdot t + G^{(1)} \quad t \in [0, \eta_1], \quad (3.5)$$

$$g_2(t) := P = \text{const.} \quad t \in [\eta_1, \eta_2], \quad (3.6)$$

$$g_3(t) := \pm S_{\max} \cdot (t - \eta_2) + P \quad t \in [\eta_2, \tau], \quad (3.7)$$

where P denotes the gradient strength at the plateau phase, and η_1 and η_2 denote the boundaries of the linear segments (i.e., the time points at which the slew rate is changed). Depending on the polarity at which S_{\max} is driven in $g_1(t)$ and $g_3(t)$, one of the four gradient bases is generated:

	concave	convex	increasing	decreasing
g_1 , sign of S_{\max}	+1	-1	+1	-1
g_3 , sign of S_{\max}	-1	+1	+1	-1

Each of the linear gradient segments g_1 , g_2 , and g_3 is associated with a distance in k -space that is accumulated by the respective segment:

$$\Delta k_1 := \gamma \int_0^{\eta_1} g_1(t) dt, \quad (3.8)$$

$$\Delta k_2 := \gamma \int_{\eta_1}^{\eta_2} g_2(t) dt, \quad (3.9)$$

$$\Delta k_3 := \gamma \int_{\eta_2}^{\tau} g_3(t) dt. \quad (3.10)$$

Note that ultimately these three k -space portions need to sum up to the anticipated full distance Δk between the two consecutive control points. From the definition of the gradient basis functions, three linear equations can be formulated for the bases variables P , η_1 , and η_2 . These equations ensure that the three gradient segments produce a continuous gradient wave shape (Eq. 3.11 and 3.12) and accumulate the desired distance in k -space (Eq. 3.13):

$$P \stackrel{!}{=} g_1(\eta_1), \quad (3.11)$$

$$G^{(2)} \stackrel{!}{=} g_3(\tau), \quad (3.12)$$

$$\Delta k \stackrel{!}{=} \Delta k_1 + \Delta k_2 + \Delta k_3. \quad (3.13)$$

Additionally, the basis functions need to satisfy two inequalities, that specify the sequence of slew rate switching time points and the gradient magnitude constraint:

$$0 \leq \eta_1 \leq \eta_2 \leq \tau, \quad (3.14)$$

$$|P| \leq G_{\max} \quad \text{for } t \in [0, \tau]. \quad (3.15)$$

Note that the gradient slew rate constraints S_{\max} must not be considered anymore, as this condition is directly implemented via the ramps of the gradient basis function. The generation of valid gradient wave shapes that satisfy the linear and non-linear constraints, was realized by two mappings, D and S . The first mapping is used to specify the set of valid durations \mathbb{T} for a given set of local problem parameters $G^{(1)}$, $G^{(2)}$, and Δk :

$$D : \begin{pmatrix} G^{(1)} \\ G^{(2)} \\ \Delta k \end{pmatrix} \mapsto \mathbb{T} \subseteq \mathbb{R}_+ . \quad (3.16)$$

The mapping D ensures that, as long as the duration τ is chosen from \mathbb{T} , one of the four basis functions can be used in order to generate a valid gradient wave shape, according to the problem parameters $G^{(1)}$, $G^{(2)}$, and Δk , and the constraints (Eq. 3.11 to Eq. 3.15). The exact shape of the gradient waveform (with duration $\tau \in \mathbb{T}$) is computed using a second mapping S , namely

$$S : \begin{pmatrix} G^{(1)} \\ G^{(2)} \\ \Delta k \\ \tau \end{pmatrix} \mapsto \begin{pmatrix} P \\ \eta_1 \\ \eta_2 \end{pmatrix} \quad (3.17)$$

where the shape of the local gradient waveform is defined by the parameters P , η_1 , and η_2 . Due to the non-linearity of the gradient magnitude and slew rate constraints, the domain mapping D and the solution mapping S are implemented by a variety of case differentiations.

3.1.3 The Domain Mapping D and the Solution Mapping S

The mapping D is used to specify the set \mathbb{T} of durations for which a valid piece-wise linear gradient waveform $G(t)$ can be found that obeys the design parameters $(G^{(1)}, G^{(2)}, \Delta k)$ and the system constraint G_{\max} . Without exception, for a set of design parameters, \mathbb{T} itself consists of three subsets; each of the subsets is associated with one of the four gradient basis functions. As an example, let $0 < G^{(1)} < G^{(2)}$ and $\Delta k > 0$ (Fig. 3.2, top). The fastest possible way to accumulate Δk by a gradient waveform is given either by a concave triangular wave shape or a concave trapezoidal wave shape, if the plateau value P would exceed the G_{\max} constraint. To increase the duration of the gradient segment, the gradient strength at the plateau P is decreased, until $P = G^{(2)}$. At this point the basis function type changes from the concave to the increasing wave shape. Durations τ in this range define the domain of the concave wave shape, \mathbb{T}_{cav} . Decreasing the plateau gradient strength P even further within $G^{(1)} < P < G^{(2)}$ changes the shape of the increasing basis function. The set of durations defines the respective domain \mathbb{T}_{inc} . As soon as the plateau gradient strength reaches $G^{(1)}$, i.e., $P \leq G^{(1)}$, the wave shape changes again, from the increasing to the convex basis function. The last one of the three sub-domains always has an infinite reach, meaning, that the trajectory segment can be arbitrarily decelerated without any further change of the basis function type. Obviously, the full domain of valid gradient durations \mathbb{T} is given by the union of the three sub-domains, in this example by

$$\mathbb{T} := \mathbb{T}_{\text{cav}} \cup \mathbb{T}_{\text{inc}} \cup \mathbb{T}_{\text{vex}} . \quad (3.18)$$

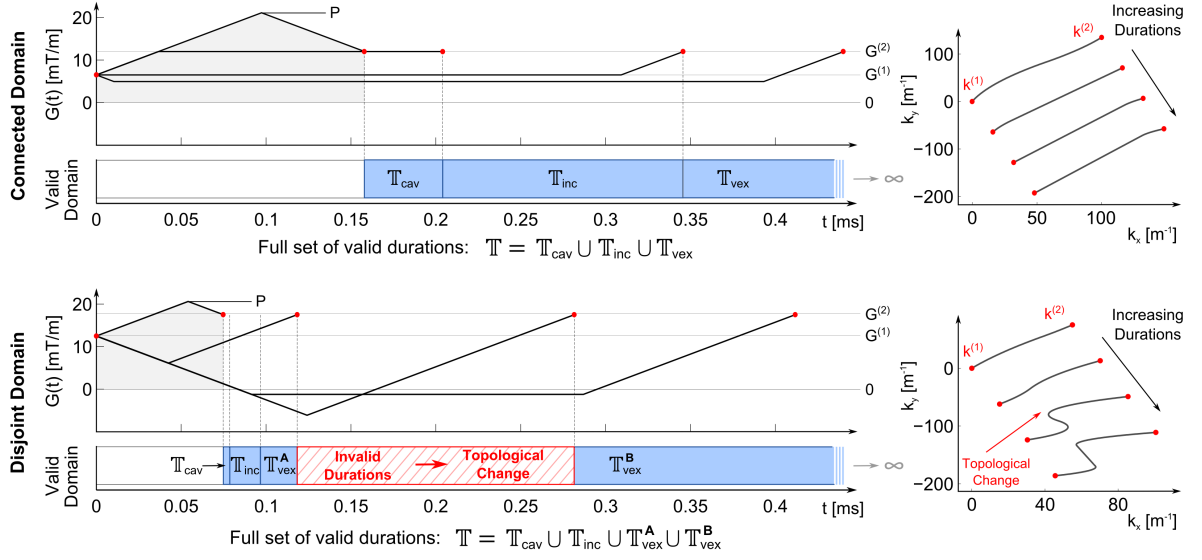


Figure 3.2: Evolution of Gradient Waveforms: for two different sets of problem parameters (*top*: $G^{(1)} = 6.5$ mT/m, $G^{(2)} = 12.0$ mT/m, $\Delta k = 100.0$ m $^{-1}$; *bottom*: $G^{(1)} = 12.5$ mT/m, $G^{(2)} = 17.5$ mT/m, $\Delta k = 55.0$ m $^{-1}$), the evolution of the gradient waveforms for different durations is shown. In addition, the valid domain of durations \mathbb{T} is illustrated at the bottom of each plot. Usually, three of the four basis functions are required to represent all possible waveforms to connect the two control points in 1-D (in this example: concave, increasing, convex). The example at the bottom exhibits a disjoint sub-set $\mathbb{T}_{\text{vex}} = \mathbb{T}_{\text{vex}}^{\text{A}} \cup \mathbb{T}_{\text{vex}}^{\text{B}}$.

The variation of the gradient waveforms for varying durations τ is illustrated in Fig. 3.2, top row. For each of the three basis functions, the respective domains \mathbb{T}_{cav} , \mathbb{T}_{inc} , \mathbb{T}_{vex} of valid durations are depicted underneath the gradient waveforms itself. Additionally, the k -space trajectories associated with each gradient waveform are shown on right hand side (for better visibility, the different trajectories are shifted against each other).

An important aspect, however, is that in certain cases the full domain \mathbb{T} will not be of connected nature, but will consist of two disjoint sub-sets. In this case – starting with the smallest valid duration τ – the gradient waveform cannot be arbitrarily decelerated. In other words, there are certain $\hat{\tau} > \tau$, for which the slew rate constraint S_{max} does not allow the gradient magnitude to be switched rapidly enough to traverse the two control points in the requested duration $\hat{\tau}$. In this case, the gradient magnitude $G(t)$ has to switch its polarity in order to achieve the anticipated distance in k -space, Δk . In other words an *S*-turn needs to be introduced to the trajectory. This disjoint behavior is depicted in Fig. 3.2, bottom row: the invalid durations in the domain (red dashed region) lead to a *topological change* of the associated gradient trajectory.

In order to fully specify the set of valid gradient waveform durations, three bounds are necessary for the set \mathbb{T} to be fully specified:

$$\mathbb{T} = [L_1, U_1] \cup [L_2, \infty) . \quad (3.19)$$

Note that $U_1 < L_2$ only holds if the trajectory changes its topology when increasing the duration of the gradient waveform. The three bounds L_1 , U_1 , and L_2 are computed based on an analytic expression that depends on the gradient strengths $G^{(1)}$ and $G^{(2)}$, the distance Δk of the two control points and the gradient magnitude and slew rate constraints. Due to the complexity of the analytic expressions for L_1 , U_1 , and L_2 , no mathematical equations are given at this

point. The derivation, however, is straight forward: the solution can be obtained by solving the Eqs. 3.11 to 3.13 with respect to a number of case differentiations

$$\begin{array}{ll}
 \text{a) } 0 < G^{(1)} < G^{(2)} & \text{d) } 0 < G^{(2)} < G^{(1)} \\
 \text{b) } G^{(1)} \leq 0 < G^{(2)} & \text{e) } G^{(2)} \leq 0 < G^{(1)} \\
 \text{c) } G^{(1)} < G^{(2)} \leq 0 & \text{f) } G^{(2)} < G^{(1)} \leq 0
 \end{array}$$

as well as

$$\text{A) } \Delta k < 0 \qquad \text{B) } \Delta k \geq 0 ,$$

including information for which durations the type of basis function changes. For a set of problem parameters $G^{(1)}$, $G^{(2)}$, and Δk , the smallest valid local duration τ is hence given by

$$\tau = \min \{ \mathbb{T} \} = \min \{ D(G^{(1)}, G^{(2)}, \Delta k) \} . \quad (3.20)$$

Eq. 3.20 can be interpreted as a local objective function that depends on the gradient strengths at the two control points. Accordingly, the local duration can be minimized by solving the constrained optimization problem

$$\begin{aligned}
 \tau_{\min} &= \arg \min_{G^{(1)}, G^{(2)}} \left(\min \{ \mathbb{T} \} \right) \\
 &\text{subject to } |G^{(1)}|, |G^{(2)}| \leq G_{\max} . \quad (3.21)
 \end{aligned}$$

In other words: the gradient strengths $G^{(1)}$ and $G^{(2)}$ at the control points $k^{(1)}$ and $k^{(2)}$ are optimized to allow for the fastest possible traversal of the control points. For a given set of gradient design parameters $G^{(1)}$, $G^{(2)}$, Δk , and an arbitrary (but valid) gradient waveform duration $\tau \in \mathbb{T}$, the mapping S is then used to define the exact shape of the gradient waveform, which is specified by the parameters η_1 , η_2 , and P of the basis function. The derivation of the (less complicated) mapping S is very similar to the mapping D . Considering the case differentiations given by the inequalities in a) to f) as well as A) and B), the linear equations given in Eq. 3.11 to 3.13 are solved. As opposed to the domain mapping D , where the expressions are solved for the duration τ of the gradient waveform segment (these durations define \mathbb{T}), the linear equations are now solved for the gradient shape parameters η_1 , η_2 , and P , for a given duration τ .

3.1.4 Global Trajectory Design

Although the mapping D was derived on a local one-dimensional scale (i.e., only describing the solution of a single gradient basis in a single dimension), it can be used to obtain time-optimal gradient trajectories on the global scale (i.e., including multiple control points in multiple dimensions). This can be achieved by first extending the domain mapping D to the local multi-dimensional problem (two control points in three-dimensional k -space), and afterwards to the global three-dimensional problem (N control points in three-dimensional k -space).

For two consecutive control points $\mathbf{k}^{(1)}$ and $\mathbf{k}^{(2)}$ in three-dimensional k -space with the respective gradient strength vectors $\mathbf{G}^{(1)}$ and $\mathbf{G}^{(2)}$ at these two k -space locations, the smallest possible local duration is given by

$$\tau = \min \left\{ \mathbb{T}_x \cap \mathbb{T}_y \cap \mathbb{T}_z \right\} \quad (3.22)$$

where

$$\begin{aligned} \mathbb{T}_x &= D \left(G_x^{(1)}, G_x^{(2)}, \Delta k_x \right), \\ \mathbb{T}_y &= D \left(G_y^{(1)}, G_y^{(2)}, \Delta k_y \right), \\ \mathbb{T}_z &= D \left(G_z^{(1)}, G_z^{(2)}, \Delta k_z \right). \end{aligned} \quad (3.23)$$

The expression in Eq. 3.22 states that the smallest valid duration τ is equal to the smallest duration contained by the union of the three valid domains \mathbb{T}_x , \mathbb{T}_y , \mathbb{T}_z , meaning that for the given duration, a solution must exist in each of the three gradient dimensions. In this local example, the gradient vectors in the control points $\mathbf{k}^{(1)}$ and $\mathbf{k}^{(2)}$, namely

$$\mathbf{G}^{(1)} = \left(G_x^{(1)}, G_y^{(1)}, G_z^{(1)} \right) \text{ and} \quad (3.24)$$

$$\mathbf{G}^{(2)} = \left(G_x^{(2)}, G_y^{(2)}, G_z^{(2)} \right), \quad (3.25)$$

are only constrained by G_{\max} . Similarly to Eq. 3.21 these gradient strengths can be chosen so as to minimize the duration of the segment that connects the two control points:

$$\begin{aligned} \tau_{\min} &= \arg \min_{\mathbf{G}^{(1)}, \mathbf{G}^{(2)}} \left(\underbrace{\min \left\{ \mathbb{T}_x \cap \mathbb{T}_y \cap \mathbb{T}_z \right\}}_{=: f^{(1)}(\mathbf{G}^{(1)}, \mathbf{G}^{(2)})} \right) \\ &\text{subject to } \|\mathbf{G}^{(1)}\|_{\infty}, \|\mathbf{G}^{(2)}\|_{\infty} \leq G_{\max}. \end{aligned} \quad (3.26)$$

Analogously, for the global multidimensional gradient waveform, the duration T of the entire gradient waveform is given by the sum of the local durations $\tau^{(q)}$, namely

$$T = \sum_{q=1}^{N-1} \tau^{(q)} = \sum_{q=1}^{N-1} \min \left\{ \mathbb{T}_x^{(q)} \cap \mathbb{T}_y^{(q)} \cap \mathbb{T}_z^{(q)} \right\}. \quad (3.27)$$

Obviously, the duration T of the gradient waveform highly depends on the gradient strength vectors $\mathbf{G}^{(1)}, \dots, \mathbf{G}^{(N)}$ in the control points. On the local scale, it is trivial to find a set of gradient strengths $\mathbf{G}^{(q)}$ and $\mathbf{G}^{(q+1)}$ that minimizes the q -th gradient segment. On the global scale, this is not possible, because every gradient vector $\mathbf{G}^{(q)}$ influences two gradient segments, the $q - 1$ -th and the q -th segment. Therefore, the gradient strengths need to be chosen so as to accelerate both affected gradient segments equally.

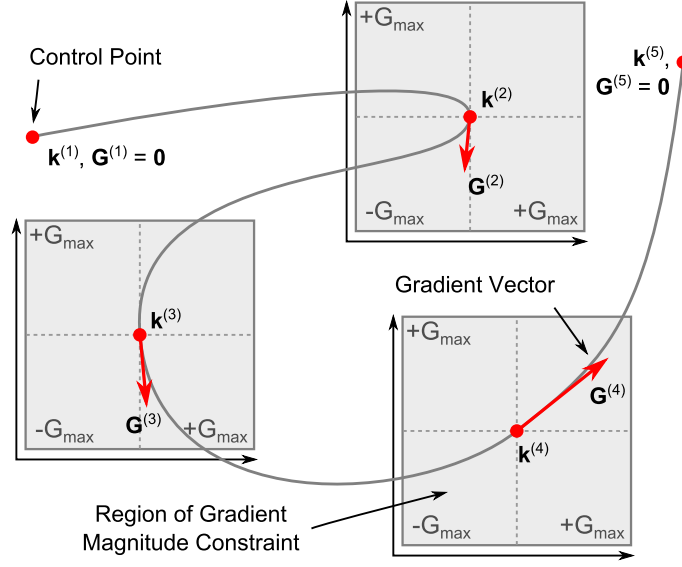


Figure 3.3: Constrained Optimization: Illustration of the time-optimal gradient design scheme, for given control points $\mathbf{k}^{(1)}, \dots, \mathbf{k}^{(5)}$, the gradient vectors $\mathbf{G}^{(2)}, \dots, \mathbf{G}^{(4)}$ (arrows) are optimized within the control regions (gray squares) to accelerate the gradient trajectory. The gradient vectors in the first and last control point, $\mathbf{G}^{(1)}$ and $\mathbf{G}^{(5)}$, are fixed at zero.

This is achieved by optimizing the gradient strengths numerically with respect to the constraint $\|\mathbf{G}^{(q)}\|_{\infty} \leq G_{\max}$ so to avoid consecutive deceleration and acceleration of the trajectory $\mathbf{k}(t)$. Hence, the *optimal* duration T_{\min} is given by

$$T_{\min} = \arg \min_{\mathbf{G}^{(1)}, \dots, \mathbf{G}^{(N)}} \left(\underbrace{\sum_{q=1}^{N-1} \min \{ \mathbb{T}_x^{(q)} \cap \mathbb{T}_y^{(q)} \cap \mathbb{T}_z^{(q)} \}}_{=: f(\mathbf{G}^{(1)}, \dots, \mathbf{G}^{(N)})} \right)$$

subject to $\|\mathbf{G}^{(q)}\|_{\infty} \leq G_{\max}, q = 1, \dots, N.$ (3.28)

The above formulation generates a set of gradient vectors $\mathbf{G}^{(1)}, \dots, \mathbf{G}^{(N)}$ that minimizes the full duration T (i.e., the sum of all local segments) rather than only a local segment.

As opposed to the *Optimal Control* method proposed by Lustig et al. [71], the *Gradient Basis Function* method formulates the gradient design problem as a constrained optimization of the gradient strength vectors in the control points, subject to the G_{\max} constraint. The general idea is depicted in Fig. 3.3 where five control points are defined to span a k -space trajectory. The gradient strengths of the three intermediate control points are optimized to accelerate the trajectory; the respective valid regions of the gradient strength vectors are illustrated as gray squares surrounding the control points. The first and last control points are not optimized, but fixed to zero gradient strength.

The objective function f in Eq. 3.28 is derived in a straight forward manner, based on the mapping D . Many of the commonly used numerical optimization methods make use of the first (Jacobian) and possibly the second (Hessian) derivative of the objective function (i.e., the duration) with respect to the optimization variables (i.e., the gradient strengths at the control points) at each iteration to determine the search direction and the step size. Both the domain

mapping D and the resulting objective function f are given in a semi-analytic manner. This fact allows for direct computation of the derivatives with respect to the gradient strength vectors. This does not only avoid computationally expensive numerical estimation of the derivatives (e.g., via finite differences) but also ensures accurate first and second derivatives and thus better convergence of the optimization routine.

After the optimal gradient strength vectors at the control point locations are found, the resulting gradient waveforms specified by the basis function parameters P , η_1 , and η_2 are computed using the mapping S via

$$\begin{bmatrix} P_x^{(q)}, (\eta_1)_x^{(q)}, (\eta_2)_x^{(q)} = S\left(G_x^{(q)}, G_x^{(q+1)}, \Delta k_x^{(q)}, \tau^{(q)}\right) \\ P_y^{(q)}, (\eta_1)_y^{(q)}, (\eta_2)_y^{(q)} = S\left(G_y^{(q)}, G_y^{(q+1)}, \Delta k_y^{(q)}, \tau^{(q)}\right) \\ P_z^{(q)}, (\eta_1)_z^{(q)}, (\eta_2)_z^{(q)} = S\left(G_z^{(q)}, G_z^{(q+1)}, \Delta k_z^{(q)}, \tau^{(q)}\right) \end{bmatrix} \quad \text{with } q = 1, \dots, N - 1. \quad (3.29)$$

3.1.5 Further Constraints

Up to this point it was assumed that every control point in three-dimensional k -space possesses overall three degrees-of-freedom in the optimization, given by the gradient strength vectors

$$\mathbf{G}^{(q)} = \left(G_x^{(q)}, G_y^{(q)}, G_z^{(q)}\right). \quad (3.30)$$

This means that every gradient strength vector from the cubical domain

$$\mathbf{G}^{(q)} \in [-G_{\max}, +G_{\max}]^3 \quad (3.31)$$

is accessible by the optimization routine in an attempt to shorten the duration of the gradient waveform. An alternative strategy is to limit the number of degrees-of-freedom for a subset of control points to impose a desired shape of the gradient trajectory. Two exemplary types of control point constraints are described in the following:

- 1) The gradient strength vectors can be kept at a fixed value in the optimization. For example, the first and last control point may be set to zero to reflect to the scanner's resting state (see Fig. 3.3).
- 2) Directional vectors can be defined in certain control points to prescribe the direction of the resulting gradient trajectory. This is particularly useful to enforce the anticipated shape of the gradient trajectory to be designed.

For the directional constraints, rather than providing three degrees of freedom $G_x^{(q)}$, $G_y^{(q)}$, and $G_z^{(q)}$ for the optimization, the gradient strength vector is defined by a single variable $g^{(q)}$ and a prescribed directional vector $\mathbf{c}^{(q)} \in \mathbb{R}^3$ by

$$\mathbf{G}^{(q)} := g^{(q)} \cdot \frac{\mathbf{c}^{(q)}}{\|\mathbf{c}^{(q)}\|_\infty} \quad \text{subject to } |g^{(q)}| \leq G_{\max}. \quad (3.32)$$

With respect to Fig. 3.3 this means that the valid control region (grey square) reduces to a single line with limited length pointing along $\mathbf{c}^{(q)}$.

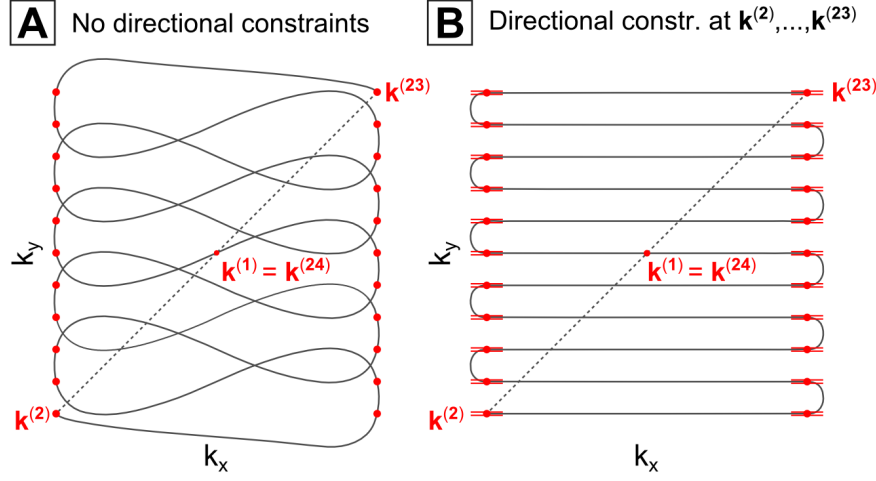


Figure 3.4: EPI Control Points: two trajectories based on a set of EPI-like control points, without directional constraints **(A)** and with directional constraints $\mathbf{c} = (0, 1)$ for $\mathbf{k}^{(2)}, \dots, \mathbf{k}^{(23)}$ **(B)**. The directional constraints enforce the anticipated shape of the trajectory to ensure a uniform sampling density while slightly increasing the duration.

A design example that utilizes both fixed and directional constraints of the control points is depicted in Fig. 3.4 where a set of control points is arranged to design an EPI like k -space trajectory. The trajectory in **(A)** does not utilize directional constraints, but only fixed constraints on the first and last control point, $\mathbf{k}^{(1)}$ and $\mathbf{k}^{(24)}$. As a consequence the optimization procedure designs a gradient trajectory that exploits the degrees of freedom to a maximum extent. A typical result is the accumulation of velocity in phase encoding direction k_y , as the trajectory moves along the frequency encoding direction k_x . This feature allows for accelerating the *blips* of the EPI trajectory. The resulting shape, however, deviates substantially from common EPI trajectories, because the frequency encoding lines are not planar anymore. On the other hand, directional constraints were defined in Fig. 3.4 **(B)** that enforce the gradient trajectory to traverse the control points horizontally, namely

$$\mathbf{c}^{(q)} = (0, 1) \quad , \quad q = 2, \dots, 23. \quad (3.33)$$

Obviously, defining fixed and/or directional constraints for a gradient trajectory necessarily disregards strictly time-optimal solutions, in favor of the anticipated shape. Other types of constraints – beyond fixed gradient strengths and directional vectors – may also be defined, for example those including multiple control points simultaneously.

3.1.6 Analytic Derivatives

According to Eq. 3.19, the sets \mathbb{T}_x , \mathbb{T}_y , and \mathbb{T}_z of the valid gradient segment durations are characterized by three bounds for which analytic expressions – and thus analytic derivatives – exist. The intersection of the three sets (whose minimum value determines the local duration τ) is given by

$$\mathbb{T} := \mathbb{T}_x \cap \mathbb{T}_y \cap \mathbb{T}_z \quad (3.34)$$

with

$$\mathbb{T}_x = [L_{1,x}, U_{1,x}] \cup [L_{2,x}, \infty) \quad (3.35a)$$

$$\mathbb{T}_y = [L_{1,y}, U_{1,y}] \cup [L_{2,y}, \infty) \quad (3.35b)$$

$$\mathbb{T}_z = [L_{1,z}, U_{1,z}] \cup [L_{2,z}, \infty) \quad (3.35c)$$

which means that

$$\tau = \min \{ \mathbb{T} \} \in \{ L_{1,x}, L_{2,x}, L_{1,y}, L_{2,y}, L_{1,z}, L_{2,z} \} . \quad (3.36)$$

Therefore, the Jacobian and Hessian of τ with respect to the gradient strength vectors is given by the Jacobian and Hessian of the *active bound* in Eq. 3.36. In particular, only the derivatives with respect to a single gradient dimension in the full Jacobian $\nabla f^{(1)}$ are non-zero, namely

$$\begin{aligned} \mathbf{x}: (\nabla f)^{(1)} &= \left(\frac{\partial f}{\partial G_x^{(1)}}, 0, 0, \frac{\partial f}{\partial G_x^{(2)}}, 0, 0 \right) \\ \mathbf{y}: (\nabla f)^{(1)} &= \left(0, \frac{\partial f}{\partial G_y^{(1)}}, 0, 0, \frac{\partial f}{\partial G_y^{(2)}}, 0 \right) \\ \mathbf{z}: (\nabla f)^{(1)} &= \left(0, 0, \frac{\partial f}{\partial G_z^{(1)}}, 0, 0, \frac{\partial f}{\partial G_z^{(2)}} \right) \end{aligned} \quad (3.37)$$

for \mathbf{x} , \mathbf{y} , and \mathbf{z} denoting the dimension of the active bound and

$$\nabla^{(1)} = \left(\frac{\partial}{\partial G_x^{(1)}}, \frac{\partial}{\partial G_y^{(1)}}, \frac{\partial}{\partial G_z^{(1)}}, \frac{\partial}{\partial G_x^{(2)}}, \frac{\partial}{\partial G_y^{(2)}}, \frac{\partial}{\partial G_z^{(2)}} \right) . \quad (3.38)$$

The Jacobian of the full objective function f is then computed by combination of the Jacobian vectors of the single segments $(\nabla f)^{(1)}, \dots, (\nabla f)^{(N-1)}$.

Equivalently, an analytic expression of the Hessian matrix of the objective f with respect to the gradient strength vectors \mathbf{G} , $H_f(\mathbf{G})$ can be derived. In general, the Hessian of f reads

$$H_f(\mathbf{G}) = \begin{pmatrix} \frac{\partial^2 f}{\partial G_x^{(1)} \partial G_x^{(1)}} & \frac{\partial^2 f}{\partial G_x^{(1)} \partial G_y^{(1)}} & \frac{\partial^2 f}{\partial G_x^{(1)} \partial G_z^{(1)}} & \frac{\partial^2 f}{\partial G_x^{(1)} \partial G_x^{(2)}} & \cdots & \frac{\partial^2 f}{\partial G_x^{(1)} \partial G_z^{(N)}} \\ \frac{\partial^2 f}{\partial G_y^{(1)} \partial G_x^{(1)}} & \frac{\partial^2 f}{\partial G_y^{(1)} \partial G_y^{(1)}} & \frac{\partial^2 f}{\partial G_y^{(1)} \partial G_z^{(1)}} & \frac{\partial^2 f}{\partial G_y^{(1)} \partial G_x^{(2)}} & \cdots & \frac{\partial^2 f}{\partial G_y^{(1)} \partial G_z^{(N)}} \\ \frac{\partial^2 f}{\partial G_z^{(1)} \partial G_x^{(1)}} & \frac{\partial^2 f}{\partial G_z^{(1)} \partial G_y^{(1)}} & \frac{\partial^2 f}{\partial G_z^{(1)} \partial G_z^{(1)}} & \frac{\partial^2 f}{\partial G_z^{(1)} \partial G_x^{(2)}} & \cdots & \frac{\partial^2 f}{\partial G_z^{(1)} \partial G_z^{(N)}} \\ \frac{\partial^2 f}{\partial G_x^{(2)} \partial G_x^{(1)}} & \frac{\partial^2 f}{\partial G_x^{(2)} \partial G_y^{(1)}} & \frac{\partial^2 f}{\partial G_x^{(2)} \partial G_z^{(1)}} & \frac{\partial^2 f}{\partial G_x^{(2)} \partial G_x^{(2)}} & \cdots & \frac{\partial^2 f}{\partial G_x^{(2)} \partial G_z^{(N)}} \\ \vdots & \vdots & \vdots & \vdots & \ddots & \vdots \\ \frac{\partial^2 f}{\partial G_z^{(N)} \partial G_x^{(1)}} & \frac{\partial^2 f}{\partial G_z^{(N)} \partial G_y^{(1)}} & \frac{\partial^2 f}{\partial G_z^{(N)} \partial G_z^{(1)}} & \frac{\partial^2 f}{\partial G_z^{(N)} \partial G_x^{(2)}} & \cdots & \frac{\partial^2 f}{\partial G_z^{(N)} \partial G_z^{(N)}} \end{pmatrix} . \quad (3.39)$$

With m and n denoting one of the gradient dimensions x , y , z , respectively, the entries in $H_f(\mathbf{G})$ can be given a general form, namely

$$\frac{\partial^2 f(\mathbf{G})}{\partial G_m^{(i)} \partial G_n^{(j)}} = \frac{\partial}{\partial G_m^{(i)}} \cdot \frac{\partial \left(f^{(j-1)}(G_n^{(j-1)}, G_n^{(j)}) + f^{(j)}(G_n^{(j)}, G_n^{(j+1)}) \right)}{\partial G_n^{(j)}}. \quad (3.40)$$

The second term on the right hand side only depends on the gradient strength components superscripted by $j-1$, j , and $j+1$ as well as the gradient dimension n . If the right hand side of Eq. 3.40 satisfies $m \neq n$ (different gradient dimension) or $i \notin \{j-1, j, j+1\}$, the derivative vanishes. This leaves the Hessian matrix $H_f(\mathbf{G})$ in a sparse form, namely

$$H_f(\mathbf{G}) = \begin{pmatrix} (H_f)_{1,1} & 0 & 0 & (H_f)_{4,1} & 0 & 0 & \dots & 0 \\ 0 & (H_f)_{2,2} & 0 & 0 & (H_f)_{5,2} & 0 & \dots & 0 \\ 0 & 0 & (H_f)_{3,3} & 0 & 0 & (H_f)_{6,3} & \dots & 0 \\ (H_f)_{1,4} & 0 & 0 & (H_f)_{4,4} & 0 & 0 & \dots & 0 \\ 0 & (H_f)_{2,5} & 0 & 0 & (H_f)_{5,5} & 0 & \dots & 0 \\ 0 & 0 & (H_f)_{3,6} & 0 & 0 & (H_f)_{6,6} & \dots & 0 \\ \vdots & \vdots & \vdots & \vdots & \vdots & \vdots & \ddots & \vdots \\ 0 & 0 & 0 & 0 & 0 & 0 & \dots & (H_f)_{N,N} \end{pmatrix}. \quad (3.41)$$

3.1.7 Continuity and Differentiability

In certain cases, the objective function $f(\mathbf{G})$ exhibits discontinuities due to topological changes of the gradient trajectory when applying finite changes of the gradient strength vectors. Additionally, continuous differentiability is not present everywhere. If the associated dimension of the active bound of a gradient segment changes, a kink occurs in the objective, meaning that no derivative can be given at that point. A numerical approximation of the derivatives, e.g., via finite differencing, in presence of these discontinuities usually results in quasi-infinite estimates of the derivatives that lead to infeasible step sizes taken by the optimizer. Due to the fact that analytic derivatives can be utilized by the optimization routine, the discontinuities did not impair the optimization problem significantly. In contrast, most gradient-based solvers – such as gradient descent or Newton-type methods – do exhibit problems in close vicinity to regions where the objective function has non-continuous derivatives. In this case, the optimizer jumps back and forth between the regions of continuous differentiability while only negligibly decreasing the objective function, leading to very poor convergence or even divergence.

To improve the convergence characteristics, the objective function can be modified such that the derivatives are smoothed artificially. As was shown before (Eq. 3.22) the objective function value $f^{(q)}$ of a single gradient segment, for a given set of gradient strength vectors $\mathbf{G}^{(q)}$ and $\mathbf{G}^{(q+1)}$, is given by the smallest duration τ contained by the union of the sets \mathbb{T}_x , \mathbb{T}_y , and \mathbb{T}_z . In any case, this minimum duration is equal to one of the lower bounds that define the sets of valid durations in the three gradient dimensions x , y , or z . The derivative of the objective function with respect to $\mathbf{G}^{(q)}$ and $\mathbf{G}^{(q+1)}$ is equal to the derivative of the associated (active) bound of

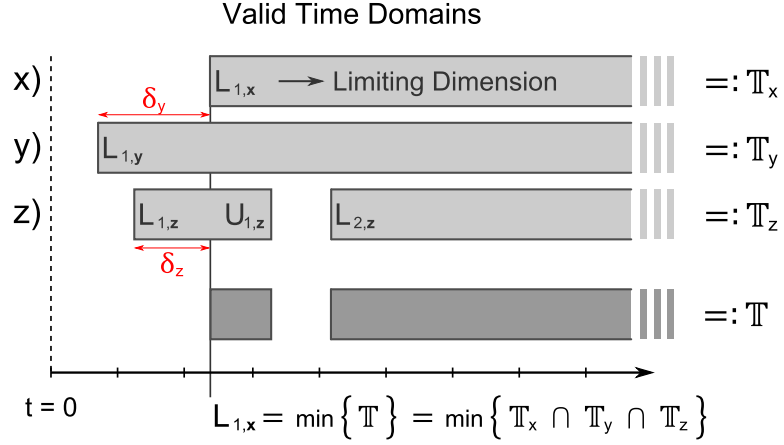


Figure 3.5: Domain of valid durations: schematic illustration of how the full domain \mathbb{T} (bottom) is composed via the intersection of the sub-domains of each gradient dimension, \mathbb{T}_x , \mathbb{T}_y , and \mathbb{T}_z (top). Each sub-domain is specified by a set of bounds given by $(L_{1,x})$, $(L_{1,y})$, and $(L_{1,z}, U_{1,z}, L_{2,z})$ for the x , y , and z axis, respectively. In this case, the x gradient is setting the limit $\tau = L_{1,x}$ over the three gradient dimensions.

\mathbb{T}_x , \mathbb{T}_y , or \mathbb{T}_z . Accordingly, a discontinuity of the derivative occurs if the active bound switches as $\mathbf{G}^{(q)}$ or $\mathbf{G}^{(q+1)}$ are varied. As a consequence, the distance of the current gradient segment duration τ to the lower bounds of the sets in the other gradient dimensions is a measure of the distance to the non-differentiable kink in the objective function. In an attempt to smooth the derivative at these locations, the derivative of the inactive bound with respect to $\mathbf{G}^{(q)}$ or $\mathbf{G}^{(q+1)}$ is inversely weighted by this distance and added to the exact analytic derivative at τ . In other words, the exact analytic derivatives are smoothed in a small neighborhood of $\mathbf{G}^{(q)}$ and $\mathbf{G}^{(q+1)}$, where the level of smoothing is specified by the inverse weighting used in the derivative summation.

As an example, it is assumed that $\tau = L_x < L_y, L_z$ and, for simplicity, that the three sets of valid durations are connected, namely

$$\mathbb{T}_x = [L_x, \infty) , \mathbb{T}_y = [L_y, \infty) , \mathbb{T}_z = [L_z, \infty) . \quad (3.42)$$

The expressions of the Jacobian of the objective function given in Eq. 3.37 are then modified, yielding

$$\begin{aligned} \nabla f^* = & \left(\frac{\partial L_x}{\partial G_x^{(1)}}, e^{-\delta_y \lambda^{-1}} \frac{\partial L_y}{\partial G_y^{(1)}}, e^{-\delta_z \lambda^{-1}} \frac{\partial L_z}{\partial G_z^{(1)}}, \dots \right. \\ & \left. \dots \frac{\partial L_x}{\partial G_x^{(1)}}, e^{-\delta_y \lambda^{-1}} \frac{\partial L_y}{\partial G_y^{(1)}}, e^{-\delta_z \lambda^{-1}} \frac{\partial L_z}{\partial G_z^{(1)}} \right) \end{aligned} \quad (3.43)$$

where

$$\delta_y = L_y - L_x \text{ and } \delta_z = L_z - L_x . \quad (3.44)$$

The derivative of the inactive bounds (i.e., the derivatives of L_y and L_z) are inversely weighted by the distances δ_y and δ_z of the active to the inactive bounds and used to assemble a smoothed version of the Jacobian ∇f^* . A similar approach is used, if the sets are disjoint. In this case the

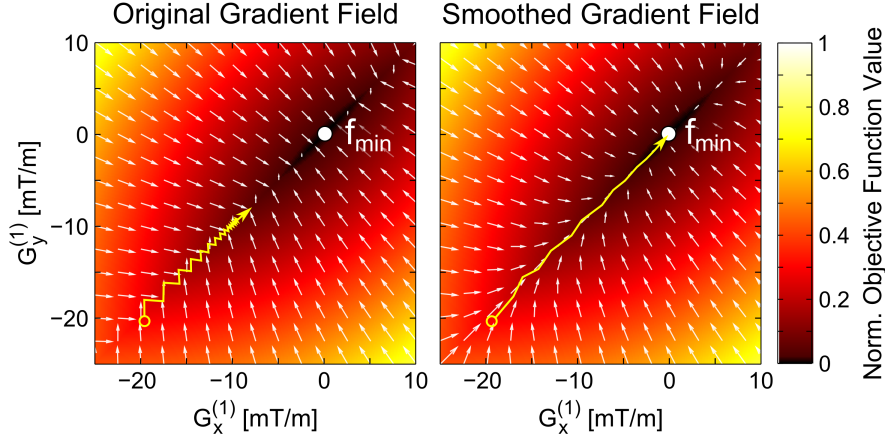


Figure 3.6: Smoothed Gradient Field: for an exemplary local objective function $f^{(1)}$ the objective function values $f^{(1)}(G_x^{(1)}, G_y^{(1)})$ and the gradient field $\nabla f^{(1)}(G_x^{(1)}, G_y^{(1)})$ are shown, for varying gradient vectors $(G_x^{(1)}, G_y^{(1)}) \in \mathbb{G}^2 = [-G_{\max}, +G_{\max}]^2$. The alternating – and thus time-consuming – iteration path (left) is effectively avoided by smoothing the underlying gradient field (right).

respective active bound ($L_{1,x}$ or $L_{2,x}$ in this example) and the closest of the two inactive bounds in the two other dimensions ($L_{1,y}$ or $L_{2,y}$, $L_{1,z}$ or $L_{2,z}$) are chosen. The approach is depicted in Fig. 3.5: for the three gradient dimensions, the domains \mathbb{T}_x , \mathbb{T}_y , and \mathbb{T}_z are shown as well as their intersection \mathbb{T} at the bottom. In this case the smallest valid gradient segment duration $\tau \in \mathbb{T}$ is equal to $L_{1,x}$ (active bound), leaving the x direction as the limiting dimension. The inactive bounds $L_{1,y}$ and $L_{1,z}$ are weighted by δ_y and δ_z to compose the smoothed derivative. An equivalent approach is applied to the Hessian matrix $H_f(\mathbf{G})$ where the second derivatives of the inactive bounds are inversely weighted by their distance to the active bound. Despite the simplicity of this approach, the smoothed Jacobian and Hessian version proved very helpful in supporting the solver during the minimization procedure, in particular avoiding undesired behavior in the periphery of kinks in the objective and possibly premature termination. In Fig. 3.6 an original (*left*) and smoothed (*right*) local two-dimensional objective $f^{(1)}$ (as a function of the first gradient vector $\mathbf{G}^{(1)} = (G_x^{(1)}, G_y^{(1)})$) are shown. The gradient vector field $(\nabla f)^{(1)}(G_x^{(1)}, G_y^{(1)})$ is superimposed to the objective function and an exemplary search path used by the gradient descent solver is shown. The back-and-forth behavior (*left*) is substantially reduced by use of the smoothed derivatives (*right*).

3.1.8 Convexity and Stationary Points

Unfortunately, the objective function f does not possess convexity, i.e., neither conventional convexity nor pseudo- or quasi-convexity [74]. This is due to the fact that the duration τ of a single gradient segment does not necessarily vary continuously with respect to the gradient magnitudes $G^{(1)}$ and $G^{(2)}$. In Fig. 3.7, the objective function f with respect to the gradient strengths $G^{(1)}$ (x -axis) and $G^{(2)}$ (y -axis) is shown for varying Δk (decreasing from left to right). The objective function clearly exhibits discontinuities, for $\Delta k > 0$ (B and C) in the top right region, for $\Delta k < 0$ (E and F) at the bottom left. With respect to the associated gradient trajectory, this means that the curve may change its topology at these discontinuities. This property of the global objective function results from the non-linear constraint on the gradient slew rate and cannot be overcome.

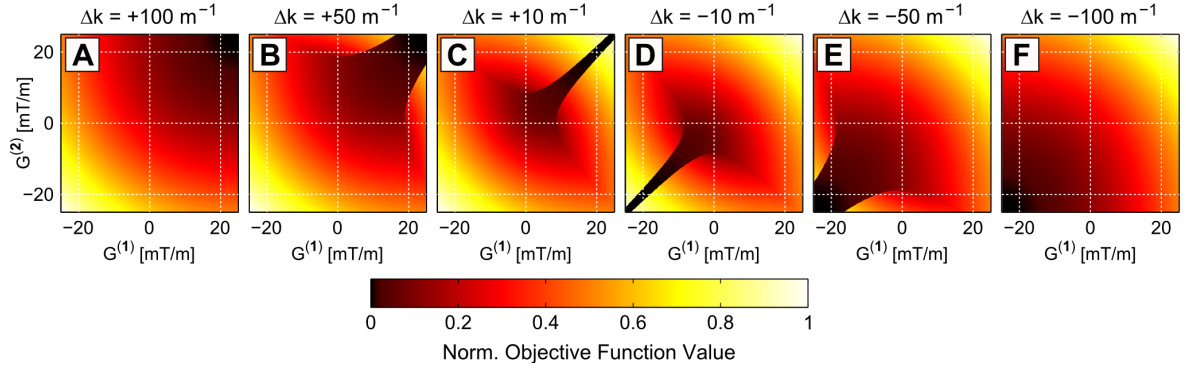


Figure 3.7: Structure of the local objective function: minimum durations for a one-dimensional waveform depending on the gradient strengths in the two control points for varying positive Δk (A,B,C) and negative Δk (D,E,F).

Despite the lack of convexity, the global minimum of the objective function can still be found by gradient descent methods as long as every stationary point (or in a relaxed formulation: any local minimum) of the objective function is a global minimum. In this case the convergence rate cannot be quantified (unlike for convex functions), i.e., the optimization routine requires a non-deterministic number of iterations until the global minimum is identified. This property is referred to as *invexity* [52] and has been investigated in the frame of non-linear optimization as a further generalization of *convexity*:

A differentiable function $\varphi : \mathbb{R}^n \rightarrow \mathbb{R}$ is called *invex* if there exists a vector valued function $\boldsymbol{\eta}$ such that

$$\varphi(x) - \varphi(y) \geq \boldsymbol{\eta}^T(x, y) \cdot \nabla \varphi(y), \quad (3.45)$$

for all x and y . Note that for $\boldsymbol{\eta}(x, y) = x - y$, the definition of convexity arises naturally from the invexity, meaning that every invex function is convex, but the opposite does not hold. Two important properties of invex functions can be identified:

- (1) A differentiable function φ is invex if and only if every stationary point is a global minimum.
- (2) The sum of invex functions $\varphi_1, \dots, \varphi_n$, with respect to the same $\boldsymbol{\eta}$ is invex with respect to $\boldsymbol{\eta}$.

Although invexity is only defined for differentiable functions φ it is assumed that numerically, the objective function (using the analytically computed derivatives and the proposed smoothing of the Jacobian and Hessian) behaves benign in that sense. The full objective function f is composed as a sum of the local objective functions of each gradient segment,

$$f^{(q)}(\mathbf{G}^{(q)}, \mathbf{G}^{(q+1)}) \text{ with } (\mathbf{G}^{(q)}, \mathbf{G}^{(q+1)}) \in \mathbb{G}^6, \quad (3.46)$$

where $\mathbb{G} := [-G_{\max}, +G_{\max}]$ is the control region of the optimizer. In fact, the local objective $f^{(q)}$ is convex in the major part of \mathbb{G}^6 . From the minimum of this convex region, however, a "canyon"-like path may reach through the convex region to the true global minimum (see Fig. 3.7, D and E). The reason for this *canyon*-feature are the topological changes that the gradient trajectory may undergo in certain cases. The objective function $f^{(q)}$ can be considered a six-dimensional equivalent of the objective shown in Fig. 3.8. Note that from any point within the control region \mathbb{G}^6 a (strictly descending) search path leads towards the center and, from that, through the "canyon" to the global minimum, i.e., there is only a single local minimum

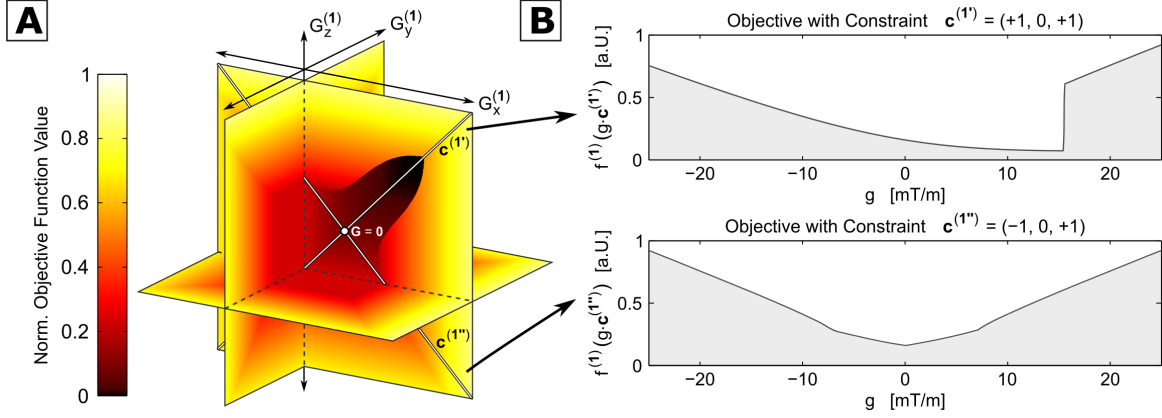


Figure 3.8: Structure of the objective function in 3-D: (A) shows the three-dimensional invex objective function of a single segment $f^{(q)}(\cdot, \mathbf{G}^{(q+1)})$ for an exemplary fixed $\mathbf{G}^{(q+1)}$ as a simplification of the full six-dimensional objective possessing the same structure, (B): objective function of a single segment utilizing a directional constraint that maintains invexity (two solid lines in A).

of $f^{(q)}$ in the domain \mathbb{G}^6 . The control point constraints introduced in Sec. 3.1.5, however, may impair the structure of the objective function (in a way that invexity does no longer exist), if the constraints are not set cautiously. For a directional constraint set for the q -th control point $\mathbf{k}^{(q)}$, the respective local objective function becomes

$$f^{(q)}(\mathbf{G}^{(q)}, \mathbf{G}^{(q+1)}) \rightarrow f^{(q)}(g^{(q)}\mathbf{c}^{(q)}, \mathbf{G}^{(q+1)}), \quad (3.47)$$

meaning that $f^{(q)}(\mathbf{G}^{(q)}, \mathbf{G}^{(q+1)})$ is sampled along the straight line defined by $g^{(q)}\mathbf{c}^{(q)}$. The dependence of $f^{(q)}$ on $g^{(q)}$ is pseudo-convex and thus invex [4], in particular because the line intersects the point of origin. This can also be seen in Fig. 3.8 (B), where the three-dimensional objective function $f^{(q)}(\cdot, \mathbf{G}^{(q+1)})$ is shown for an exemplary $\mathbf{G}^{(q+1)}$. The constraint $\mathbf{c}^{(q)}$ is equivalent to sampling the objective function along the straight line $g^{(q)}\mathbf{c}^{(q)}$, resulting in pseudo-convexity. On the contrary, fixing the gradient strength at certain control points may render the local objective function $f^{(q)}$ (and thus the global objective f) non-invex, if the gradient strength in the control point is chosen excessively large (i.e., the "zero" constraint $\mathbf{G}^{(1)} = \mathbf{G}^{(N)} = \mathbf{0} = \text{const.}$ which is usually used for the first and last control point is not affected by this degradation).

Invexity of the local objective functions $f^{(q)}$ can be translated to invexity of the full objective function f . In order to do so, a system of equations is formulated, using

$$\varphi_q(\mathbf{G}) := f^{(q)}(\mathbf{G}^{(q)}, \mathbf{G}^{(q+1)}) \quad (3.48)$$

for $q = 1 \dots, N-1$ and $\mathbf{G} := [\mathbf{G}^{(1)}, \dots, \mathbf{G}^{(N)}]$ (i.e., \mathbf{G} without subscript refers to the combination of all gradient strength vectors, i.e., $\mathbf{G} \in \mathbb{G}^{3N}$). Using the definition of invexity given in Eq. 3.45 and inclusion of the vector valued function $\boldsymbol{\eta}$ results in a system of inequalities

$$\begin{aligned} \varphi_1(\mathbf{G}_a) - \varphi_1(\mathbf{G}_b) &\geq \boldsymbol{\eta}(\mathbf{G}_a, \mathbf{G}_b)^\top \cdot \nabla \varphi_1(\mathbf{G}_b) \\ \varphi_2(\mathbf{G}_a) - \varphi_2(\mathbf{G}_b) &\geq \boldsymbol{\eta}(\mathbf{G}_a, \mathbf{G}_b)^\top \cdot \nabla \varphi_2(\mathbf{G}_b) \\ &\vdots \\ \varphi_{N-1}(\mathbf{G}_a) - \varphi_{N-1}(\mathbf{G}_b) &\geq \boldsymbol{\eta}(\mathbf{G}_a, \mathbf{G}_b)^\top \cdot \nabla \varphi_{N-1}(\mathbf{G}_b) \end{aligned} \quad (3.49)$$

for all $\mathbf{G}_a, \mathbf{G}_b \in \mathbb{G}^{3N}$. In matrix notation, the system can be written as

$$\begin{bmatrix} \Delta\varphi \end{bmatrix} \geq \begin{bmatrix} J \end{bmatrix} \cdot \begin{bmatrix} \boldsymbol{\eta} \end{bmatrix} \quad (3.50)$$

where $[J]$ denotes the Jacobian matrix

$$[J] = \begin{bmatrix} \nabla\varphi_1(\mathbf{G}_b) \\ \vdots \\ \nabla\varphi_{N-1}(\mathbf{G}_b) \end{bmatrix}. \quad (3.51)$$

Using Eq. 3.37 and 3.38 the Jacobian $[J]$ can be given in a sparse form, reducing the system of inequalities to

$$\begin{bmatrix} \nabla^{(1)}\varphi_1 & \nabla^{(2)}\varphi_1 & 0 & \dots & \dots \\ 0 & \nabla^{(2)}\varphi_2 & \nabla^{(3)}\varphi_2 & 0 & \dots \\ \vdots & & & \ddots & \end{bmatrix} \cdot \begin{bmatrix} \boldsymbol{\eta}^{(1)} \\ \boldsymbol{\eta}^{(2)} \\ \vdots \end{bmatrix} \leq \begin{bmatrix} \Delta\varphi \end{bmatrix} \quad (3.52)$$

where at least one entry in

$$\nabla^{(q)}\varphi_i = \left(\frac{\partial\varphi_i}{\partial G_x^{(q)}}, \frac{\partial\varphi_i}{\partial G_y^{(q)}}, \frac{\partial\varphi_i}{\partial G_z^{(q)}} \right) \quad (3.53)$$

is non-zero. In any case the system of $N - 1$ equations for N variables is under-determined, i.e., infinitely many valid solutions for $\boldsymbol{\eta}$ exist that satisfy the inequality. The same holds, if constraints for the control points are included as depicted above. In case of directional constraints specified by $\mathbf{c}^{(q)}$, the expressions in Eq. 3.52 change to

$$\nabla^{(q)}\varphi_i = \frac{\partial\varphi_i}{\partial g^{(q)}} \text{ and } \boldsymbol{\eta}^{(q)}(\mathbf{G}_a, \mathbf{G}_b) \rightarrow \boldsymbol{\eta}^{(q)}(\mathbf{G}_a, \mathbf{G}_b), \quad (3.54)$$

which reduces both the number of equations and number of variables by two. In case of a fixed gradient strength constraint at the q -th control point, both the number of equations and the number of variables reduce by three, because there is no degree-of-freedom associated with the respective control point. The fact that the system of inequalities can be solved guarantees that the sum of all local objective functions

$$\sum_{q=1}^{N-1} \varphi_q(\mathbf{G}) = \sum_{q=1}^{N-1} f^{(q)}(\mathbf{G}^{(q)}, \mathbf{G}^{(q+1)}) = f(\mathbf{G}) \quad (3.55)$$

is invex (as long as invexity holds for the local objective functions itself, as was stated above). Therefore, every local minimum of f with respect to \mathbf{G} is a global minimum. Note that due to the fact that up to two of the three entries in Eq. 3.53 may vanish, different $\mathbf{G}_a, \mathbf{G}_b$ may result in different gradient trajectories, however, with the same optimal duration $T_{\min} = f(\mathbf{G}_a) = f(\mathbf{G}_b)$. For example, different optimization methods that use different strategies on how to handle the derivatives and the estimation of the step size may result in different gradient trajectories with the same duration.

3.1.9 Formal Complexity

For the *Optimal Control* method proposed by Lustig et al. [71] a formal time complexity of $\mathcal{O}(L)$ can be given where L denotes the number of samples of the path constraint $\mathbf{k}(a)$ with arc-length parameterization $a \in [0, a_{\max}]$ along which the gradient waveforms are to be computed. For the *Gradient Basis Function* method presented in this section, an evaluation of the objective function has a time complexity of $\mathcal{O}(N - 1)$ where N denotes the number of control points. The number of iterations required for convergence greatly depends on the arrangement of the control points – particularly on the distance of subsequent control points in k -space – as well as on the gradient hardware constraints. In general two types of control point arrangements can be differentiated:

- 1) If the absolute distance of subsequent control points in all gradient dimensions is sufficiently large (e.g., $|\Delta k| \geq 100 \text{ m}^{-1}$) the local objective function becomes quasi-convex (see Fig. 3.7, A and B).
- 2) Decreasing the distance of consecutive control points creates a more complex invex objective function that requires a non-deterministic runtime for convergence.

Because the effect of each gradient strength vector $\mathbf{G}^{(a)}$ on the k -space trajectory is limited to only a few neighboring gradient segments, the situation may occur that the parts of the trajectory with distant control points are quickly optimized while the parts with control points that are placed more closely require additional iterations. Therefore, the expected computational expense is mainly determined by the greatest (local) complexity of the control point arrangement, i.e., only placing few of the control points close to one another may increase the runtime of the entire gradient optimization process.

3.2 | Joint Optimization of Gradient and RF Waveforms

The previous section was dedicated to the development of a method for the design of time-optimal gradient waveforms. The design method is "guided" by an ordered set of control points that the associated k -space trajectory must traverse. The strategy of how to place these control points in k -space greatly depends on the problem type (transmission or reception), the FOV/FOX, and the number of RF coils (that determines the level by which k -space can be undersampled without degrading the reception or excitation quality). For transmission applications the optimal control point locations are further determined by the spatial pattern of the excitation target and off-resonance effects present in the FOX. In the following section, a framework for the design of ultra-short RF pulses for 3-D spatially selective excitations is derived [27, 29, 30]. The gradient waveform design method developed in the previous section is embedded in a joint RF and gradient optimization framework. The problem of control point placement is approached by prescribing the general arrangement of the control point sequence by simple shape parameters denoted by φ and optimizing the shape parameters instead of the control points itself.

3.2.1 Optimization Strategy

Formally, the joint RF and gradient design approach is stated as

$$\min_{\varphi, \mathbf{b}} \left\{ \underbrace{\|A(\varphi) \mathbf{b} - \mathbf{m}^{\text{tar}}\|_2^2 + \alpha \|\mathbf{b}\|_2^2 + f_{\beta}(T(\varphi))}_{\psi(\varphi, \mathbf{b})} \right\}, \quad (3.56)$$

where $A(\varphi)$ is the small tip-angle encoding matrix relating the RF waveform vector \mathbf{b} (all channels are concatenated to form a single column vector) to the transverse magnetization. The target magnetization vector is denoted \mathbf{m}^{tar} . The vector φ contains the shape parameters of the k -space trajectory which are optimized along with the RF waveform (the encoding matrix $A(\varphi)$ incorporates these parameters via the resulting k -space trajectory). Two regularization terms are added to the least-squares objective function to control the total RF power $\|\mathbf{b}\|_2^2$ (regularization strength controlled by α) and the duration of the RF/gradient pulse $T(\varphi)$ (controlled by a regularization function f_{β}).

The RF power regularization parameter α was chosen so as to restrict the peak RF power below the maximum amplifier peak power (150 V). This parameter was set by computing RF pulses with values of α varying from 10^{-5} to 10^{-2} in a logarithmic manner using the initial guess of the k -space trajectory. In other words, the search for the regularization parameter α was performed only once at the beginning of the optimization and kept constant during the optimization of the shape parameters. For regularization of the pulse duration, the penalty function is given by

$$f_{\beta}(T) = \begin{cases} 0 & \text{for } T < T_{\text{max}} \\ \beta \sqrt{\epsilon^2 + (T - T_{\text{max}} + \epsilon)^2} & \text{for } T \geq T_{\text{max}} \end{cases} \quad (3.57)$$

where T_{max} denotes the pulse duration limit, β denotes the regularization strength, and ϵ denotes the transition width between the two phases of the penalty function. For durations $T < T_{\text{max}}$ the function vanishes and the objective function is not penalized. For durations $T \geq T_{\text{max}}$ the function f_{β} is roughly equal to βT . Therefore, the function f_{β} is a smoothly varying increasing function for pulse durations greater than T_{max} with a transition width between the constraining

and non-constraining phases controlled by ϵ . In this work, it was found that a value of the parameter ϵ of 1.5 ms worked well for all pulses. On the other hand, the parameter β controls the strength of the pulse duration penalty. Empirically, it was found that the optimization results did not depend strongly on the specific value of β and that a value of $\beta = 2$ consistently yielded pulses shorter than 5 ms for all trajectory types.

The problem stated in Eq. 3.56 is solved using a nested optimization approach, i.e., the joint optimization is divided into an inner optimization loop (fast) over the RF waveform with a fixed gradient waveform and an outer optimization loop (slow) over the k -space shape parameters

$$\min_{\varphi} \left\{ \underbrace{\min_{\mathbf{b}} \{ \psi(\varphi, \mathbf{b}) \}}_{\text{Inner Loop: RF}} + \beta T(\varphi) \right\}, \quad (3.58)$$

Outer Loop: Shape Parameters

where $\psi(\varphi, \mathbf{b})$ denotes the regularized flip angle error, as depicted in Eq. 3.56.

In the small flip angle regime, and for a fixed k -space trajectory $\mathbf{k}(t)$, the transverse magnetization is given by [86, 45]

$$M_T(\mathbf{r}) = i\gamma M_0 \sum_{c=1}^C s^{(c)}(\mathbf{r}) \int_0^T b^{(c)}(t) e^{i\gamma \Delta B_0(\mathbf{r})(t-T)} e^{i\langle \mathbf{k}(t), \mathbf{r} \rangle} dt \quad (3.59)$$

where $s^{(c)}(\mathbf{r})$ and $b^{(c)}(t)$ denote the spatial sensitivity and the RF waveform of the c -th transmit channel, respectively, and $\Delta B_0(\mathbf{r})$ is the off-resonance map converted in Tesla. Discretization of the continuous integral and concatenation of the spatial locations at which Eq. 3.59 is evaluated yields a well-known system of linear equations between the RF pulse \mathbf{b} and the magnetization \mathbf{m} :

$$\mathbf{m} = A(\varphi) \mathbf{b} \quad (3.60)$$

where the elements of $A(\varphi)$ are easily deduced from Eq. 3.59. For a given target magnetization \mathbf{m}^{tar} and a fixed gradient waveform (meaning that φ is constant), the RF design problem, therefore, reads as

$$\min_{\mathbf{b}} \left\{ \left\| A(\varphi) \mathbf{b} - \mathbf{m}^{\text{tar}} \right\|_2^2 + \alpha \|\mathbf{b}\|_2^2 \right\}. \quad (3.61)$$

Note that Eq. 3.61 can be re-formulated as an unconstrained optimization problem using the normal equations

$$\mathbf{C} := A(\varphi)^H A(\varphi) + \alpha^2 \mathbf{I} \quad \text{and} \quad \mathbf{d} := A(\varphi) \mathbf{m}^{\text{tar}} \quad (3.62)$$

with $(\cdot)^H$ denoting the complex conjugate transpose and \mathbf{I} denoting the identity matrix. This problem is solved using the conjugate gradient algorithm as implemented in Matlab R2014b (The Mathworks Inc., Natick, MA, USA).

To enforce robustness of the designed RF pulses with respect to off-resonance effects, the gradient and RF waveforms are not only designed at the Larmor frequency but also at two off-resonance frequencies (± 50 Hz), referred to as *spatio-spectral* RF pulse design [107]. This

is implemented by stacking the respective encoding matrices computed at fixed off-resonance deviations (which are added to the B_0 map), namely

$$A := \begin{bmatrix} A_{-50 \text{ Hz}} \\ A_{0 \text{ Hz}} \\ A_{+50 \text{ Hz}} \end{bmatrix} \quad \text{and} \quad \mathbf{m} := \begin{bmatrix} \mathbf{m}^{\text{tar}} \\ \mathbf{m}^{\text{tar}} \\ \mathbf{m}^{\text{tar}} \end{bmatrix}. \quad (3.63)$$

The problem of optimization of the RF waveforms on a fixed k -space trajectory is a linear least-squares problem that can be solved relatively quickly (using convex optimization methods). In contrast, optimization of the gradient shape parameters is non-linear and, therefore, more difficult and time-consuming. The outer optimization loop (over the k -space trajectory shape parameters) of Eq. 3.58 is solved using a non-linear constrained sequential quadratic programming (SQP) algorithm as implemented in Matlab (function `fmincon`). The derivatives of the outer objective function with respect to φ are computed via finite differencing using a constant step size ($\epsilon = 2 \cdot 10^{-2}$). This optimization is performed subject to constraints on minimum ($\check{\varphi}$) and maximum ($\hat{\varphi}$) values of the shape parameters φ :

$$\check{\varphi}_q \leq \varphi_q \leq \hat{\varphi}_q \quad \text{for } q = 1, 2, \dots \quad (3.64)$$

For positive shape parameters, such as the number of shells or the number of revolutions per shell, an obvious choice for the respective constraint is $\check{\varphi}_q = 0$ to impose that the shape parameters are never set to negative values by the optimization process. For other parameters, the tolerated upper and lower bounds were adjusted so as to avoid excessively long pulse durations (e.g., longer than 20 ms). In this work, which was focused on brain imaging, the extent of all k -space trajectories was limited to a box in 3-D k -space with a maximum k -space extent of 100 m^{-1} in all dimensions (which corresponds to $\hat{\varphi}_{1/2/3} = 100 \text{ m}^{-1}$ for all trajectories). On the other hand, lower bound constraints on the k -space extent shape parameters were set to small values to prevent the trajectory from collapsing on itself (values of $\check{\varphi}_{1/2/3} = 10 \text{ m}^{-1}$ were used). In practice, the lower and upper bound constraints on k -space extent were never reached (i.e., these were non-binding constraints).

3.2.2 Parameterization of 3-D k -space Trajectories

Given a set of shape parameters, control points are placed in 3-D k -space using simple geometry rules outlined in Figs. 3.9, 3.11, and 3.13. These control points form the skeleton of the k -space trajectory. Note that instead of optimizing the individual locations of the control points (which would result in a large number of degrees-of-freedom to be optimized), the control points are optimized via the shape parameters φ . In this work, overall three types of k -space trajectories are studied: 3-D concentric shells, stack-of-spirals, and cross trajectories.

Shells Trajectory

The shells trajectory (Fig. 3.9) consists of a number of concentric shells (the number of shells is optimized by the joint gradient and RF design routine) that are parameterized using seven shape parameters. The first three shape parameters compress or stretch the entire trajectory in k_x , k_y , and k_z (φ_1 , φ_2 , φ_3). Two shape parameters vary the number of shells (φ_4) and the number of revolutions per shell (φ_5). The last two parameters control the local sampling density of the k -space trajectory: φ_6 controls the number of revolutions of the centermost shells while φ_7

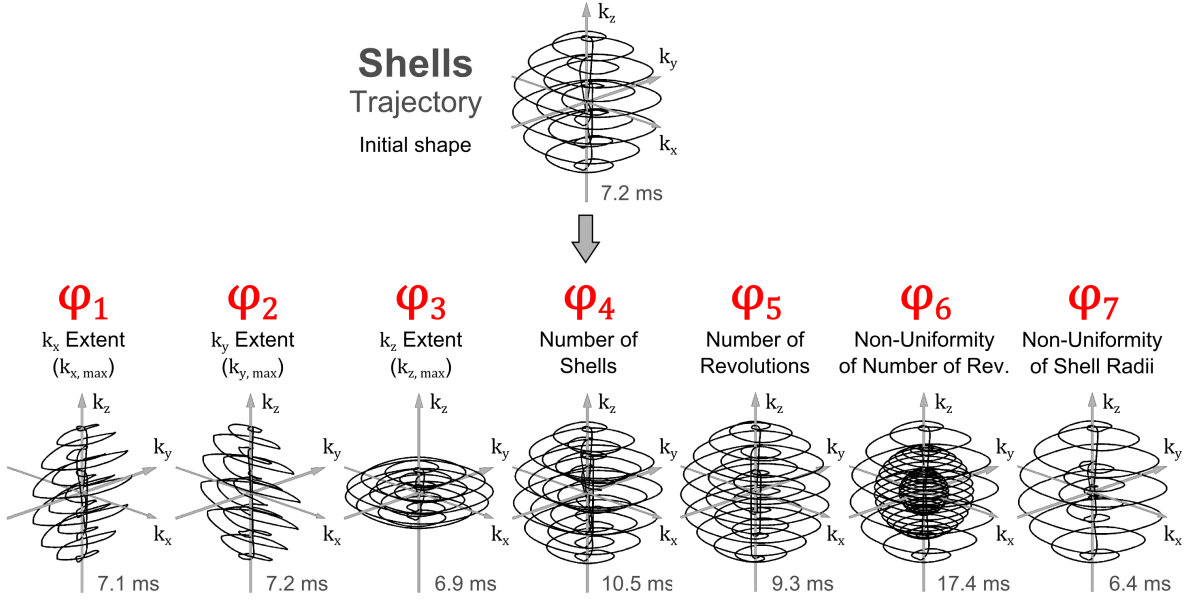


Figure 3.9: Visual depiction of the effect of shape parameters on the shells k -space trajectory. The effect of each parameter is shown by comparison with an "undeformed" trajectory at the top (the illustrated parameter changes are relatively large in order to facilitate visualization of the effect of each parameter).

controls the relative distance between consecutive shells. For example, increasing φ_7 causes the rate of variation of the radii of concentric shells (from inner to outer shell) to increase and thus results in a decrease of the sampling density at the periphery of k -space compared to the center (this is similar to the parameterization of variable-density spirals). Note that the parameters φ_4 and φ_5 are of integer type (in a following section we explain how these parameters are handled in the optimization process without causes discontinuities in the objective function).

Mapping of Shape Parameters to Control Points

In detail, the number N of concentric shells is controlled by the shape parameter φ_4 via

$$N := \lfloor \varphi_4 \rfloor, \quad (3.65)$$

where φ_4 is constrained to be in the range $[2.0, 7.5]$ (a.u.). The control points forming the n -th shell are placed along a 3-D curve that is given by the following equations:

$$\begin{aligned} k_x^{(n)}(t) &= R_x^{(n)} \cdot \sin\left(\frac{t}{2 \cdot c^{(n)}}\right) \cdot \cos(t) \\ k_y^{(n)}(t) &= R_y^{(n)} \cdot \cos\left(\frac{t}{2 \cdot c^{(n)}}\right) \cdot \sin(t) \\ k_z^{(n)}(t) &= R_z^{(n)} \cdot \cos\left(\frac{t}{2 \cdot c^{(n)}}\right) \end{aligned} \quad (3.66)$$

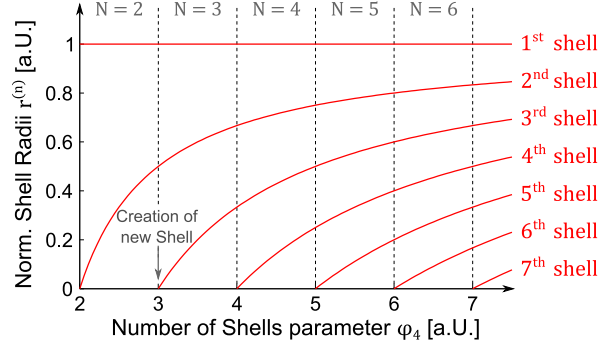


Figure 3.10: Dependence of the number of shells N (number of curves) and their radii $r^{(n)}$ (function values of the curves) as a function of the continuous number of shells shape parameter φ_4 . Note that the shell radii vary continuously with φ_4 to ensure that the shells do not overlap (no intersection of the curves). When φ_4 crosses an integer quantity, a new shell is created with zero extent (new curve at $r^{(n)} = 0$).

where t is the parametric variable, $c^{(n)}$ denotes the number of revolutions for shell index n and $R_x^{(n)}$, $R_y^{(n)}$, and $R_z^{(n)}$ are the radii of the shells along the three k -space dimensions (in m^{-1}). Control points are placed at a regular interval of the parameter t along this 3-D curve

$$t = 0, \frac{\pi}{4}, \frac{\pi}{2}, \frac{3\pi}{4}, \dots, 2\pi \cdot c^{(n)} \quad (3.67)$$

which yields four control points per shell revolution for each shell. The radii $R^{(n)}$ of the shells depend on two shape parameters, φ_4 (total number of shells) and φ_7 (rate of variation of the radii of the shells when one moves away from the k -space center, this parameter is constrained to be in the range $[0.5, 2.0]$ in a.u.). Note that these parameters control the radii of the shells indirectly, as follows: first, normalized radii of all shells in the trajectory are computed (the first shell has the greatest radius, the last shell the smallest):

$$r^{(n)} = \frac{\varphi_4 - n}{\varphi_4 - 1}. \quad (3.68)$$

This formulation properly implements the handling of an integer parameter: As a new shell is created, its normalized radius is automatically 0 (cf. Fig. 3.10). Note that the normalized radii depend on φ_4 and not on $N := \lfloor \varphi_4 \rfloor$, which means that as φ_4 increases (but does not cross a new integer value which would indicate the creation of a new shell), the radii of the shells change as well.

In the second step, the actual shell radii are computed using the normalized radii $r^{(n)}$ as follows:

$$\begin{aligned} R_x^{(n)} &:= (r^{(n)})^{\varphi_7} \cdot \varphi_1 \\ R_y^{(n)} &:= (r^{(n)})^{\varphi_7} \cdot \varphi_2 \\ R_z^{(n)} &:= (r^{(n)})^{\varphi_7} \cdot \varphi_3, \end{aligned} \quad (3.69)$$

i.e., the normalized radii are first adjusted by φ_7 (non-uniformity of rate of variation of the radii) and then multiplied by $\varphi_{1/2/3}$ (maximum extent in $k_{x/y/z}$, range $[10.0, 100.0]$ in m^{-1}) to yield the final radii of the shells along the three k -space dimensions. A value of $\varphi_7 > 1$ indicates an oversampling of the center of k -space (inner shells are closely spaced), whereas with a value $0 < \varphi_7 < 1$ the opposite effect is achieved (imposes oversampling of the k -space periphery).

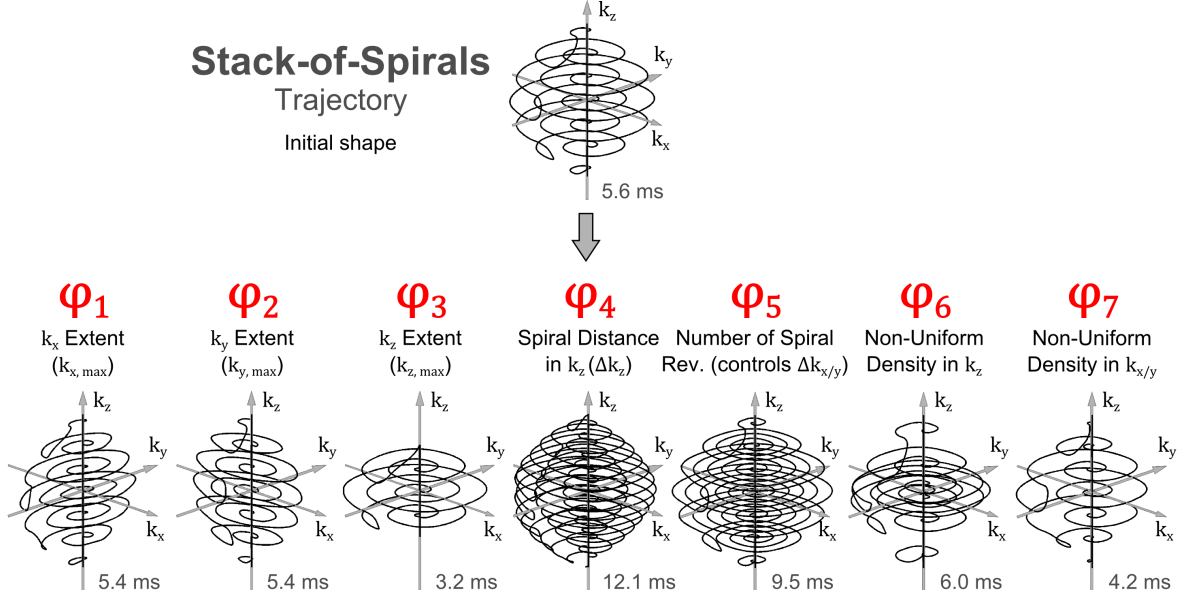


Figure 3.11: Visual depiction of the effect of shape parameters on the stack-of-spirals k -space trajectory. The effect of each parameter is shown by comparison with an "undeformed" trajectory at the top (the illustrated parameter changes are relatively large in order to facilitate visualization of the effect of each parameter).

Finally, the number of revolutions per shell $c^{(n)}$ is computed from φ_5 (controls number of revolutions of the entire trajectory, and is constrained to be in the range $[1.0, 10.0]$ in a.u.), φ_6 (rate of variation of number of revolutions as a function of the shell radius, range is $[-8.0, +8.0]$ in a.u.), and the normalized radii introduced in Eq. 3.68:

$$c^{(n)} = r^{(n)} \delta^{(n)} \varphi_5 \quad (3.70)$$

where

$$\delta^{(n)} = \begin{cases} (1 - r^{(n)}) \cdot \varphi_6 + 1 & \text{for } \varphi_6 \geq 0 \\ -r^{(n)} \cdot \varphi_6 + 1 & \text{for } \varphi_6 < 0 \end{cases} \quad (3.71)$$

Note that the number of revolutions $c^{(n)}$ for the n -th shell increases linearly with the radius of that shell in order to maintain a uniform distance in k_z between consecutive revolutions for all shells. The quantity $\delta^{(n)}$ can be used to increase the sampling density of either the center or the periphery of k -space. This quantity itself is computed from the shape parameter φ_6 as shown in Eq. 3.71. E.g., a value of the shape parameter φ_6 of $+1$ doubles the number of revolutions for the inner shell compared to the outer shell whereas a value of -1 has opposite effect, as it doubles the number of revolutions of the outer shells compared to the inner shell.

Stack-of-Spirals Trajectory

Another type of k -space trajectory parameterized in this work are stack-of-spirals (Fig. 3.11) using seven shape parameters. As with shells trajectories, φ_1 , φ_2 , and φ_3 control the extent of the entire trajectory in k_x , k_y , and k_z . φ_4 is the distance of consecutive spirals in k_z which, together with the k_z extent (φ_3), controls the number of spirals in the stack. φ_5 is the number

of revolutions per spiral which, together with the extent in k_x (φ_1) and k_y (φ_2) controls the in-plane sampling density. φ_6 controls the rate of variation of the distance between spirals in k_z (increasing φ_6 increases the distance between consecutive spirals as one moves away from the k -space center, which in turn decreases the sampling density at high k_z compared to $k_z = 0$). φ_7 controls the rate of variation of the radial velocity of each spiral and, therefore, affects the sampling density in the periphery of (k_x, k_y) compared to the center (variable density spirals). Because φ_3 and φ_4 can change the number of spirals in the stack they are considered integer parameters.

Mapping of Shape Parameters to Control Points

The stack-of-spirals consists of a number of N spirals that are stacked on top of each other in the k_z direction. N is controlled via

$$N := 2 \cdot \left\lfloor \frac{\varphi_3}{\varphi_4} \right\rfloor + 1, \quad (3.72)$$

where φ_3 controls the maximum extent in k_z (range is [10.0, 100.0] in m^{-1}) and φ_4 is the k_z distance between consecutive spirals (range is [1.0, 30.0] in m^{-1}). For a single spiral with index n , the control points are placed on the following 3-D curve:

$$\begin{aligned} k_x^{(n)}(t) &= R_x^{(n)} \cdot \left(\frac{t}{t_{\max}^{(n)}} \right)^{\varphi_7+1} \cdot \sin(t) \\ k_y^{(n)}(t) &= R_y^{(n)} \cdot \left(\frac{t}{t_{\max}^{(n)}} \right)^{\varphi_7+1} \cdot \sin(t) \\ k_z^{(n)} &= \pm \left| \frac{N+1-2n}{N-1} \right|^{\varphi_6+1} \cdot \varphi_4. \end{aligned} \quad (3.73)$$

Control points are placed at values of the parameter

$$t = 0, \frac{\pi}{4}, \frac{\pi}{2}, \frac{3\pi}{4}, \dots, t_{\max} \quad (3.74)$$

yielding four control points per spiral revolution. $R_x^{(n)}$ and $R_y^{(n)}$ denote the radii of the spirals in k_x and k_y , and are indirectly controlled by the algorithm. Specifically they are computed from $\varphi_{1/2}$ (maximum k -space extent in $k_{x/y}$, range is [10.0, 100.0] in m^{-1}) as:

$$\begin{aligned} R_x^{(n)} &= H^{(n)} \cdot \varphi_1 \\ R_y^{(n)} &= H^{(n)} \cdot \varphi_2 \end{aligned} \quad (3.75)$$

where

$$H^{(n)} = \left(0.5 \left(1 + \cos \left(\frac{k_z^{(n)} \pi}{\varphi_3} \right) \right) \right)^{2/5}. \quad (3.76)$$

In other words, the radii of the spirals in $k_{x/y}$ are proportional to the shape parameters $\varphi_{1/2}$ with the proportionality constant $H^{(n)}$, where $H^{(n)}$ is a window function shown in Fig. 3.12. As shown on this figure, $H^{(n)}$ ensures that spirals located away from the k -space center have a smaller radius than those at the center of k -space, which is important for the algorithm to

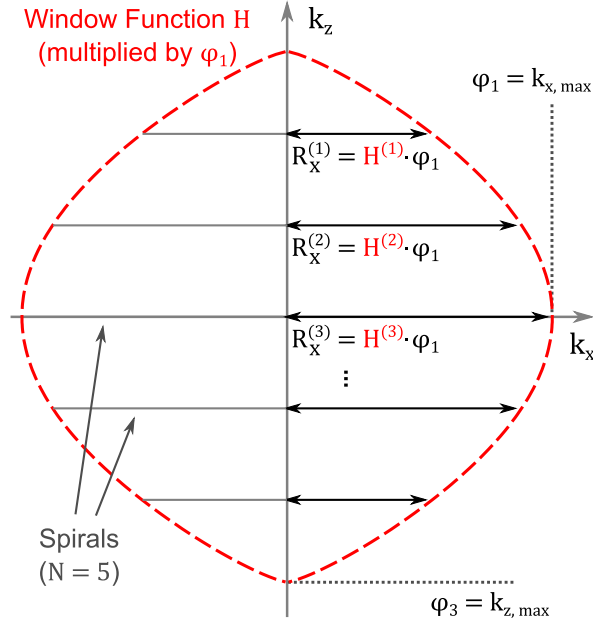


Figure 3.12: Parameterization of the radii of spirals in the stack-of-spirals trajectory. The window function $H^{(n)}$ (dashed curve, in this plot the window function is scaled to $\varphi_1 = k_{x,\max}$) ensures that spirals have a smaller radius $r^{(n)}$ at high k_z and a radius of zero at $k_{z,\max}$.

properly sample the center of k -space even in the case of a very short pulse. Additionally, this parameterization automatically handles properly the creation of a new spiral entity. Indeed, when a new pair of spirals is created at $\pm k_{z,\max}$, these are automatically assigned radii of 0 both in the k_x and k_y direction thus ensuring a smooth variation of the objective function.

The spirals that we use in this work are variable density spirals (this can be seen on Fig. 3.11), with a rate of variation in the transverse direction controlled by φ_7 (range is $[0.5, 2.0]$ in a.u.). In the k_z direction, the spacing between consecutive spirals is controlled by φ_4 and φ_6 as shown in the third line of Eq. 3.73. Specifically, k_z depends on the index of the spiral n and is proportional to φ_4 , which controls the distance of subsequent spirals in the k_z direction. As in the transverse direction, the rate of variation of the distance between consecutive spirals may be non-linear and is controlled by the "non-linearity parameter" φ_6 (range in $[0.5, 3.0]$ in a.u.). If $\varphi_6 = 1$, all the spirals in the stack are spaced equally. Values of $0 < \varphi_6 < 1$ impose oversampling of the high k_z regions compared to the low k_z region. Values of $\varphi_6 > 1$ imposes oversampling of the k -space center compared to the k -space periphery.

Finally, the maximum value of the parametric variable for each spiral, $t_{\max}^{(n)}$, depends on φ_5 (number of revolutions of the entire trajectory, range is $[1.0, 10.0]$ in a.u.) as well as the window function $H^{(n)}$ (since spirals with smaller radius need less revolutions to achieve the same sampling density in the $k_{x,y}$ plane), which leads to

$$t_{\max} = c^{(n)} \cdot 2\pi, \quad c^{(n)} = \varphi_5 \cdot H^{(n)} \quad (3.77)$$

where $c^{(n)}$ denotes the number of revolutions for the n -th spiral.

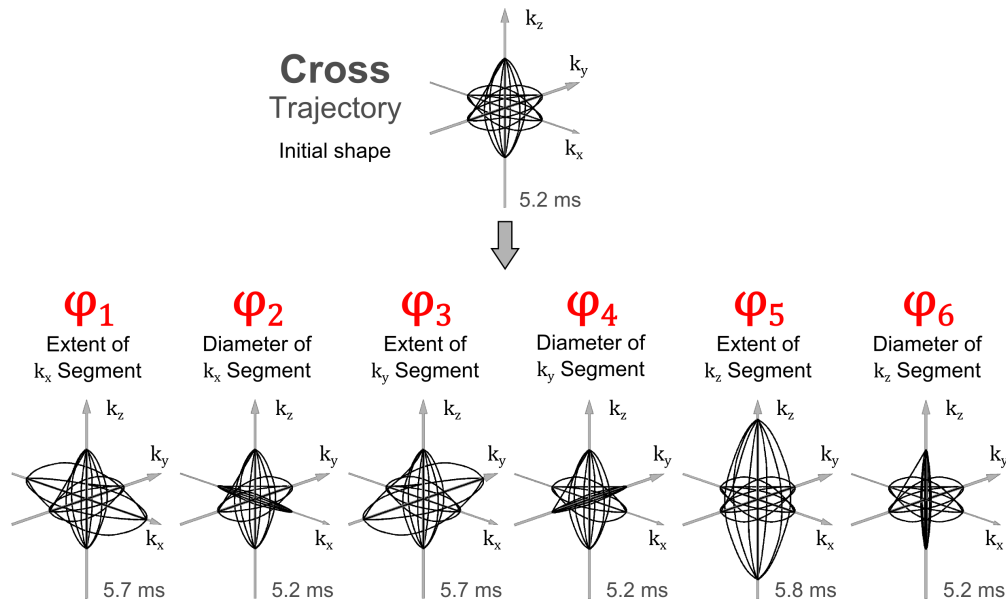


Figure 3.13: Visual depiction of the effect of shape parameters on the cross k -space trajectory. The effect of each parameter is shown by comparison with an "undeformed" trajectory at the top (the illustrated parameter changes are relatively large in order to facilitate visualization of the effect of each parameter).

Cross Trajectory

The final type of sampling pattern studied in this work is the cross k -space trajectory (Fig. 3.13). This trajectory densely samples k -space along the k_x , k_y and k_z axes in a way that resembles the Fourier transform of a cubic targets (the hypothesis is that this trajectory is well suited for cubic target regions). The trajectory consists of three distinct segments covering the k_x , k_y and k_z axes. The segments themselves consist of concentric 2-D elliptic curves that sample a roughly cylindrical region around each k -space axis. Each segment is parameterized by two shape parameters. The first parameter (φ_1 for k_x , φ_3 for k_y and φ_5 for k_z) controls the extent of the trajectory along the axis under consideration while the second (φ_2 for k_x , φ_4 for k_y and φ_6 for k_z) specifies the diameter of the segment in the direction perpendicular to the k -space axis. All six parameters for this cross shape are continuous (no integer parameters).

Mapping of Shape Parameters to Control Points

For the cross trajectory, the control points are directly placed in 3-D k -space as the 3-D trajectory itself has no closed-form expression. Each cross trajectory is composed of three segments, and every segment is composed of a variable number of revolutions (in this work, two revolutions were used for the k_x and k_y segments, and three revolutions for the k_z segment). Revolutions connect the minimum negative and the maximum positive extent of the trajectory along the axis under consideration and then return to the minimum negative extent (see Fig. 3.13). Each revolution is defined using four control point.

In the following example a single revolution of the k_x segment of a cross trajectory is considered. For this revolution, the first ($\mathbf{k}^{(1)}$) and third control point ($\mathbf{k}^{(3)}$) are placed on the k_x axis at $+\varphi_1$ and $-\varphi_1$, where φ_1 is the shape parameter controlling the maximum extent k_x of the entire trajectory (range is $[10.0, 100.0]$ in m^{-1}). The second ($\mathbf{k}^{(2)}$) and fourth control point ($\mathbf{k}^{(4)}$) are placed in the plane perpendicular to the k_x axis at $k_x = 0$. The distance of these control points

to the k -space origin (and thus the diameter of the k_x segment) is given by the product of φ_1 (maximum k -space extent) and φ_4 (this parameter controls the ratio of the diameter and the maximum k -space extent of the k_x segment, and its range is [0.05, 1.0] in a.u.). Subsequent revolutions are then established by rotating this set of control points (and thus the associated first revolution) around the k_x axis. In summary, the four control points of a single revolution of the k_x segment are given by

$$\begin{aligned}
 \mathbf{k}^{(1)} &= [-\varphi_1, & 0, & 0] \\
 \mathbf{k}^{(2)} &= [0, & +\sin(\theta)\varphi_1\varphi_4, & +\cos(\theta)\varphi_1\varphi_4] \\
 \mathbf{k}^{(3)} &= [+\varphi_1, & 0, & 0] \\
 \mathbf{k}^{(4)} &= [0, & -\sin(\theta)\varphi_1\varphi_4, & -\cos(\theta)\varphi_1\varphi_4]
 \end{aligned} \tag{3.78}$$

where θ denotes the rotation angle of the revolution around the k_x axis. Finally, control points are added for each segment so as to exactly sample the k_x , k_y , and k_z axis, which was found to be important for cubic excitation targets.

3.2.3 Integer Shape Parameters

As explained in the previous sections, some shape parameters are of integer type. Because the proposed optimization method uses a gradient-based solver for minimization of the objective function in Eq. 3.59, which only handles continuous parameters, integer parameters are converted into continuous parameters (for example, a value of the parameter φ_4 in a shells trajectory equal to 3.9 means that the trajectory contains 3 shells). To avoid discontinuities of the objective function as these parameters are varied by the optimizer, the following strategy was employed: When an integer parameter is increased by the optimizer so that it crosses an integer quantity (e.g., φ_4 in a shells trajectory increases from 3.9 to 4.1 which signifies that the number of shells increases from 3 to 4), the additional entity created by this increase (e.g., the new shell in the previous example) is associated with an infinitely small k -space extent. As a consequence, as this new entity is created, the objective function and pulse duration do not vary in a discontinuous manner. Alternatively, one might decide to remove such integer parameters from the optimization, however, it was found that these are very powerful degrees-of-freedom used by the optimizer to fine-tune the local sampling density of the trajectory to the magnetization pattern and B_1^+ maps at hand. For the stack-of-spirals trajectory, when changing φ_3 and φ_4 such that a new spiral needs to be added to the stack, two spirals are added in a symmetric fashion at $\pm k_{max}$.

3.2.4 Gradient Trajectory Design

Depending on the anticipated pulse duration and the type of trajectory, up to ≈ 50 control points are placed in k -space. For the shells and stack-of-spirals trajectory four control points were used per shell/spiral revolution positioned at 90° from each other. For the cross trajectory control points were placed at the tips and at the center of each k -space axis segment, also resulting in four control points per revolution along the axis of the segment.

The shortest smooth gradient trajectory $\mathbf{k}(t)$ connecting these control points in the order prescribed is computed in a way that satisfies the gradient amplitude (G_{\max}) and slew rate (S_{\max}) constraints, namely

$$\left\| \frac{d}{dt} \mathbf{k}(t) \right\|_{\infty} \leq G_{\max} \quad \text{and} \quad \left\| \frac{d^2}{dt^2} \mathbf{k}(t) \right\|_{\infty} \leq S_{\max} \quad (3.79)$$

using the *Gradient Basis Function* presented in Sec. 3.1 [28, 26]. In short, this approach stitches together piece-wise linear gradient segments, which results in piece-wise quadratic k -space segments. The duration and slope of the gradient segments are optimized using a minimization algorithm subject to the gradient system performance constraints. Optimization of the individual G_x , G_y , and G_z segments is performed such that the k -space trajectory passes through all control points in the shortest time (the trajectory shape between control points is not pre-determined and is optimized by the algorithm). This semi-analytic optimization approach is fast (e.g., 5 seconds on a single CPU for the design of a 10 ms 3-D k -space trajectory) and numerically highly stable. In other words, small perturbations of the control points positions result in small perturbations of the gradient waveforms without oscillations and divergence problems [28, 26] which can affect other approaches such as optimal control techniques [109, 55, 71, 120]. It was found that high numerical stability of the gradient waveform design is crucial in the proposed joint gradient and RF waveform optimization framework. Indeed, instabilities such as oscillations and small violations of the gradient system performance constraints result in discontinuous variations of the objective function in Eq. 3.58 and, therefore, cause premature termination of the optimization process and poor excitation performance of the RF pulse.

3.2.5 Evaluation of the Proposed Method

The proposed optimization framework was evaluated for head imaging at 7 Tesla using an 8-channel pTx system ("Step 2" pTx system, Magnetom 7 T, Siemens, Erlangen) loaded with a realistic 3-D-printed head phantom with three compartments (bone, brain, and everything else) that was described elsewhere [47]. The B_1^+ and B_0 maps were measured using the product saturated TurboFLASH B_1^+ mapping [38] and the gradient echo field mapping sequences, respectively, at a matrix size of $128 \times 128 \times 20$ in a field-of-view (FOV) of $20 \times 20 \times 12 \text{ cm}^3$ (Fig. 3.14). To reduce the computation time in the optimization process, the B_1^+ and B_0 maps were undersampled by a factor of two in the x and y directions (no undersampling in the slice direction), resulting in an effective voxel size of $3.0 \times 3.0 \times 6.0 \text{ mm}^3$. The pulses studied in this work were evaluated using Bloch simulation using these measured field maps as well as experiments. All pulse optimizations were performed on a 64 bit Windows machine with an Intel Xeon CPU W 3565 processor with 8 cores (3.2 GHz) and 16 GB of RAM.

Shells, stack-of-spirals, and cross trajectories were optimized for two 10° flip angle excitation targets: Excitation of a $4 \times 4 \times 4 \text{ cm}^3$ cube for reduced FOV imaging and excitation of the brain only for fat suppression (Fig. 3.14, bottom right). Both targets were blurred with a Gaussian kernel with $\sigma = 3 \text{ mm}$ and $\sigma = 1 \text{ mm}$ for the cube and brain target, respectively. The initial shape parameters of the three k -space trajectories were chosen so as to uniformly sample k -space up to $50 - 60 \text{ m}^{-1}$ in the three directions in less than 5 ms which corresponds to 6-fold undersampling. This is done in two steps: First, the spacing between sampling points (i.e., the sampling density) in 3-D k -space is chosen so as to roughly match the ratio of number of channels and the size of the FOX. In other words, k -space is undersampled by a factor equal to the number of transmit

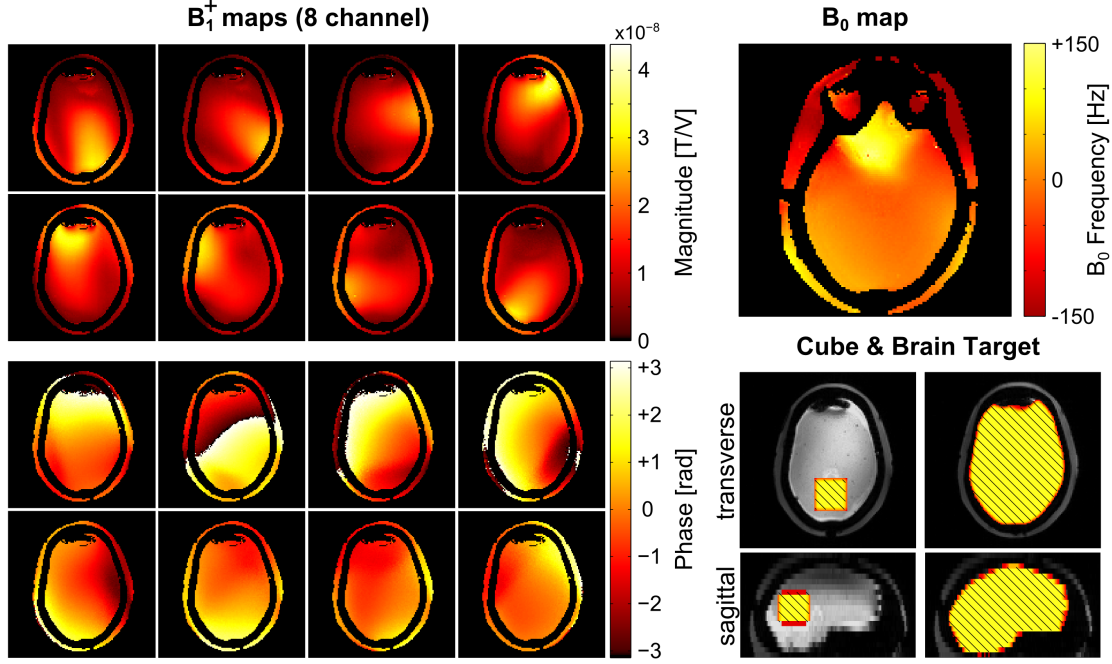


Figure 3.14: Coil sensitivity (B_1^+) and off-resonance maps (B_0) and target magnetization profiles used in this work for evaluation of the proposed approach. A different slice is shown for the B_0 map that shows the characteristic B_0 frontal lobe hot-spot (this slice is part of the stack being optimized). The cubic target has a dimension of $4 \times 4 \times 4 \text{ cm}^3$. The brain target covers the whole brain and excludes other tissues such as the skull, dura, fat, muscle, etc. Both target flip angle distributions are uniform within the excited volumes and equal to 10° .

channels. Second, keeping this sampling density constant, the extent of the trajectory in k_x , k_y , and k_z is increased in a uniform manner (same extent in all three spatial directions) until the pulse duration constraint is equal to the maximum duration tolerated (5 ms in this work). Additionally, RF pulses were designed using so-called SPINS trajectories as proposed by Malik et al. [73]. SPINS are analytic 3-D spherical spiral k -space trajectories with parameters controlling the maximum extent, the radial velocity, and the sampling density of the trajectory at the center and periphery of k -space. These SPINS trajectories as well as shells trajectories optimized by the proposed method were used for flip angle uniformization (whole head) as well as excitation of a cube target magnetization pattern. SPINS pulses were initially proposed only for flip angle uniformization and, in their original implementation by Malik et al., were kept very short (less than 1 ms). For the purpose of spatially selective excitation (e.g., excitation of the cube pattern), the length of the SPINS pulses was increased to 5 ms in order to sample the periphery of k -space as well.

All trajectories were designed using gradient system constraints of $G_{\max} = 40 \text{ mT/m}$ and $S_{\max} = 150 \text{ T/m/s}$. RF and gradient waveforms were designed with temporal sampling of $10 \mu\text{s}$. The RF power Tikhonov regularization strength (α in Eq. 3.56) was adjusted so as to limit the peak voltage to 150 V for all pulses per channel (this results in peak B_1^+ field strengths of 6.2, 6.2, 5.3, 6.6, 6.2, 6.2, 5.8, 6.2 μT for transmit channels #1 to #8). The pulse duration regularization parameters (Eq. 3.57) were adjusted so as to yield pulses with duration shorter than 5 ms. The performance of the RF pulses is characterized in terms of normalized root-mean-square

error (NRMSE). Denoting the achieved and the target flip angle distributions as FA_p and FA_p^{tar} (p denotes the pixel index), the RMSE and NRMSE [%] are computed via

$$\text{RMSE} = \sqrt{\frac{1}{P} \sum_{p=1}^P (FA_p - FA_p^{\text{tar}})^2} \quad (3.80)$$

$$\text{NRMSE} = \frac{\text{RMSE}}{FA_{\text{max}}^{\text{tar}} - FA_{\text{min}}^{\text{tar}}}. \quad (3.81)$$

3.3 | Off-resonance Robust Slice Excitation

The joint gradient and RF pulse optimization framework presented in the previous section was developed specifically for exciting 3-D spatially selective magnetization patterns. For this purpose, trajectories were utilized that sampled 3-D excitation k -space rather uniformly, as dictated by the 3-D energy pattern of the excitation targets (namely cubical and brain-shaped targets). It was further demonstrated how ΔB_0 effects can be incorporated into the RF design optimization in order to improve the practicability of the pulses. These ΔB_0 effects become more prominent as the field strength increases (e.g., from 3 T to the latest 7 T MR technology). In presence of large off-resonance effects, even the simplest tasks like slice-selective excitations become very challenging. In this section, an extension of the joint gradient and RF optimization framework will be derived that allows for computing RF pulses for uniform slice excitation in presence of both B_1^+ inhomogeneities and ΔB_0 effects (to achieve both uniform slice-excitation *and* off-resonance robustness). The proposed method has been presented by Davids et al. [32].

3.3.1 Spokes Pulses

The most basic approach to reduce B_1^+ -induced flip angle variations during slice-excitation is RF-shimming. In this case the slice-selective RF-pulses played on the different transmit channels are weighted differently, with the weights being tailored to the in-plane flip angle variation resulting from the non-uniform B_1^+ maps. In many cases, however, the degrees-of-freedom offered by the RF-shimming approach (i.e., the level of spatial flip angle modulation that can be generated by the different transmit channels) are insufficient to achieve acceptable uniformization of the flip angle maps.

A commonly used approach to design slice-selective RF pulses with more degrees-of-freedom with respect to the achievable in-plane flip angle variations (to achieve more uniform flip angle maps) are so-called *Spokes* pulses [99]. These pulses utilize *spokes trajectories* that sample excitation k -space along multiple straight lines oriented in parallel to the slice-selective axis (most often the k_z axis). On each spoke and each transmit channel, a sinc RF pulse is played in order to achieve slice-selection. One spoke is usually placed at the center of the $k_{x/y}$ plane ($k_{x/y} = \mathbf{0}$), i.e., this spoke corresponds to a regular slice-selective RF pulse. The remaining spokes are shifted away from the center of the $k_{x/y}$ plane in order to generate an in-plane flip angle modulation, depending on the location of the spoke in $k_{x/y}$ (i.e., the distance to the k -space center). A spoke located very close to $k_{x/y} = \mathbf{0}$ will excite a slice with a low-frequency spatial flip angle modulation, whereas shifting the spoke further away from the center of the $k_{x/y}$ plane will increase the spatial modulation frequency of the flip angle map. If the positions of the spokes are chosen appropriately (usually on the order of 5 m^{-1} in both k_x and k_y), the spatial flip-angle modulation can be tailored (by choosing different complex weights for each spoke and each transmit channel, similar to RF-shimming) such that the B_1^+ -induced flip angle variations are compensated. Spokes pulses are very easy to design, since there is no need to perform a full optimization of the RF waveforms (only a few degrees-of-freedom to be optimized, given by "number of channels" \times "number of spokes").

The good performance of spokes pulses, however, breaks down as soon as off-resonance effects are present in the FOX. The capability of spokes pulses to achieve robustness against these ΔB_0 effects is intrinsically limited by the k -space sampling structure of the spokes trajectory. This

can be illustrated by means of the small tip angle solution of the Bloch equation (here given for a single transmit channel for simplicity):

$$M_T(\mathbf{r}) = i\gamma M_0 \int_0^T B_1^+(t, \mathbf{r}) \underbrace{e^{i\langle \mathbf{k}(t), \mathbf{r} \rangle}}_{k\text{-space encoding}} \underbrace{e^{i\gamma \Delta B_0(\mathbf{r})(t-T)}}_{\text{Dephasing from off-resonance}} dt . \quad (3.82)$$

As was described before, the transverse magnetization $M_T(\mathbf{r})$ is given by the Fourier transform of the applied B_1^+ -field, with the Fourier pair given by $\langle \mathbf{k}(t), \mathbf{r} \rangle$. Variations of the static magnetic field denoted by ΔB_0 cause a spatially varying dephasing of the magnetization that leads to signal dropouts. For the off-resonance term in Eq. 3.82, a Taylor expansion can be given, resulting in

$$\Delta B_0(\mathbf{r}) = \Delta B_0(\mathbf{0}) + \mathbf{r} \nabla (\Delta B_0(\mathbf{0})) + \mathfrak{R}(\mathbf{r}) , \quad (3.83)$$

where $\mathfrak{R}(\mathbf{r})$ is used to denote any off-resonance terms of order ≥ 2 . Using this Taylor expansion, the dephasing term in Eq. 3.82 can be reformulated, yielding

$$\begin{aligned} & \exp\left(i\gamma \Delta B_0(\mathbf{r})(t-T)\right) \dots \\ & \dots = \exp\left(i\gamma \Delta B_0(\mathbf{0})(t-T)\right) \cdot \exp\left(i\gamma \mathbf{r} \cdot \nabla (\Delta B_0(\mathbf{r}_0))(t-T)\right) \cdot \exp\left(i\gamma \mathfrak{R}(\mathbf{r})(t-T)\right) \\ & = \underbrace{\exp\left(i\gamma \Delta B_0(\mathbf{0})(t-T)\right)}_{\substack{\mathbf{0th-order:} \\ \text{Constant offset}}} \cdot \underbrace{\exp\left(i\langle \mathbf{r}, \mathbf{k}_{\Delta B}(t) \rangle\right)}_{\substack{\mathbf{1st-order:} \\ \text{Shift in } k\text{-space}}} \cdot \underbrace{\exp\left(i\gamma \mathfrak{R}(\mathbf{r})(t-T)\right)}_{\substack{\mathbf{Higher order:} \\ k\text{-space blurring}}} \end{aligned} \quad (3.84)$$

where

$$\mathbf{k}_{\Delta B}(t) = \gamma \nabla (\Delta B_0(\mathbf{r}_0))(t-T) . \quad (3.85)$$

The above rearrangement illustrates that the different ΔB_0 -order-terms can be associated with different effects to the spatial encoding. The 0th-order term induces a global offset of the resonance frequency, which usually can be accounted for very easily by B_0 shimming. The 1st-order term of the ΔB_0 field mimics an additional unwanted gradient field and, therefore, induces a time-dependent shift of the k -space coordinate by $\mathbf{k}_{\Delta B}(t)$. The higher order terms cannot be associated with a unique k -space shift but generate a non-linear uncertainty or "blurring" of the k -space coordinate.

The k -space shift arising from the 1st-order ΔB_0 -term generates bending-like deformations of the slice profile that are commonly referred to as the *potato-chip* effect. This bending effect is most prominent if the different spokes are driven at an opposite gradient polarity. For a 2-spokes pulse this means that the first spoke is traversed from $-k_z$ to $+k_z$ whereas the second spoke is traversed from $+k_z$ to $-k_z$ (or vice versa), as depicted on the left side of Fig. 3.15. The k -space error induced by the 1st-order ΔB_0 -term is illustrated as a blue shift in the $k_{x/y}$ plane. Note that the k -space shift is largest at the beginning of the RF pulse and vanishes at the very end of the pulse. This time dependence is due to the fact that k -space information deposited at the beginning of the pulse accumulates ΔB_0 -induced phase errors throughout the full pulse duration,

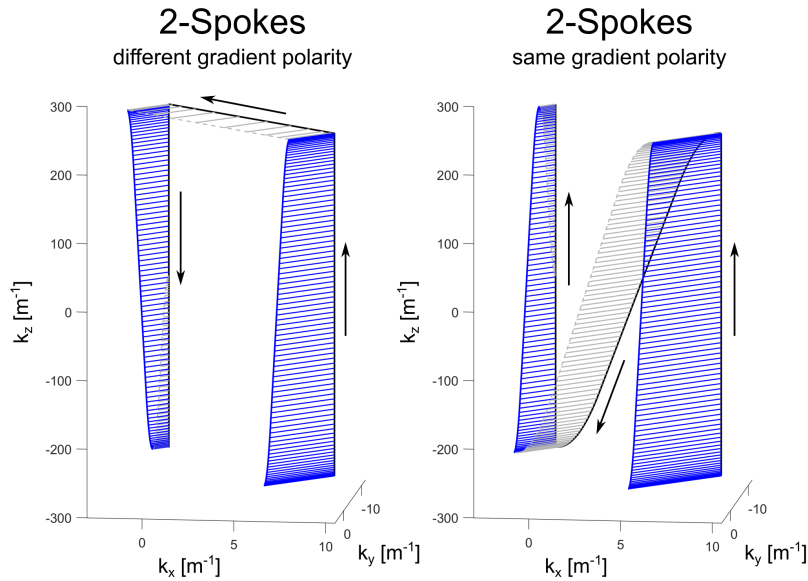


Figure 3.15: Depiction of 2-spokes trajectories where the spokes are played with opposite gradient polarity (left) and the same polarity (right). Playing the spokes with the same polarity (meaning that the first spoke needs to be refocused before playing the second spoke) ensures that the ΔB_0 -induced k -space errors (shown in blue) produce more similar slice deformations which reduces the overall signal loss.

whereas information deposited at the very end of the pulse does not have time to accumulate significant phase errors. As a result of the k -space error, the spokes are "tilted", creating the common bending effect of the slice.

One approach to reduce the level of slice bending is to refocus the z -gradient of the first spoke and playing the second spoke with the same gradient polarity (as shown in Fig. 3.15, right). Although this does not reduce the k -space shift induced by the 1st-order ΔB_0 -terms (in fact, the maximum shift increases due to the longer pulse duration), the two spokes are tilted in k -space in a similar fashion (compared to the case of opposing gradient polarity). As a result, the two spokes create a similar slice bending effect, leading to less signal dropouts. This technique can partially recover signal loss arising from the 1st-order ΔB_0 -term, but is not capable of recovering signal loss arising from the higher-order ΔB_0 -terms. These terms cannot be clearly associated with a k -space shift (like the 1st-order term) and, therefore, create an uncertainty or "blurring" effect at the k -space location. In theory these effects can be accounted for by performing a full RF pulse optimization with enforced robustness to off-resonance effects (in an attempt to restore the blurred k -space information), however, if and only if the k -space trajectory provides enough degrees-of-freedom to recover the k -space information in the $k_{x/y}$ plane. Due to the sparsity of the spokes trajectories in the $k_{x/y}$ -plane (every spoke samples exactly one location in $k_{x/y}$), this type of trajectory does not provide enough degrees-of-freedom to compensate for these effects.

3.3.2 The Corkscrew Trajectory

In order to overcome the limitations of the spokes pulses – in particular the sparse sampling density in the $k_{x/y}$ plane – a new type of k -space trajectory is proposed. In general, three

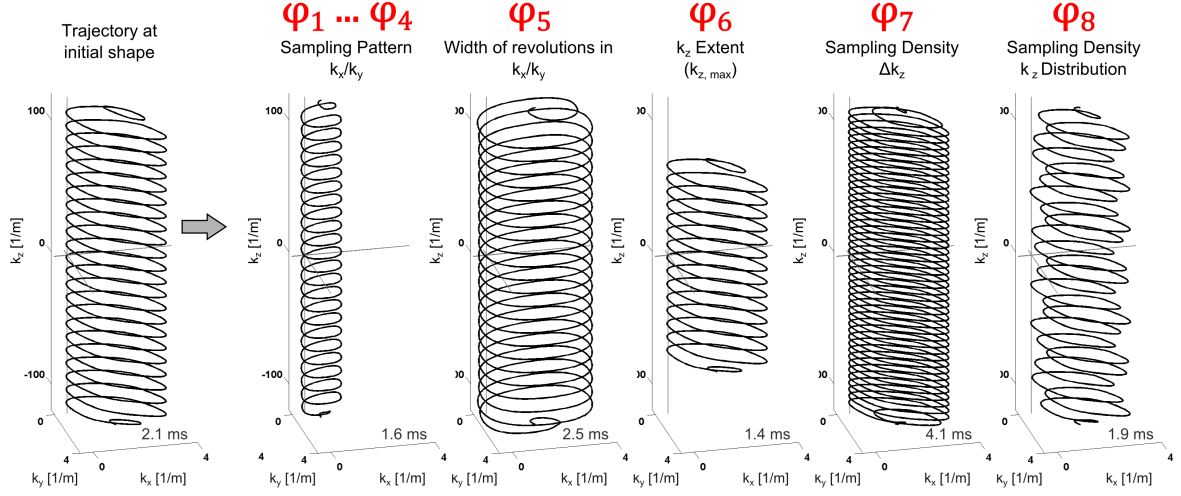


Figure 3.16: Visual depiction of the effect of the shape parameters on the corkscrew k -space trajectory. The effect of each parameter is shown by comparison with the "undeformed" trajectory on the left (the illustrated parameter changes are relatively large in order to facilitate visualization of the effect of each parameter).

requirements of the gradient trajectory can be stated to achieve both flip angle mitigation and off-resonance robustness:

- 1) A homogeneous sampling density along the k_z axis in order to achieve accurate slice-selection.
- 2) A flexible sampling density in the k_x/y plane in order to create degrees-of-freedom for the RF pulse optimization to improve the flip-angle mitigation *and* the off-resonance compensation capability.
- 3) A gradient trajectory that samples excitation k -space in a more structured way from $+k_z$ to $-k_z$ (or alternatively from $-k_z$ to $+k_z$) without reversal of the k_z direction. It was found that this way of sampling the k_z axis is intrinsically more robust to off-resonance effects.

To realize these trajectory features, a so-called *Corkscrew* trajectory was designed (see Fig. 3.16) that is parameterized by overall eight shape parameters $\varphi = (\varphi_1, \dots, \varphi_8)$. The corkscrew trajectory samples excitation k -space along a helical path following the slice-selection axis. The distance of two subsequent helical revolutions is chosen so as to achieve a certain size of the field-of-excitation. The base area of the helical path in the k_x/y -plane is defined by an ellipse of certain length, width, and rotation angle. Every revolution of the helical path is defined by overall four control points in k -space. For the n -th revolution the control points are given by

$$\begin{aligned}
 \mathbf{k}^{(1)} &= \begin{bmatrix} \varphi_1 & \varphi_2 & \varphi_6 - n\varphi_7 \end{bmatrix} \\
 \mathbf{k}^{(2)} &= \begin{bmatrix} \frac{1}{2}(\varphi_1 + \varphi_3) + \varphi_5 \cdot r_1 & \frac{1}{2}(\varphi_2 + \varphi_4) + \varphi_5 \cdot r_2 & \varphi_6 - \left(n + \frac{1}{4}\right)\varphi_7 \end{bmatrix} \\
 \mathbf{k}^{(3)} &= \begin{bmatrix} \varphi_3 & \varphi_4 & \varphi_6 - \left(n + \frac{2}{4}\right)\varphi_7 \end{bmatrix} \\
 \mathbf{k}^{(4)} &= \begin{bmatrix} \frac{1}{2}(\varphi_1 + \varphi_3) - \varphi_5 \cdot r_1 & \frac{1}{2}(\varphi_2 + \varphi_4) - \varphi_5 \cdot r_2 & \varphi_6 - \left(n + \frac{3}{4}\right)\varphi_7 \end{bmatrix}
 \end{aligned} \tag{3.86}$$

with

$$\mathbf{r} = (r_1, r_2) = \frac{[(\varphi_4 - \varphi_2), -(\varphi_3 - \varphi_1)]}{\|[(\varphi_4 - \varphi_2), -(\varphi_3 - \varphi_1)]\|_2} . \quad (3.87)$$

The shape parameters and their respective bounds are defined as follows:

φ_1	k_x coordinate of first elliptical tip	$[-20, +20]$ in m^{-1}
φ_2	k_y coordinate of first elliptical tip	$[-20, +20]$ in m^{-1}
φ_3	k_x coordinate of second elliptical tip	$[-20, +20]$ in m^{-1}
φ_4	k_y coordinate of second elliptical tip	$[-20, +20]$ in m^{-1}
φ_5	width of the helical revolutions in the $k_{x/y}$ plane	$[5, 40]$ in m^{-1}
φ_6	k_{\max} along the k_z axis	$[300, 1000]$ in m^{-1}
φ_7	distance Δk_z of two subsequent revolutions	$[2, 100]$ in m^{-1}
φ_8	modulation strength of the $k_{x/y}$ sampling density	$[0, 1]$ in a.u.

The last shape parameter φ_8 is used to slightly modify the scaling of subsequent revolutions in the $k_{x/y}$ -plane, which was found to be helpful to improve the condition of the resulting system matrix, and as a result to improve the fidelity of the slice-selective RF pulse. This modulation is implemented by multiplication of the k_x and k_y control point coordinates by the following scaling term $\Psi(k_z)$ (i.e., the scaling term varies with the k_z location of the control points):

$$\Psi(k_z) := 1 - \varphi_8 \cdot \frac{1}{2} \left(1 + \cos \left(\frac{k_z}{\sqrt{2}\varphi_7} \cdot 2\pi \right) \right) . \quad (3.88)$$

The k_x and k_y coordinates of the control points are then modulated via

$$k_x \rightarrow k_x \cdot \Psi(k_z) + \frac{1}{2} (\varphi_1 + \varphi_3) \cdot (1 - \Psi(k_z)) \quad \text{and} \quad (3.89)$$

$$k_y \rightarrow k_y \cdot \Psi(k_z) + \frac{1}{2} (\varphi_2 + \varphi_4) \cdot (1 - \Psi(k_z)) . \quad (3.90)$$

3.3.3 Slice-Selective RF Pulse Design

In order to improve the applicability of the joint gradient and RF optimization framework described in Sec. 3.2 with respect to the design of slice-selective RF pulses, a few adjustments were made. For the inner loop of Eq. 3.58 in which the RF waveforms are optimized on a constant k -space trajectory, the least squares pulse optimization was replaced by a magnitude least squares (MLS) optimization. The objective function of the MLS RF optimization reads

$$\min_{\mathbf{b}} \left\{ \left\| |A(\boldsymbol{\varphi}) \mathbf{b}| - |\mathbf{m}^{\text{tar}}| \right\|_2^2 + \alpha \|\mathbf{b}\|_2^2 \right\} . \quad (3.91)$$

Note that although the system of equations is solved on complex variables, the residual error between achieved magnetization $A(\boldsymbol{\varphi}) \mathbf{b}$ and target magnetization \mathbf{m}^{tar} is evaluated in terms of the magnitude $|\cdot|$ of the respective quantities. This means, that the phase of the magnetization is not considered by the objective function, as this is not relevant for many imaging sequences. However, releasing the phase constraint effectively divides the number of variables that the system of equations is solved for by a factor of two, i.e., MLS RF pulses usually perform significantly better than RF pulses which have been optimized in a conventional least squares sense. Note that the objective function in Eq. 3.91 is non-linear which generally does not allow to use fast

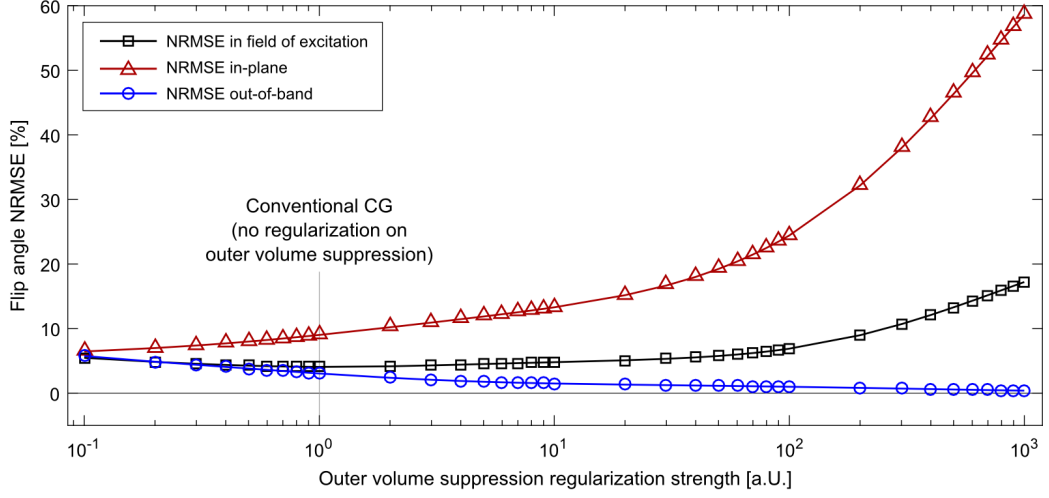


Figure 3.17: Effect of the outer volume regularization strength λ on the flip angle fidelity in the entire field-of-excitation, FOX (black squares), for the in-plane voxels (red triangles), and in the outer volume (blue circles).

convex optimization methods. To overcome this, the MLS optimization was performed using the *phase adoption* method which reformulates the single non-linear optimization problem as a series of linear optimization problems. Specifically, Eq. 3.91 is approached by solving multiple least squares RF optimization problems $k = 1, 2, \dots, N$ given by

$$\min_{\mathbf{b}_k} \left\{ \left\| C(\boldsymbol{\varphi}) \mathbf{b}^k - \mathbf{d}^k \right\|_2^2 \right\} \quad \text{with} \quad \mathbf{d}^k := |\mathbf{d}^{\text{tar}}| \cdot e^{j \text{Arg}(C(\boldsymbol{\varphi}) \mathbf{b}^{k-1})} \quad (3.92)$$

where again normal equations were employed to use fast conjugate gradient solvers:

$$C := A(\boldsymbol{\varphi})^H A(\boldsymbol{\varphi}) + \alpha^2 I \quad \text{and} \quad \mathbf{d} := A(\boldsymbol{\varphi}) \mathbf{m}^{\text{tar}} \quad (3.93)$$

Note that for each sub-problem with superscript k a magnetization target \mathbf{d}^k is used whose phase was chosen according to the solution of the previous RF optimization $k - 1$. In other words, the phase of the target magnetization is adjusted after each optimization in order to iteratively release this constraint from the optimization.

A second modification has been implemented to improve the goodness of the slice-selectivity, i.e., to enforce signal suppression in the outer volume. This can be achieved by performing the pulse optimization such that the evaluation of the total flip angle error (which is minimized by the pulse optimization) uses different weights for voxels located in the slice and in the outer volume. This weighting is applied both to the system matrix and the target magnetization. Let

$$A(\boldsymbol{\varphi})_{\text{inner}} / A(\boldsymbol{\varphi})_{\text{outer}} \quad \text{and} \quad \mathbf{m}_{\text{inner}}^{\text{tar}} / \mathbf{m}_{\text{outer}}^{\text{tar}} \quad (3.94)$$

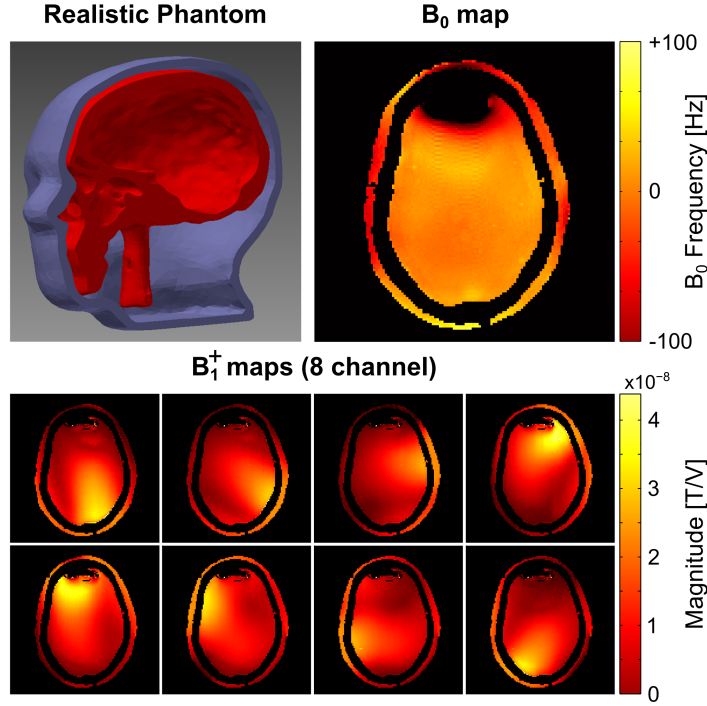


Figure 3.18: *Top left:* Realistic head phantom [48] used for evaluation of the RF-shimming and spokes pulses as well as the proposed corkscrew RF pulse. *Top right:* ΔB_0 map showing the characteristic hot-spot in the frontal lobe. This slice was used for evaluation of the different RF pulses. *Bottom:* B_1^+ maps of the 8 channel transmit coil array.

be sub-matrices and sub-vectors that only include the columns that are associated with in-plane voxels ("inner") and outer volume voxels ("outer"). The normal equations given by Eq. 3.93 are then adjusted towards

$$C := \begin{bmatrix} A(\varphi)_{\text{inner}} \\ \lambda A(\varphi)_{\text{outer}} \end{bmatrix}^H \begin{bmatrix} A(\varphi)_{\text{inner}} \\ \lambda A(\varphi)_{\text{outer}} \end{bmatrix} + \alpha^2 I \quad \text{and} \quad (3.95)$$

$$\mathbf{d} := \begin{bmatrix} A(\varphi)_{\text{inner}} \\ \lambda A(\varphi)_{\text{outer}} \end{bmatrix} \begin{bmatrix} \mathbf{m}_{\text{inner}}^{\text{tar}} \\ \lambda \mathbf{m}_{\text{outer}}^{\text{tar}} \end{bmatrix}^T. \quad (3.96)$$

The weighting factor λ is used to adjust the balance between enforcing B_1^+ mitigation to improve the in-plane flip angle fidelity ($\lambda < 1$) and enforcing accurate slice-selection without residual signals in the outer volume ($\lambda > 1$). For $\lambda = 1$ the problem to be solved is the same as stated in Eqs. 3.92 and 3.93. The effect of the outer-volume suppression regularization parameter λ is illustrated in Fig. 3.17. It can be observed that the weighting parameter λ can be adjusted so as to remove residual signals in the outer-volume (blue dots) at the cost of reduced in-plane flip angle fidelity (red triangles).

3.3.4 Evaluation of the proposed Method

The proposed corkscrew RF pulse strategy was evaluated by exciting a slice in a head region in which significant off-resonance frequencies are present. For this purpose, we used a realistic head phantom consisting of four compartments: bone, brain, muscle, internal air cavities [48] (see Fig. 3.18, top left). This phantom creates the characteristic ΔB_0 hot-spot in the frontal lobe due to susceptibility effects, see Fig. 3.18 (top right). The corkscrew RF pulse was designed to excite a slice exactly in this region. Additionally, a number of more common slice-excitation approaches was used to design RF pulses, namely a simple Birdcage mode excitation (#1), RF-shimming (#2), and 2-spokes pulses without and with enforcing robustness to ΔB_0 effects (#3 and #4). The B_1^+ and B_0 maps were measured at 7 Tesla using a matrix size of $128 \times 128 \times 115$ in a FOV of $20.5 \times 20.5 \times 11.5 \text{ cm}^3$ (Fig. 3.18), resulting in a voxel size of $1.6 \times 1.6 \times 1.0 \text{ mm}^3$. The gradient system constraints were set to $G_{\max} = 40 \text{ mT/m}$ and $S_{\max} = 150 \text{ T/m/s}$. The RF power Tikhonov regularization strength (α in Eq. 3.91) was adjusted so as to limit the peak voltage to 150 V. For the target magnetization, a slice with a thickness of 3 mm at a flip angle of 10° was chosen. The flip angle mitigation was performed only in the brain (i.e., excluding the dura from the optimization ROI).

3.4 | Prediction of Magnetostimulation Thresholds

The previous sections investigated strategies to make optimal use of the gradient coils in the frame of multi-dimensional pTx RF pulses for excitation of 3-D spatially selective target magnetization. Constraining the gradient waveforms by maximum strength and slew rate (G_{\max} and S_{\max}) and the RF waveforms by the maximum voltage applied to the transmit coils (V_{\max}) is a rather conservative but effective way to reduce electric fields and their undesired effects (PNS and SAR, respectively). In the following section a more fundamental approach is used to reduce PNS: A framework is developed that can predict PNS induced by realistic coil geometries using a realistic body model for EM field simulation, a detailed atlas of human nerve fibers and a neurodynamic model [31, 34, 33].

3.4.1 Workflow

In order to model PNS in the body induced by the switching of electromagnetic fields created by an external coil, we follow the workflow depicted in Fig. 3.19. The proposed framework has three major components: A) a surface-based whole body tissue model used for calculation of the internal electromagnetic (EM) fields, B) a detailed atlas of the nerve fibers in the human body embedded in the same anatomical model, C) a numerical framework to model the nerve dynamics in presence of external E -fields. In short, the following steps are performed to generate the PNS threshold curves for a given coil geometry:

- Step 1** We preprocess the surface body model to be compatible with finite element EM field simulations and prepare the nerve atlas to be compatible with the neurodynamic model. This preprocessing step is only required once and can be reused for the analysis of multiple coil geometries.
- Step 2** The magnetic and electric fields in the body model generated from a time-varying current applied to the coil are simulated using commercial EM field simulation platforms such as CST (Darmstadt, Germany) or Sim4Life (Zurich MedTech AG, Zurich, Switzerland).
- Step 3** The atlas of human peripheral nerve fibers is superimposed on the fields. The simulated electric fields are projected onto the nerves and integrated to obtain the effective electric potential along the fiber. This provides the relevant electric entity that can lead to action potential generation and is used as an input to the neurodynamic model.
- Step 4** The neurodynamic model is evaluated providing the response of the nerve fiber to the external electric potentials. The nerve fiber model returns the internal membrane potentials. An action potential (AP) is recognized as a sudden membrane depolarization in response to a small increase in the applied fields.

3.4.2 Surface Body Model

The realistic body model was based on the anatomical surface data developed by Zygote (American Fork, UT, USA), which is shown in Fig. 3.20. The Zygote anatomical data includes 12 different tissue classes: skeleton, muscular system, respiratory system, digestive system, nervous system, circulatory system, connective tissue, integumentary system, lymphatic system, urinary system, and endocrine system. Each tissue class is described by a single surface mesh. Since the Zygote model was initially developed for teaching and visualization purposes, further processing

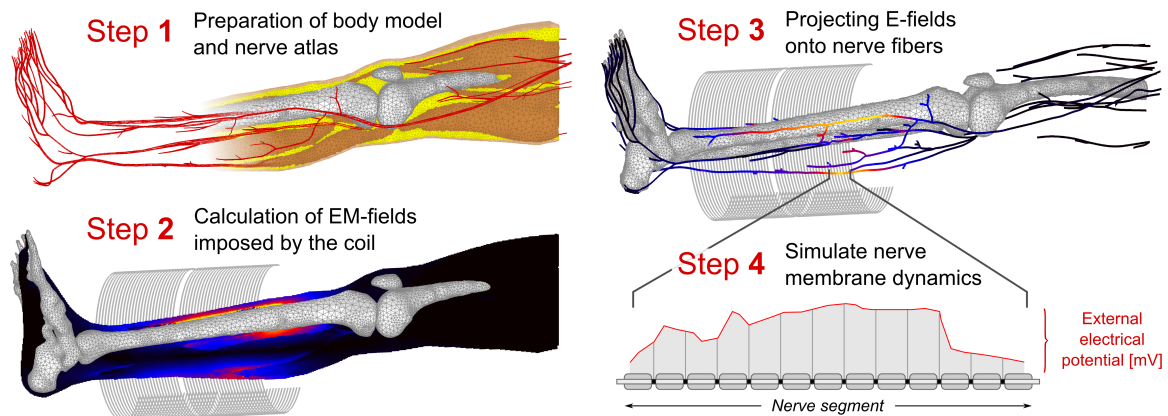


Figure 3.19: Flowchart of the PNS simulation process. *Step 1:* Preparation of the body model and nerve atlas (only required once). *Step 2:* EM fields imposed by the coil are calculated. *Step 3:* The electric field for a given coil current waveform is interpolated and projected onto the nerve fiber. *Step 4:* Nerves response is calculated to determine if an AP has been initiated. If no AP is reached, steps 3 and 4 are repeated with a higher amplitude coil current waveform until PNS is observed.

was required in order to guarantee that it can be used in conjunction with electromagnetic simulation platforms. Specifically, the input surface mesh to the EM simulation platform requires an orientable 2-manifold mesh without self-intersections and without intersections of the different tissue classes. To achieve this, we first discretized the surface mesh data to obtain a voxel model at 1 mm isotropic resolution for each tissue class (Fig. 3.21, Step 1 and 2). The voxels of all tissue classes were combined into a single voxel model. Skin tissue voxels were added by performing a morphological dilation algorithm of the outer body hull, assuming a skin thickness of approx. 3 mm (i.e., 3 voxels). Every interior voxel that was not assigned to any of the tissue classes at this point was defined as fatty tissue (we found that this assumption yields distributions of fatty tissue very similar to well-established body models like the Virtual Population 3.0 [44]). This voxelized model guarantees a single label per voxel.

We performed a multi-domain surface segmentation of the 1 mm voxel model using the Computational Geometry Algorithms Library (CGAL, [114]). The output surface mesh of the segmentation generates a non-intersecting closed surface mesh for each tissue class where all neighboring tissues align perfectly (Fig. 3.21, Step 3), i.e., neighboring tissues share the exact same faces without creating empty regions or overlaps. However, the resulting surface meshes do not necessarily establish 2-manifold geometries. In the context of surface triangulations, this means that every edge of a mesh is used by exactly two faces. Physically, 0-manifold or 1-manifold features of a mesh correspond to geometric structures that become infinitely thin or small. Therefore, it is necessary to remove these invalid features from the surface mesh. For that purpose a method was implemented (using Matlab, The MathWorks, Natick, MA, USA) to repair any existing surface mesh error and thus prepare the surface meshes for usage in the EM field simulations. This pre-processing includes elimination of 0-manifold and 1-manifold features, removal of excessively small faces/structures and low-quality faces (i.e., very long and thin faces). In short, this surface mesh repair routine first deletes the faces that correspond to a mesh error. In general this deletion creates holes in one or more of the tissue surfaces. The routine then identifies possible face configurations to close these holes without causing new surface mesh errors or empty regions. The process is repeated until all surface errors are repaired. An important advantage of this approach over commonly used mesh repair tools is that all tissue

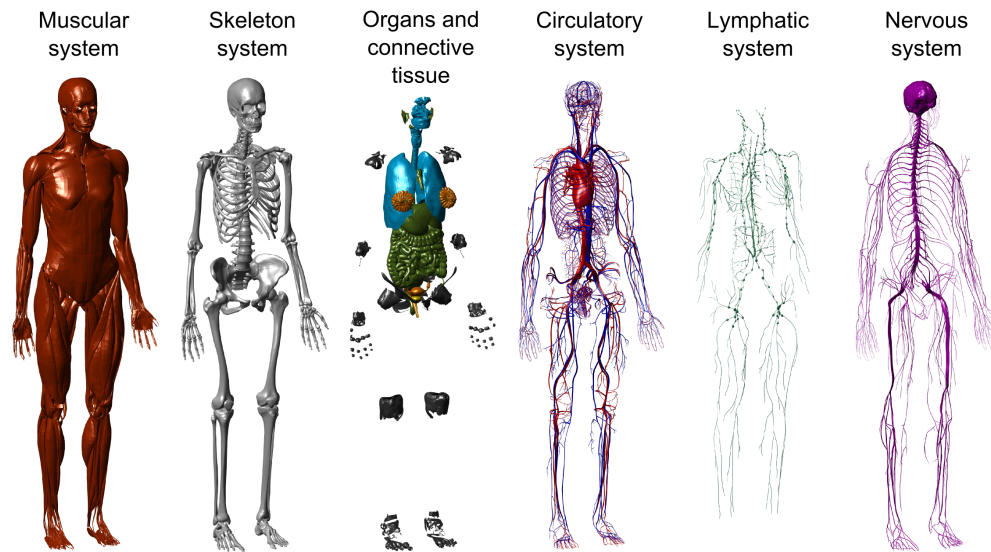


Figure 3.20: Visual depiction of the Zygote anatomical surface data that was used to generate the body model. The surface data was initially developed for visualization/teaching purposes and needed to be pre-processed in order to generate a non-intersecting watertight surface model for each tissue class.

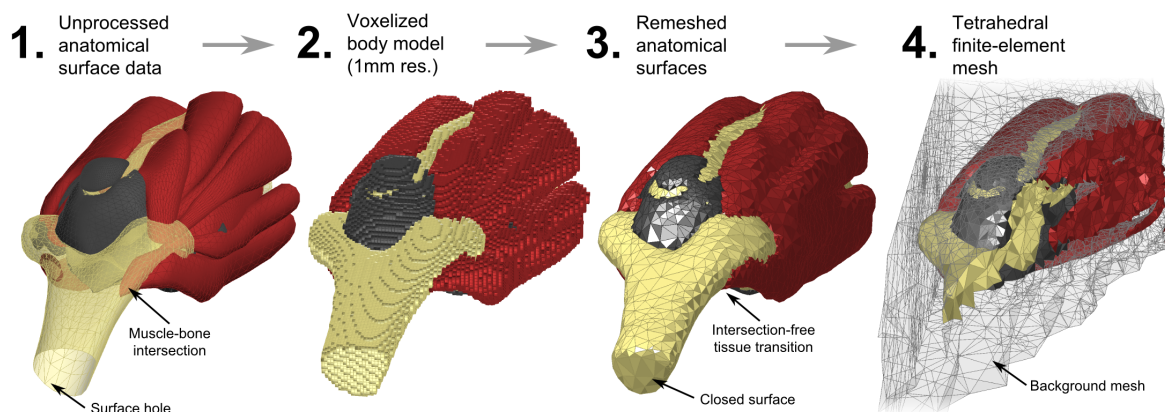


Figure 3.21: Processing pipeline of an exemplary body model region (elbow region, including muscle, bone, articular capsule): **1**) Unprocessed anatomical surface data (provided by Zygote), **2**) Discretized (voxel) body model with 1mm voxel size, **3**) Watertight intersection-free surfaces (obtained via segmentation of the voxel model), **4**) Cross-section of an exemplary tetrahedral mesh (computed using CGAL [114]), similar to the mesh generated by CST Microwave Studio for finite-element EM field simulations.

surfaces are processed simultaneously in order to ensure that a correction step that is applied to one tissue surface does not introduce intersections or errors in any neighboring tissue surface. Although the creation of the surface body model is computationally intensive (even starting with a commercial meshed model), it only has to be done once per body model. The different tissue classes were assigned electromagnetic properties (conductivity and permittivity) using the frequency-dependent Gabriel database [41]. Note that the permittivity increases dramatically as frequency becomes very low, and our simulations reflect this. The final surface body model is shown in Fig. 3.22. It can then be used in an EM field simulation environment (such as CST or Sim4Life) in order to generate a tetrahedral or hexahedral finite-element mesh for calculation of the EM fields (an exemplary tetrahedral finite element mesh is shown in Fig. 3.21, Step 4).

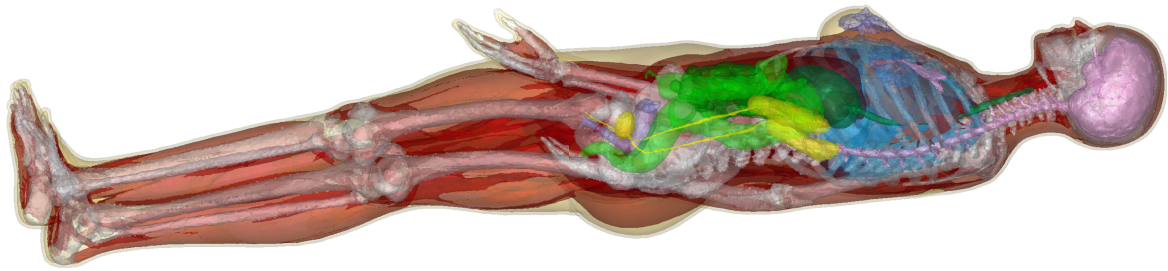


Figure 3.22: Surface-based whole body model used for the simulation of the electromagnetic fields.

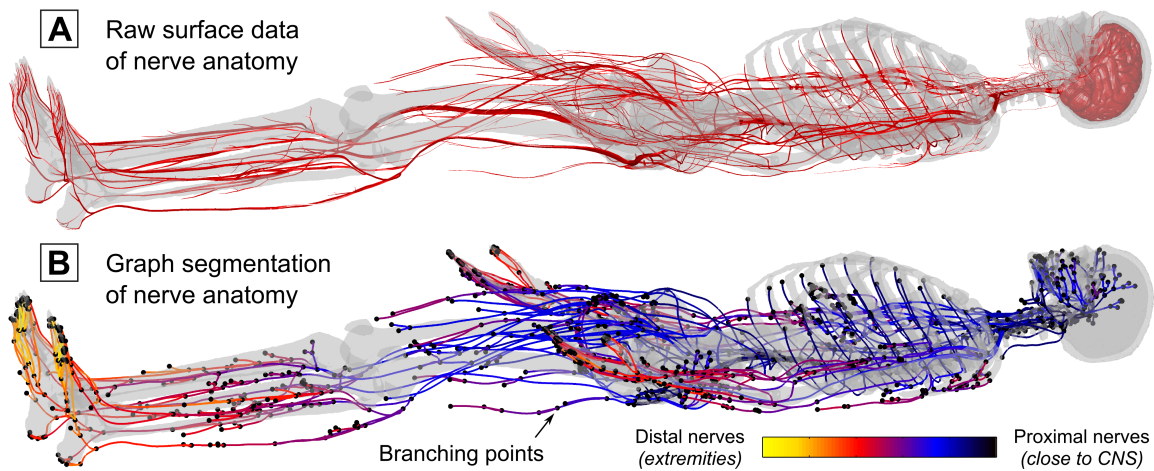


Figure 3.23: (A) Human nervous system model as surface data with skeletal system (transparent gray) for reference. (B) Extracted nerve centerlines color coded by distance from the CNS.

3.4.3 Nerve Atlas

The Zygote anatomical model was used, as opposed to more commonly used body models such as the Virtual Family [44] since the Zygote model includes a detailed atlas of the peripheral nerves. However, like the organ surface mesh data in the model, some preprocessing was necessary to use this nerve atlas information in conjunction with the PNS membrane dynamics model. Specifically, from the original Zygote nerve atlas (Fig. 3.23 A), we extracted paths of the peripheral nerve bundles as 3-D curves with labels at their three types of phylogenetic points; starting point, end-point, and any branching point as shown in Fig. 3.23. The starting point of the peripheral nerve fibers was the central nervous system (CNS), most frequently the spinal cord and the end-point was typically a distal extremity.

We define "nerve tracks" as individual nerve bundle segments between any of the phylogenetic points identified in the previous step. The model contains approximately 1600 nerve tracks. The nerve tracks between the phylogenetic points are represented in 3-D by centerline curves that follow the center of the surface mesh of each nerve track. This was achieved by first applying a so-called *geodesic distance* algorithm that computes the shortest path along the edges of the surface mesh that connects the two phylogenetic points. The resulting 3-D curve runs along the surface of the mesh (i.e., on the surface of the "nerve tube"). In order to obtain the nerve centerline from this (i.e., the curve running along the center of the "nerve tube"), we first voxelized the entire nerve tree at 0.1 mm resolution and computed the distance measure of this voxelized nerve tree.

The distance measure specifies, for each voxel, the distance to the nearest surface of the nerve tracks. Note that the distance measure is greatest for the center points of the nerve tube. The centerline curve was generated from these center points. Finally, a free-knots B-spline is fit to the centerline curve for smoothing and to avoid excessively high (unrealistic) curvatures of the nerve tracks. The final nerve atlas after this processing is shown in Fig. 3.23B, which has been color-coded by the number of branch points between the nerve track and the CNS.

3.4.4 Integrity of Body Model and Nerve Atlas

The complexity of the surface based body model and the nerve atlas requires a further processing step to ensure that the nerve fibers do not intersect with the bone surface or the outer hull of the body model. The method that is used for generation of the surface body model is based on a discretization (i.e., voxelization) of the Zygote anatomical data, followed by a resegmentation of the voxel model using closed triangular surfaces. As was described in Sec. 3.4.2 this is an effective way to generate a watertight manifold triangulation from arbitrary surface data (having intersections, holes, non-manifold geometries, etc.) while simultaneously simplifying the surface model to reduce the computation time of the EM field simulations (the level of simplification is controlled via the surface segmentation algorithm). This model simplification, however, may lead to intersections of some of the nerve fibers with the bones or the outer hull of the body model (causing nerves being located outside the body). Although these intersections are usually very mild (approx. 1 mm), the affected nerve tracks cannot be evaluated. In particular the interpolation of the electric field along nerve fibers that intersect bone or air regions leads to a sudden drop or peak of the electric field. This renders the nerve segment unrealistically sensitive, i.e., the PNS threshold would be under-estimated.

To remove these bone/air-nerve-intersections from the surface body model, a repair routine was developed that identifies and repairs these intersections. The different steps of the repair pipeline are illustrated in Fig. 3.24, that shows an exemplary intersection of a nerve segment with the bone surface. The repair pipeline is based on the following steps:

- Step 1:** The intersected surface is inflated by a value that corresponds to the minimum tolerated distance between the nerve fiber and the bone surface, in this case 2 mm. This means that whenever the distance between nerve fibers and the bone surface is less than 2 mm, this is considered an intersection.
- Step 2:** The points of the nerve path are projected onto the inflated surface, i.e., for each point of the 3-D path (blue), the closest point on the inflated surface is identified (red curve). The distance between the nerve path (blue) and the projected path (red) is a measure of the "intersection depth" (and thus a measure of the level of deformation that is required to repair the intersection).
- Step 3:** For the projected points the closest nodes of the bone surface are identified. Note that these nodes need to be shifted in order to remove the bone/air-nerve-intersections. A distance threshold is used to control the number of nodes that are associated with each projection point. A scattered interpolation is used to interpolate the "intersection depth" onto the surface nodes. Each node is moved by this value along the inverse node normal in an attempt to remove the intersection (note that by convention, node/face normals of triangular surfaces are pointing outwards).

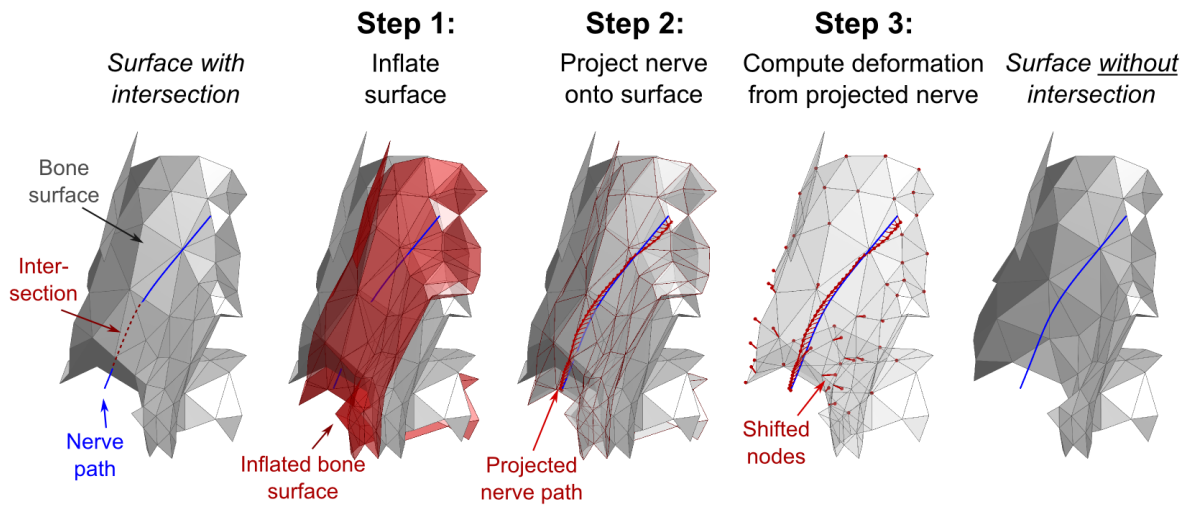


Figure 3.24: Processing pipeline to repair intersections of nerve fibers with the body model. *Step 1:* Inflate surface to create safety margin between nerve and body model (2 mm), *Step 2:* project nerve onto inflated surface to estimate "intersection depth", *Step 3:* use scattered interpolation to determine the shift of the surface nodes from the "intersection depth". The nodes are shifted along the inverse node normal to remove the intersection.

3.4.5 Nerve Membrane Model

The electric fields calculated in the body model were projected onto the nerve fiber path and integrated to obtain potential differences along the fibers. These spatially varying potentials V_{ext} were modulated by the driving waveform of the coil and fed into the circuit model with myelin and node of Ranvier parameters. The McIntyre-Richardson-Grill model (MRG) [79, 78] was used to simulate the response of the nerve to the voltage potentials induced along the fiber by the external fields. The MRG electrical nerve model is based on a double-cable representation of the myelinated axons (the inner cable models the axon, the outer cable models the myelin insulation sheath). Electrically speaking, these cables are connected in parallel, as shown in Fig. 3.25. The MRG model, unlike simpler models like the Hodgkin-Huxley Model [60, 40] or the SENN model [96, 95, 80], explicitly models action potential (AP) initiation. The effect of the local myelin insulation sheath on the excitability of the nerve is explicitly included, making this model more appropriate for simulation of PNS, since peripheral nerves are heavily myelinated. Since the myelin sheath insulates the axon, the nerve is most sensitive to the induced electric field at the locations of the nodes of Ranvier where the axon is in direct contact with the extra-cellular space. Each of the three nerve compartments (axon, myelin, and node of Ranvier) is modeled by RC-circuits with capacitance and resistance properties specific to each compartment (for the exact electrical parameters, see McIntyre et al. [79]). In order to be able to simulate action potential initiation, the RC-circuit model of the nodes of Ranvier compartments includes non-linear terms, implemented as voltage-dependent resistances that model the sodium and potassium ion channels. This means that once the nerve fiber is strongly depolarized, the membrane becomes permeable for sodium and potassium ions (in the electric model this is represented as a small resistance), which leads to a large current flowing through the membrane and thus to an action potential. The different RC-circuits are connected via conductances that specify the transaxial and axial conductivity of the nerve. This allows modeling of the propagation of action potentials along the nerve fiber at realistic conduction velocities (approximately 25 m/s to more than 100 m/s, depending on the axon diameter).

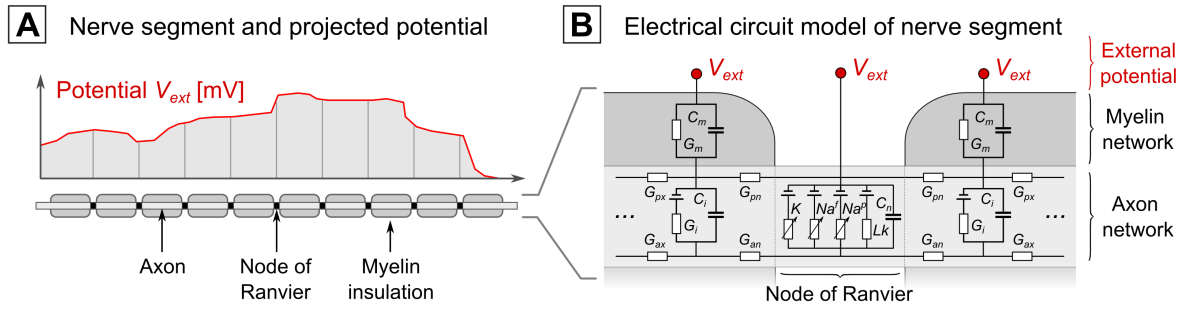


Figure 3.25: (A) Schematic of the discretization of the potential V_{ext} along the nerve segment with respect to the nodes of Ranvier. V_{ext} is determined from integrating the induced electric field calculated in Step 2. Node spacing is assigned based on estimated fiber diameter. (B) Electrical equivalent circuit for the MRG nerve model on each side of a node of Ranvier. Action potentials are created when the transmembrane potential change becomes greater than approximately 20 mV.

The MRG electrical circuit is mathematically represented as a set of coupled differential equations. The input to the model is the external electric potential changes V_{ext} imposed by the external coil. In this work, we compute these potentials using electromagnetic simulation and by interpolation of the resulting electric fields along the nerve fiber paths. The output of the model is the resulting transmembrane potential change over time at each compartment of the nerve fiber model. These transmembrane potential changes are analyzed to decide whether or not an action potential has been initiated. Each track of our nerve atlas was tagged with information about local nerve fiber diameters that we obtained from the literature [36]. These fiber diameters were used to feed the correct parameters into the MRG nerve membrane model. For example, in Table 1 of their paper, McIntyre et al. [79] provide the model parameters of the MRG model which vary with axon diameter for 9 different diameters (ranging from 5.7 μm to 16.0 μm). This includes the thickness of the myelin insulation sheath that increases with fiber diameter. Stated conversely, the conductance of the myelin compartment decreases with fiber diameter. The spacing of the nodes of Ranvier also increases with the fiber diameter, from 0.5 mm for a 5.7 μm fiber to 1.5 mm for a 16.0 μm fiber. Together, the increase in both the myelin sheath thickness and node of Ranvier spacing with nerve diameter results in much higher excitability for large diameter fibers compared to smaller ones. Additionally McIntyre et al. provide fixed parameters (non-varying with diameter) in Table 2 of their paper [79]. To provide a full set of membrane model parameters for each nerve track in our nerve tree, we assigned nerve diameters based on the type of nerve fibers present in the nerve track. If any motor nerve fibers are present, we assumed large fiber diameters of 16.0 μm . For nerve tracks that only consist of sensory nerves (e.g., the digital nerve branches in the fingers, the sural nerve in the calf, or the posterior cutaneous nerve in the shoulder), we assigned smaller nerve fiber diameters (10.0 μm). Autonomous nerve bundles (e.g., those controlling the digestive or cardiovascular system) usually contain very small fibers (in the order of 2 μm diameter). Note that we are still refining the nerve fiber properties of our nerve atlas, as more detailed information becomes available (e.g., via studies of nerve conduction velocities that can be correlated with the fiber diameter).

3.4.6 Generation of PNS Threshold Curves

The PNS threshold is defined as the smallest external field modulation strength that initiates an action potential. The PNS threshold depends on the frequency of the external electromagnetic

excitation, the coil geometry, and the subject's anatomy, which modulates both the strength of the electric field and its orientation with respect to the nerve fiber. To compute the PNS threshold curve, we modulated the spatial map of electric potentials (output of the electromagnetic simulation) interpolated along the nerve fiber by a sinusoidal waveform of different frequencies ramping the amplitude up for each frequency. We recorded the amplitude ΔB_{\min} that initiated an AP. This titration process is depicted in Fig. 4.16. After finding the threshold that initiates an AP for a given coil and body position, the PNS threshold is plotted as a function of the excitation frequency. Calculated PNS threshold curves are shown in Figs. 4.17 and 4.18.

Processing the entire nerve tree at once is infeasible for a number of reasons. A single run of the MRG model requires solving a large set of coupled differential equations and is computationally expensive (simulation of the MRG model was performed within the NEURON environment [59]). The computational complexity increases with the total length of nerves in the model (i.e., with the number of nodes of Ranvier). For the leg coil, approximately 8.6 meters of nerve fibers need to be analyzed (resulting in approximately 5700 nodes of Ranvier and 63000 electrical compartments). For the arm simulation, there are 10.3 meters of nerve fibers resulting in 6900 nodes of Ranvier and 75900 electrical compartments. When solving the underlying differential equation, we used a time step of $0.5 \mu\text{s}$ for a 1 kHz coil current waveform and decreased this value linearly for higher frequencies (i.e., independently from the frequency every bipolar pulse is resolved by 2000 time points). Thus, a smaller time step was used than other nerve model simulations. For example McIntyre et al. suggested that (using a block pulse to stimulate the model) a time step of 1 to $5 \mu\text{s}$ would accurately solve the differential equation of the MRG neurodynamic model. Our analysis of the convergence of the solution to the differential equations underlying the MRG neurodynamic model suggested a smaller time-step was needed. We do not know if this difference was derived from a more conservative convergence criterion or reflects a more complicated temporal dynamics within the nerve model for our situation. The stimulus consisted of 15 sinusoidal periods, resulting in durations of 32.6 ms to 1.5 ms for coil current frequencies of 0.46 kHz to 10.3 kHz. Note that based on these parameters, calculation of PNS threshold curves using the entire nerve tree would require at least a week of computation time (assuming that no parallelization is used). Processing the entire nerve tree also results in a high computational overhead. For example, if a nerve track branches into a major track and a minor track, the part of the nerve prior to the branching point will be simulated twice: once as being part of the major track and once as being part of the minor track (unless the nerve track is divided appropriately). To increase computational efficiency, we divided the nerve tree into smaller sub-segments without any branches, where each sub-segment has a reasonable length (ideally less than 100 nodes of Ranvier). We refer in this work to these sub-segments of the nerve tree as *nerve segments*. Dividing the nerve tree into smaller nerve segments also means dividing the underlying differential equation, which may cause numerical instabilities and artefacts at the boundaries of the nerve segments. Therefore, we implemented methods to identify the locations of the nerve tree, where dividing the nerve fiber into multiple nerve segments only has a mild effect on the model accuracy and, therefore, on the resulting PNS thresholds. Rattay and others [93, 2] showed that the second spatial derivative of the extracellular potential along the fiber can be considered the main determinant (also referred to as "activation function") of nerve stimulation. This metric is often used to guide the development of electromagnetic coils for neuro-stimulation or neuro-modulation devices [23]. As a consequence, an electric potential pattern that varies only linear along the fiber does not generate an activation function (no stimulation of the nerve). Instead the electric potential leads to a constant current flow along the fiber without any current flowing through the membrane. This means that the external

electric field is not effective at depolarizing the membrane and the nerve segment will not initiate an action potential in this region. Thus these regions can be safely ignored when searching for the PNS threshold. We found that dividing the nerve tree into nerve segments at these locations only has negligible effects on the excitability of the nerves and, therefore, on the AP thresholds. After defining the nerve segments (we simplified the nerve model to 304 and 359 nerve segments for the leg and arm stimulations, respectively) we further reduced computation time by solving the MRG model only for those segments where the electric potential leads to a substantial flow of current through the membrane (possibly leading to an AP). Note that the definition of individual nerve segments also allows for a heavy computational parallelization since every nerve segment can be excited and simulated independently.

3.4.7 Preliminary Sensitivity Analysis

In order to estimate the sensitivity of the PNS threshold curves to the nerve atlas (i.e., to the path of the nerve segments relative to other tissue structures), we have conducted a preliminary sensitivity analysis. The nerve segments are particularly sensitive to spatial deformations that alter the curvature of the segments (e.g., only applying shifts to a nerve segment within a linearly varying electric potential does not influence the stimulation threshold). In order to implement a spatial uncertainty of the nerve segments path, we defined a tube of a certain radius (2 mm and 4 mm) following the nerve segment and allowed the nerve to traverse the tube along a flexible path. This is achieved by using a 3-D Gaussian deformation field: for each spatial dimension we randomly distributed 10 three-dimensional Gaussians within the bounding box of the nerve segments (overall 30 Gaussians). The standard deviation of the Gaussians (2 cm in this example) determines the smoothness of the deformation; the function value of the sum of Gaussians determines the local deformation strength along the different axes. The weighting of the 30 Gaussians was chosen randomly such that 1) the deformed nerve segment remains within the tube (this limits the maximum local deformation), and 2) the segment does not intersect the bone tissue or outer hull of the body (for example for superficial nerve segments). We generated 20 deformed nerve segments for tube radii of 2 mm and 4 mm and computed PNS threshold curves for each segment. We then use the standard deviation of the PNS thresholds over the 20 segments as means of the sensitivity of the predicted threshold curves to the path of the nerve segment.

3.4.8 Validation against Experimentally Measured Thresholds

We compared our simulated PNS threshold curves with those measured experimentally using leg and arm solenoid coils applied to healthy volunteers [101]. The two coils were simulated based on their described dimensions and geometry using CST's frequency domain solver which uses a low-frequency approximation of Maxwell's equations. The coils were modeled using infinitely thin, perfect electrical conductor current paths. Boundaries were modeled as a box of perfect electrical conductors (PEC) enclosing the entire simulation domain 50 cm away from the tissue model or the coil (low-frequency FEM solvers usually require PEC boundary constraints). We found that this PEC boundary spacing is reasonable for these two simulation setups and that increasing the boundary spacing to 500 cm altered the tissue electric field maps by only about 1-2%. The experimental comparison data was taken in an open setting (approximately "free space"). But we note that MRI gradients are used within the more complex conducting environment of the magnet and its cryostat, which might need to be taken into account for MRI gradient studies.

The simulated leg coil consisted of 54 turns in a single layer (length of 24 cm, diameter of 19 cm); the arm coil consisted of 72 turns in two layers (length of 17 cm, diameter of 11 cm). The body model was placed inside the coils to mimic the experimental setup as closely as possible, although only the photo in the published paper provided guiding information. In the simulations, only the leg (until 30 cm above the hip joint) and the arm (including the shoulder joint) were simulated as the effects of the coils are limited to these regions.

3.4.9 Sinusoidal vs. Trapezoidal Waveforms

MRI gradient encoding most often uses trapezoidal waveforms where electric field generation is confined to well-defined pulses during the ramps of the trapezoid. It is well documented that for a given peak B -field strength, the trapezoidal waveform has increased PNS thresholds compared to a sinusoidal waveform [56, 62]. Furthermore, it has been observed that the PNS thresholds increase linearly with the pulse duration (ramp rise-time) [18]. In order to determine if our model captures these two observations, we applied both sinusoidal and trapezoidal waveforms using ramp rise times relevant to MRI (from 0.1 to 1.0 ms). The PNS thresholds (applied solenoid B -field amplitude) as a function of pulse duration were assessed in terms of linearity with a linear fit and in terms of the chronaxie times (i.e., the slope of the linear fit).

3.5 | PNS Simulations of Whole-Body Gradient Coils

In the previous section a framework was developed for the prediction of PNS thresholds based on arbitrary coil geometries. The first evaluation of the framework was done based on leg/arm solenoid coils, i.e., based on rather simple coil geometries. In this section, preliminary results are shown, that illustrate the feasibility of the proposed PNS simulation framework to simulate actively shielded whole-body gradient coils that have a substantially more complex wire pattern (compared to solenoid coils). The simulated MRI gradient coil geometries were provided by a major MR system manufacturer and are in clinical use. The gradient coil performance is characterized by a maximum gradient strength of $G_{\max} = 40 \text{ mT/m}$ and a maximum slew rate of $S_{\max} = 200 \text{ T/m/s}$.

3.5.1 Electromagnetic Field Simulation

For simulation of EM fields imposed by the MR gradient coils, a surface-based body model consisting of overall 19 different tissue classes was used:

- | | | | |
|-------------------|---------------------|-------------------|-----------|
| - bladder | - connective tissue | - lung | - spleen |
| - body fluid | - fatty tissue | - muscular tissue | - stomach |
| - bone | - glandular tissue | - skin | - trachea |
| - brain | - heart | - small intestine | - uterus |
| - large intestine | - liver | - spinal cord | |

The body model was placed head-centered in the gradient coils and was cropped at about $z = 75 \text{ cm}$ (i.e., the legs at about 20 cm above the knee joints were excluded) to reduce the computation time. The EM field simulations were based on a hexahedral rather than a tetrahedral finite-element solver, Sim4Life (ZMT Zurich MedTech AG, Zurich, Switzerland). Although a tetrahedral mesh provides superior performance in terms of geometric accuracy and convergence of the EM solver, the generation of the mesh itself becomes increasingly complex for larger surface-based models. In particular, the intersection check of the different tissue classes that is routinely performed by most of the tetrahedral finite-element simulation platforms becomes computationally very costly (runtime increases exponentially with the number of faces of the body model and the number of tissue classes). This can be overcome by using a hexahedral finite-element mesh which can be generated very efficiently from the surface-based models used in this work.

For the mesh, an isotropic resolution (corresponding to the size of the hexahedral elements) of $1 \times 1 \times 1 \text{ mm}^3$ was used, resulting in about 130 million mesh cells. The EM fields were simulated using a fast magneto-quasistatic (MQS) solver (see also Sec. 2.3.3.3). In this low-frequency approximation, the electric fields are decoupled from the magnetic fields by first computing the magneto-static vector potential denoted by $\mathbf{A}(\mathbf{r})$. The vector potential is solved such that the resulting magnetic field satisfies $\mathbf{B}(\mathbf{r}) = \nabla \times \mathbf{A}(\mathbf{r})$, with the magnetic field being computed using the Bio-Savart law, namely

$$\mathbf{B}(\mathbf{r}) = \frac{\mu_0}{4\pi} \int_C \frac{d\mathbf{l} \times \mathbf{r}'}{|\mathbf{r}'|^3} . \quad (3.97)$$

In the above equation C denotes the path of current flow (i.e, the path of the simulated wire pattern, Fig. 3.26), and $d\mathbf{l}$ denotes a differential wire element. From the vector potential $\mathbf{A}(\mathbf{r})$,

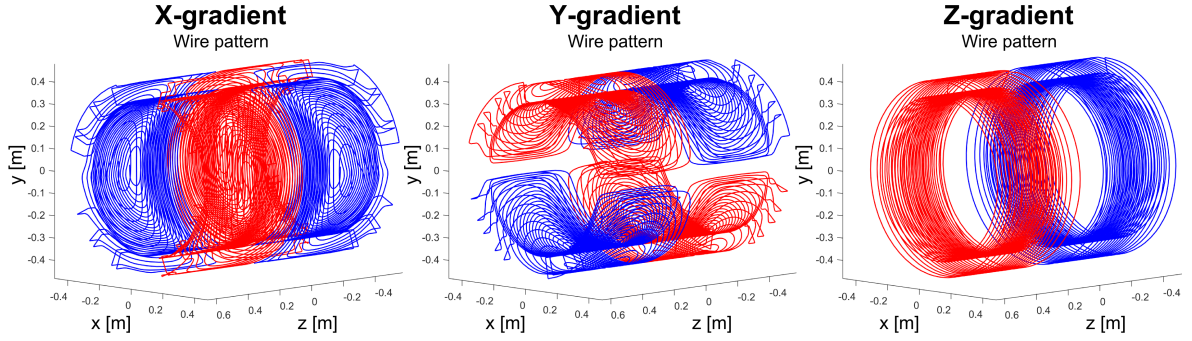


Figure 3.26: Wire patterns of the three actively-shielded MRI gradient coils simulated in this work. The coils can create a maximum gradient strength of 40 mT/m at a maximum slew rate of 200 T/m/s.

the electric fields $\mathbf{E}(\mathbf{r})$ are solved using the low-frequency approximation of Maxwell's equations, given by

$$\nabla \cdot \sigma(\mathbf{r}) \nabla \phi(\mathbf{r}) = -i\omega \nabla \cdot [\sigma(\mathbf{r}) \mathbf{A}(\mathbf{r})] \quad (3.98)$$

where $\phi(\mathbf{r})$ denotes the scalar electric potential, $\sigma(\mathbf{r})$ denotes the spatially varying conductivity of the body model, and ω denotes the simulated angular frequency. It was shown before that this approximation holds ([12, 10]) as displacement currents are negligible at frequencies in the low kilohertz range. Simulation of the electromagnetic fields was based on an excitation frequency of 1 kHz. The electric fields are computed only in conductive media (i.e., excluding the air) meaning that no boundary constraint needs to be defined (as opposed to the tetrahedral mesh simulations using CST where the magnetic and electric fields were not decoupled using a magneto-quasistatic approximation; in this case PEC boundaries were employed).

3.5.2 Experimental Data and PNS Simulations

During the federal approval process of the simulated MR gradient coils, healthy human subject experiments have been conducted in order to assess the capability of the coils to generate PNS [56]. These studies have been approved by the Ethics Board and supervised by a physician at all times. The stimulation experiments have been conducted based on 65 healthy subjects (34 male, 31 female, age 27.7 ± 6.5). Two types of bipolar gradient waveforms were assessed: trapezoidal and sinusoidal waves. The waveforms are characterized by the pulse duration τ , plateau time (flat top) δ , and the gradient modulation strength ΔG (taken from zero to the maximum gradient strength of the bipolar waveform), see Fig. 4.20. Note that the modulation strength of the magnetic field (ΔB) and the modulation of gradient field (ΔG) are related by a scaling factor (which is the gradient efficiency in [mT/m] per unit magnetic field in [mT]), but otherwise interchangeable. The stimulation experiments were performed for pulse durations τ varying between 0.2 ms and 1.2 ms, using a constant plateau (flat top) time of $\delta = 0.5$ ms. The applied trapezoidal and sinusoidal gradient waveforms consisted of 128 bipolar pulses, resulting in an overall train length of 89.6 ms (for pulse durations of 0.2 ms) up to 217.6 ms (for pulse durations of 1.2 ms). Additionally to simulating the X, Y, and Z-gradient coils separately, combinations of multiple gradient axes, namely "X-Y" and "X-Y+Z", were assessed. The main motivation for this was, that using the X and Z-gradient coils, only a few of the subjects experienced very mild PNS sensations for the stimulation pulses that were achievable using the gradient system. Note that for the combination of two gradient axes, both the available gradient magnitude and slew

rate performance increase by a factor of $\sqrt{2}$; for a combination of all three gradient axes, the performance increases by a factor of $\sqrt{3}$.

The process for simulation of the PNS threshold curves is similar to the titration process performed for the leg/arm solenoid coils. In the PNS simulations based on gradient coils, the titration process (i.e., iteratively increasing the field modulation strength until PNS is observed) was performed with respect to the smallest gradient modulation strength ΔG_{\min} that created PNS. Because of computational limitations, the simulations were performed using 16 bipolar pulses (instead of 128 bipolar pulses used in the experiments), and scaling the PNS thresholds to 128 bipolar pulses. The scaling factor was derived from the experimental data that investigated the effect of the number of bipolar pulses on the PNS threshold, namely that $\Delta G_{\min} (128 \text{ pulses}) \approx 93.53\% \Delta G_{\min} (16 \text{ pulses})$ [56].

4

Results

4.1 | Design of Optimal Gradient Waveforms

The *Gradient Basis Function* method was implemented in Matlab R2013a (The MathWorks, Natick, MA, USA), using the Optimization Toolbox (in particular the non-linear constraint optimizer, `fmincon`) and a number of openly available solvers to perform the minimization of the objective function. The entire framework, including methods for two- and three-dimensional gradient waveform design and visualization is available from the author via request.

4.1.1 Design of a 2-D Spiral Trajectory

A first example of the resulting gradient waveforms is depicted in Fig. 4.1: in this case, a simple uniform spiral trajectory was designed using four control points per spiral revolution. The gradient system constraints were set to $G_{\max} = 25$ mT for the magnitude and $S_{\max} = 150$ T/m/s for the slew rate constraint (a detailed description of the optimization solvers used in this work is given in the next paragraph). Figure 4.1 shows both the k -space trajectory (*left*) and the associated gradient waveforms (*right*) in k_x and k_y . Additionally, every odd time interval between two subsequent control points is highlighted in grey. It can be observed that the gradient waveform in between two control points and in single gradient dimension corresponds to one of the four introduced gradient basis functions. The parameters of the bases (namely the length and strength of each linear gradient segment) are directly related to the gradient strengths at the control points. These are optimized by the design framework to globally accelerate the trajectory, thus

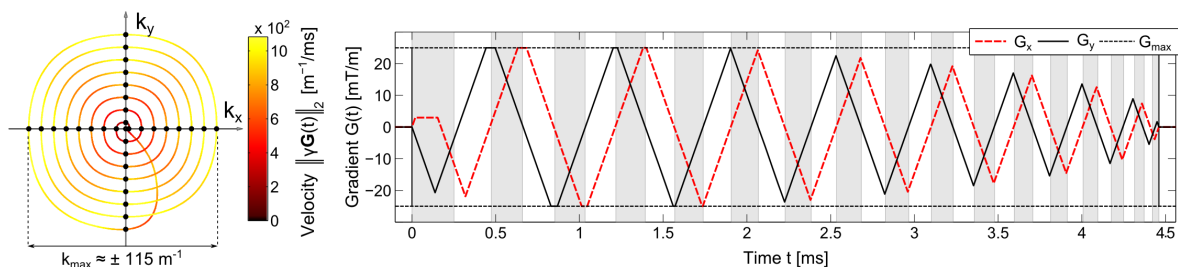


Figure 4.1: Simple spiral k -space trajectory (*left*) and associated gradient waveforms (*right*) designed using the *Gradient Basis Function* method. The time intervals in between two control points are highlighted in grey one every other. Note that the gradient waveforms in each dimension are assembled by concatenating one basis function per time interval and gradient axis.

Solver	General Performance				Numerical Stability			
	(A)	(B)	(C)	(D)	(E)	(F)	(G)	
	Dur. Improv. to OC ¹ [%]	Dur. Optimality [%]	Iterations	Runtime [s]	Control Point Error [m ⁻¹]	G _{max} Error [mT/m]	S _{max} Error [T/m/s]	
Optimal Control method								
OC ¹	-	0.0	-	16.1 ± 1.8	1.4 · 10 ⁻¹ ± 1.6 · 10 ⁻¹	0.6 ± 2.5	4922 ± 4665	
OC ²	-	0.0	-	1378.6 ± 122.6	5.6 · 10 ⁻³ ± 1.5 · 10 ⁻³	0.01 ± 0.03	1923 ± 6763	
Gradient Basis Function method								
IP ¹	8.4 ± 1.8	1.2	44 ± 32	3.5 ± 1.7	5.5 · 10 ⁻¹² ± 3.7 · 10 ⁻¹¹	0.0	0.0	
IP ²	8.5 ± 1.7	1.2	41 ± 31	2.4 ± 1.0	6.5 · 10 ⁻¹² ± 3.4 · 10 ⁻¹¹	0.0	0.0	
SPG	9.0 ± 1.7	7.6	238 ± 179	4.7 ± 3.2	1.7 · 10 ⁻¹² ± 6.7 · 10 ⁻¹³	0.0	0.0	
LNL	9.2 ± 1.8	89.8	204 ± 213	12.2 ± 13.4	1.8 · 10 ⁻¹² ± 7.1 · 10 ⁻¹³	0.0	0.0	

Table 4.1: Comprehensive Evaluation Results: For 300 testing datasets the table summarizes the results for the overall six methods and setups. For each method the general performance is evaluated based on the duration benefit according to the *Optimal Control* method, the rate at which the respective method achieved the best solution throughout all methods, the number of iterations required for convergence (does not apply to the *Optimal Control* method), and the average runtime. Furthermore, the numerical stability is quantified based on the accuracy in traversing the control points as well as the conformity with the gradient magnitude and slew rate constraints.

minimizing the duration of the gradient waveform. The fact that the trajectory consists of piece-wise quadratic trajectory segments (due to the use of piece-wise linear gradient segments) leads to a shape of the spiral that deviates from a conventional spiral. In particular, note that slight edges are introduced (primarily at the center of k -space). These mild deformations, however, allow the control points of the spiral to be traversed significantly faster compared to a conventional spiral.

4.1.2 Comprehensive Evaluation using Random Trajectories

The performance of the proposed gradient design method was assessed using k -space trajectories computed from 300 sets of randomly distributed control points ($N = 40$) in two-dimensional k -space. For each set, time-optimal gradient waveforms were computed, firstly, using the *Optimal Control* method proposed by Lustig et al. [71] using its updated version [120] and, secondly, using the *Gradient Basis Function* method. The control points were distributed within $\mathbf{k}^{(q)} \in [-k_{max}, +k_{max}]^2$ with $k_{max} = 150 \text{ m}^{-1}$, resulting in k -space trajectories of approximately 10 ms length (using $G_{max} = 25 \text{ mT}$, $S_{max} = 150 \text{ T/m/s}$).

For the *Optimal Control* method, temporal sampling times of $\Delta t = 2 \cdot 10^{-3} \text{ ms}$ (in the following denoted as OC¹) and $\Delta t = 2 \cdot 10^{-4} \text{ ms}$ (denoted as OC²) were used. The objective function of the *Gradient Basis Function* method (see Eq. 3.28) was minimized using a variety of different constrained optimization algorithms, including convex and non-convex solvers, linear and non-

linear solvers and methods utilizing the analytic Jacobian and Hessian of the objective function. The solvers showing the most promising convergence characteristics were:

IP¹ the Matlab-intern *Interior-Point* solver [14] utilizing the analytic Jacobian only,

IP² the same *Interior-Point* solver utilizing both the Jacobian and Hessian,

SPG a *Spectral Projected Gradient* method¹ [5, 105], utilizing the analytic Jacobian,

LNL a local non-linear solver from the *SolvOpt*-package², using the analytic Jacobian.

Global optimization methods (such as *Simulated Annealing* approaches) have been abandoned relatively early due to their disproportionately high computational expense and bad convergence properties for this particular problem type. Each optimization was initialized with $\mathbf{G}^{(a)} = \mathbf{0}$ for all control points, using fixed gradients $\mathbf{G}^{(1)} = \mathbf{G}^{(N)} = \mathbf{0} = \text{const.}$ for the first and last control point. The gradient strength vectors in all control points have been optimized without defining directional constraints.

A performance summary of the *Optimal Control* methods (OC¹ and OC²) and the *Gradient Basis Function* method using the four different solvers is given in Tab. 4.1. For each method the average gain in terms of the achieved duration compared to the *Optimal Control* method (column A), the rate at which the respective method achieved the shortest overall duration (column B), and the average number of iterations and runtime (column C and D) are shown. All results obtained using the *Gradient Basis Function* method (independently of the used minimization solver) achieved a significant gain over the *Optimal Control* method in terms of the duration of the gradient waveforms (at least 8.4%, IP¹) while reducing the computation time by at least 25% (IP¹ to OC¹) up to factors of up to 570 (IP² to OC²). The performance of the different optimization solvers greatly varies in terms of the resulting duration and the computation time. Taking advantage of both the analytic Hessian and Jacobian matrices in the Interior-Point solver (IP²) compared to only using the Jacobian (IP¹) only yields a small benefit in terms of the achieved duration (0.1% gain) but reduces the computational runtime by 30% (from 3.5 s to 2.4 s). Both Interior-Point methods, however, failed to converge to the global minimum in about 97.6% of the test cases. An improved performance was achieved using the Spectral Projection Gradient method (SPG) that generated the overall shortest gradient waveforms in 7.6% of all test cases. The most promising solver, however, was the Local Non-Linear method (LNL) that produced optimal results in 89.8% of all test cases, at the cost of a significant increase in computation time (12.2 s compared to 2.4 s - 4.7 s for the other solvers). In average, the gradient waveforms obtained by the LNL method were 9.2% shorter than the ones computed using the *Optimal Control* method. However, this evaluation reveals that – despite the benign invex objective function that is free of local minima and despite the applied smoothing of the derivatives – any minimization solver may fail to find the *exact* optimum if excessively complicated sets of control points are used.

4.1.3 Numerical Stability I: Control Point Traversal

The *Optimal Control* method and the *Gradient Basis Function* method were evaluated in terms of numerical stability: firstly, in terms of accurately traversing the set of control points and, secondly, in terms of the conformity of the designed gradient waveforms with the gradient

¹www.cs.ubc.ca/~schmidtm/Software/minConf.html

²www.uni-graz.at/imawww/kuntsevich/solvopt/

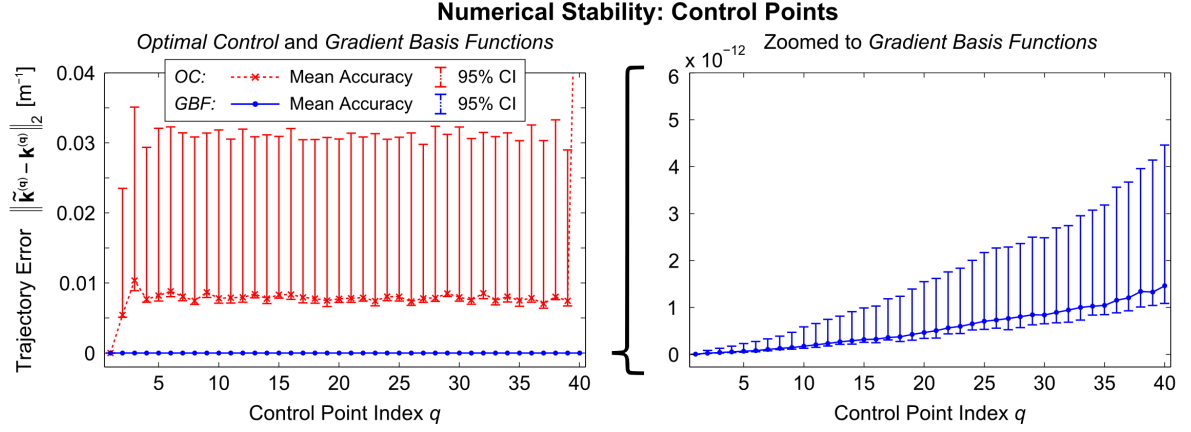


Figure 4.2: Accuracy of Control Point Traversal: for both the *Optimal Control* method (left) and *Gradient Basis Function* method (right), the accuracy of the traversal of the anticipated control points within the random datasets is shown. The accuracy is defined as the Euclidean distance $\epsilon^{(q)}$ of the closest point on the trajectory $\mathbf{k}(t)$ to the anticipated control point $\mathbf{k}^{(q)}$. For each control point $\mathbf{k}^{(q)}$, $q = 1, \dots, 40$, the trimmed mean (excl. 5% outliers) and the 95% confidence interval over all datasets are shown.

magnitude and slew rate constraints. For each of the control points $\mathbf{k}^{(1)}, \dots, \mathbf{k}^{(N)}$, the time points $0 \leq \hat{t}^{(1)} \leq \hat{t}^{(2)} \leq \dots \leq \hat{t}^{(N)} \leq T$ were determined at which the trajectory gets closest to the anticipated control point:

$$\hat{t}^{(q)} := \arg \min_{t \in [\hat{t}^{(q-1)}, T]} \left(\|\mathbf{k}(t) - \mathbf{k}^{(q)}\|_2 := \epsilon^{(q)} \right). \quad (4.1)$$

The minimal distance $\epsilon^{(q)}$ is taken as a measure of accuracy for the traversal of the control points. For the *Gradient Basis Function* method, the analytic gradient waveforms obtained using Eq. 3.29 were used in conjunction with a linear interpolation scheme to solve Eq. 4.1. Note that due to the piece-wise linear gradient waveforms, a linear interpolation of the gradient waveform results in accurate samples $\mathbf{G}(t)$ for arbitrary time points t . For the *Optimal Control* method, a spline interpolation of the sampled k -space trajectory $\mathbf{k}(t)$ was used. To avoid that the spline interpolation itself (which was used to compute the path constraint $\mathbf{k}(a)$, $a \in [0, a_{\max}]$) introduces errors with respect to the control point traversal, the accuracy of this interpolation scheme was evaluated. The path constraint traverses the control points with an effective error of zero ($\epsilon^{(q)}$ less than the machine epsilon).

All sets of randomly placed control points along with the resulting k -space trajectories were assessed. Figure 4.2 illustrates the error performance of both the *Optimal Control* method (left) and the *Gradient Basis Function* method (left and right): for each control point index $\mathbf{k}^{(1)}, \dots, \mathbf{k}^{(N)}$, $q = 1, \dots, 40$, the trimmed mean of the achieved control point accuracy (removing 1% outliers) as well as the 95% confidence interval over all datasets are shown. Additionally the mean value and standard deviation of the control point error are given in Tab. 4.1, column E. The k -space trajectories obtained using the *Optimal Control* method exhibit a rather constant error over all control points. Apparently, the trajectory accumulates errors – particularly in regions where the path constraint possesses a high curvature – in different directions. In most cases, these errors remain acceptable due to cancellation. However, significant outliers occurred on a regular basis: the average of the highest 1% error values is given by $0.27 \pm 0.18 \text{ m}^{-1}$, with an overall maximum error of 0.93 m^{-1} . The deviation of the k -space trajectory from the

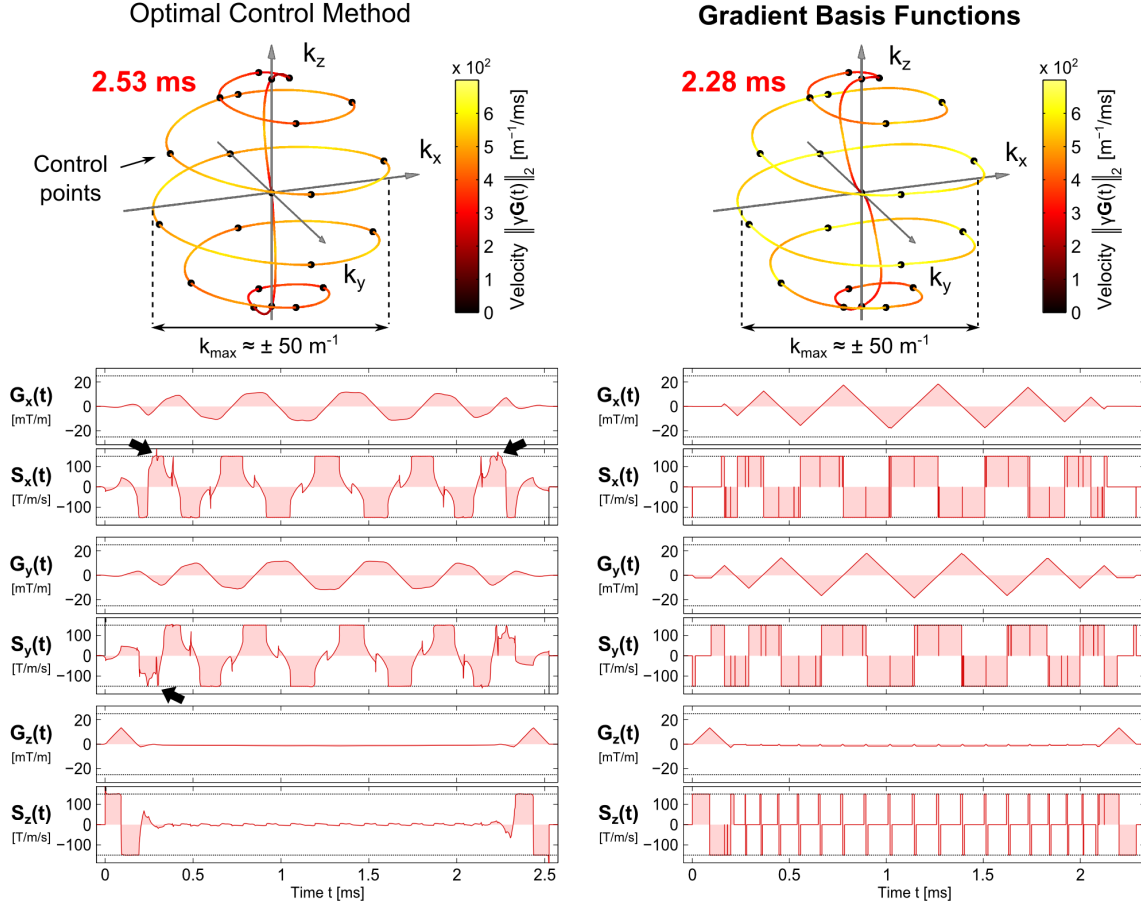


Figure 4.3: Concentric-Shells trajectories in 3-D k -space as well as gradient and slew rate waveforms design by the *Optimal Control* method (left) and the *Gradient Basis Function* method (right). The gradient waveforms obtained using *Optimal Control* are impaired by slew rate oscillations that cause violations of the respective constraint (black arrows). The *Gradient Basis Function* method is free of significant numerical instabilities.

anticipated control points can be reduced by using a smaller time step when solving the differential equation underlying the *Optimal Control* method. In the evaluation, reducing the time step from $\Delta t = 2 \cdot 10^{-3}$ ms (OC^1) to $\Delta t = 2 \cdot 10^{-4}$ ms (OC^2) improved the control point accuracy by roughly two orders of magnitude, however, at the cost of an excessive increase in computation time (factor of approx. 85).

In contrast, the *Gradient Basis Function* method accumulates error in a more systematic manner, almost increasing linearly with the index q of the control point. Due to the semi-analytic objective function and the semi-analytic representation of the gradient waveforms, the accumulated error is insignificant: in comparison with the *Optimal Control* method, the error induced by the *Gradient Basis Function* method is reduced by ten orders of magnitude, with an overall maximum error of $8.41 \cdot 10^{-10}$ m^{-1} .

4.1.4 Numerical Stability II: Gradient Constraints

A second aspect of the numerical accuracy of the proposed method, namely the strict compliance of the generated gradient waveforms with the gradient magnitude (G_{\max}) and slew rate (S_{\max}) constraints, was assessed. The gradient waveforms obtained using the *Optimal Control* method

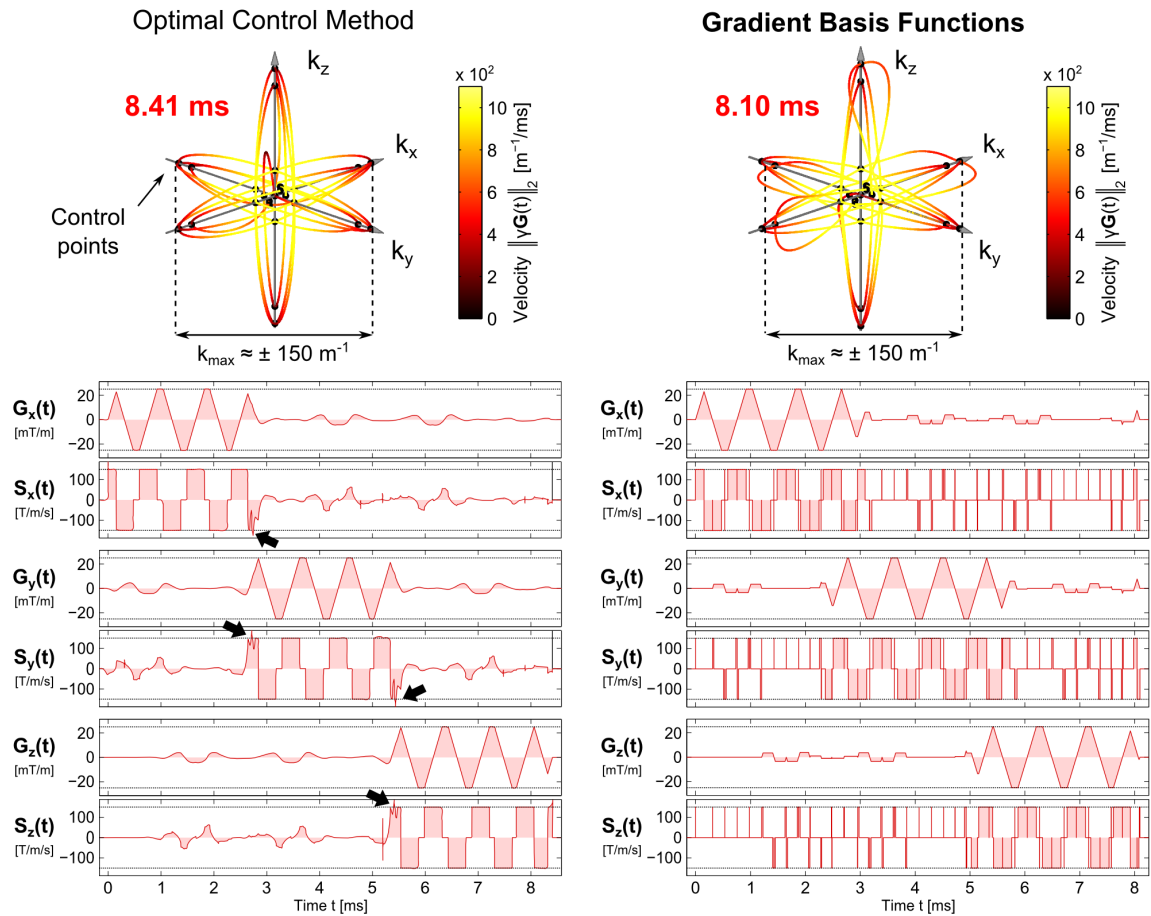


Figure 4.4: Cross trajectories in 3-D k -space as well as gradient and slew rate waveforms design by the *Optimal Control* method (left) and the *Gradient Basis Function* method (right). The gradient waveforms obtained using *Optimal Control* are impaired by slew rate oscillations that cause violations of the respective constraint (black arrows). The *Gradient Basis Function* method is free of significant numerical instabilities.

exhibit violations of these constraints – particularly of the slew rate constraint – for almost every set of random control points. The average maximum slew rate violation over all test cases was $4922 \pm 4665 \text{ T/m/s}$ (overall maximum violation: 29627 T/m/s) which corresponds to a violation of the slew rate constraint ($S_{\text{max}} = 150 \text{ T/m/s}$) by a factor of 30 (cf. Tab. 4.1, column F and G). These severe constraint violations predominantly occur at only few gradient samples, but render the entire gradient waveforms useless if no post-processing is applied (such as thresholding). Violations with respect to the gradient magnitude constraint ($G_{\text{max}} = 25 \text{ mT/m}$) were less severe; the average maximum gradient magnitude violation was $0.6 \pm 2.5 \text{ mT/m}$ (overall maximum violation: 36.5 mT/m). During the analysis of the *Optimal Control* method it was found that the underlying differential equation becomes particularly unstable if the path constraint contains sharp edges. At these locations, the computation of the curvature is very sensitive to numerical instabilities. The resulting oscillations in the gradient magnitude and slew rate waveforms could not be avoided entirely, even if the sampling time was significantly reduced (OC^1 to OC^2): the G_{max} constraint violation could be decreased by a factor of 60 (0.6 mT/m to 0.01 mT/m) and the S_{max} violation by a factor of 2.5 (4922 T/m/s to 1923 T/m/s). In many cases, these numerical instabilities lead to an increased trajectory error (as depicted above)

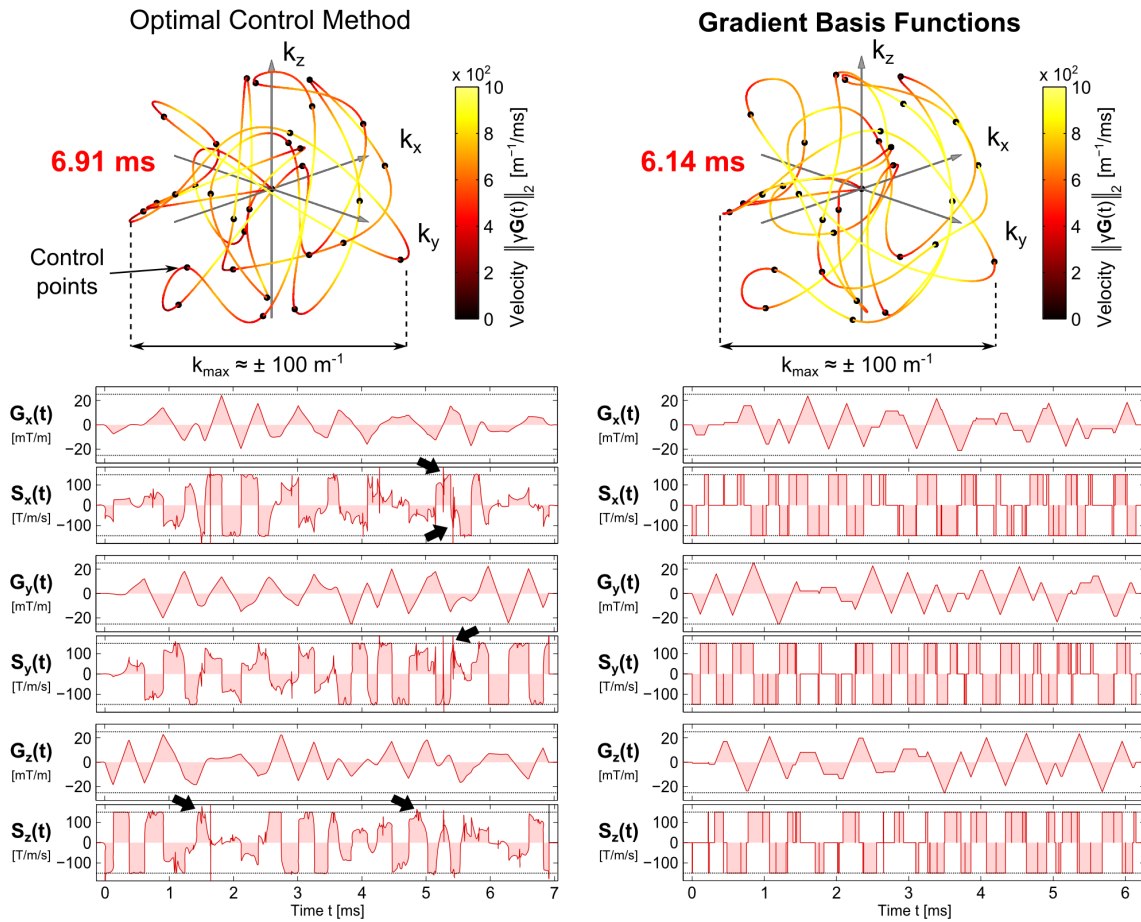


Figure 4.5: Random trajectories in 3-D k -space as well as gradient and slew rate waveforms design by the *Optimal Control* method (left) and the *Gradient Basis Function* method (right). The gradient waveforms obtained using *Optimal Control* are impaired by slew rate oscillations that cause violations of the respective constraint (black arrows). The *Gradient Basis Function* method is free of significant numerical instabilities.

that cannot be easily corrected for. In contrast, the *Gradient Basis Function* method respects the gradient magnitude and slew rate constraints without exception: all sets of random control points resulted in gradient waveforms that are fully conform with the gradient system constraints.

4.1.5 Three-dimensional Examples

Finally three-dimensional k -space trajectories were designed using both the *Optimal Control* method and the *Gradient Basis Function* method. The first set of control points was arranged to define a concentric shells trajectory (based on a single shell), with four control points per shell revolution. The k -space trajectory and associated gradient magnitude and slew rate waveforms for the shells trajectory are shown in Fig. 4.3. A second set of control points was defined to produce a cross-shaped k -space trajectory which is used for excitation of cube-shaped target patterns (see next section). The results of the cross trajectory and gradient waveforms are illustrated in Fig. 4.4. Finally, a 3-D version of a random trajectory was designed by randomly placing control points in k -space, the results of which are shown in Fig. 4.5. This type of k -space trajectory is commonly used in sparse receive and transmit approaches. For all three examples,

fixed gradient strengths of $\mathbf{G}^{(1)} = \mathbf{G}^{(N)} = \mathbf{0}$ have been defined, without incorporating directional constraints for the *Gradient Basis Function* method.

It can be observed that the *Optimal Control* method (left column of Figs. 4.3, 4.4, and 4.5) performs well as long as the underlying curve (obtained via spline interpolation of the control points) is smooth and possesses a rather low curvature. Both the shells and cross trajectory, however, have regions with relatively high curvature: right at the beginning and the end of the shells trajectory (at $t \approx 0.3$ ms and $t \approx 2.4$ ms in Fig. 4.3), and for the cross trajectory in between the k_x , k_y , and k_z segments (at $t \approx 2.6$ ms and $t \approx 5.4$ ms in Fig. 4.4). These high curvature parts induce slew rate oscillations that, in turn, cause violations of the respective slew rate constraint (these parts are highlighted by black arrows). Note that for the random trajectory (Fig. 4.5), these slew rate oscillations occur throughout the entire gradient waveform. On the contrary, no oscillations or constraint violations occurred for the gradient waveforms that were designed using the *Gradient Basis Function* method (right column of Figs. 4.3, 4.4, and 4.5). Additionally, the *Gradient Basis Function* methods achieves a gain with respect to the duration of the gradient waveforms of 11 % (2.53 ms to 2.28 ms) for the concentric shells trajectory, a gain of 4 % (8.41 ms to 8.10 ms) for the cross trajectory, and a gain of 13 % (6.91 ms to 6.14 ms) for the random trajectory.

4.2 | Three-Dimensional Spatially Selective Excitations

4.2.1 Convexity Analysis

Figure 4.6 shows the results of our analysis of the convexity of the optimization problem in Eq. 3.58 for the shells, stack-of-spirals, and cross trajectories and the two different target magnetizations (cube target in the top row, brain target in the bottom row). For all six pulses, we show the flip angle NRMSE as a colormap and the pulse duration (iso-contour lines of constant pulse duration) as functions of some of the shape parameters being optimized. These results illustrate that the flip angle error and pulse duration metrics vary continuously as a function of all parameters, even the integer parameters that control the number of shells (φ_4) and the number of spirals in the stack-of-spirals trajectories (φ_3). The well-conditioned overall topology of the flip angle error objective and pulse duration penalty make them well suited for optimization, which is due to the careful handling of non-continuous integer shape parameters as well as the numerical stability and robustness of the gradient trajectory design method [28, 26]. The topology of the objective function (flip angle error plus pulse duration) clearly depends on the target magnetization profile and the type of gradient trajectory. In general, we do not expect it to be a convex function of the shape parameters, which is clearly visible for the cross trajectory/brain target panel (bottom right) of Fig. 4.6. In this case, the objective function seems to show a slight worsening of the non-convexity problem (i.e., the number of local minima seems to increase) at long pulse durations.

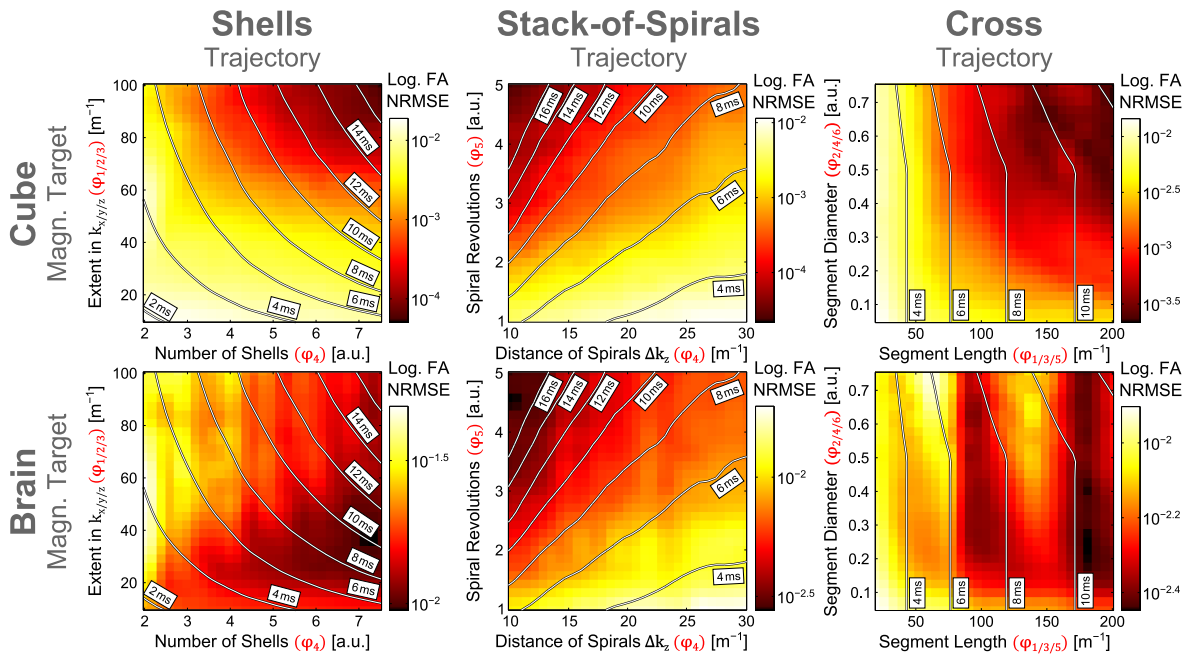


Figure 4.6: Topology of the objective function in Eq. 3.58 as a function of a subset of the shape parameters for the shells, stack-of-spirals and cross k -space trajectories. The flip angle (FA) error (colormap) and pulse duration (iso-contours) metrics, which are combined to form the total objective function used in our optimization framework, are shown for both the cube and brain target magnetization patterns. Although these optimization metrics are not convex with respect to the shape parameters, they vary continuously with respect to these variables and are, therefore, well suited for optimization.

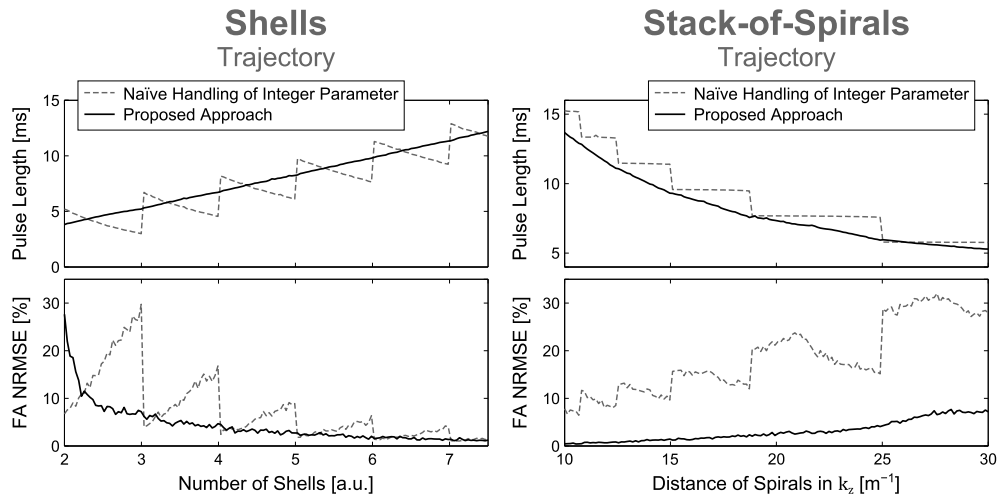


Figure 4.7: Plot of the pulse duration and flip angle NRMSE metrics as a function of the integer shape parameters for the shells and stack-of-spirals trajectories. These integer shape parameters control non-continuous features of the trajectories such as the number of shells (φ_4) and the number of spirals (φ_4) in the shells and stack-of-spirals trajectories, respectively. For each trajectory and optimization metric, we show two ways of computing the metrics. In the first naïve way, the integer parameters are varied in the same way as other continuous parameters. In the second way, which is used in the proposed framework, every time the integer parameter crosses a value that triggers the creation of a new "entity" (e.g., a new shell or a new spiral), the resulting new entity is created with zero k -space extent. This simple strategy removes large discontinuities in the objective function and thus renders it more suitable to optimization.

Figure 4.7 shows graphs of the pulse duration and flip angle error as a function of integer parameters controlling the number of shells and number of spirals in the shells and stack-of-spirals trajectories, respectively. The pulse duration and flip angle metrics are plotted as computed with the proposed approach for handling integer-type parameters (see Sec. 3.2.3) and a "naïve" approach that does not handle integer shape parameters in any particular way (in this approach, when a new "entity" is created, e.g., a shell or a spiral, it is not associated with zero k -space extent). This figure shows that naïve handling of integer parameters leads to discontinuities in both the pulse duration and flip angle error metrics, a problem that is easily solved by using the proposed approach.

4.2.2 Trajectory Optimization

Fig. 4.8, 4.9, and 4.10 show the results of our joint optimization approach applied to shells (Fig. 4.8), stack-of-spirals (Fig. 4.9), and cross trajectories (Fig. 4.10). Each trajectory was optimized for excitation of the cube (left) and brain (right) target patterns. For each type of trajectory and each target pattern, we show results for the unoptimized trajectory (1st column), the trajectory optimized at Larmor frequency (no off-resonance constraints other than the B_0 map, 2nd column), and the optimized trajectory using the spatio-spectral RF pulse design (with off-resonance constraints at ± 50 Hz in addition to the B_0 map, 3rd column). For each of the 18 pulses (3 trajectories \times 2 targets \times 3 optimization strategies), we show the k -space trajectory (top), the achieved flip angle map (center), and the off-resonance performance in terms of flip angle NRMSE as a function of the offset frequency (bottom). Table 4.2 summarizes these results as well as computation times. In Fig. 4.11, the RF and gradient waveforms of the optimized shells pulse for brain-only excitation are shown.

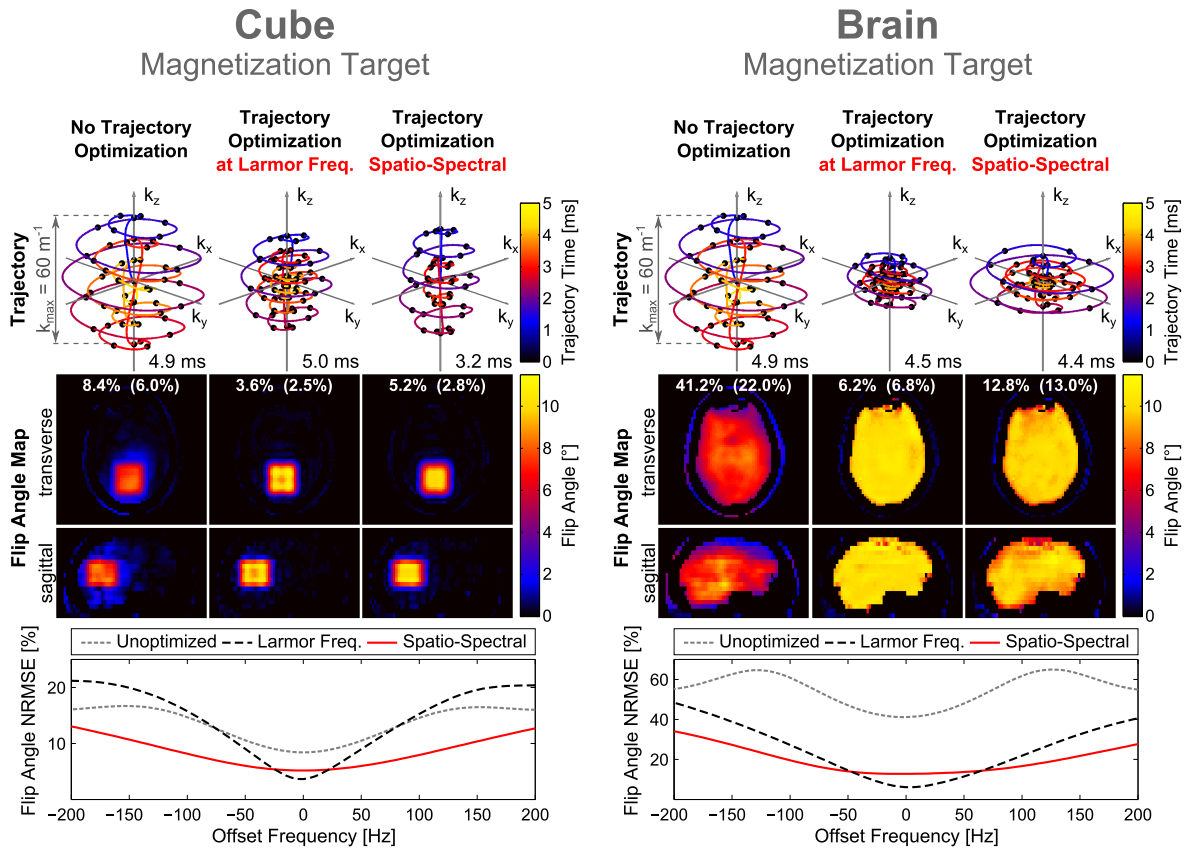


Figure 4.8: k -space trajectories and flip angle profiles obtained with the shells trajectory for excitation of the cube and brain-only target patterns (10°). For each target, three sets of results are shown corresponding to optimization of the RF waveform alone (left), joint optimization of the RF and gradient waveforms (center), and joint optimization with enforced off-resonance robustness (right). The two white numbers give the flip angle NRMSE in the entire FOX and outside of the cubic/brain-only target region (in parentheses). For each set of results, the off-resonance performance was evaluated in terms of the flip angle NRMSE as a function of the offset frequency (bottom).

For both target magnetization patterns and all three types of trajectories, optimization of the k -space trajectory resulted in a significant improvement of the flip angle pattern (the flip angle performance improvement ranged from $\times 1.4$ to $\times 2.3$ for the cube target and $\times 2.4$ to $\times 6.6$ for the brain target when optimizing the gradient waveforms at Larmor frequency, i.e., without off-resonance constraints). For the cube magnetization target (left-hand side of Fig. 4.8, 4.9, and 4.10), the overall best performance was achieved by the cross trajectory (NRMSE 3.4 %, performance improvement $\times 1.4$), followed by the shells (NRMSE 3.6 %, performance improvement $\times 2.3$) and the stack-of-spirals trajectory (NRMSE 3.7 %, performance improvement $\times 2.1$). The performance improvement was less pronounced for the cross trajectory ($\times 1.4$) and the cube magnetization target, which is due to the acceptable performance of the unoptimized pulse in this case. Although the three trajectory types generated similar flip angle patterns, they have widely different k -space profiles which emphasizes the non-convexity of the gradient optimization problem. For the brain magnetization target (right-hand side of Fig. 4.8, 4.9, and 4.10), the best performance after shape optimization at the Larmor frequency was achieved by the shells trajectory which almost completely suppressed signal outside the brain in these simulations (NRMSE 6.2 %, performance improvement $\times 6.6$). This followed by the cross

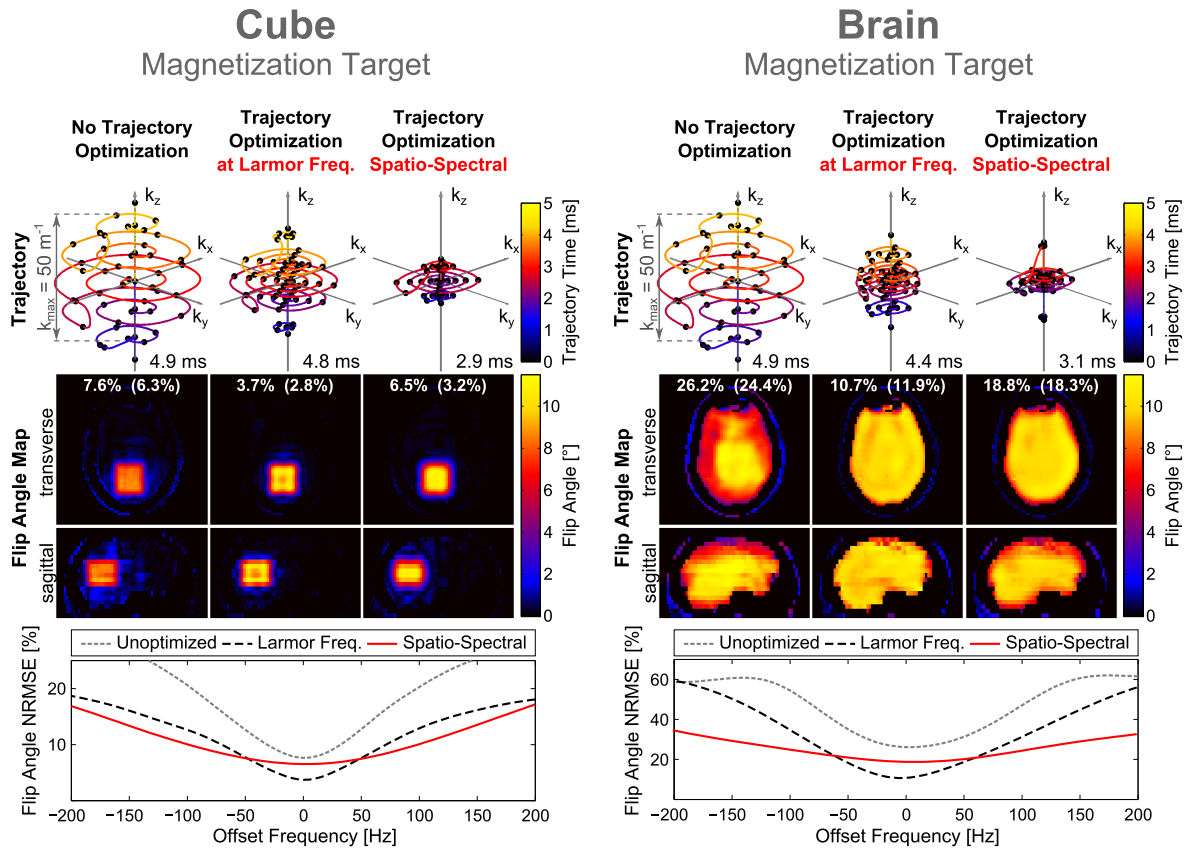


Figure 4.9: k -space trajectories and flip angle profiles obtained with the stack-of-spirals trajectory for excitation of the cube and brain-only target patterns (10°). For each target, three sets of results are shown corresponding to optimization of the RF waveform alone (left), joint optimization of the RF and gradient waveforms (center), and joint optimization with enforced off-resonance robustness (right). The two white numbers give the flip angle NRMSE in the entire FOV and outside of the cubic/brain-only target region (in parentheses). For each set of results, the off-resonance performance was evaluated in terms of the flip angle NRMSE as a function of the offset frequency (bottom).

(NRMSE 9.8 %, performance improvement $\times 4.6$) and the stack-of-spirals trajectories (NRMSE 10.7 %, performance improvement $\times 2.4$).

Enforcing robustness to off-resonance effects during trajectory optimization (spatio-spectral pulse design) reduced the accuracy of the achieved flip angle maps at the Larmor frequency but improved the excitation quality over the $[-50 \text{ Hz}, +50 \text{ Hz}]$ frequency range. Compared to optimization at the Larmor frequency, the spatio-spectral design resulted in shorter trajectories with increased sampling density in the center of k -space at the cost of decreased sampling density at higher k -space frequencies, resulting in a slight blurring of the achieved magnetization pattern compared to pulses optimized at the Larmor frequency alone.

In Fig. 4.13, we show a comparison of two SPINS pulses with 1 ms and 5 ms duration with optimized shells trajectories. These three trajectories (1 ms SPINS, 5 ms SPINS, 5 ms Shells) were used for two excitation scenarios: Flip angle uniformization in the whole head (A) and excitation of a cube target pattern (B). The 1 ms SPINS pulse performs well for the flip angle uniformization problem, but is obviously a poor choice for the spatially selective excitation problem. On the other hand, the 5 ms SPINS pulse is able to sample k -space up to 60 m^{-1} and has a surprisingly good performance for excitation of the cube pattern (interestingly, the 5 ms SPINS

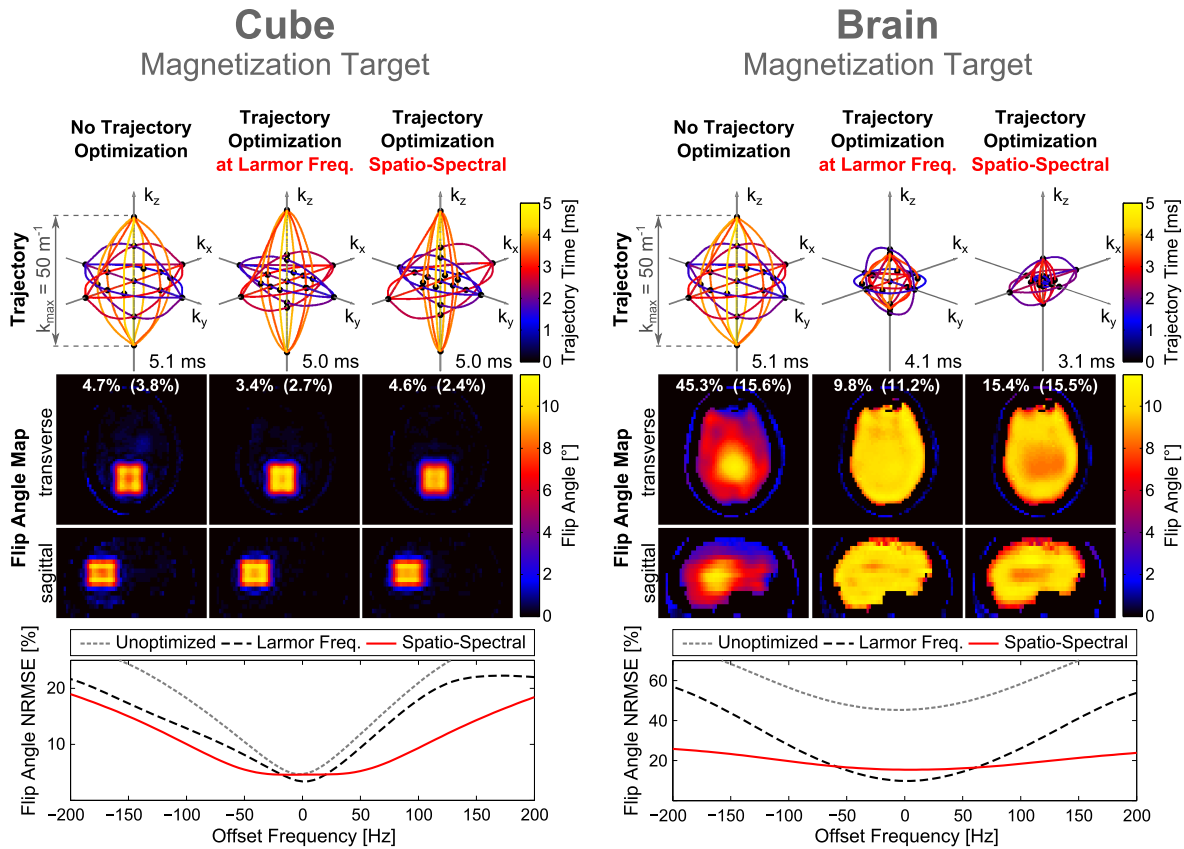


Figure 4.10: k -space trajectories and flip angle profiles obtained with the cross trajectory for excitation of the cube and brain-only target patterns (10°). For each target, three sets of results are shown corresponding to optimization of the RF waveform alone (left), joint optimization of the RF and gradient waveforms (center), and joint optimization with enforced off-resonance robustness (right). The two white numbers give the flip angle NRMSE in the entire FOX and outside of the cubic/brain-only target region (in parentheses). For each set of results, the off-resonance performance was evaluated in terms of the flip angle NRMSE as a function of the offset frequency (bottom).

performs less well than the 1 ms SPINS pulse for flip angle uniformization due to its lower k -space sampling density at the center of k -space. As a result of this trajectory not "spending" a lot of time at the center of k -space, the RF power used at these locations is high and, therefore, the pulse is strongly peak power limited, which explains its poor flip angle performance). For the more challenging spatial selection problem (cube target), the use of optimized pulses proved especially beneficial. This is shown by the histogram of flip angle values outside the cube mask showing a much lower signal level with the optimized shells trajectory than with the unoptimized 5 ms SPINS pulse.

Finally, we evaluated our optimized RF pulses on our 7T 8-channels pTx system: Fig. 4.12 of the Supporting Material shows two GRE images corresponding to RF pulses based on an unoptimized k -space trajectory (shell trajectory) and a trajectory optimized using our approach. The target excitation pattern is a cube of 10° flip angle. We also show the Bloch simulation of the optimized pulse. The trajectory shape optimization significantly reduces residual signals outside of the field of excitation. Deviations between the GRE image and the Bloch simulation for this pulse (center and right) are clearly visible, which are likely due to eddy current effects. As was suggested by

Target	Trajectory	Unoptimized Trajectory	Trajectory Optimization (at Larmor Frequency)			Trajectory Optimization (Spatio-Spectral Design)		
		NRMSE (Duration)	NRMSE (Duration)	Improv. Factor	Runtime	NRMSE (Duration)	Improv. Factor	Runtime
Cube	Shells	8.4% (4.9 ms)	3.6% (5.0 ms)	×2.3	3.5 h	5.2% (3.2 ms)	×1.6	5.1 h
	SOS	7.6% (4.9 ms)	3.7% (4.8 ms)	×2.1	2.3 h	6.5% (2.9 ms)	×1.2	2.5 h
	Cross	4.7% (5.1 ms)	3.4% (5.0 ms)	×1.4	2.7 h	4.6% (5.0 ms)	×1.0	7.7 h
Brain	Shells	41.2% (4.9 ms)	6.2% (4.5 ms)	×6.6	2.5 h	12.8% (4.4 ms)	×3.2	3.9 h
	SOS	26.2% (4.9 ms)	10.7% (4.4 ms)	×2.4	0.8 h	18.8% (3.1 ms)	×1.4	1.3 h
	Cross	45.3% (5.1 ms)	9.8% (4.1 ms)	×4.6	1.1 h	15.4% (3.1 ms)	×2.9	2.6 h

Table 4.2: Flip angle NRMSE, pulse duration, performance improvement factor (ratio of the flip angle NRMSE with and without optimization of the gradient trajectory), and computation time for the 18 pulses designed in this work (2 target magnetization profiles × 3 types of trajectories × 3 optimization strategies: RF alone, joint RF and gradient at Larmor frequency, and joint RF and gradient spatio-spectral design).

the work of several authors [72, 124], this is due to the fact that we did not map the actual gradient waveforms played on the system.

All pulses computed in this work were shorter than 5 ms, which shows that accurate excitation of complex 3-D magnetization patterns is possible using eight pTx channels and a clinical gradient system using reasonable excitation pulse duration, even when enforcing robustness to off-resonance effects.

Because a number of RF pulses need to be computed at every iteration of the shape parameter optimization loop, our joint RF and gradient optimization was rather time consuming. Computation times ranged from 0.8 to 3.5 hours for the shape optimization at Larmor frequency and from 1.3 to 7.7 hours for the spatio-spectral design. All computations were performed without acceleration and could be significantly shortened using multi-threaded CPU or GPU implementations.

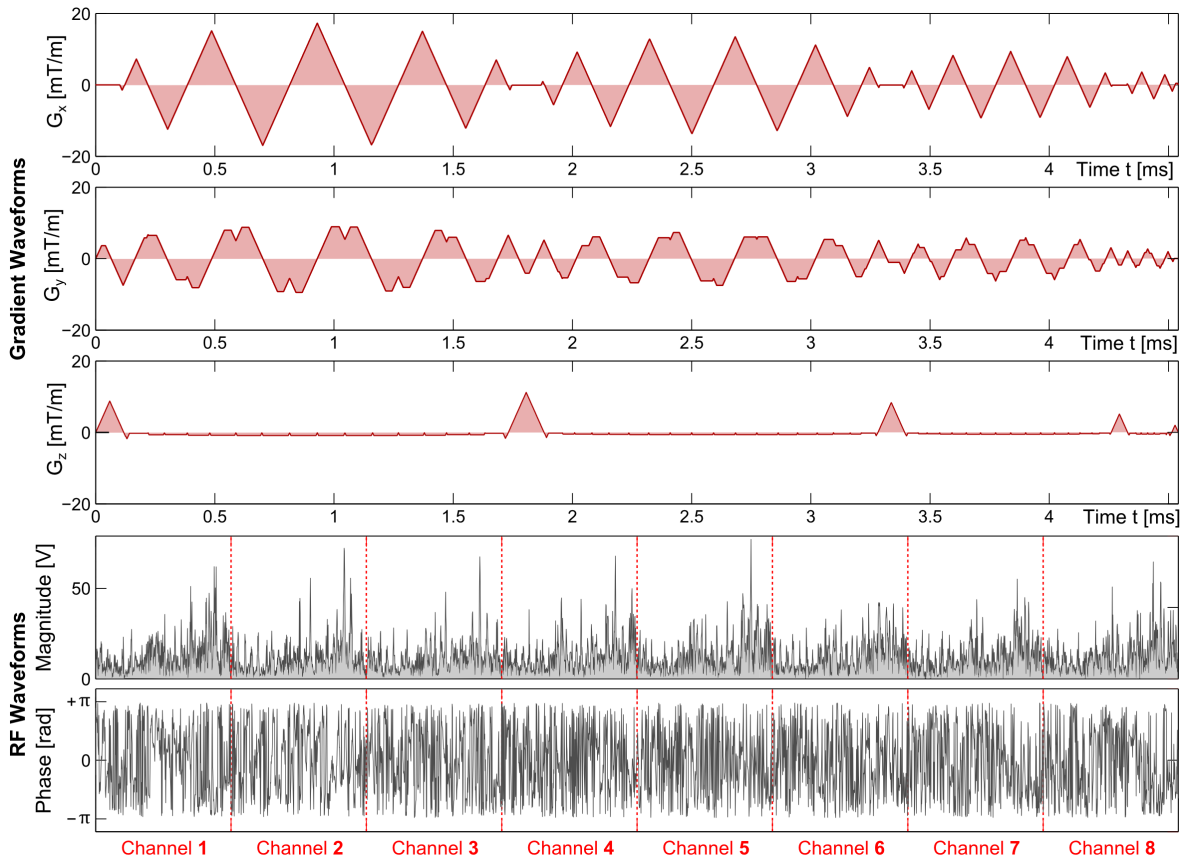


Figure 4.11: Gradient (top) and RF waveforms (bottom) for an optimized shells trajectory exciting the brain target (this pulse corresponds to the results of Fig. 4.8). We show the concatenated RF magnitude and phase waveforms for the 8-channel transmit coil (i.e., the intervals separated by red dashed vertical lines corresponds to a full pulse duration of 4.5 ms). The piece-wise linear gradient segments yield piece-wise quadratic k -space segments.

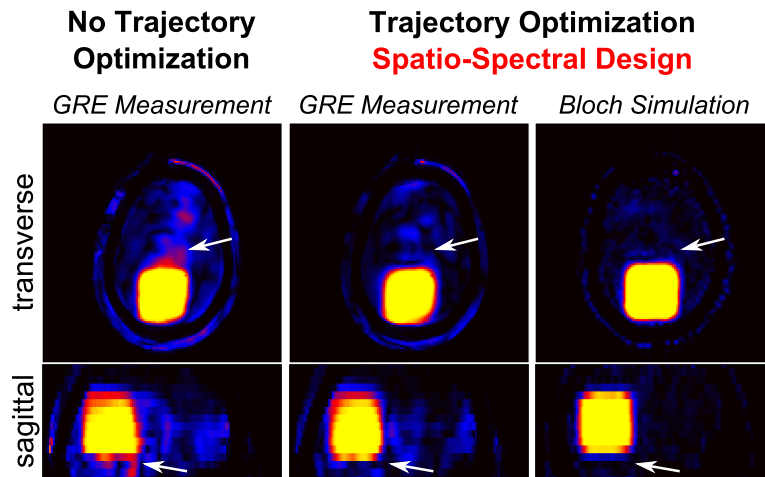


Figure 4.12: Experimental evaluation of two shell pulses (left: Unoptimized, right: Optimized) for excitation of a cubic region of excitation in the realistic 3-D printed head phantom described in the Methods section. GRE images were obtained using our 8-channel pTx head system (7 Tesla). Differences between the measured GRE profile and the Bloch simulation of the optimized pulse (two rightmost columns) are likely due to the fact that we did not map the actual gradient waveforms in this set of experiments.

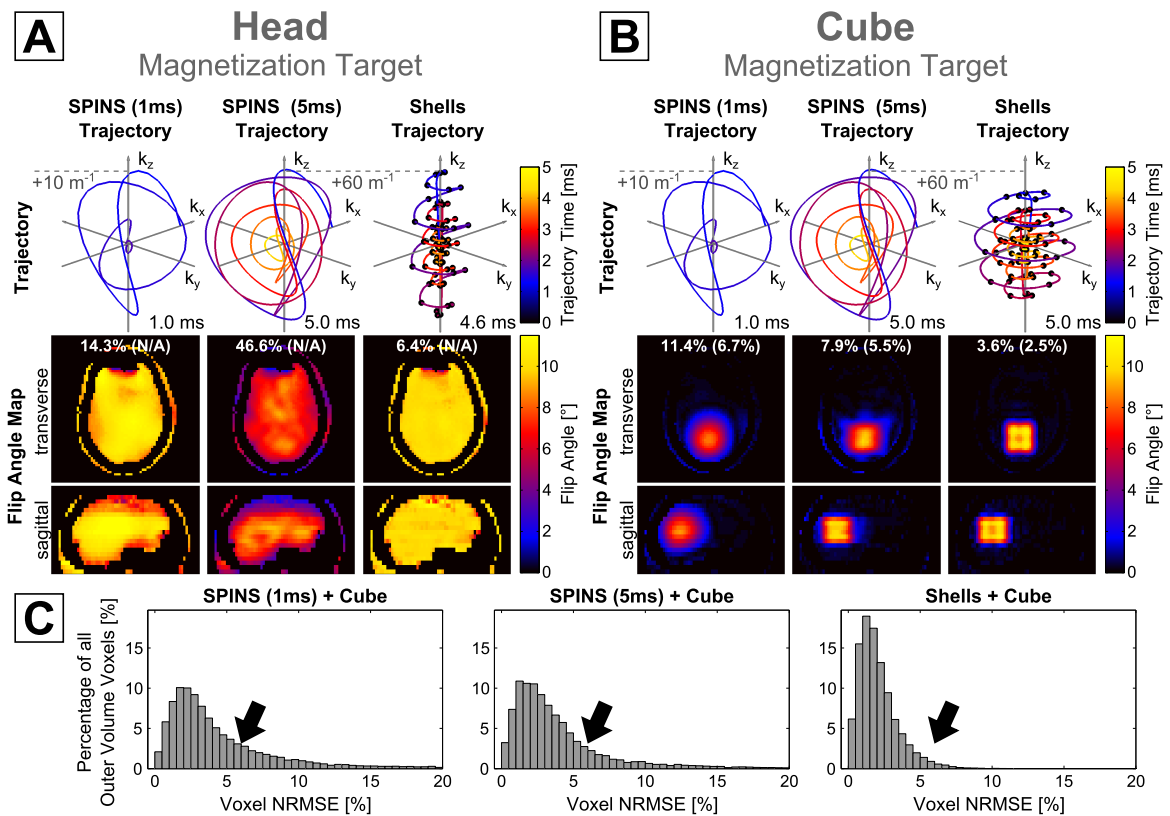


Figure 4.13: k -space trajectories and flip angle profiles for the 1 ms SPINS pulse, 5 ms SPINS pulse, and optimized shells trajectories obtained using our approach. Results are shown for both a uniform excitation in the whole head (A) and excitation of a cubic pattern (B). All pulses utilize the gradient system at maximum performance. The two white numbers give the flip angle NRMSE in the entire FOV and outside of the cubic target region (in parentheses, does not apply for the head target). The optimized shell trajectory shows improved performance compared to the SPINS trajectories for the spatial selection problem, which is quantified by the histogram of values outside the target mask shown in (C).

4.3 | Off-resonance Robust Slice Excitation

Figure 4.14 illustrates the results of the five different slice-selective RF pulse strategies in terms of the used gradient trajectory (top), the achieved in-plane flip angle maps on-resonance and at off-resonance frequencies of 50 Hz and 150 Hz (center) and the achieved slice profiles (bottom). The following types of RF pulses are depicted:

- Column 1:** RF coil driven in birdcage mode, no optimization of the RF waveforms (i.e., no utilization of parallel transmission capabilities)
- Column 2:** RF-shimming pulse, MLS optimization of the complex weights for the sinc RF waveform played on each transmit channel
- Column 3:** 2-spokes pulse, MLS optimization of the complex weight for the sinc RF waveforms played on each channel/spoke
- Column 4:** 2-spokes pulse, MLS optimization of the complex weights for the sinc RF waveforms played on each channel/spoke with enforced robustness to off-resonance effects
- Column 5:** Corkscrew pulse, full gradient and RF-MLS optimization with enforced robustness to off-resonance effects

4.3.1 Spokes RF Pulses

Without any utilization of parallel transmission capabilities (birdcage mode RF pulse, column 1), the resulting in-plane flip angle map experiences significant variations and is, therefore, not usable for imaging. On the other hand, optimizing the complex weights of the sinc pulse played on each transmit channel using an MLS optimization (RF-shimming, column 2) significantly reduces in-plane flip angle variations (reduction of the flip angle NRMSE from 27% to 5.9%) but remaining inhomogeneities are present (variation up to $\pm 4^\circ$). Note that the RF-shimming pulse has reasonable robustness to off-resonance effects: in presence of ΔB_0 frequencies of 150 Hz the NRMSE increases from 5.9% to 9.6%.

The B_1^+ mitigation performance can be improved by adding a second spoke to the gradient trajectory, in this case placed at $\mathbf{k}_{x/y} = 5 \text{ m}^{-1}$ (2-spokes, column 3). The MLS optimized 2-spokes pulse reduces the in-plane flip angle NRMSE (compared to the RF-shimming pulse) from 5.9% to 4.0%, at the cost of a substantial increase of the RF pulse duration (from 2.0 ms to 4.4 ms). The good B_1^+ mitigation performance of the 2-spokes pulse, however, is completely lost in presence of off-resonance effects: adding a ΔB_0 field dramatically reduces the in-plane flip angle fidelity: the NRMSE increases from 4.0% (at 0 Hz) to 20.0% (at 50 Hz) and 24% (at 150 Hz), i.e., the RF pulse is extremely sensitive to these off-resonance effects. If the 2-spokes pulse is optimized simultaneously at on- and off-resonance frequencies in order to improve the robustness (2-spokes off-resonance robust, column 4), the gain in B_1^+ mitigation (from RF-shimming to 2-spokes) is lost: the performance of this RF pulse in terms of flip angle uniformity and off-resonance robustness becomes essentially the same as the performance of the RF-shimming pulse. This is due to the fact that spokes pulses in general do not allow for off-resonance effects to be incorporated into the RF design problem. In other words, spokes pulses (using 1 or 2 spokes in this example) allow either for good B_1^+ mitigation *or* ΔB_0 robustness, but not both at the same time.

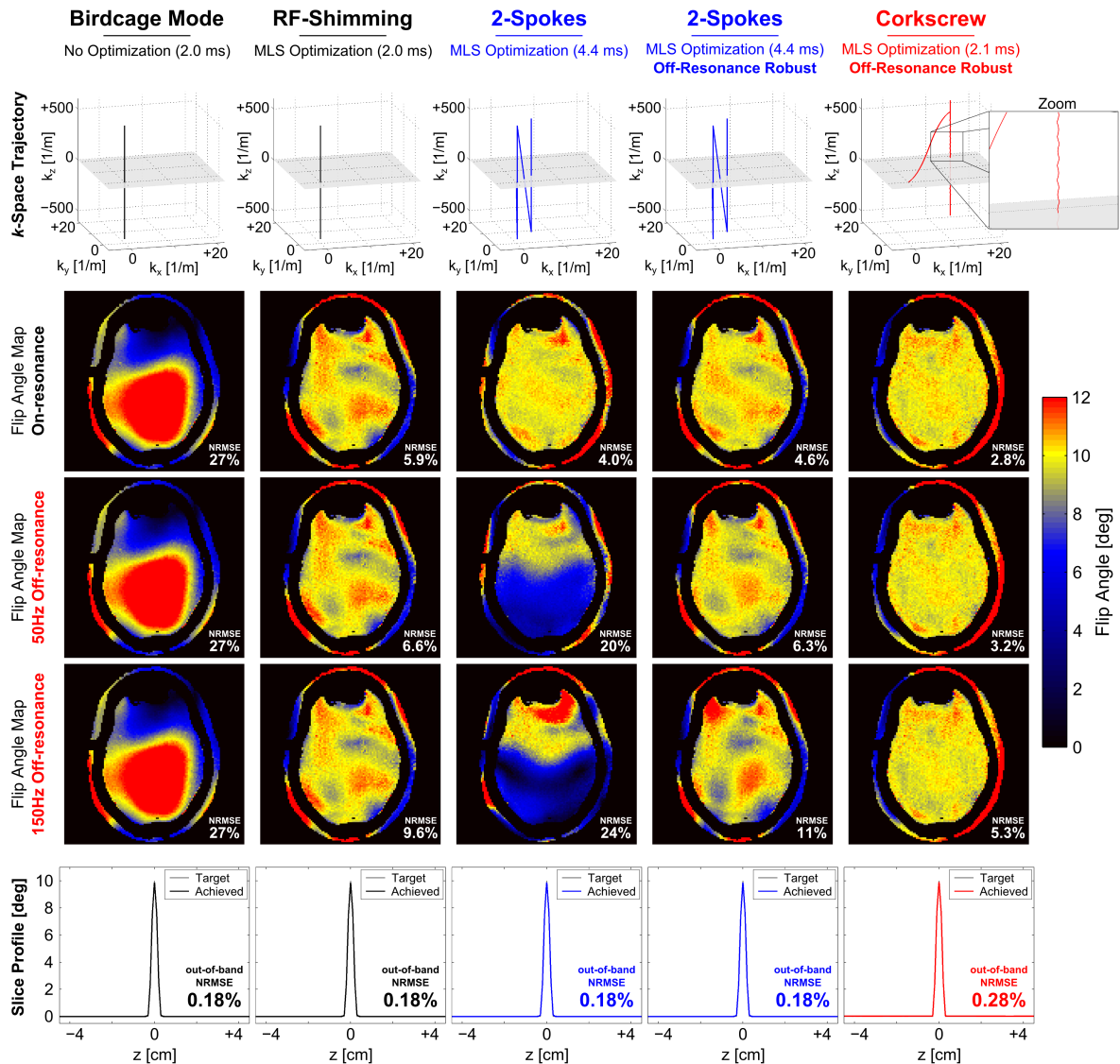


Figure 4.14: Results of the five slice-excitation pulse strategies investigated in this work. For each RF pulse the k -space trajectory (1st row), the flip angle maps on-resonant and off-resonant (2nd to 4th row), and the achieved slice profiles are shown (5th row).

4.3.2 Corkscrew RF Pulse

Figure 4.14, column 5 shows the results of the corkscrew pulse for which the gradient and MLS RF waveforms were optimized using the proposed joint optimization framework. It can be seen that the shape optimizer shifted the corkscrew trajectory far away from the center of the $k_{x/y}$ plane (to about $k_{x/y} = 20 \text{ m}^{-1}$) while only mild modulations in the $k_{x/y}$ -plane were employed (see zoomed view of the gradient trajectory). This mild modulation of the sampling density, however, allows for the ΔB_0 induced k -space errors to be efficiently compensated, resulting in a consistently good in-plane flip angle performance both on-resonant (2.8% NRMSE) and off-resonant (3.2% and 5.3% NRMSE, respectively).

Figure 4.14, bottom row, shows the slice profiles of the five simulated RF pulses. The pulses that are based on analytic sinc waveforms for slice-selection (column 1 to 4) achieve almost

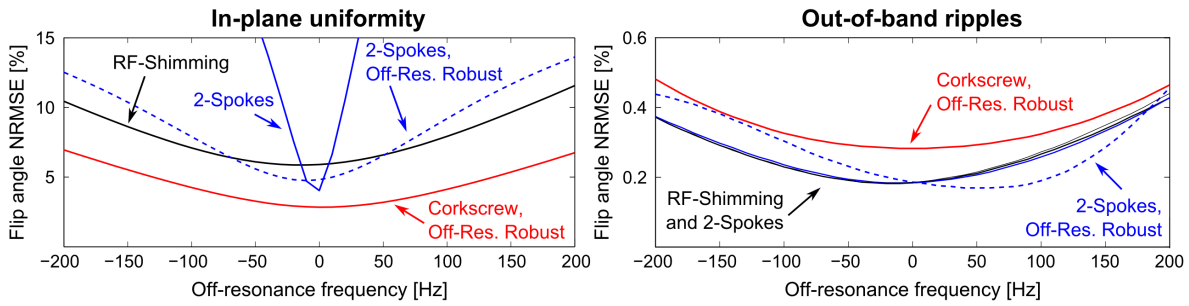


Figure 4.15: Off-resonance performance of the five slice-selective RF pulses in terms in-plane (left) and out-of-band (right) flip angle NRMSE as a function of the off-resonance frequency.

perfect slice-selection (out-of-band NRMSE is 0.18 % in all four examples). The corkscrew pulse achieves a slightly higher out-of-band NRMSE of 0.28 % which is still sufficiently good to be used for imaging.

In Fig. 4.15, a full analysis of the off-resonance robustness is shown in terms of flip angle error as a function of the off-resonance frequency, both for the in-plane uniformity (left) and out-of-band ripples (right). As was already observed in the flip angle maps, the spokes pulses (black and blue curves) achieve either flip angle mitigation or off-resonance robustness, but not both at the same time. The corkscrew pulse (red curve) achieves a flip angle performance (both in-plane and in the outer-band) which is consistently good in a wide range of off-resonance frequencies.

4.4 | Prediction of Magnetostimulation Thresholds

4.4.1 Neurodynamic Model Stimulation

Figure 4.16 shows the time evolution of the membrane potential for a $16.0\ \mu\text{m}$ fiber diameter in response to an applied external waveform. Figure 4.16 A shows the external electric potential imposed by the coil at the different nodes of Ranvier. This spatially varying electric potential pattern is modulated in time by the 1 kHz sinusoidal waveform shown in Fig. 4.16 B. The resulting membrane dynamics are shown in Fig. 4.16 C: in this 2-D plot, the vertical axis specifies the spatial location along the nerve segment and the horizontal axis specifies time. During the first two sinusoidal half-lobes, the nerve segment is alternatively hyperpolarized (green) and depolarized (red) but only the third half-lobe initiates an action potential (yellow) in the upper part of the segment. This action potential then propagates along the nerve segment without significant further perturbation by the external electric potential's waveform. After this first action potential the nerve membrane recovers (this is the refractory period during which the ion-channel pumps are active and no action potential can be evoked) and a second and third action potential are initiated by the 7th and 11th sinusoidal half-lobe, respectively.

4.4.2 Effect of Fiber Diameter

Figure 4.17 A shows PNS threshold curves for a nerve segment in the leg for varying values of the fiber diameter ($5.7\ \mu\text{m}$ to $16.0\ \mu\text{m}$). The field modulation strength (vertical axis) is normalized to the PNS threshold for the largest fiber ($16.0\ \mu\text{m}$ diameter) at the 10.4 kHz modulation frequency.

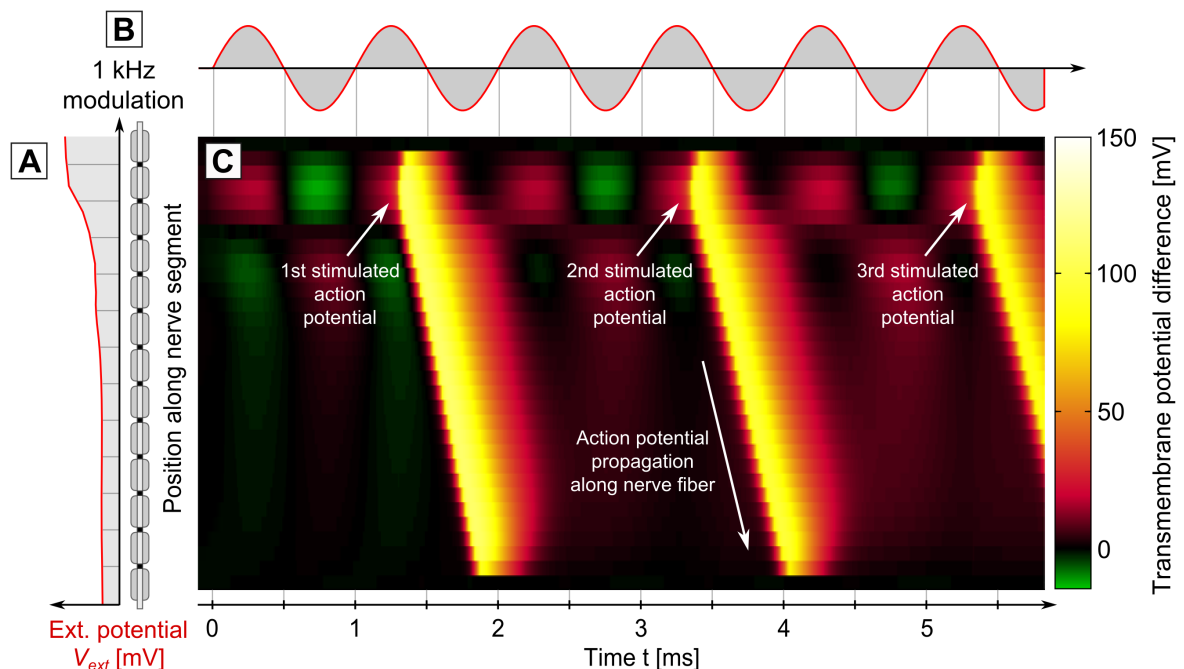


Figure 4.16: Exemplary evaluation of the nerve membrane model. (A) Potential created by coil along the nerve segment (V_{ext}). (B) Time modulation of V_{ext} (1 kHz sinusoid at 125% of the PNS threshold). (C) The transmembrane potential as a function of space (position along the nerve, vertical axis) and time (horizontal axis) showing the creation of an action potential which then travels with a fixed velocity in space.

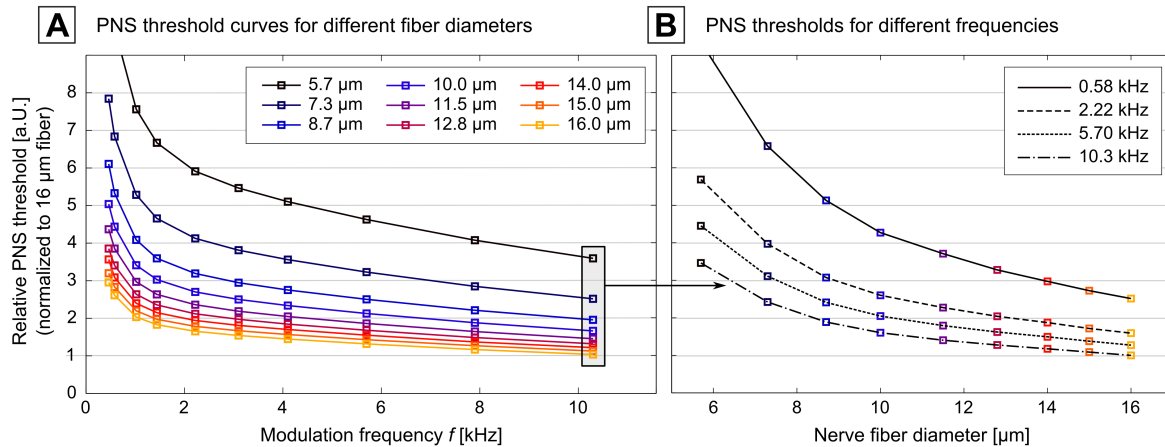


Figure 4.17: (A) PNS thresholds as a function of the frequency of the applied coil current (sinusoidal current) for different fiber diameters. The largest fibers show the lowest threshold (i.e., they are easiest to stimulate). (B) PNS thresholds as a function of fiber diameter, while keeping the frequency constant.

These PNS threshold curves coincide with experimental observations [121, 37] and theoretical predictions [80, 3, 15] that nerve fibers with a large diameter are more easily excited than smaller fibers. The threshold for the smallest diameter fiber is about 3.5 fold that of the largest fiber simulated (16.0 μm). In Fig. 4.17 B, we show PNS thresholds as a function of fiber diameter, for given constant frequencies of the applied fields. Note that the PNS thresholds change very quickly for small fiber diameters and rather slowly for large fibers.

Figure 4.18 shows the PNS simulation thresholds as a function of applied field frequency for the leg and arm coils. The electric field magnitude is shown overlaid on the anatomical model. Figure 4.18 also shows the resulting simulated PNS threshold curves as well as the measured thresholds from Saritas et al. [101]. The measured values represent the median over 26 subjects (error bars indicate 25th and 75th percentile). The B -field generated by the modeled coil agrees well (within 1%) with the experimental value (measured values: 214 μT for the leg coil, 410 μT for the arm coil, simulated values: 211.86 μT for the leg coil, 407.1 μT the arm coil). The electric field maps show that the electric field patterns are significantly modulated by the anatomical details of the model. Electric field hotspots occurred in tissues with low conductance, such as layers of fatty tissues separating different muscle fiber bundles and in regions where the conductivity is significant but the geometry narrows (e.g., the tibialis anterior muscle whose width becomes very small close to the shin bone region, arrow in Fig. 4.18 B). Although the average measured PNS thresholds (gray region) from the 26 subjects and the simulated PNS thresholds (red curve) are in good overall good agreement, there is some deviation in the low-frequency region of the PNS curves for both the leg and arm stimulations. However, the experimental values also exhibit increased variance in this frequency range. We repeated the PNS simulations using a range of spatial deformations applied to the most sensitive nerves, allowing the nerve segments to vary freely within a tube surrounding the unaltered nerve segment. For a tube radius of 2 mm (4 mm) the PNS thresholds computed for 20 deformed nerve segments in the arm showed a standard deviation of 15% (30%). The leg example showed an uncertainty of 6% and 14% for the 2 mm and 4 mm tube, respectively.

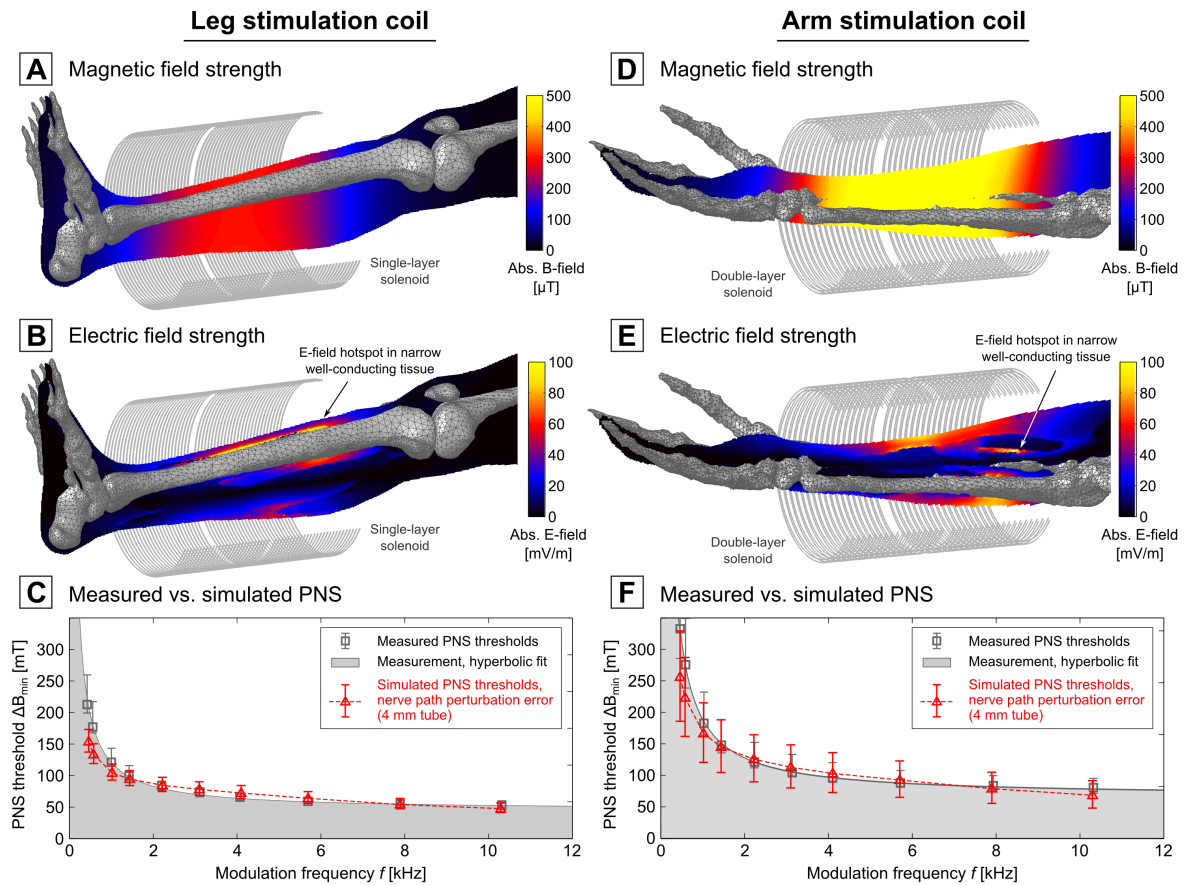


Figure 4.18: Calculated PNS thresholds as a function of coil current frequency for a leg coil and an arm coil compared to previously published experimentally measured thresholds [101]. In **C** and **F** we plot the measured and simulated PNS thresholds (amplitude of applied B -field which creates an action potential) as a function of coil current frequency. The error bars in the simulated PNS thresholds (red boxes) derive from the nerve path sensitivity analysis. Namely they represent the standard deviation of the thresholds over the 20 segments simulated within the 4 mm tube around the atlas nerve center.

4.4.3 PNS Simulations in the Leg and Arm Solenoid Coils

In Fig. 4.19 we illustrate the coil configurations and E -field maps, overlaid by the simulated nerve segments (red dots indicate boundaries of the individual nerve segments). In the zoomed images, the nerve segments with lowest stimulation thresholds are shown (these segments determine the PNS threshold curves shown in Fig. 4.18). The bottom row of Fig. 4.19 shows the electric potential and its second derivative of these two nerve segments (this is proportional to the amount of current entering or leaving the membrane [93, 2]). The kinks of these nerve segments in high E -field regions (positions 2 and 3 at the left, position 2 at the right) cause a sudden change in slope of the electric potential along the nerve segment, leading to a large inflow or outflow of current (peaks in the second derivative of the electrical potential). In both the leg and arm situation, the stimulated nerve segments pass through a rather high E -field region (maximum E -field strengths along the excited segments were 66.6 mV/m in the leg and 47.7 mV/m in the arm for 1 A applied coil current). However, it is the high curvature of these nerve segments that plays a major factor in making these segments particularly sensitive to the applied E -field.

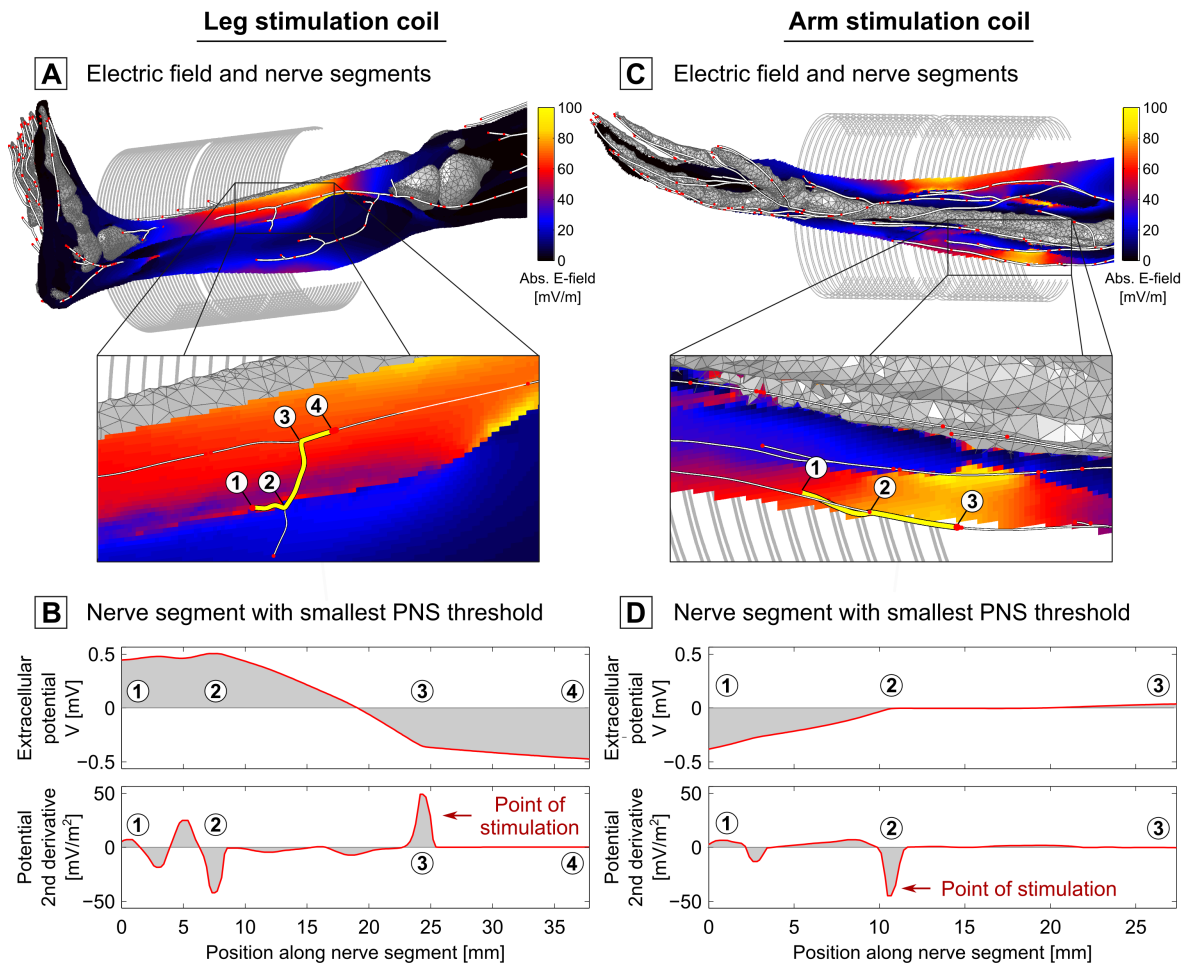


Figure 4.19: Simulated nerve segments (red dots indicate end points of each nerve segment), superimposed onto the coil configurations and E -field maps (**A** and **C**). In the zoomed images, the nerve segments with smallest stimulation thresholds are depicted. In **B** and **D**, we show, for these nerve segments, the external electrical potential and its second derivative (which is proportional to the current flow through the membrane).

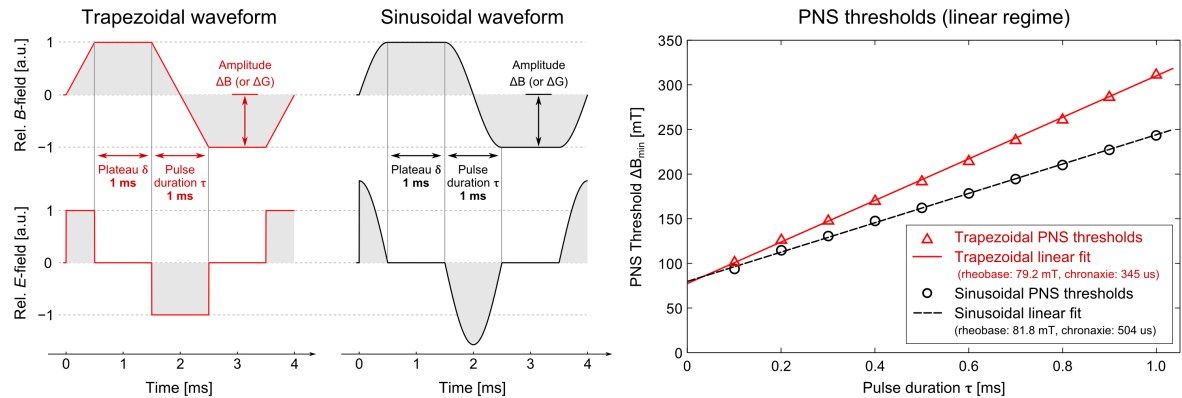


Figure 4.20: Trapezoidal and sinusoidal B -field waveforms and the resulting E -field pulses (plateau duration 1 ms, pulse durations between 0.1 and 10 ms, overall 10 bipolar pulses) and the resulting PNS thresholds as a function of pulse duration (i.e., in the linear regime).

4.4.4 Sinusoidal vs. Trapezoidal Waveforms

Figure 4.20 shows the trapezoidal and sinusoidal waveforms studied and the pulse durations during which dB/dt (and thus an electric field) is present. Figure 4.20 also shows the PNS thresholds for the arm coil as a function of pulse duration as well as the linear fit. The MRG neurodynamic model used in this work reproduces the increase of the PNS thresholds for trapezoidal pulses. The linear fit of the sinusoidal ($R^2 = 0.9913$) and trapezoidal thresholds ($R^2 = 0.9947$) reveals chronaxie times of 504 μ s and 345 μ s, respectively, which is in very good agreement with experimental data [94].

4.5 | Simulated PNS Thresholds for Gradient Coils

4.5.1 Magnetic Fields

Figure 4.21 shows the simulated magnetic fields of the X, Y, and Z gradient coils (from left to right); for each coil the B_z component (required for spatial encoding) in the region-of-linearity (ROL) produced by 1 A applied coil current is shown (top row). At the bottom of Fig. 4.21, the maximum intensity projection (MIP) of the B -field magnitude is shown in coronal (left sub-panel) and sagittal plane (right sub-panel). It can be observed that, although only the B_z field component in the ROL is needed for spatial encoding of the spins, the concomitant fields (i.e, the field components not needed for encoding) are responsible for the highest magnetic field strengths (especially in the region $0.1 \text{ m} < z < 0.5 \text{ m}$). The plot of the B_z component at the top of Fig. 4.21 illustrates that the gradient coils produce linearly varying B_z components along the x , y , and z axes (note that the plots of the B_z field component use different spatial axes). The shown iso-contour lines are spaced at $5 \mu\text{T}$. The efficiency of the three gradient coils in terms of achieved linear B_z field gradient for 1 A applied to the gradient coil is given by 0.093 mT/m (for the X-gradient), 0.098 mT/m (for the Y-gradient), and 0.091 mT/m (for

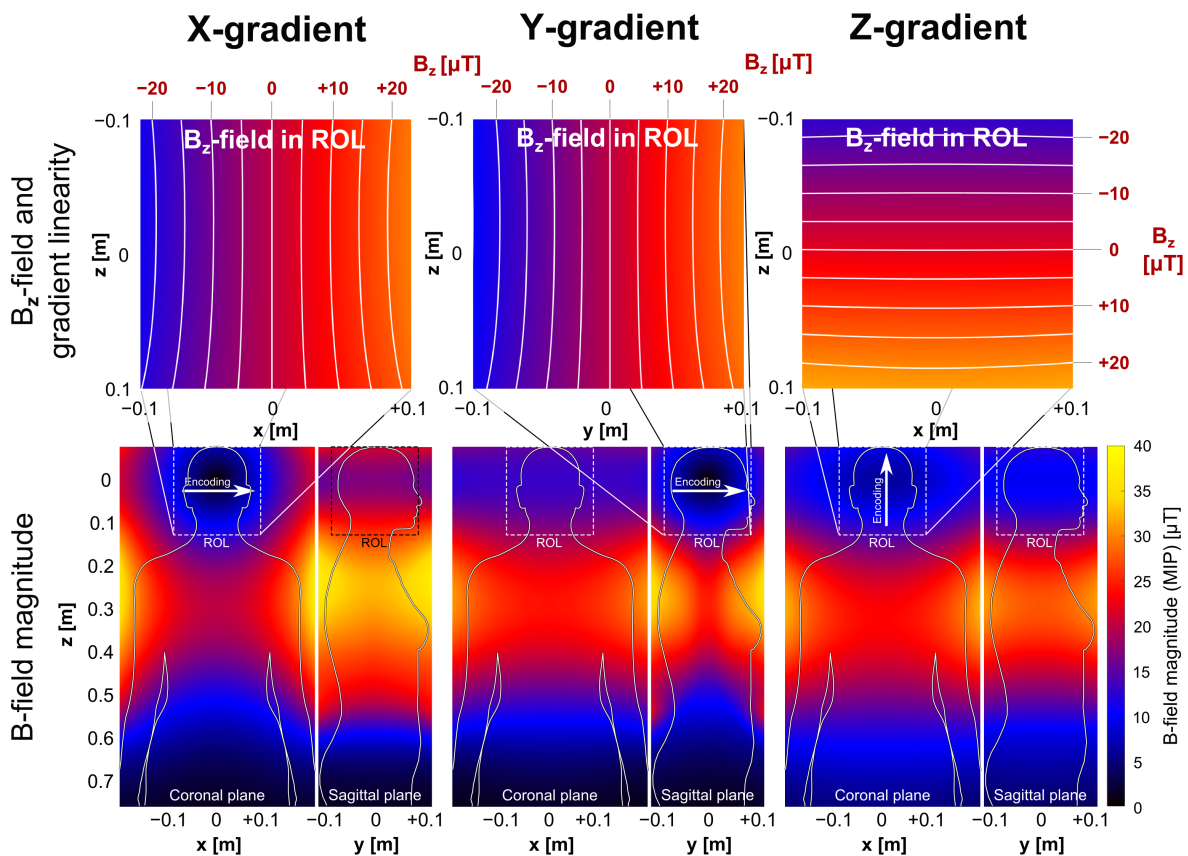


Figure 4.21: Magnetic fields produced by the gradient coils at 1 A applied current: the top row shows the B_z -field produced in the region-of-linearity (dashed lines in the bottom plots). The iso-contour lines are spaced at $5 \mu\text{T}$. The bottom row shows the maximum intensity projection of the B -field magnitude in the coronal (left sub-panel) and sagittal (right sub-panel) plane.

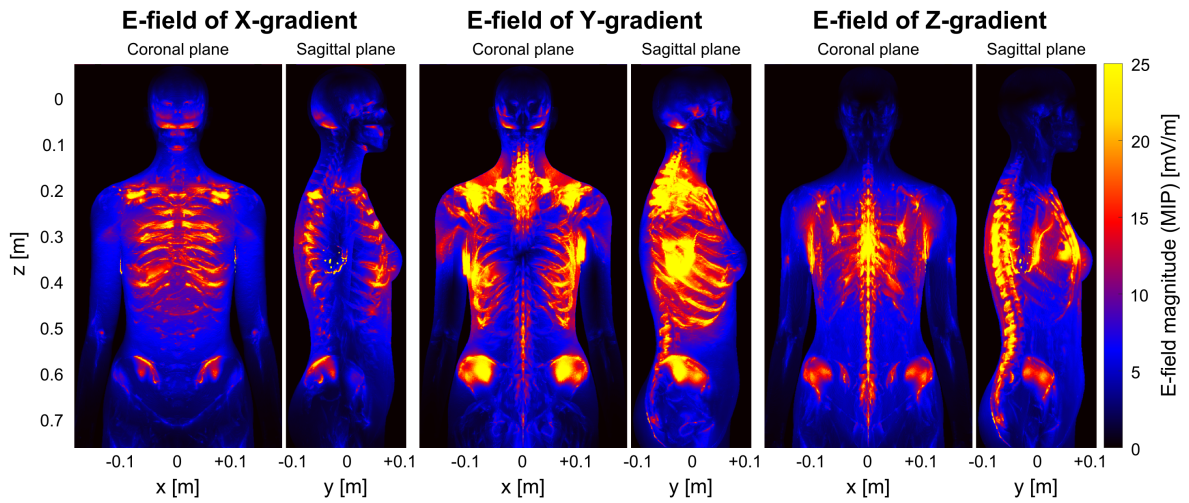


Figure 4.22: Electric fields (maximum intensity projection) induced by the gradient coils for 1 A applied current modulated with a 1 kHz sine wave (coronal plane in the left sub-panel, sagittal plane in the right sub-panel).

the Z-gradient). This means that in order for the X-gradient to produce the maximum nominal gradient strength of $G_{\max} = 40$ mT/m, a current of 430 A is needed.

4.5.2 Electric Fields

The electric field strength induced by the three gradient coils for an applied current of 1 A modulated at 1 kHz is shown in Fig. 4.22. For each gradient coil the maximum intensity projection (MIP) of the E -field magnitude is shown in the coronal (left sub-panel) and sagittal plane (right sub-panel). The electric fields are heavily shaped by the conductive body model, creating a highly heterogeneous field pattern (this is in contrast to the magnetic fields shown in Fig. 4.21 for which the body model is mostly transparent). The regions of significant E -field strength are predominantly located at the region of highest magnetic field strength ($0.1 \text{ m} < z < 0.5 \text{ m}$). The X-gradient produces high E -fields at the dorsal and ventral parts of the rib bones and close to the hips. The Y-gradient caused high E -field magnitudes in the shoulder regions, at the left/right regions of the ribs, as well as close to the hip bones. The E -fields imposed by the Z-coil are predominantly located close to the spine and to the sternum. Note that the overall E -field strength produced by the Y-gradient coil is substantially higher, than the E -fields induced by the X/Z-gradient axes due to the larger cross-section of the body in the coronal plane.

4.5.3 E-Fields along Nerve Fibers

In Fig. 4.23 (top row), the E -field magnitude interpolated at the locations of the nerve fibers is depicted. The bottom row shows the magnitude of the E -field pointing along the direction of the nerve fibers (i.e., the magnitude of the E -field projected onto the nerve paths). This projected E -field component leads to an axial current flow along the nerve fiber path and, therefore, may lead to generation of an AP. Note that the effective entity for generation of PNS (*activation function*) is the spatial derivative of the E -field along the nerve fiber (i.e., the second spatial derivative of the potential changes which are fed to the neurodynamic model). The X-gradient (Fig. 4.23, left) produces the overall smallest axial current flow along the nerves. Some nerve segments in the neck and the upper arm as well as some of the intercostal nerves are affected

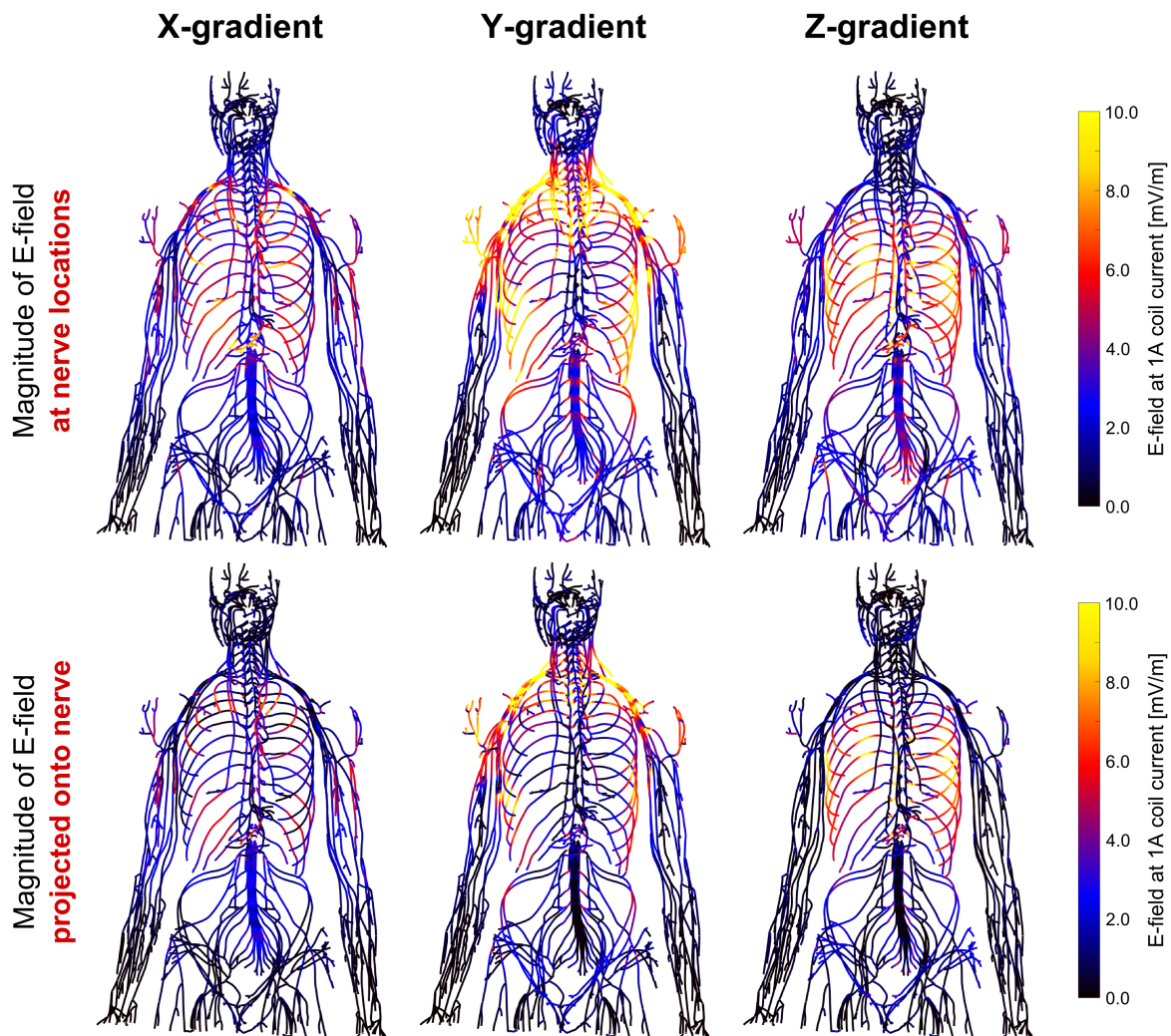


Figure 4.23: *Top row:* magnitude of the E -field interpolated at the locations of the nerve fibers in the human body model. *Bottom row:* magnitude of the E -field pointing along the direction of the nerve fiber path, i.e., the E -field as projected onto the nerve fiber. This field component determines the amount of current flowing in the axial direction of the nerve fiber.

by the induced electric fields. A more effective E -field pattern in terms of PNS generation (i.e., higher strength *and* orientation along the nerve fibers) is produced by the Z-gradient coil (Fig. 4.23, right). In this case the E -fields induce an increased current flow along the intercostal nerves. Compared to the X and Z-gradient coils (whose induced currents along the nerves are rather small), the E -fields generated by the Y-gradient produce a substantial current flow along the nerve fibers. This current flow arises from the high E -field strength (resulting from the large body cross-section in the X-Z-plane) in combination with nerve fibers that run in a very similar plane. Large levels of axial current flow occur in the neck, shoulders, and the intercostal nerves. These results highlight that it is the local E -field strength in conjunction with the orientation of the nerve fibers present in the same region that affect the level of "effective" interaction with the nervous system.

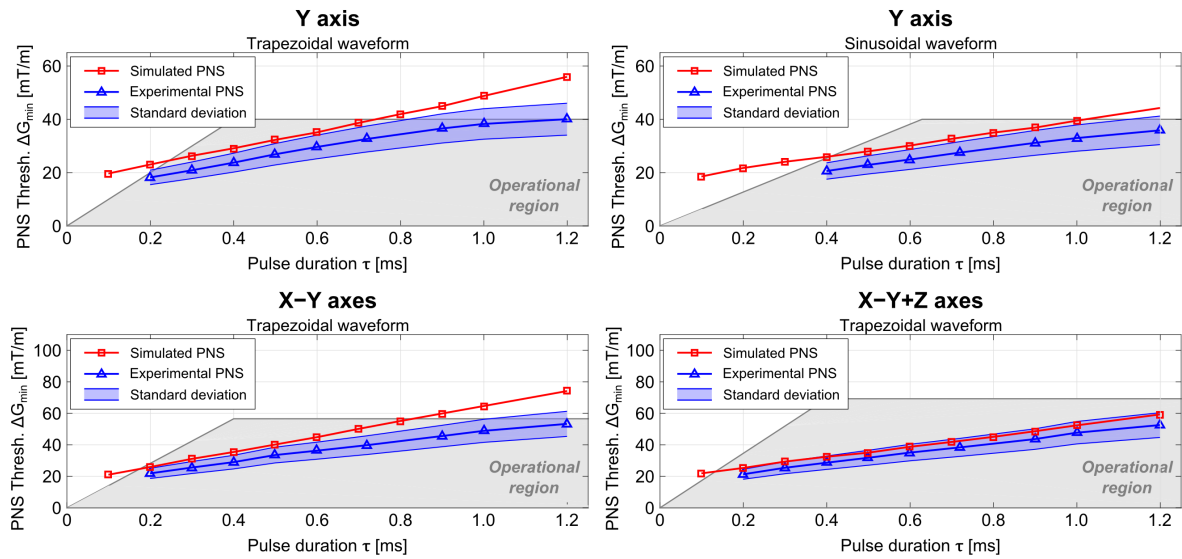


Figure 4.24: Simulated (red) and experimental (blue) PNS threshold curves for the three gradient coils in terms of the minimum gradient magnitude ΔG_{\min} as a function of the pulse duration τ that caused PNS. The top row shows the Y-gradient results for trapezoidal (left) and sinusoidal waveforms (right). Bottom row shows PNS threshold curves for the "X-Y" and "X-Y+Z" gradient combinations (both for trapezoidal waveforms).

4.5.4 Simulated vs. Measured PNS Thresholds

PNS threshold curves were generated for the three gradient coils, using both trapezoidal and sinusoidal waveforms with varying pulse durations. Figure 4.24 shows the PNS threshold curves obtained in the clinical study (blue, including the standard deviation over all subjects) and based on the PNS simulation framework (red). The top row shows the results of the Y-gradient for trapezoidal (left) and sinusoidal (right) waveforms, the bottom row shows the results for the coil combinations "X-Y" (left) and "X-Y+Z" (right), both evaluated using trapezoidal waveforms only. PNS thresholds are given in terms of smallest gradient modulation strength (ΔG_{\min}) for a given pulse duration τ (equal to the trapezoidal rise time) that lead to AP generation. The grey area in the background illustrates the operational region of the gradient coil (determined by the G_{\max} and S_{\max} constraints). Note that the operational region is different for trapezoidal and sinusoidal pulse shapes, since the sinusoidal ramp has a higher maximum slew rate than a trapezoidal ramp (leading to a higher maximum pulse strength, see Fig. 4.20). Furthermore note, that the operational region increases when multiple gradient coils are driven in parallel, i.e., for two simultaneous axes, G_{\max} and S_{\max} of the combined gradient field increase by a factor of $\sqrt{2}$ (and by a factor of $\sqrt{3}$ when using all three gradient axes simultaneously).

It can be observed that the PNS simulation framework is capable of reproducing experimentally obtained threshold characteristics for highly complex wire patterns like the simulated MRI gradient coils with reasonable accuracy. The simulated PNS threshold curves are right "on top" of the standard deviation of the experimentally obtained data (the standard deviation over all subjects was approx. 15% for all setups). The NRMSE of the four simulated PNS threshold curves with respect to the experimental thresholds is given by 19.83% (Y-axis, trapezoidal), 16.51% (Y-axis, sinusoidal), 21.09% ("X-Y" axes, trapezoidal), and 8.51% ("X-Y+Z" axes, trapezoidal). Despite the generally good agreement between simulated and experimental PNS threshold curves, these preliminary results indicate some systematic deviation that goes beyond the expected intra- and inter-subject variation. The complex interference of the electric fields that occurs when

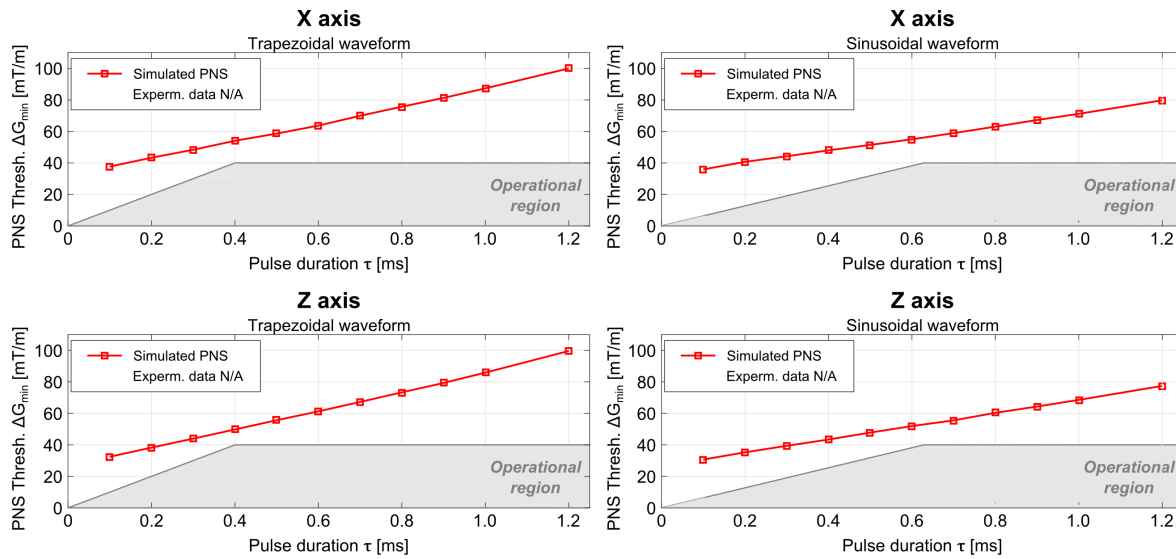


Figure 4.25: Simulated PNS threshold curves for the X and Z-gradient coils in terms of the minimum gradient magnitude ΔG_{\min} as a function of the pulse duration τ that caused PNS. Note that no experimental data was available for these axes (PNS thresholds are beyond the operational region shown in grey).

combining multiple gradient axes seems to be well reproduced by the simulations: for the gradient axes combinations "X-Y" and "X-Y+Z", the simulated and experimental PNS thresholds change consistently (compared to the single axis experiments using only the Y-gradient coil). Note that for some data points of the experimental PNS threshold curves, the gradient system performance limits did not allow to accurately determine the PNS thresholds: in these cases, the respective threshold value was set to the maximum gradient modulation strength achievable by the gradient system to define a conservative estimate. In Fig. 4.24, this applies to the Y-axis using trapezoidal waveforms (top left) and the "X-Y" axes combination (bottom left), in both case for pulse durations of 1.2 ms.

In the simulations of the Y-axis and the "X-Y+Z" coil combination, a motor nerve of the suprascapular nerve in the neck region was stimulated that innervates muscles attached to the scapula, namely the infraspinatus and supraspinatus muscles. For the "X-Y" coil combination a segment of the radial nerve was stimulated, that innervates triceps muscles as well as muscles in the posterior osteofascial compartment in the forearm. This is in good agreement with observations made during the experiments where some subjects felt sensations in the upper arm/shoulder region.

Figure 4.25 shows the simulated PNS thresholds for the X and Z-gradient coils for both trapezoidal and sinusoidal waveforms. For these gradient axes, no experimental data could be obtained due to limitations of the power amplifiers, that only permitted generation of sub-threshold pulses. The simulated PNS threshold curves, however, are in agreement with this result, in that all simulated thresholds are located beyond the operational region of the gradient system (i.e., outside of the grey area).

5

Discussion

5.1 | Optimal Gradient Waveform Design

In the first part of this work, a novel method for the design of time-optimal gradient trajectories defined by a set of k -space control points was developed and evaluated. A set of four *Gradient Basis Functions* was defined that represent low-level gradient wave shapes (like triangular or trapezoidal shapes). Each gradient basis function consists of three piece-wise linear gradient segments. The entire gradient waveform in each dimension is assembled by concatenating these basis functions. The free parameters of the basis functions – given by the gradient strength vectors in each control point – are optimized using a constrained minimization algorithm, subject to the gradient magnitude constraints (the gradient slew rate constraint is incorporated in the definition of the basis functions; i.e., there is no need to further consider this constraint during the numerical optimization). Note that the *Gradient Basis Function* does not require a pre-defined path constraint. Instead, the shape of the trajectory in between subsequent control points serves as an additional degree-of-freedom to further accelerate traversal of the control points (resulting in an acceleration of $\approx 9\%$ compared to standard methods). Due to the closed-form objective function and semi-analytic expressions for the Jacobian and Hessian, the *Gradient Basis Function* method can generate time-optimal gradient waveforms within few seconds without any significant numerical perturbations (no error in exact traversal of the control points and no violations of the gradient system constraints).

A comprehensive comparison of the *Gradient Basis Function* method with the *Optimal Control* method was performed using gradient waveforms that were computed based on sets of randomly distributed k -space control points. Furthermore, examples for more practical 3-D gradient trajectories (concentric shells and cross trajectories) were given. The question of how to sample k -space efficiently greatly depends on the application. For example, several frameworks for designing short spatially selective excitation pulses have been proposed that compute a set of control points with great impact on the excitation fidelity [16, 35] using an orthogonal matching pursuit [7]. In this approach, the requirement of accurately traversing the control points outweighs other aspects like uniform sampling density. In other applications that utilize uniform gradient trajectories, the selection of feasible control points may be more complex. If control points are chosen to design common 3-D trajectories like concentric shells or stacks-of-spirals, the utilization of additional constraints (like fixed gradient strengths, directional constraints, etc.) proved very effective in enforcing the anticipated shape (and thus the k -space sampling pattern) of the trajectory.

The *Gradient Basis Functions* were defined such that every piece-wise linear gradient segment is driven at the slew rate constraint (e.g., at the ramps of a trapezoid) or kept at a constant gradient strength (e.g., at the trapezoidal flat top phase). This is an important property of the proposed method, because during the numerical optimization of the gradient strengths in the control points, the slew rate constraint (S_{\max}) is not considered any further (the optimization is only constrained by the gradient magnitude constraint (G_{\max})). However, for certain types of trajectories, this fact makes the resulting gradient waveforms rather challenging for the scanner's gradient system. In fact, the proposed gradient design method often creates rather short phases at which the gradient magnitude is changed at the maximum slew rate, causing short "spikes" in the slew rate waveforms (see. Figs. 4.3, 4.4, and 4.5). In most case, however, these spikes can be removed in a very simple post-processing step. For example, if an exemplary 1 ms gradient waveform in between two control points is only switched for a 0.1 ms phase at $+S_{\max}$, while being constant during the remaining 0.9 ms, this section of the gradient can be modified such that the gradient is switched at 10% of $+S_{\max}$ during the entire 1 ms phase. This simple step does not change the total integral of the gradient waveform (i.e., traversal of the control points is maintained), but creates a smoother trajectory that is less challenging for the gradient system amplifiers.

Another aspect to improve the practicability of the resulting gradient waveforms might be to smooth the waveforms to reduce the level of eddy currents created by the rapid switching of the fields. Since modifications applied to a time-optimal gradient waveform necessarily introduce constraint violations, the gradient waveform need to be decelerated mildly to ensure that the smoothed gradients are conform with the gradient system specifications. Promising results were achieved using a gradient waveform smoothing based on an adjusted radial basis function approximation [103, 102]. This smoothing approach guarantees that the integral of the gradient waveforms (and thus the traversal of the control points) is maintained and the gradient system constraints are satisfied. Additionally, the impulse response function of the gradient system may be useful to predistort the generated waveforms in a way that eddy current effects are compensated. A powerful approach called the *Gradient Impulse Response Function* (GIRF) method has been proposed by Vannesjo et al. [119].

Vaziri et al. published an extension of the *Optimal Control* method [120]. For simple spiral trajectories, deformations were applied to the k -space path constraint that shortened the duration by up to 10 %, referred to as *Rounded Diamond Trajectories*. These deformed spiral trajectories are very similar to those designed by the *Gradient Basis Function* method proposed in this work, using four control points per spiral revolution (cf. Fig. 4.1). Note that the proposed diamond spirals represent a special solution of the time-optimal trajectory design problem. As opposed to that, the *Gradient Basis Function* method is capable of designing k -space trajectories based on an arbitrary set of control points (i.e., with an arbitrary shape), beyond spiral trajectories.

Additionally to the ability of designing strictly time-optimal gradient waveforms, the proposed method can be used to design gradient waveforms tailored to specific applications. For example, with respect to parallel transmission applications, the gradient waveforms can be decelerated locally in order to reduce the SAR (similar to the VERSE principle [54]). This can be achieved by scaling down the gradient strength vectors in the control points and by choosing sub-optimal durations for the gradient segments that connect two subsequent control points (sub-optimal durations can be chosen very easily, because the domain mapping D defines the set of all valid durations, for which the solution mapping S can generate a valid gradient waveform). Both approaches can reduce the k -space velocity locally, which results in reduced RF power deposition and thus lower SAR.

5.2 | Joint Gradient and RF Optimization

In the second part of this work a joint optimization of gradient and pTx RF waveforms for improved excitation of arbitrary 3-D excitation patterns was presented. The gradient trajectories are parameterized using a small number of shape parameters that are optimized numerically using a nested optimization process (the inner optimization loop is the RF design on a constant k -space trajectory, the outer loop is the k -space trajectory optimization). It was found that reducing the dimensionality of the gradient optimization problem by optimization of global shape parameters as opposed to the position of individual control points (there are ≈ 50 control points in a typical trajectory) was critical to yield smooth trajectories with few sharp turns. This yielded fast trajectories that used the gradient system at maximum performance and, in turn, accurate excitations using RF pulses shorter than 5 ms using a conventional clinical gradient system ($G_{\max} = 40$ mT/m and $S_{\max} = 150$ T/m/s).

Although the k -space trajectories are parameterized using a small number of shape parameters, the precise contour of these trajectories in 3-D k -space is defined using control points (there is a one-to-one mapping between a given set of shape parameters and the position of the individual control points in 3-D k -space). Therefore, a key ingredient of the proposed approach is a gradient trajectory design tool that is able to compute trajectories passing through the control points at maximum speed while satisfying the gradient magnitude and slew rate constraints of the gradient system. For this, the method presented in Sec. 3.1 was used [28, 26]. A major advantage of this approach is its high numerical stability. In other words, small perturbations of the position of the control points yield only small changes in the optimal gradient waveforms in this method, which is not always the case with other gradient waveform design strategies such as optimal control methods [109, 55, 71, 120]. Advantages of the proposed approach include its high numerical stability, the fact that gradient performance limits are exactly satisfied (i.e., no G_{\max}/S_{\max} violations) and that the k -space trajectory is guaranteed to exactly traverse the prescribed control points (for an extensive comparison between this gradient trajectory design approach and optimal control, see Fig. 4.2 and Tab. 4.1 which show better performance of the proposed semi-analytic approach in these three metrics compared to optimal control). Because a numerical minimization is used for optimization of the trajectory shape parameters, excellent numerical stability of the gradient waveform design method must be guaranteed for a large class of possible trajectories, including complex non-smooth trajectories that may not be optimal but still need to be explored by the optimization process to converge to the final solution. It was found in this work that the presence of small oscillations, numerical instabilities, and small violations of the gradient system constraints in the gradient waveform design step, which are very hard to avoid when using optimal control methods, prevented convergence of the k -space trajectory optimization process.

The simulations and experiments performed in this work showed that optimization of the shape parameters had a profound effect on the k -space trajectories. The optimization process resulted in trajectories that sampled 3-D k -space in a highly heterogeneous manner in an apparent effort to focus the RF energy to k -space regions that maximally impact the flip angle distribution. For the shells and stack-of-spirals trajectories, the result of the trajectory optimization was a compression of the overall trajectory compared to the unoptimized case. This is likely due to the fact that the coil used in this work has only one row of eight transmit channels and, therefore, creates only mild variations of B_1^+ in the z -direction, which in turn prevents the algorithm from under-sampling k -space in this direction. Under the constraint of limited pulse duration, increasing the sampling density along the z -direction causes $k_{z,\max}$ to decrease for the shells

and stack-of-spirals trajectories. This result was also observed when using a cross trajectory to excite the brain target pattern (Fig. 4.10) but not when using the cross to excite a cubic magnetization target. This is probably due to the fact that the cross trajectory almost perfectly matches the energy deposition pattern of a cube in 3-D k -space, and the algorithm does not change the initial cross trajectory significantly in this case. When robustness to off-resonance effects is enforced, the shape optimization procedure concentrated the energy of the trajectory to the center of k -space. This reduced the resolution of the achieved excitation profile, but significantly improved the off-resonance performance due to the shorter pulse duration.

The parameterized trajectories studied in this work allow the optimizer to adjust the k -space sampling density in a way that is highly non-uniform and tailored to the B_1^+ maps as well as the target magnetization pattern. However, an unwanted property of the optimization problem stated in Eq. 3.56 is the dependence of the optimized result on the initial value of the trajectory shape parameters. It was found that properly setting up the initial values of the shape parameters is crucial. This is related to the fact that the optimization problem that is attempted to be solved is highly non-convex (see Fig. 4.6). In order to initialize the optimization process, the shape parameters were chosen so as to sample the k -space volume defined by the outer portion of the 3-D trajectory more or less uniformly. A choice of initial shape parameters that should be avoided is one associated with a level of k -space undersampling that is beyond the acceleration capability of the transmission coil array (e.g., for an 8-channel transmit array the initial level of undersampling must not exceed a value of 8). Another important consideration is to choose an initial trajectory with a duration that is below the maximum tolerated duration (5 ms in this case). Otherwise early iterations are used to reduce the pulse duration without improvement in the flip angle error which unnecessarily increases computation time.

During the development of the joint gradient and RF pulse optimization framework, it was found that implementation details were important to ensure fast convergence of the proposed method. As discussed previously, a robust and numerically highly stable gradient trajectory design algorithm is crucial. Additionally, shape parameters that were of integer type warranted special treatment in the optimization process. Indeed, the shape parameters control non-continuous features of the trajectory such as the number of shells or the number of spirals per stack. As was shown in Fig. 4.7, a "naïve" implementation of the optimization of these parameters leads to large discontinuities in the optimization metrics (both the flip angle NRMSE and the pulse duration, which is penalized in the objective function), which would cause the algorithm to diverge or stop prematurely. A simple solution to this problem is to vary these integer parameters in a way that the creation of a new "entity" (such as a new shell or new spiral) does not cause discontinuities in the objective function. This is achieved by initializing newly created entities with infinitely small k -space extent (see Sec. 3.2.3).

The topology of the least-squares objective function optimized in this work as a function of the shape parameters depends heavily on the type of gradient trajectory and the target flip angle pattern (see Fig. 4.6). It is clear from these investigations that the objective function is continuous but not convex and has several local minima. Therefore, convergence of the proposed approach is limited to local minima (i.e., it cannot be guaranteed that the best of all possible gradient waveforms satisfying the maximum pulse duration constraint of 5 ms can be found in every case). At any rate, the local pulse solutions found by the proposed algorithm seem to be "good enough" as they yield significantly improved flip angle profiles compared to unoptimized gradient waveforms.

In Sec. 3.3 an extension of the RF pulse design framework is presented to allow the design of pulses for uniform slice excitation in presence of severe off-resonance effects (like those present

close to the frontal lobe). In such regions uniform slice excitation is an open problem. The commonly used *Spokes* pulses that achieve very good performance with respect to flip angle uniformization are extremely sensitive to off-resonance effects. If these effects are incorporated in the design of the spokes pulses, the solver usually chooses to only use one of the spokes (the one centered in the $k_{x/y}$ plane) which then results in a common RF shimming pulse. Expressed differently, common spokes pulses can only achieve good flip angle uniformity *or* robustness to off-resonance effects, but not both at the same time. The preliminary results presented in this work illustrate that the proposed shape optimization applied to *Corkscrew* trajectories may overcome these limitations. This was illustrated by designing an RF pulse that achieves uniform slice excitation in the head (close to the frontal lobe) in a wide range of off-resonance frequencies. However, the question whether or not this observation can be confirmed in an experimental setup needs to be addressed. Additionally, an effect that has not yet been investigated is through-slice dephasing from intra-voxel ΔB_0 gradients. However, this effect can easily be incorporated in the design problem stated by Eq. 3.91.

A significant limitation of the proposed trajectory shape optimization approach is its rather long computation time: For the shape optimization at the Larmor frequency computation times ranged from 0.8 to 3.5 hours in the examples studied in this work. Enforcing robustness to off-resonance effects further increased runtime (ranges from 1.3 to 7.7 hours), because of the increased complexity of the RF design problem. In its present form, the technique is, therefore, not usable for patient-specific joint optimization of RF and gradient trajectories. However, computation time could be easily decreased by using multi-threaded implementations, especially using graphical processing units (GPU). For example, an acceleration factor of 100, which is common for applications amenable to GPU acceleration, would yield computation times between 0.5 and 2.1 minutes. Note that matrix operations (like those employed in this work) are highly parallelizable, therefore, optimization of the RF waveform on a constant gradient trajectory, which is the computational bottleneck of the proposed approach, could probably be widely accelerated in this way.

5.3 | Prediction of Magnetostimulation Thresholds

In the last part of this work, a simulation framework was presented for estimating the PNS thresholds for electromagnetic coils such as MRI gradient coils or MPI drive coils operating in the low kHz-range. In the first step, the electromagnetic fields created by the coil are calculated in a realistic body model, as has been reported in numerous previous studies. The effect of these fields on realistic nerve models is predicted, including the relative geometry between field and nerve. The full body peripheral nerve model incorporates the properties of the myelinated fibers allowing the non-linear effect of the fields on membrane potentials to be calculated. The modeled time-dependent waveform is increased in steps to identify the lowest applied field (and thus current amplitude) which initiates an action potential. The location of the stimulation can also be recorded. This process is evaluated by comparing to the published experimental PNS threshold curves for two MPI solenoid coil geometries and three actively-shielded commercial MRI gradient coils.

The PNS simulation method achieved a reasonable agreement with the experimental leg/arm PNS threshold curves, although the lower frequencies studied (0.5 kHz to 1 kHz) had some deviation from the experiments. In this frequency range the threshold is changing very rapidly with frequency and the experimental data has a relatively high inter-individual variance, suggesting

increased variance with patient anatomy. For the MPI applications, the relevant frequency range will likely be above this range (e.g. above 10 kHz), suggesting a good possibility for accurately predicting thresholds. For MRI, frequencies from 0.5 kHz to 2 kHz are relevant for stimulation by the readout gradient. For example, EPI gradient readouts are generally in the 0.75 kHz to 1.5 kHz range. Nonetheless, even a relative prediction between two coil design models can inform the gradient coil optimization process. Furthermore, it is expected that the accuracy of the predicted PNS thresholds in the low kHz-range can be improved by using multiple body models (with matching nerve atlases) of different ages, body-mass indices, and genders. At this stage, the calculations of the PNS threshold was performed for a single female body model and does not yet include estimation of the uncertainty due to the normal biological and anatomical variability of patients undergoing MRI and MPI scans. Experimental results show that the standard deviation across individuals for PNS can be on order of 40% [128, 101], which requires the generation of additional body models, ideally capturing the anatomical variability of the subject population as well as slight differences in placement of the subject within the coil. Current use of experimentally determined thresholds is limited to population average thresholds for a given MRI gradient coil design in setting regulatory limits [20]. The simulation determined PNS thresholds can initially be used in a similar way; to mimic population averages with a small number of body models to allow comparison between MRI gradient designs during an iterative optimization. Full characterization of the population variance will require extensive work and patient-specific modeling of PNS is likely even further off in the future.

The experimental data obtained by Saritas et al. [101] to which the simulated PNS thresholds of the two solenoid coils are compared, possessed a threshold variation over the studied individuals (25th to 75th percentile) of about 30% to 40% for the arm stimulation case and 20% to 28% for the leg stimulation. The results of the preliminary sensitivity analysis to deformations of the nerves relative to other tissues in the model indicate that the model is sensitive to the nerve shape and location relative to other tissues to a level similar to the variability of the experimental data. Note that there are other sources of variability expected for the estimation of PNS thresholds such as variations in the placement of patients in the coil (non-biological), as well as electromagnetic tissue properties *in-vivo* (biological). Another deviation between the simulated and experimental PNS threshold curves are their slightly different shapes (when plotted as a function of frequency). This is likely due to the fact that there are aspects of action potential initiation and propagation that are not yet fully captured by the MRG neurodynamic model. The MRG model is, however, currently one of the most sophisticated nerve models available. The PNS simulation procedure can be updated when more detailed membrane models become available, and might also prove a useful tool for refining these models.

Recordings made by Saritas et al. during the stimulation experiments indicate that the most prominent sites were the proximal forearm and the proximal tibia region, i.e., roughly at the proximal ends of the two stimulation coils (personal communication with Emine Saritas, March 12, 2017). Both motor and sensory sensations occurred in the experiments. In the arm simulations performed in this work, stimulations originated in a branch of the radial nerve that (among others) innervates several muscles at the proximal forearm close to the elbow joint (including extensor carpi radialis longus muscle, extensor carpi radialis brevis muscle, supinator muscle and others). For the leg simulation, the AP first occurred in a sensory nerve: a branch of the saphenous nerve in the proximal tibia region. Although there is reasonable agreement between the site of stimulation reported in the experimental study and simulation results, it is difficult to be sure that the model identified the same nerve segment experienced by the human subjects.

Only modest experimental data is available on the quantitative relationship between the excitability of a nerve fiber and its axon diameter, making it very hard to verify whether the used MRG neurodynamic model correctly describes this relationship. However, from the neurodynamic modelling perspective it is well established that for very small fiber diameters (in the order of $1\ \mu\text{m}$) the stimulation threshold is proportional to the "inverse square" fiber diameter. When increasing the fiber diameter up to $20\ \mu\text{m}$ this relationship progressively approaches an "inverse square root" relationship [80]. This behavior can be verified by a logarithmic plot of the threshold curves shown in Fig. 4.17 B and evaluating the slope of these curves at different fiber diameter points (for example, in the logarithmic plot a slope of -2.0 indicates an "inverse square" relationship, a slope of -0.5 an "inverse square root" relationship). In the simulations carried out in this work, a slope of -1.4 at $5\ \mu\text{m}$ and -1.1 for $16\ \mu\text{m}$ were found which is consistent with previous observations (a slope of -2.0 at $2\ \mu\text{m}$ and a slope of -0.5 at $20\ \mu\text{m}$, with a continuous progression for intermediate diameters). However, some deviation is expected due to the effect of the myelin insulation which is not explicitly modeled in the other neurodynamic models. These previously published results indicate that the MRG neurodynamic model satisfactorily describes the dependence of the PNS thresholds on axon diameter.

In this work the PNS threshold is defined as the field modulation strength where the first AP is initiated in any of the nerve segments in the simulated part of the body model. In fact for very sensitive areas of the human body (skin, lips) it is well known that even a single AP in a single sensory nerve fiber already produces a sensible perception [85]. However, for motor nerves (which are the nerves that are first stimulated in the arm solenoid), a single AP in a single nerve fiber may not produce a sensible muscle contraction. Nonetheless it is expected that the PNS threshold for single AP generation is very close to the threshold for a perceivable sensation for two reasons. Firstly, motor nerves possess a rather short refractory period in the order of $2\ \text{ms}$, allowing for a repetition frequency of about $500\ \text{Hz}$ (the refractory period decreases when increasing the fiber diameter, meaning that motor nerves achieve a higher AP repetition frequency than sensory nerves [8]). Since the stimulation pulses used in this work usually have the same or higher frequencies ($460\ \text{Hz}$ to $10.6\ \text{kHz}$), the stimulation pulse at the PNS thresholds will generate multiple APs, one after each recovery cycle (roughly every 2 to $3\ \text{ms}$ [66], cf. Fig. 4.16). Secondly, for healthy subjects the fiber diameter distribution of motor nerves in a single nerve fiber is rather sharp meaning that the different nerve fibers possess very similar stimulation thresholds [36] (as opposed, e.g., to patients suffering from Multiple Sclerosis, where demyelination of the nerve fibers causes of broader distribution of the stimulation thresholds). Along with the fact that the entire nerve fiber bundle can be considered to experience the same local electric field, this means that the threshold for the very first AP in a single fiber (which may not be perceivable, especially for motor nerves) and the threshold for initiation of a larger number of APs in various fibers of the same nerve bundle (causing a perceivable sensation) should only differ very mildly.

It was found that accurate modeling of the PNS threshold curves required very careful definition of the "nerve segments", which are used in this work to split the whole-body nerve tree into computationally manageable sections. For example if an external electric field stimulates the nerve segment at the periphery of the nerve (as opposed to the central nodes of Ranvier of the segment), this often leads to an underestimation of PNS thresholds. On the other hand, if nerve segments are defined with knowledge of the electric field in order to guarantee that the strongest electric potential change always occurs at the center of a segment, accurate prediction of AP initiation is possible. This approach was validated by comparison of PNS stimulation of very long nerve segments.

The results obtained in this work indicate that the nerve membrane dynamics are rather sensitive to even small anatomical details of the body model. In fact, small structures, especially bottle-necking structures, may have a more prominent impact on the electric field hotspots than large, uniform structures. In the simulations presented in this work, the largest E -field hotspots often occurred in regions where a well-conducting tissue geometry narrows (as highlighted in Fig. 4.18 B and 4.18 E). Additionally it was found that thin layers of low conductivity tissues (like fatty tissue) enclosed by high conductivity tissues (like muscles) may act as a capacitance creating high E -fields in the insulating layer. If a nerve fiber passes through these regions, this might facilitate stimulation. However, the effect of the level of detail of the body model on the accuracy of the PNS threshold curves has not yet been quantified. Ideally the body model should be simplified as much as possible (to decrease computation time of the EM field simulations), while ensuring accurate PNS threshold curves. Additional investigations are needed to determine the most important properties of the body model such as the required number of tissue classes, distribution of fatty tissue, or spatial properties of the tissue objects (note that a rather large thickness of 3 mm was used for the skin, which significantly simplified meshing).

The detailed nerve atlas was, of course, central to the PNS simulations in this work. PNS is modulated by the relative angle of the imposed electric field to the nerve fiber. Thus the PNS effect is different from scalar parameters such as Specific Absorption Rate (SAR) which quantifies energy deposition from the much faster oscillations of the applied radio frequency (RF) field which are in the MHz range. The electric fields responsible for SAR are too fast for the nerve membranes to respond to, and simply cause heating of the electrically lossy tissue. Thus SAR is determined by the strength and duration of the applied RF fields, the magnitude of the induced E -fields and the conductivity of the tissue. SAR is relevant at considerably higher frequencies than considered in the PNS simulations performed in this work. Roughly speaking, SAR becomes the dominant concern for applied fields above 5 MHz. In contrast, PNS is the dominant concern for the oscillation frequencies of approx. 500 Hz to 10 kHz studied here. Unlike SAR where only the magnitude of the E -field matters both the strength and direction relative to the nerve segment determine the local PNS threshold. This, together with the observed electric field hot-spots, means that it is critical to know the exact locations and orientations of the nerves with respect to the rest of the body model. The information about location and orientation of the major nerve fibers is encoded by the developed nerve atlas and no manual user input of the nerve fiber properties or location/orientation is required beyond classifying the segment as motor, sensory or autonomous for which a diameter assignment of 16 μm , 10 μm or 2 μm was made (another source of fiber diameter information is measurement of the nerve conduction velocity that depends linearly on the fiber diameter, however, these studies are limited to a few major nerve tracks like radial, sural, tibia nerves [24]). The detailed nerve properties for each of these diameters are then dictated by McIntyre et al. [79]. Nonetheless, experimental threshold measurements show variance across individuals suggesting that the use of multiple body models may be useful to get a more complete simulation of the range of responses. The experimental variance might also result from variations in body position within the coil. The relative importance of these two sources of variance could be assessed from studies re-positioning an individual subject and noting the variance of the PNS thresholds. Finally, while the magnetic field produced by the modeled coils is uniform, the E -field pattern is far from uniform. This underscores the importance of the geometry of the conductive tissues in shaping the current flow, thus the electric field is in contrast to the near transparency of the body to the magnetic field at the studied frequencies. It also suggests the importance of the nerve model accurately reflecting nerve locations within the tissue.

The simulations carried out in this work (Fig. 4.17) are consistent with previous physiological experiments [121, 37] and theoretical investigations [80, 3, 15] showing that nerves with larger fiber diameters are excited more easily than smaller ones and, therefore, tend to determine the PNS threshold. This is fortunate for the efforts made in this work since it means that it may not be necessary to model the smallest fibers. In the human body, the largest fibers are those that innervate the neuromuscular spindles, so-called A- α fibers, with fiber diameters of about 10-20 μm and conduction velocities of up to 120 m/s [108]. Muscular spindles are motor receptors that detect information about length changes of a muscle. The associated nerves transmit this information to the CNS that initiates a reflex in terms of a muscle contraction (such as the patellar reflex or "knee reflex"). This phenomenon is often observed in MRI experiments where PNS sensations in the extremities are experienced as reflex-like muscle contractions. It seems to be a reasonable assumption, that any nerve bundle that contains motor nerves also contains at least a small fraction of these large nerve fibers. The AP generation observed at the PNS threshold for the arm case (Fig. 4.18 F) resulted from stimulation of this kind of motor nerve fibers with 16 μm diameter. For nerve bundles that solely contain sensory nerves (such as in the fingers that do not contain muscle tissue), the largest nerve fibers are so-called A- β fibers whose diameter is in the range of 7-15 μm with conduction velocities of up to 70 m/s (in the leg case shown in Fig. 4.18 C, a sensory nerve fiber was stimulated first). Unmyelinated nerve fibers such as the ones controlling the digestive system (so-called C-fibers, in the order of 1 μm diameter, up to 2 m/s conduction velocity) are hard to stimulate by external E -fields and, therefore, may be ignored in this context. The same holds for cardiac nerves, that possess an up to 200-fold higher stimulation threshold compared to motor fibers [61]. However, there is evidence [104] that the thresholds for PNS and cardiac stimulation converge for long pulse durations. It would be interesting to see if an extension of the proposed PNS simulation framework could validate this effect, however, several changes to this model would be needed. The MRG neurodynamic model used in this work was designed for fiber diameters ranging from 5 μm to 16 μm and may not be suitable for simulation of cardiac nerves (having fiber diameters of approx. 1 μm). Thus other neurodynamic model approaches that are more appropriate to autonomous nerve fibers are needed [70, 116]. Another possibility is to extrapolate the MRG model parameters to these fiber diameters, however, it needs to be ensured that these extrapolated parameters model the associated nerve fibers reasonably well. An updated neurodynamic model, together with a more complete depiction of cardiac nerves than found in the Zygote model may allow the expansion of the simulation approach beyond motor and sensory nerves, and shed light on the relationship between cardiac and peripheral nerve thresholds.

In Sec. 4.5, preliminary PNS simulation results based on three actively-shielded MRI gradient coils are shown. The experimental and simulated PNS threshold curves were obtained for both trapezoidal and sinusoidal gradient waveforms using single gradient axis stimulation ("X", "Y" and "Z") and combined gradient axes stimulation (in particular "X-Y" and "X-Y+Z"). There was reasonable agreement between the experimental and simulated PNS threshold curves, although the PNS simulations overestimated the experimental threshold curves. The simulated thresholds were 10 – 20% higher than the measured thresholds and thus right "on top" of the experimental standard deviation of 15%. We believe that this overestimation may be ascribed to different aspects: Firstly, it has often been observed that women tolerate higher magnetic field strengths before experiencing PNS. Most certainly, this is due to the combination of (on average) higher body fat percentage and smaller body cross-section (compared to men) which both decrease the strength of the electric fields imposed by the gradient coils. Hopefully, this gender-specific threshold dependence can be reproduced in the future work by development of a second male

body model. A second reason for overestimation of the experimental PNS thresholds might be the spatial resolution of the EM field simulation which was limited to 1 mm for the gradient coil simulations due to the hexahedral simulation mesh used in this case (tetrahedral simulation meshes which were used for simulation of the leg/arm solenoid coils allow for much higher spatial resolution of the body model and the induced EM fields). Other aspects like the level of detail of the surface body model required for accurate PNS prediction (especially with respect to crucial features like thin layers of fatty tissue that often induce electric field hot-spots due to capacitance effects) are subject to future investigations. We are currently improving the processing pipeline of the body model generation to preserve anatomical features which we have found to be important in order to accurately reproduce PNS thresholds. Despite the slight overestimation of the PNS thresholds, we believe that these preliminary gradient coil results demonstrate the applicability of our PNS simulation framework to highly complex wire patterns (especially given the complexity of the entire PNS prediction pipeline).

In this work, we concentrate on introducing and validating our modeling framework. The degree to which this framework can improve MRI gradient or MPI coil design is an important open question. The introduced methods are, at best, necessary, but not sufficient for improving design and may not be better than existing approaches which note that PNS correlates well with volume of the linear region of the gradient for conventional designs [128]. It is, therefore, likely that simply modulating existing designs, such as scaling or mildly altering wire density will result in PNS threshold changes that are already described by the current PNS scaling arguments. To go beyond this, unconventional design approaches will likely be needed, especially those that introduce degrees-of-freedom which can be exploited in an optimization framework. To this end, we note that new approaches are starting to emerge, such as the recent PatLoc coil comprising 84 independently drivable loops [68], that perhaps offer both the degrees-of-freedom and necessary departure from standard design, but currently this observation is unproven.

Despite the role PNS plays in limiting the application of kHz-range magnetic fields in MRI and MPI methods, relatively few tools exist to predict PNS thresholds based on a specific coil wire pattern. Instead proxies for direct prediction, such as the volume or length [128, 69, 122] of the linear gradient region are used to inform the design. In this work, we build on previous work simulating the relevant E -fields in the human body to attempt to predict stimulation thresholds and locations based on nerve and tissue geometry rather than coil metrics such as length or volume of the linear gradient region. We also build on previous work assessing how E -fields induced in the human body interact with a nerve segment, informed from dynamic nerve models. We add a general nerve atlas, labeled with the relevant nerve model parameters and in registration with the predicted local E -fields to be able to accurately predict PNS thresholds for experimental coil configurations.

6

Summary

This thesis presents methods to characterize and minimize the effect of electric fields arising from rapid switching of the gradient and RF fields to accelerate spatial encoding and signal excitation in MRI.

In the first part of this work, a robust method for the design of time-optimal gradient waveforms subject to G_{\max} and S_{\max} constraints was developed. The shape of the gradient trajectory is specified by an ordered set of control points in k -space. This means that unlike most previously proposed methods, this approach does not require a path constraint in k -space. Instead the exact shape between control points is chosen by the optimizer so as to minimize the total duration. The gradient waveforms are assembled by concatenation of piece-wise linear gradient segments (yielding piece-wise quadratic trajectory segments). The exact length and slope of each linear gradient segment is optimized via a numerical optimization. The number of degrees-of-freedom to be optimized is reduced by formulating semi-analytic *Gradient Basis Functions* (that define a general arrangement of the linear gradient segments like triangular or trapezoidal shapes). As a result of this semi-analytic waveform representation, the optimization can be performed very quickly (within a few seconds) and is not prone to numerical perturbations. Compared to the leading competing Optimal Control approach, significant improvements were achieved in terms of duration of the trajectory (in average 9.2% acceleration), computation time (acceleration by at least 25% up to factors of 500), and robustness (no significant numerical instabilities).

In the second part of this work, the previously described Gradient Basis Function method was used to design 3-D spatially selective excitation pulses using multiple transmit channels (parallel transmission or pTx). A method is proposed for the joint optimization of gradient and pTx RF waveforms. The method derives solutions that equally exploit the gradient system (constrained by maximum strength and slew rate) and the RF system (characterized by sensitivity profiles, number of transmit channels, peak power and off-resonance characteristics). The joint optimization framework was implemented as a nested optimization problem: the inner optimization loop optimizes the RF waveforms for a given gradient trajectory, and the outer loop optimizes the shape of the trajectory. This shape optimization is performed by defining a small set of shape parameters of the k -space trajectory. The shape parameters define simple geometric properties of the k -space trajectory like the sampling density along different k -space axes or the maximum k -space frequency to be covered by the trajectory. The shape parameters were carefully defined to ensure that the trajectory (and thus the flip angle error) vary smoothly. The definition of shape parameters effectively reduces the number of degrees-of-freedom from several hundreds to less than ten. The framework was demonstrated for overall four trajectory types: Concentric

Shells, Stack-of-Spirals, Cross trajectories (these were used to excite 3-D magnetization targets) as well as Corkscrew trajectories for uniform slice-excitation in presence of severe off-resonance effects. It was demonstrated that the proposed joint optimization framework yields ultra-short 3-D selective RF pulses (less than 5 ms) with excellent flip angle performance (cubic target with 3.4% NRMSE, brain-shaped target with 6.2% NRMSE). Additionally, it was shown that using a spatial-spectral pulse design to improve robustness to off-resonance frequencies significantly alters the k -space trajectory solutions and improves the practical performance of the pulses. The framework was further applied to the problem of designing RF pulses for uniform slice-excitation in presence of off-resonance frequencies. It was demonstrated that the proposed Corkscrew RF pulses might overcome the limitations of the commonly used Spokes pulses, which either achieve uniform slice-profiles or robustness to off-resonance effects, but not both at the same time. The first results obtained using Corkscrew RF pulses indicate that the slice uniformity was improved by at least a factor of two, while maintaining this level of uniformity in a wide range of off-resonance frequencies (± 200 Hz). A major limitation of the proposed gradient and pTx RF design method is the computation time (up to a few hours per RF pulse), however, this can be significantly shortened by using GPU computations (which usually achieves acceleration factors of 100 and more).

The last part of this thesis investigated a more fundamental approach to overcoming gradient switching limitations. Since current gradient systems can be constructed that can operate with performance limits (G_{\max} and S_{\max}) that cannot be applied to humans due to PNS, tools are needed to study the origins of these biological limitations. Ultimately a method is needed that allows PNS thresholds to be included in the gradient coil optimization process as an additional penalty term, in a similar way that field generation efficiency, linearity and heating are currently incorporated. Despite being a major constraint, PNS is only considered indirectly in the coil design process, mainly through limiting the size of the linear gradient region; a poor proxy for the actual PNS thresholds. In this work, a method was proposed that allows prediction of PNS thresholds for realistic coil geometries for the first time. With this method, the PNS threshold of a gradient wire pattern can be evaluated in the design stage, allowing iterative improvements of performance with respect to this metric in a similar fashion to what is currently done for electrical efficiency and heating metrics. For these simulations, a novel high-resolution body model for use in electromagnetic field simulations was developed. A pre-processing pipeline was developed that generates a watertight non-intersecting surface-based representation of the body model. This type of body model can be processed by tetrahedral and hexahedral finite-element methods to simulate the magnetic and electric fields induced by the coil geometry under consideration. To evaluate the capability of the electric fields to cause PNS, a nerve atlas was developed that exactly matches the body model used for the field simulations. The nerve atlas encodes the path of the major peripheral nerve tracks in the human body (about 1800 nerve tracks are included). Each single nerve track is labeled with properties of the nerve fibers, including the axon diameter which affects the excitability of the nerves. The simulated electric fields are superimposed to the nerve atlas, projected onto the path of the nerves and then integrated to obtain electric potential changes along the nerve fibers. The effect of these electric potential changes (including possible action potentials) is simulated using a double-cable electrical circuit model of mammalian nerve fibers, referred to as the McIntyre-Richardson-Grill model. The potential changes along the nerve fiber are modulated in time by the coils driving waveform and increased in strength until an action potential is predicted by the neurodynamic model in one of the nerves (an action potential is taken as an indicator for PNS). This stimulation process is performed for different

frequencies, pulse lengths, and pulse shapes yielding characteristic PNS threshold curves. These threshold curves are usually obtained experimentally (using clinical studies based on healthy human subjects) and thus can only be assessed after the design process (after construction of the coil). The proposed simulation framework was evaluated based on simple leg/arm solenoid coils as well as commercial actively-shielded MR gradient coils. It was shown – for the very first time – that clinically obtained PNS threshold curves can be reproduced using a realistic body model in conjunction with a nerve atlas and a neurodynamic model. This is the first tool that allows to assess the PNS capability of gradient coils at the design phase, without building expensive prototype coils.

Bibliography

1. Basser, P. J. and Roth, B. J. Stimulation of a myelinated nerve axon by electromagnetic induction. *Medical and Biological Engineering and Computing*, 29(3):261–268, 1991.
2. Basser, P. J., Wijesinghe, R. S., and Roth, B. J. The activating function for magnetic stimulation derived from a three-dimensional volume conductor model. *IEEE Transactions on Biomedical Engineering*, 39(11):1207–1210, Nov 1992.
3. Basser, P. J. Scaling Laws for Myelinated Axons Derived From an Electronic Core-Conductor Model. *Journal of Integrative Neuroscience*, 03(02):227–244, 2004.
4. Ben-Israel, A. and Mond, B. What is invexity? *The Journal of the Australian Mathematical Society. Series B. Applied Mathematics*, 28(1):1–9, 1986.
5. Birgin, E. G., Martinez, J. M., and Raydan, M. Nonmonotone Spectral Projected Gradient Methods on Convex Sets. *SIAM J. Optim.*, 10(4):1196–1211, Jan 2000.
6. Bloch, F. Nuclear induction. *Physical review*, 70(7-8):460, 1946.
7. Blumensath, T. and Davies, M. E. On the difference between orthogonal matching pursuit and orthogonal least squares. 2007.
8. Borg, K. and Borg, J. Conduction velocity and refractory period of single motor nerve fibres in antecedent poliomyelitis. *Journal of Neurology, Neurosurgery & Psychiatry*, 50(4):443–446, 1987.
9. Börnert, P. and Aldefeld, B. On spatially selective RF excitation and its analogy with spiral MR image acquisition. *Magnetic Resonance Materials in Physics, Biology and Medicine*, 7(3):166–178, 1998.
10. Bossetti, C. A., Birdno, M. J., and Grill, W. M. Analysis of the quasi-static approximation for calculating potentials generated by neural stimulation. *Journal of neural engineering*, 5(1):44, 2007.
11. Bottomley, P. A. Spatial Localization in NMR Spectroscopy in Vivo. *Annals of the New York Academy of Sciences*, 508(1):333–348, 1987.
12. Bowtell, R. and Bowley, R. Analytic calculations of the E-fields induced by time-varying magnetic fields generated by cylindrical gradient coils. *Magnetic Resonance in Medicine*, 44(5):782–790, 2000.
13. Budinger, T. F., Fischer, H., Hentschel, D., Reinfelder, H.-E., and Schmitt, F. Physiological effects of fast oscillating magnetic field gradients. *Journal of computer assisted tomography*, 15(6):909–914, 1991.

14. Byrd, R. H., Hribar, M. E., and Nocedal, J. An Interior Point Algorithm for Large-Scale Nonlinear Programming. *SIAM J. Optim.*, 9(4):877–900, Jan 1999.
15. Carbutaru, R. and Durand, D. M. Axonal stimulation under MRI magnetic field z gradients: A modeling study. *Magnetic Resonance in Medicine*, 38(5):750–758, 1997.
16. Chen, D., Bornemann, F., Vogel, M., Sacolick, L., Kudielka, G., and Zhu, Y. Sparse parallel transmit pulse design using orthogonal matching pursuit method. In *Proceedings of the 17th Annual Meeting of ISMRM, Honolulu, Hawaii, USA*, page 171, 2009.
17. Chronik, B. A. and Ramachandran, M. Simple anatomical measurements do not correlate significantly to individual peripheral nerve stimulation thresholds as measured in MRI gradient coils. *Journal of Magnetic Resonance Imaging*, 17(6):716–721, 2003.
18. Chronik, B. A. and Rutt, B. K. Simple linear formulation for magnetostimulation specific to MRI gradient coils. *Magnetic Resonance in Medicine*, 45(5):916–919, 2001.
19. Cohen, M. S., Weisskoff, R. M., Rzedzian, R. R., and Kantor, H. L. Sensory stimulation by time-varying magnetic fields. *Magnetic Resonance in Medicine*, 14(2):409–414, 1990.
20. International Electrotechnical Commission: Medical electrical equipment – Part 2–33: Particular requirements for the safety of magnetic resonance diagnostic devices. Technical report, IEC 60601-2-33, 2010.
21. Courant, R., Friedrichs, K., and Lewy, H. Über die partiellen Differenzengleichungen der mathematischen Physik. *Mathematische Annalen*, 100(1):32–74, 1928.
22. Dale, B. M. and Duerk, J. L. Time-optimal control of gradients. In *Proceedings of the 10th Annual Meeting of ISMRM, Honolulu, Hawaii, USA*, page 2361, 2002.
23. Danner, S. M., Wenger, C., and Rattay, F. *Electrical stimulation of myelinated axons: An interactive tutorial supported by computer simulation*. VDM, Saarbrücken, 2011.
24. Daube, J. R. and Rubin, D. I. Nerve conduction studies. *Aminoff's Electrodiagnosis in Clinical Neurology*, 6:290–6, 2012.
25. Davey, K. R., Cheng, C. H., and Epstein, C. M. Prediction of magnetically induced electric fields in biological tissue. *IEEE Transactions on Biomedical Engineering*, 38(5):418–422, May 1991.
26. Davids, M., Ruttorf, M., Zöllner, F., and Schad, L. Fast and Robust Design of Time-Optimal k-Space Trajectories in MRI. *Medical Imaging, IEEE Transactions on*, 34(2): 564–577, Feb 2015.
27. Davids, M., Guérin, B., Schad, L. R., and Wald, L. L. Optimization of fast k-space trajectories for 3D spatially selective parallel excitations. *Proceedings of the 22nd Annual Meeting of ISMRM, Milan, Italy*, 2014.
28. Davids, M., Ruttorf, M., Zöllner, F. G., and Schad, L. R. Fast and robust design of time-optimal k-space trajectories. *Proceedings of the 22nd Annual Meeting of ISMRM, Milan, Italy*, 2014.

29. Davids, M., Guérin, B., Schad, L. R., and Wald, L. L. Ultra-fast inner volume excitations with parallel transmission at 7 Tesla using fully optimized B₀-robust k-space trajectories. *Proceedings of the 23rd Annual Meeting of ISMRM, Toronto, Canada*, 2015.
30. Davids, M., Schad, L. R., Wald, L. L., and Guérin, B. Fast three-dimensional inner volume excitations using parallel transmission and optimized k-space trajectories. *Magnetic Resonance in Medicine*, 76(4):1170–1182, 2015.
31. Davids, M., Guérin, B., Schad, L. R., and Wald, L. L. Realistic Simulation of Peripheral Nerve Stimulations in Magnetic Particle Imaging for Improved MPI Molecular Imaging in Humans. *Proceedings of the World Molecular Imaging Congress, New York, NY, USA*, 2016.
32. Davids, M., Guérin, B., Wald, L. L., and Schad, L. R. B₀-Robust Slice-Selective Excitations for Ultra-High Field with Flip-Angle Mitigation Using Parallel Transmission. *Proceedings of the 24th Annual Meeting of ISMRM, Singapore*, 2016.
33. Davids, M., Guérin, B., Schad, L. R., and Wald, L. L. Wald. Predicting Magnetostimulation Thresholds in the Peripheral Nervous System using Realistic Body Models. *Scientific Reports, UK*, page 5316, 2017.
34. Davids, M., Guérin, B., Schad, L. R., and Wald, L. L. Modeling of Peripheral Nervous Stimulation Thresholds in Realistic Body Models. *Proceedings of the 25th Annual Meeting of ISMRM, Honolulu, HI, USA*, 2017.
35. Deniz, C. M., Chen, D., Alon, L., Brown, R., Fautz, H.-P., Sodickson, D. K., and Zhu, Y. Sparse Parallel Transmit Excitation Trajectory Design for Rapid Inner-Volume Excitation. *Proceedings of the 21st Annual Meeting of ISMRM, Salt Lake City, Utah, USA*, 2013.
36. Dyck, P. J. and Thomas, P. K. *Peripheral Neuropathy*. Elsevier, 4 edition, 2005.
37. Enoka, R. M. Activation order of motor axons in electrically evoked contractions. *Muscle & nerve*, 25(6):763–764, 2002.
38. Fautz, H., Vogel, M., Gross, P., Kerr, A., and Zhu, Y. B₁ mapping of coil arrays for parallel transmission. In *Proceedings of the 16th Annual Meeting of ISMRM, Toronto, Canada*, page 1247, 2008.
39. Frahm, J., Merboldt, K., Hänicke, W., and Haase, A. Stimulated echo imaging. *Journal of Magnetic Resonance (1969)*, 64(1):81 – 93, 1985.
40. Frankenhaeuser, B. and Huxley, A. F. The action potential in the myelinated nerve fibre of *Xenopus laevis* as computed on the basis of voltage clamp data. *The Journal of Physiology*, 171(2):302–315, 1964.
41. Gabriel, C. Compilation of the Dielectric Properties of Body Tissues at RF and Microwave Frequencies. Technical report, King's College London (United Kingdom), Department of Physics, 1996.
42. Glover, P. M. Interaction of MRI field gradients with the human body. *Physics in Medicine and Biology*, 54(21):R99, 2009.

43. Goodwill, P. W. and Conolly, S. M. The X-Space Formulation of the Magnetic Particle Imaging Process: 1-D Signal, Resolution, Bandwidth, SNR, SAR, and Magnetostimulation. *IEEE Transactions on Medical Imaging*, 29(11):1851–1859, Nov 2010.
44. Gosselin, M.-C., Neufeld, E., Moser, H., Huber, E., Farcito, S., Gerber, L., Jedensjö, M., Hilber, I., Gennaro, F. D., Lloyd, B., Cherubini, E., Szczerba, D., Kainz, W., and Kuster, N. Development of a new generation of high-resolution anatomical models for medical device evaluation: the Virtual Population 3.0. *Physics in Medicine and Biology*, 59(18): 5287, 2014.
45. Grissom, W., Yip, C.-Y., Zhang, Z., Stenger, V. A., Fessler, J. A., and Noll, D. C. Spatial domain method for the design of RF pulses in multicoil parallel excitation. *Magnetic Resonance in Medicine*, 56(3):620–629, 2006.
46. Groppa, S., Oliviero, A., Eisen, A., Quartarone, A., Cohen, L., Mall, V., Kaelin-Lang, A., Mima, T., Rossi, S., Thickbroom, G., et al. A practical guide to diagnostic transcranial magnetic stimulation: report of an IFCN committee. *Clinical Neurophysiology*, 123(5): 858–882, 2012.
47. Guérin, B., Stockmann, J., Baboli, M., Stenger, A. V., and Wald, L. L. Fully optimized time-shifted radio-frequency spoke pulses for simultaneous reduction of intra-voxel dephasing, flip-angle non-uniformity and the specific absorption rate at ultra-high field using parallel transmission. *Proceedings of the 23rd Annual Meeting of ISMRM, Toronto, Canada*, 2015.
48. Guérin, B., Stockmann, J. P., Baboli, M., Torrado-Carvajal, A., Stenger, A. V., and Wald, L. L. Robust time-shifted spoke pulse design in the presence of large B₀ variations with simultaneous reduction of through-plane dephasing, B₁₊ effects, and the specific absorption rate using parallel transmission. *Magnetic Resonance in Medicine*, pages 540–554, 2015.
49. Haacke, E. M., Brown, R. W., Thompson, M. R., and Venkatesan, R. *Magnetic resonance imaging: physical principles and sequence design*, volume 1. Wiley-Liss New York:, 1999.
50. Haase, A., Frahm, J., Matthaei, D., Hänicke, W., Bomsdorf, H., Kunz, D., and Tischler, R. MR imaging using stimulated echoes (STEAM). *Radiology*, 160(3):787–790, 1986. PMID: 3737918.
51. Handler, W. B., Harris, C. T., Scholl, T. J., Parker, D. L., Goodrich, K. C., Dalrymple, B., Van Sass, F., and Chronik, B. A. New head gradient coil design and construction techniques. *Journal of Magnetic Resonance Imaging*, 39(5):1088–1095, 2014.
52. Hanson, M. A. On sufficiency of the Kuhn-Tucker conditions. *J. Math. Anal. Appl.*, 80(2): 545 – 550, 1981.
53. Hardy, C. J. and Cline, H. E. Spatial localization in two dimensions using NMR designer pulses. *Journal of Magnetic Resonance (1969)*, 82(3):647 – 654, 1989.
54. Hargreaves, B. A., Cunningham, C. H., Nishimura, D. G., and Conolly, S. M. Variable-rate selective excitation for rapid MRI sequences. *Magnetic Resonance in Medicine*, 52(3): 590–597, 2004.

55. Hargreaves, B. A., Nishimura, D. G., and Conolly, S. M. Time-optimal multidimensional gradient waveform design for rapid imaging. *Magnetic Resonance in Medicine*, 51(1):81–92, 2004.
56. Hebrank, F. X. and Gebhardt, M. SAFE model – a new method for predicting peripheral nerve stimulation in MRI. In *Proceedings of the 8th Annual Meeting of ISMRM, Denver*, page 2007, 2000.
57. Hendrikse, J., van der Grond, J., Lu, H., van Zijl, P. C., and Golay, X. Flow Territory Mapping of the Cerebral Arteries With Regional Perfusion MRI. *Stroke*, 35(4):882–887, 2004.
58. Hestenes, M. R. and Stiefel, E. Methods of conjugate gradients for solving linear systems. *Journal of Research of the National Bureau of Standards*, 49(6), Dec 1952.
59. Hines, M. L. and Carnevale, N. T. The NEURON simulation environment. *Neural computation*, 9(6):1179–1209, 1997.
60. Hodgkin, A. L. and Huxley, A. F. A quantitative description of membrane current and its application to conduction and excitation in nerve. *The Journal of physiology*, 117(4): 500–544, 1952.
61. Irnich, W. Electrostimulation by time-varying magnetic fields. *Magnetic Resonance Materials in Physics, Biology and Medicine*, 2(1):43–49, 1994.
62. Irnich, W. and Hebrank, F. X. Stimulation threshold comparison of time-varying magnetic pulses with different waveforms. *Journal of Magnetic Resonance Imaging*, 29(1):229–236, 2009.
63. Irnich, W. and Schmitt, F. Magnetostimulation in MRI. *Magnetic Resonance in Medicine*, 33(5):619–623, 1995.
64. Jansen, J. F. A., Backes, W. H., Nicolay, K., and Kooi, M. E. 1H MR Spectroscopy of the Brain: Absolute Quantification of Metabolites. *Radiology*, 240(2):318–332, 2006. PMID: 16864664.
65. Katscher, U., Börnert, P., Leussler, C., and van den Brink, J. S. Transmit sense. *Magnetic Resonance in Medicine*, 49(1):144–150, 2003.
66. Kimura, J., Yamada, T., and Rodnitzky, R. Refractory period of human motor nerve fibres. *Journal of Neurology, Neurosurgery & Psychiatry*, 41(9):784–790, 1978.
67. Krasteva, V. T., Papazov, S. P., and Daskalov, I. K. Peripheral nerve magnetic stimulation: influence of tissue non-homogeneity. *BioMedical Engineering OnLine*, 2(1):19, 2003.
68. Kroboth, S., Layton, K. J., Jia, F., Littin, S., Yu, H., Hennig, J., and Zaitsev, M. Optimization of a switching circuit for a matrix gradient coil. *Proceedings of the 24th Annual Meeting of ISMRM, Singapore*, 2016.
69. Lee, S.-K., Mathieu, J.-B., Graziani, D., Piel, J., Budenheim, E., Fiveland, E., Hardy, C. J., Tan, E. T., Amm, B., Foo, T. K.-F., et al. Peripheral nerve stimulation characteristics of an asymmetric head-only gradient coil compatible with a high-channel-count receiver array. *Magnetic resonance in medicine*, 2015.

70. Luo, C. H. and Rudy, Y. A model of the ventricular cardiac action potential. Depolarization, repolarization, and their interaction. *Circulation Research*, 68(6):1501–1526, 1991.
71. Lustig, M., Kim, S.-J., and Pauly, J. M. A Fast Method for Designing Time-Optimal Gradient Waveforms for Arbitrary k-space Trajectories. *IEEE Transactions on Medical Imaging*, 27(6):866–873, 2008.
72. Malik, S. J. and Hajnal, J. V. 3D-FSE Inner Volume Imaging using 3D selective excitation. *Proceedings of the 22nd Annual Meeting of ISMRM, Milan, Italy*, 2014.
73. Malik, S. J., Keihaninejad, S., Hammers, A., and Hajnal, J. V. Tailored excitation in 3D with spiral nonselective (SPINS) RF pulses. *Magnetic Resonance in Medicine*, 67(5): 1303–1315, 2012.
74. Mangasarian, O. L. Pseudo-convex functions. *Journal of the Society for Industrial & Applied Mathematics, Series A: Control*, 3(2):281–290, 1965.
75. Mansfield, P. and Harvey, P. R. Limits to neural stimulation in echo-planar imaging. *Magnetic Resonance in Medicine*, 29(6):746–758, 1993.
76. Mansfield, P., Howseman, A. M., and Ordidge, R. J. Volumar imaging using NMR spin echoes: echo-volumar imaging (EVI) at 0.1 T. *Journal of Physics E: Scientific Instruments*, 22(5):324, 1989.
77. Mao, W., Chronik, B. A., Feldman, R. E., Smith, M. B., and Collins, C. M. Consideration of magnetically-induced and conservative electric fields within a loaded gradient coil. *Magnetic Resonance in Medicine*, 55(6):1424–1432, 2006.
78. McIntyre, C. C. and Grill, W. M. Extracellular Stimulation of Central Neurons: Influence of Stimulus Waveform and Frequency on Neuronal Output. *Journal of Neurophysiology*, 88 (4):1592–1604, 2002.
79. McIntyre, C. C., Richardson, A. G., and Grill, W. M. Modeling the Excitability of Mammalian Nerve Fibers: Influence of Afterpotentials on the Recovery Cycle. *Journal of Neurophysiology*, 87(2):995–1006, 2002.
80. McNeal, D. R. Analysis of a Model for Excitation of Myelinated Nerve. *Biomedical Engineering, IEEE Transactions on*, BME-23(4):329–337, July 1976.
81. Neufeld, E., Cassarà, A. M., Montanaro, H., Kuster, N., and Kainz, W. Functionalized anatomical models for EM-neuron Interaction modeling. *Physics in Medicine and Biology*, 61(12):4390–4401, 2016.
82. Neufeld, E., Oikonomidis, I. V., Iacono, M. I., Angelone, L. M., Kainz, W., and Kuster, N. Investigation of assumptions underlying current safety guidelines on EM-induced nerve stimulation. *Physics in Medicine and Biology*, 61(12):4466–4478, 2016.
83. Nyquist, H. Certain topics in telegraph transmission theory. *American Institute of Electrical Engineers, Transactions of the*, 47(2):617–644, 1928.
84. O'Brien, G. G., Hyman, M. A., and Kaplan, S. A study of the numerical solution of partial differential equations. *Studies in Applied Mathematics*, 29(1-4):223–251, 1950.

85. Ochoa, J. and Torebjörk, E. Sensations evoked by intraneural microstimulation of single mechanoreceptor units innervating the human hand. *The Journal of physiology*, 342:633, 1983.
86. Pauly, J., Nishimura, D., and Macovski, A. A k-space analysis of small-tip-angle excitation. *Journal of Magnetic Resonance (1969)*, 81(1):43–56, 1989.
87. Pisa, S. A Complete Model for the Evaluation of the Magnetic Stimulation of Peripheral Nerves. *The Open Biomedical Engineering Journal*, 8(1), Oct 2014.
88. Poole, M. S., While, P. T., Lopez, H. S., and Crozier, S. Minimax current density gradient coils: Analysis of coil performance and heating. *Magnetic Resonance in Medicine*, 68(2): 639–648, 2012.
89. Pruessmann, K. P. Encoding and reconstruction in parallel MRI. *NMR in Biomedicine*, 19 (3):288–299, 2006.
90. Pruessmann, K. P., Weiger, M., Scheidegger, M. B., and Boesiger, P. SENSE: sensitivity encoding for fast MRI. *Magnetic Resonance in Medicine*, 42(5):952–962, 1999.
91. RamRakhyani, A. K., Kagan, Z. B., Warren, D. J., Normann, R. A., and Lazzi, G. A um-Scale Computational Model of Magnetic Neural Stimulation in Multifascicular Peripheral Nerves. *IEEE Transactions on Biomedical Engineering*, 62(12):2837–2849, Dec 2015.
92. Rasche, V., Proksa, R., Sinkus, R., Bornert, P., and Eggers, H. Resampling of data between arbitrary grids using convolution interpolation. *IEEE Transactions on Medical Imaging*, 18 (5):385–392, 1999.
93. Rattay, F. Analysis of Models for External Stimulation of Axons. *IEEE Transactions on Biomedical Engineering*, BME-33(10):974–977, Oct 1986.
94. Recoskie, B. J., Scholl, T. J., Zinke-Allmang, M., and Chronik, B. A. Sensory and motor stimulation thresholds of the ulnar nerve from electric and magnetic field stimuli: Implications to gradient coil operation. *Magnetic Resonance in Medicine*, 64(6):1567–1579, 2010.
95. Reilly, J. P. Peripheral nerve stimulation by induced electric currents: Exposure to time-varying magnetic fields. *Medical and Biological Engineering and Computing*, 27(2):101–110.
96. Reilly, J. P., Freeman, V. T., and Larkin, W. D. Sensory Effects of Transient Electrical Stimulation - Evaluation with a Neuroelectric Model. *Biomedical Engineering, IEEE Transactions on*, BME-32(12):1001–1011, Dec 1985.
97. Roth, B. J., Cohen, L. G., Hallett, M., Friauf, W., and Basser, P. J. A theoretical calculation of the electric field induced by magnetic stimulation of a peripheral nerve. *Muscle & Nerve*, 13(8):734–741, 1990.
98. Ruohonen, J., Ravazzani, P., and Grandori, F. An analytical model to predict the electric field and excitation zones due to magnetic stimulation of peripheral nerves. *IEEE Transactions on Biomedical Engineering*, 42(2):158–161, Feb 1995.

99. Saekho, S., Yip, C.-y., Noll, D. C., Boada, F. E., and Stenger, V. A. Fast-kz three-dimensional tailored radiofrequency pulse for reduced B1 inhomogeneity. *Magnetic Resonance in Medicine*, 55(4):719–724, 2006.
100. Sanchez, H., Liu, F., Trakic, A., and Crozier, S. A Simple Relationship for High Efficiency and Gradient Uniformity Tradeoff in Multilayer Asymmetric Gradient Coils for Magnetic Resonance Imaging. *IEEE Trans. Magn.*, 43(2):523–532.
101. Saritas, E., Goodwill, P., Zhang, G., and Conolly, S. Magnetostimulation Limits in Magnetic Particle Imaging. *Medical Imaging, IEEE Transactions on*, 32(9):1600–1610, Sept 2013.
102. Sarra, S. A. and Kansa, E. J. Multiquadric radial basis function approximation methods for the numerical solution of partial differential equations. *Tech Science Press*, 2(4.1):1, 2010.
103. Schaback, R. Multivariate interpolation by polynomials and radial basis functions. *Constructive Approximation*, 21(3):293–317, 2005.
104. Schaefer, D. J., Bourland, J. D., and Nyenhuis, J. A. Review of Patient Safety in Time-Varying Gradient Fields. *Journal of Magnetic Resonance Imaging*, 12(1):20–29, 2000.
105. Schmidt, M. W., Berg, E., Friedlander, M. P., and Murphy, K. P. Optimizing costly functions with simple constraints: A limited-memory projected quasi-newton algorithm. In *International Conference on Artificial Intelligence and Statistics*, page None, 2009.
106. Schneider, J. T., Kalayciyan, R., Haas, M., Herrmann, S. R., Ruhm, W., Hennig, J., and Ullmann, P. Inner-volume imaging in vivo using three-dimensional parallel spatially selective excitation. *Magnetic Resonance in Medicine*, 69(5):1367–1378, 2013.
107. Setsompop, K., Alagappan, V., Gagoski, B. A., Potthast, A., Hebrank, F., Fontius, U., Schmitt, F., Wald, L., and Adalsteinsson, E. Broadband slab selection with B1+ mitigation at 7T via parallel spectral-spatial excitation. *Magnetic Resonance in Medicine*, 61(2):493–500, 2009.
108. Siegel, A. and Sapru, H. N. *Essential neuroscience*. Lippincott Williams & Wilkins, 2006.
109. Simonetti, O. P., Duerk, J. L., and Chankong, V. An optimal design method for magnetic resonance imaging gradient waveforms. *IEEE Transactions on Medical Imaging*, 12(2):350–360, 1993.
110. So, P., Stuchly, M., and Nyenhuis, J. Peripheral Nerve Stimulation by Gradient Switching Fields in Magnetic Resonance Imaging. *IEEE Trans. Biomed. Eng.*, 51(11):1907–1914, Nov 2004.
111. Song, A. W., Wong, E. C., and Hyde, J. S. Echo-volume imaging. *Magnetic Resonance in Medicine*, 32(5):668–671, 1994.
112. Stenger, V. A., Boada, F. E., and Noll, D. C. Three-dimensional tailored RF pulses for the reduction of susceptibility artifacts in T2*-weighted functional MRI. *Magnetic Resonance in Medicine*, 44(4):525–531, 2000.
113. Sun, H., Fessler, J. A., Noll, D. C., and Nielsen, J.-F. Joint Design of Continuous Excitation k-space Trajectory and RF pulse for 3D Tailored Excitation. *Proceedings of the 22nd Annual Meeting of ISMRM, Milan, Italy*, 2014.

-
114. The CGAL Project. *CGAL User and Reference Manual*. CGAL Editorial Board, 4.9 edition, 2016.
 115. Thulborn, K. R., Waterton, J. C., Matthews, P. M., and Radda, G. K. Oxygenation dependence of the transverse relaxation time of water protons in whole blood at high field. *Biochimica et Biophysica Acta (BBA)-General Subjects*, 714(2):265–270, 1982.
 116. Trayanova, N. A., Roth, B. J., and Malden, L. J. The response of a spherical heart to a uniform electric field: a bidomain analysis of cardiac stimulation. *IEEE Transactions on Biomedical Engineering*, 40(9):899–908, Sept 1993.
 117. Turner, R. Gradient coil design: A review of methods. *Magnetic Resonance Imaging*, 11(7):903 – 920, 1993.
 118. Twieg, D. B. The k-trajectory formulation of the NMR imaging process with applications in analysis and synthesis of imaging methods. *Medical Physics*, 10(5):610–621, 1983.
 119. Vannesjo, S. J., Haerberlin, M., Kasper, L., Pavan, M., Wilm, B. J., Barmet, C., and Pruessmann, K. P. Gradient system characterization by impulse response measurements with a dynamic field camera. *Magnetic Resonance in Medicine*, 69(2):583–593, 2013.
 120. Vaziri, S. and Lustig, M. The fastest gradient waveforms for arbitrary and optimized k-space trajectories. *2013 IEEE 10th International Symposium on Biomedical Imaging*.
 121. Verveen, A. Axon diameter and fluctuation in excitability. *Acta Morphol Neerl Scand*, 5: 79–85, 1962.
 122. Wade, T. P., Alejski, A., McKenzie, C. A., and Rutt, B. K. Peripheral Nerve Stimulation Thresholds of a High Performance Insertable Head Gradient Coil. *Proceedings of the 24th Annual Meeting of ISMRM, Singapore*, 2016.
 123. Wexler, A. Computation of electromagnetic fields. *IEEE Transactions on Microwave Theory and Techniques*, 17(8):416–439, 1969.
 124. Wu, X., Vaughan, J. T., Uğurbil, K., and Van de Moortele, P.-F. Parallel excitation in the human brain at 9.4 T counteracting k-space errors with RF pulse design. *Magnetic Resonance in Medicine*, 63(2):524–529, 2010.
 125. Ye, H., Cotic, M., Fehlings, M. G., and Carlen, P. L. Transmembrane potential generated by a magnetically induced transverse electric field in a cylindrical axonal model. *Medical & biological engineering & computing*, 49(1):107–119, 2011.
 126. Yee, K. Numerical solution of initial boundary value problems involving Maxwell's equations in isotropic media. *IEEE Transactions on antennas and propagation*, 14(3):302–307, 1966.
 127. Zelinski, A. C., Wald, L. L., Setsompop, K., Alagappan, V., Gagoski, B. A., Goyal, V. K., Hebrank, F., Fontius, U., Schmitt, F., and Adalsteinsson, E. Comparison of three algorithms for solving linearized systems of parallel excitation RF waveform design equations: Experiments on an eight-channel system at 3 Tesla. *Concepts in Magnetic Resonance Part B: Magnetic Resonance Engineering*, 31(3):176–190, 2007.

Bibliography

128. Zhang, B., Yen, Y.-F., Chronik, B. A., McKinnon, G. C., Schaefer, D. J., and Rutt, B. K. Peripheral nerve stimulation properties of head and body gradient coils of various sizes. *Magnetic Resonance in Medicine*, 50(1):50–58, 2003.
129. Zhao, H., Crozier, S., and Liu, F. Finite difference time domain (FDTD) method for modeling the effect of switched gradients on the human body in MRI. *Magnetic Resonance in Medicine*, 48(6):1037–1042, 2002.

Curriculum Vitae

Personal Information

Name: Mathias Davids
Date of birth: February 18th, 1989
Place of birth: Wismar
Marital status: Single
Father: Frank Davids
Mother: Gabriele Davids

Education

- 2014 to present** Doctoral Candidate, Computer Assisted Clinical Medicine, Medical Faculty Mannheim, Heidelberg University, Germany and A. A. Martinos Center for Biomedical Imaging, Dept. of Radiology, Massachusetts General Hospital, Charlestown, USA
Minimizing the Adverse Effects of Electric Fields in Magnetic Resonance Imaging using Optimized Gradient Encoding and Peripheral Nerve Models
- 2013** Visiting student at Martinos Center for Biomedical Imaging, Dept. of Radiology, Massachusetts General Hospital, Charlestown, USA
Completion of Master's Thesis: Fast, robust optimization of k-space trajectories for 3-D spatially selective parallel excitation
- 2011 to 2013** "Biomedical Engineering" at Heidelberg University, Germany (Master of Science, final grade 1.3)
Master's Thesis: A novel analytic approach for multidimensional RF excitation using time-optimal k-space trajectories in MRI
- 2012 to 2013** Student Assistant, Computer Assisted Clinical Medicine, Medical Faculty Mannheim, Heidelberg University, Mannheim
Development of methods for fully-automated phantom based quality evaluation for multi-center MRI studies
- 2008 to 2011** "Medical Engineering Sciences" at University of Lübeck, Germany, (Bachelor of Science, final grade 1.6)
Bachelor Thesis: Automated temperature-guided dosimetry for minimal-invasive LASER-photo-coagulation of the retina
- 1999 to 2008** Secondary School Wismar, (Abitur degree, final grade 1.2)

Publications

Peer-reviewed journal articles:

M. Davids, B. Guérin, M. Malzacher, L. Schad and L. Wald, "Predicting Magnetostimulation Thresholds in the Peripheral Nervous System using Realistic Body Models", *Scientific Reports*, (7), p. 5316, 2017

M. Davids, L. Schad, L. Wald, B. Guérin, "Fast three dimensional inner volume excitations using parallel transmission and optimized k-space trajectories", *Magnetic Resonance in Medicine*, 76 (4), pp. 1170–1182, 2016

M. Davids, M. Ruttorf, F. Zöllner, and L. Schad, "Fast and robust design of time-optimal k-space trajectories in MRI", *IEEE Transactions on Medical Imaging*, 34 (2), pp. 564–577, 2015

M. Davids, F. Zöllner, M. Ruttorf, F. Nees, H. Flor, G. Schumann, L. Schad and the IMAGEN Consortium, "Fully-automated quality assurance in multi-center studies using MRI phantom measurements", *Magnetic Resonance Imaging*, 32, pp. 771–780, 2014

Conference contributions:

M. Davids, B. Guérin, L. Schad and L. Wald, "Modeling of Peripheral Nervous Stimulation Thresholds in Realistic Body Models", *Proceedings of the 25th Annual Meeting of the ISMRM*, Honolulu, HI, USA, 2017

M. Davids, B. Guérin, L. Schad, and L. Wald., "Realistic Simulation of Peripheral Nerve Stimulations in Magnetic Particle Imaging for Improved MPI Molecular Imaging in Humans", *World Molecular Imaging Congress*, New York, USA, (2016), p.557.

M. Davids, B. Guérin, L. Wald, and L. Schad., "B0-Robust Slice-Selective Excitations for Ultra-High Field with Flip-Angle Mitigation Using Parallel Transmission". *Proceedings of the 24th Annual Meeting of the ISMRM*, Singapore, 2016

M. Davids, B. Guérin, L. Wald, and L. Schad, "Ultra-fast inner volume excitations with parallel transmission at 7 Tesla using fully optimized B0-robust k-space trajectories", *In Proceedings of the 23rd Annual Meeting of the ISMRM*, Toronto, Canada, 2015

M. Davids, B. Guérin, L. Schad, and L. Wald, "Optimization of fast k-space trajectories for 3D spatially selective parallel excitations", *In Proceedings of the 22nd Annual Meeting of the ISMRM*, Milan, Italy, 2014

M. Davids, M. Ruttorf, F. Zöllner, and L. Schad, "Fast and robust design of time-optimal k-space trajectories", *In Proceedings of the 22nd Annual Meeting of the ISMRM*, Milan, Italy, 2014

M. Davids, F. Zöllner, M. Ruttorf, F. Nees, H. Flor, G. Schumann, and L. Schad, "Automated quality determination of MRI phantom measurements for multi-center studies", Abstract band of the 43rd Annual Meeting of the German Association of Medical Physics, Jena, Germany, 2012, pp. 497–498

Awards:

Magna Cum Laude Merit Award

M. Davids, B. Guérin, L. Schad and L. Wald, "Modeling of Peripheral Nervous Stimulation Thresholds in Realistic Body Models", International Society for Magnetic Resonance in Medicine (ISMRM), Honolulu, 2017

Summa Cum Laude Merit Award

M. Davids, B. Guérin, L. Wald, and L. Schad., "B0-Robust Slice-Selective Excitations for Ultra-High Field with Flip-Angle Mitigation Using Parallel Transmission", International Society for Magnetic Resonance in Medicine (ISMRM), Singapore, 2016

Magna Cum Laude Merit Award

M. Davids, B. Guérin, L. Wald, and L. Schad, "Ultra-fast inner volume excitations with parallel transmission at 7 Tesla using fully optimized B0-robust k-space trajectories", International Society for Magnetic Resonance in Medicine (ISMRM), Toronto, 2015

Magna Cum Laude Merit Award

M. Davids, M. Ruttorf, F. Zöllner, L. Schad, "Fast and robust design of time-optimal k-space trajectories", International Society for Magnetic Resonance in Medicine (ISMRM), Milano, 2014

Magna Cum Laude Merit Award

M. Davids, B. Guérin, L. Schad, L. Wald, "Optimization of fast k-space trajectories for 3D spatially selective parallel excitations", International Society for Magnetic Resonance in Medicine (ISMRM), Milano, 2014

Scholarship for Best Student in the International Master's Program Biomedical Engineering, Medical Faculty Mannheim, Heidelberg University, 2013

Acknowledgments

Zunächst danke ich Herrn Prof. Lothar Schad für die Betreuung meiner Arbeit, die uneingeschränkte Unterstützung in den vergangenen (mittlerweile fast sechs) Jahren in verschiedensten Belangen, und im Speziellen für das Aufrechterhalten eines angenehmen und entspannten Klimas in der Arbeitsgruppe, das mir in der Form bislang nur äußerst selten begegnet ist.

A very special (English) thanks goes to Lawrence L. Wald and Bastien Guérin who (almost out of nowhere) became important mentors throughout the last years: without your guidance, experience, and support many of the findings in this work would not have been possible.

Mein besonderer Dank gilt Herrn Prof. Martin Schmelz für zahlreiche interessante und äußerst aufschlussreiche Gespräche über Anatomie und Physiologie des Nervensystems die den positiven Fortgang des letzten (und vermutlich wichtigsten) Teils der Arbeit maßgeblich unterstützt und mitbestimmt haben.

Darüber hinaus geht mein großer Dank an Matthias Malzacher für unzählige hilfreiche Diskussionen über die Tücken der Feldsimulationen und Schaltkreise (sowie für das beständige Auffüllen des Wasserfilters; ich gelobe Besserung).

Vielen Dank an Valerie Klein, die bereits in den ersten Wochen ihrer Masterarbeit wertvolle und aufschlussreiche Beiträge zu den Nervensimulationen geliefert hat.

Ein großes Dankeschön geht an Nadja Meßner, Tanja Gaa und Matthias Malzacher für die tolle und verlässliche Zusammenarbeit im Rahmen der MR Hochschulvorlesung.

Dem gesamten CKM-Team danke ich für ein grandioses, hilfsbereites und ausnahmslos angenehmes Klima in den vergangenen Jahren; die eine oder andere sportliche Betätigung (im weitest möglichen Sinne) eingeschlossen.

Für alles das was thematisch in den äußeren Rahmen dieser Arbeit *nicht* passt (und gerade deshalb über die Jahre hinweg stets erneuerten Antrieb und Durchhaltevermögen geschaffen hat) danke ich von Herzen Nils Hohmuth, Dennis Storz, Verena Brekle, Lara Hohmuth, Kira Hohmuth, Charlotte Kiessling, Carola Link, Jonathan Lommen, Barbara Wichtmann, Teresa Knorz, Ulrich Kühne, Saskia Deising, Timo Dalinghaus, Michael Steinhauser, Oliver Rode, Johanna Ries, Marie Sommer sowie Carolin und Nicolai Stern.

Zu guter Letzt geht mein größter Dank an meine Familie, die mir während meines kompletten Studiums beständig den Rücken frei gehalten hat!